

Cool Gas in Brightest Cluster Galaxies

Cool Gas in Brightest Cluster Galaxies

Proefschrift

ter verkrijging van
de graad van Doctor aan de Universiteit Leiden,
op gezag van de Rector Magnificus prof. mr. P.F. van der Heijden,
volgens besluit van het College voor Promoties
te verdedigen op donderdag 6 oktober 2011
klokke 11.15 uur

door

Johannes Bernardus Raymond Oonk

geboren te Hengelo
in 1981

Promotiecommissie

Promotor: Prof. dr. W. Jaffe

Overige leden: Dr. J. Brinchmann
Prof. dr. A. C. Fabian (University of Cambridge)
Prof. dr. F. P. Israel
Prof. dr. K. Kuijken

ISBN: 978-94-6191-031-8

Contents

	Page
Chapter 1. Introduction	1
1.1 Galaxy Clusters	1
1.2 Cool-core Clusters	1
1.3 The hot gas at $T > 10^7$ K	2
1.4 The cool gas at $T < 10^4$ K	2
1.5 This Thesis	3
1.6 Outlook	5
Chapter 2. Warm Molecular Gas in Abell 2597 and Sersic 159-03	7
2.1 Introduction	8
2.1.1 This project	10
2.2 Observations and reduction	10
2.2.1 Near Infrared Data	10
2.2.2 X-ray Data	13
2.2.3 Radio Data	14
2.3 Abell 2597 – Gas Distribution	14
2.3.1 Molecular gas	15
2.3.2 Ionised gas	16
2.4 Abell 2597 – Gas Kinematics	16
2.4.1 Molecular gas	17
2.4.2 Ionised gas	18
2.4.3 Filaments	18
2.5 Sersic 159-03 – Gas Distribution	19
2.5.1 Molecular gas	20
2.5.2 Ionised gas	20
2.6 Sersic 159-03 – Gas Kinematics	21
2.6.1 Molecular gas	21
2.6.2 Ionised gas	22
2.6.3 Filaments	22
2.7 Physical Conditions in the Warm Molecular Gas	22
2.7.1 A2597: Selected regions	23
2.7.2 S159: Selected regions	24
2.7.3 Thermal excitation of the molecular gas	24
2.7.4 Luminosity of the Warm Molecular Gas	26
2.7.5 Mass of the Warm Molecular Gas	27
2.7.6 Mass of the Ionised Gas	27
2.7.7 Stability of the Filaments	28
2.8 X-ray and Radio Emission	29

2.8.1	X-ray emission	29
2.8.2	Radio emission	30
2.9	Summary	32
2.10	Conclusions	35
A.1	58
A.2	58
A.3	58
Chapter 3.	FUV emission in Abell 2597 and Abell 2204	67
3.1	Introduction	68
3.1.1	This project	69
3.2	70
3.2.1	HST ACS-SBC imaging	70
3.2.2	Optical data	71
3.2.3	Radio data	71
3.2.4	X-ray data	72
3.3	72
3.3.1	FUV: A2597 and A2204.	72
3.3.2	Optical: A2597 and A2204	73
3.3.3	Radio and X-ray emission	73
3.3.4	Surface brightness profiles	75
3.4	Total FUV/U emission	76
3.4.1	Bruzual & Charlot 2003 SSP models	76
3.5	Excess FUV/U: Stellar Origin ?	77
3.5.1	Contamination by line emission	77
3.5.2	Removing the old stellar population	79
3.5.3	The $FUV_{v,exc}/U_{v,exc}$ excess ratio	80
3.5.4	Nebular continuum emission	81
3.5.5	Dust intrinsic to the BCG	82
3.6	Star formation	83
3.6.1	The $H\alpha$ nebula	83
3.6.2	FUV and $H\alpha$ star formation rates	84
3.6.3	Dust and gas mass estimates from A_V	85
3.7	Excess FUV/U: Non-stellar Origin ?	86
3.7.1	Active Galactic Nuclei	86
3.7.2	Non-thermal processes	86
3.8	86
3.8.1	Crawford & Fabian 1993	86
3.8.2	Hicks et al. 2010	88
3.8.3	The extinction law in BCGs	88
3.8.4	A2597 versus A2204	90
3.9	91
B.1	116
B.2	119
B.3	121

Chapter 4. Herschel photometry of brightest cluster galaxies in cooling flow clusters	123
4.1 Introduction	124
4.2 Observations	124
4.2.1 PACS Data	125
4.2.2 SPIRE Data	125
4.3 Results	126
4.4 Discussion and conclusions	128
4.5 Acknowledgements	129
Chapter 5. Herschel observations of FIR emission lines in brightest cluster galaxies	135
5.1 Introduction	136
5.2 Observations	137
5.3 Results	138
5.4 Discussion	140
5.5 Conclusions	141
5.6 Acknowledgements	141
Chapter 6. Optical Line Emission in BCGs	143
6.1 Introduction	144
6.1.1 This Project	144
6.1.2 Targets	145
6.2	145
6.3	146
6.3.1 Spatially integrated spectra	147
6.3.2 Variations along the Slit	148
6.4 Diagnostic diagrams	149
6.5	150
6.5.1 Dust	150
6.5.2 Temperature	151
6.5.3 Density	151
6.5.4 Metallicity	152
6.5.5 Ionisation Parameter	152
6.6 MAPPINGS III line modelling	153
6.6.1 Stars	154
6.6.2 AGN	155
6.6.3 Bremsstrahlung	156
6.7 Combining Stars and Bremsstrahlung	157
6.7.1 The combined model grid	157
6.7.2 Exploring the best-fit combined models	158
6.7.3 Gas heating in A2597	161
6.8	165
6.8.1 Warm, low-ionisation gas in BCGs	165
6.8.2 Comparison with previous studies	167
6.9	169
C.1	196

C.1.1 Photon spectra A2597	196
C.1.2 Ionisation fractions A2597	203
Nederlandse samenvatting	205
Curriculum Vitae	213
Nawoord	215

Chapter 1

Introduction

1.1 Galaxy Clusters

Clusters of galaxies were originally discovered by Charles Messier and William Herschel. Their extragalactic nature was first established by Vesto Slipher and Edwin Hubble. They are the most massive ($M \sim 10^{13-15} M_{\odot}$), gravitationally bound structures in the known universe and they are the objects in which the need for dark matter was first pointed out by Fritz Zwicky in 1937. Recent investigations show that the baryonic matter represents about 16% of their total mass. Dark matter makes up the remaining 84% of the mass. About 80% of the baryons are situated in the intracluster medium (ICM). The rest is situated in the stars that make up the galaxies within the cluster (e.g. see Peterson & Fabian 2006, for a recent review).

One of the major goals in modern astronomy is to understand the formation of large-scale structure and the evolution of galaxies. Galaxy clusters provide us with the means to do just this. Hierarchical structure formation dictates that the most massive objects, i.e. clusters, form last, which means now. Studying the clustering of galaxies allows us to constrain cosmological models. The dense and crowded environment strongly affects the evolution of galaxies living in clusters and allows us to study important physical processes such as gas stripping and kinematical segregation. The lensing properties of galaxy clusters also make them great tools to study their mass, the properties of dark matter and the details of high-redshift galaxies.

In recent years it has become clear that galaxy clusters are particularly well suited to study the feedback processes that are thought to inhibit gas cooling (e.g. Peterson & Fabian 2006; McNamara & Nulsen 2007). The cooling of hot gas to form stars is essential for the growth of massive galaxies. At the same time, cosmological simulations show that these galaxies require an efficient feedback mechanism to halt gas cooling at early times, preventing them from becoming too massive and too blue. The central galaxies in galaxy clusters are the most massive galaxies known. The proximity of these galaxies makes them ideal laboratories in which the details of gas cooling, galaxy growth and feedback can be studied in great detail. These feedback processes are the topic of my thesis and they play an important role in structure formation at all physical scales and times.

1.2 Cool-core Clusters

In the same way as for galaxies, clusters grow by either accreting mass from their surroundings or by cluster mergers. It is estimated that about 20% of all clusters are currently undergoing or have recently undergone a cluster merger. The remainder is in a quasi-relaxed state and about half of these have central regions showing hot X-ray emitting gas at $T \sim 10^8$ K, that is dense

enough to cool from its own radiation within a Hubble time. We call these objects *cool-core clusters*, although they are also referred to as *cooling flow clusters*. At the heart of these clusters one finds the centrally dominant (cD) galaxy. These galaxies are the largest known galaxies. They dominate over the other cluster galaxies in stellar light and hence they are also referred to as *Brightest Cluster Galaxies* (BCG).

1.3 The hot gas at $T > 10^7$ K

X-ray imaging of cool-core clusters shows that these objects contain cool central regions (e.g. Peterson & Fabian 2006). In these regions radiative cooling models imply that cooling flows with mass deposition rates up to about $1000 M_{\odot}/\text{yr}$ could operate. Typically the hot ($T \sim 10^8$ K) X-ray gas in a cool-core cluster has a cooling time less than 1 Gyr within a region of a few hundred kpc centered on the BCG. More recently, X-ray spectroscopy with the latest generation of satellites (i.e. *XMM Newton* and *Chandra*) has shown that little to no gas cools below $T \sim 10^7$ K, (e.g. Peterson & Fabian 2006). The processes responsible for halting the cooling of this hot X-ray gas are strongly debated, but generally all involve some form of reheating the gas.

The currently favored process invokes mechanical inputs from the central AGN. In this picture the central AGN acts as the thermal regulator of the ICM via energetic outflows, thus connecting the smallest scales with the largest scales in galaxy clusters. These outflows present themselves as radio jets and bubbles. Their interaction with the hot gas is inferred from their coincidence with depressions in the distribution of the X-ray emission in cool-core clusters. These depressions are known as *X-ray cavities* (e.g. Böhringer et al. 1993; McNamara et al. 2000). From a kinematical point of view the outflows contain enough energy to counter-act cooling of the hot ICM gas (Birzan et al. 2004; Dunn & Fabian 2006). However, very little is known about the detailed interaction between the non-thermal radio plasma and the surrounding hot X-ray gas.

For a typical cool-core cluster the amount of radiative cooling that needs to be balanced by re-heating is about $L_X \sim 10^{44}$ erg/s.

1.4 The cool gas at $T < 10^4$ K

Although little to none of the hot X-ray gas cools below 10^7 K, cool-core clusters do contain significant amounts of cooler gas with $T < 10^4$ K. As much as $10^{10-11} M_{\odot}$ has been found in cold ($T \sim 30$ K) H_2 from CO observations in the most massive systems (e.g. Edge 2001; Salome & Combes 2003). High spatial resolution observations show that this gas is locked up in thin, long filamentary structures within a 50 kpc region centered on the BCG (e.g. Donahue et al. 2000; Fabian et al. 2008; Salome et al. 2011).

Considerably smaller amounts of ionised and molecular gas at $T \sim 10^{2-4}$ K are also found in these systems. These gas phases represent a cooling problem in their own right, as they are far too luminous to simply be gas cooling through this temperature regime. This cool gas must therefore also be re-heated and re-ionized (e.g. Heckman et al. 1989; Voit & Donahue 1997; Jaffe et al. 2005). The most problematic phases are the ionised gas at $T \sim 10^4$ K and the warm molecular gas at $T \sim 2000$ K. The ionised gas has a typical luminosity $L_{\text{HII}} \sim 50 \times L_{\text{H}\alpha} \sim 10^{43-44}$ erg s^{-1} (Heckman et al. 1989; Crawford et al. 1999; Jaffe et al. 2005).

The warm molecular gas has a typical luminosity $L_{H_2} \sim 10 \times L_{H_2\ 1-0\ S(1)} \sim 10^{43}$ erg s⁻¹. Here we have assumed that the molecular gas is in local thermodynamic equilibrium (LTE) (e.g. Jaffe et al. 2005; Oonk et al. 2010).

The molecular gas at even lower temperatures does not contribute much to the total luminosity. If we assume LTE conditions for the molecular gas at $T \sim 400$ K, then we find a typical luminosity of $L_{H_2} \sim 3 \times L_{H_2\ 0-0\ S(1)} \sim 10^{42}$ erg s⁻¹. In the temperature regime between the molecular gas at 400 K and the CO emitting gas at 30 K the gas cooling is taken over by the far-infrared neutral and ionised lines such as [OI] at 63 μm and [CII] at 157 μm (Maloney et al. 1996). Our Herschel observations now show for the first time that cool-core BCGs emit strongly in these lines. The total emission in these far-infrared lines is about $L_{FIR,line} \sim 10^{43}$ erg s⁻¹.

The cooling problem for the cooler gas phases may seem less daunting than the cooling problem for the hot X-ray gas, because its total radiative cooling luminosity never exceeds that of the hot gas. However, there are important differences regarding the physical and temporal scales on which the heating is required. The hot X-ray gas requires a region with a size of about 200 kpc in diameter to be re-heated. The cool gas requires a similar amount of reheating in a region with a size of only 50 kpc in diameter. This means that we need a lot more energy per unit volume in order to reheat the cool gas.

The temporal scales for the required re-heating also differ vastly. The higher density cooler gas phases have a much shorter cooling time than the lower density X-ray emitting hot gas. While the hot gas may be balanced by sporadic AGN outbursts we require continuous re-heating for the cool gas.

1.5 This Thesis

In the last four years I have worked on observing and understanding the mass, temperature, excitation and dynamical structure of the baryonic gas phases in cool-core clusters. In particular I have focused on the cool gas at $T \sim 10^{2-4}$ K. These observations have allowed me to compare in detail the distribution and condition of this gas to the X-ray emitting and radio emitting structures in the central regions of these clusters. The X-ray emitting gas represents the primary source of mass in the system and radio emitting gas traces the primary source of local energy input.

Chapter 2

In chapter two we discuss near-infrared observations obtained with integral-field spectrograph *Spectrograph for INtegral Field Observation in the Near-Infrared* (SINFONI) mounted on the *Very Large Telescope* (VLT). We have observed the BCGs in the cool-core clusters *Abell 2597* and *Sersic 159-03*. Using our dedicated, self-written, reduction pipeline we map, for the first time, the ionised and warm molecular gas in three dimensions in these systems. This gas is found in filamentary structures extending out to 20 kpc from the nucleus. We find that the ionised and molecular gas are strongly coupled in both distribution, intensity and dynamics. We detect signatures of an interaction between the AGN and this gas in the central few kpc of the BCGs. However, beyond this region the gas is dynamically cold and its support

remains to be explained. In agreement with previous two dimensional investigations we show that a serious cooling problem exists for the cooler gas phases in cool-core clusters (e.g. Heckman et al. 1989; Jaffe et al. 2005). The molecular gas is found to be in LTE at $T \sim 2000$ K. This implies that the H_2 emitting gas is dense ($n \geq 10^6 \text{ cm}^{-3}$) and not in pressure equilibrium with the HII emitting gas (Jaffe et al. 2005).

Chapter 3

In chapter three we discuss far-ultraviolet (FUV) imaging obtained with the *Advanced Camera for Surveys* (ACS) mounted on the *Hubble Space Telescope* (HST) and optical imaging obtained with the *FOcal Reducer and low-dispersion Spectrograph* (FORS) mounted on the VLT. We have observed the BCGs in the cool-core clusters *Abell 2597* and *Abell 2204*. The high-resolution HST observations show that the FUV continuum emission is found to be extended in filamentary structures centered on the BCG nucleus. We map for the first time the FUV to optical continuum emission ratio in the central 20 kpc of these BCGs. We find that this ratio is high in the nuclear and filamentary regions. Interpreting the observed emission directly in terms of young stars requires the presence of a large number of very hot O-stars. The required amount of O-stars does not contradict current estimates for the starformation rates in these systems. However, upon correcting for nebular continuum emission and dust intrinsic to the BCG, the temperature of the required stars becomes a problem and a purely stellar interpretation does not suffice. Likewise, simple, non-stellar models also fail in explaining the observations. A more detailed investigation is necessary to reveal the origin of the FUV to optical emission ratio.

Chapter 4

In chapter four we discuss far-infrared (FIR) imaging obtained with the *Photodetector Array Camera and Spectrometer* (PACS) and the *Spectral and Photometric Imaging Receiver* (SPIRE) mounted on the *Herschel Space Telescope* (Herschel). We have observed the BCGs in the cool-core clusters *Abell 1068*, *Abell 2597* and *Zw3146* (*Zw3146* is also known as *ZwCl 1021.0+0426*). The FIR emission is spatially unresolved in all three systems at the resolution of the Herschel detectors. We present the first well-sampled (global) spectral energy distributions for the dust continuum emission in these cool-core BCGs. We fit the data in the 24-850 μm range with simple, modified blackbody spectra. Interpreting these fits shows that at least two temperature components are needed to fit the data. The derived dust temperatures are very similar in all three objects. The first component has a temperature around 20 K and the second component has a temperature around 50 K. The coldest component dominates the derived dust mass for these systems. The FIR-bright BCGs in *Abell 1068* and *Zw3146* have a dust mass of about $10^{8-9} M_{\odot}$. The FIR-weak BCG in *Abell 2597* has a dust mass that is lower by about a factor of ten. The gas to dust mass ratio is about 100 in all three objects.

Chapter 5

In chapter 5 we discuss FIR integral-field spectroscopy obtained with PACS mounted on the Herschel Space Telescope. We have observed the BCGs in the cool-core clusters *Abell 1068* and *Abell 2597*. We detect, for the first time, the strong, FIR, atomic cooling lines from [CII], [NII] and [OI] in these cool-core BCGs. The line emission is spatially unresolved at the resolution of PACS and imply cold, molecular gas masses in excess of $10^9 M_{\odot}$. At the current level of the absolutely flux accuracy for PACS the FIR line ratios do not differ significantly from local FIR-bright galaxies and the excitation can be explained with young stars. However, with improved calibrations this will need to be reassessed and the line ratios will also have to be investigated in the context of other excitation mechanisms such as collisional heating (Ferland et al. 2009) and heating by high-energy photons (Donahue & Voit 1991). The widths of the FIR lines are found to be consistent with optical and near-infrared measurements. However, they are considerably wider, by about 35 percent, than lower rotational (low-J) CO lines (Edge 2001; Salome & Combes 2003). The line profiles in both BCGs show evidence for more than one velocity component in the gas.

Chapter 6

In chapter 6 we discuss optical spectroscopy with FORS mounted on the VLT in combination with *MAPPINGS III* (Groves 2004) photoionisation modeling. We have observed the BCGs in the cool-core clusters *Abell 2597*, *Abell 2204* and *Sersic 159-03*. We find that these BCGs are extreme examples of dusty, Low Ionisation Nuclear Emission line Regions (LINERS) over tens of kpc. The optical [OI] to $H\alpha$ ratio is remarkably high and constant in these systems as compared to other types of galaxies. Such line ratios can not be produced by stellar excitation. Using *MAPPINGS III*, we investigate in detail three alternative excitation sources for *Abell 2597*; (i) AGN, (ii) Bremsstrahlung, and (iii) a combination of stars and Bremsstrahlung. In agreement with previous investigations we find that these models can explain most of the observed line ratios to within a factor of two. The most problematic ratios involve lines from Helium and Neon. AGN models are ruled based out on the decrease in ionisation with distance from the nucleus (Johnstone & Fabian 1988; Heckman et al. 1989). A single, diffuse, ionisation source, such as for example Bremsstrahlung is favored. Energetically, this is possible for *Abell 2597*, but only if we invoke an ultra-soft X-ray component. There is tentative evidence for the existence of such a component in *Abell 2597*. However, it is not clear if such a model can be applied to all cool-core BCGs. Alternatively, a collisional heating model involving cosmic rays has been proposed and may provide a viable solution (Ferland et al. 2009).

1.6 Outlook

In the last decade there has been an enormous increase in observational data for cool-core BCGs. Particularly, high spatial resolution X-ray data and integral-field spectroscopy in the optical, near-infrared and sub-millimeter regimes. In the coming years, new telescopes, such

as the *Atacama Large Millimeter Array* (ALMA), the *James Webb Space telescope* (JWST), the *Extended Very Large Array* (EVLA), the *Low Frequency Array* (LOFAR) and the *European Extremely Large Telescope* (E-ELT) will enter the scene.

Observations of cool-core BCGs with these telescopes will further revolutionise the field and, together with the existing data, allow us to make detailed maps of gas heating versus gas cooling at a common spatial resolution of 1 arcsec or less. This will enable us to trace gas cooling from $T=10^8$ K to $T=10$ K as a function of position in the cluster core and match it to detailed X-ray and radio maps.

Better measurements of crucial gas properties, such as density, temperature and metallicity, are urgently needed. For some gas phases, such as the warm H_2 gas, this will become possible with the new telescopes mentioned above. For other gas phases, such as the optical HII gas, new methods still need to be developed in order to further constrain these properties.

Bibliography

- Böhringer H., Voges W., Fabian A. C., Edge A. C., Neumann D. M., 1993, MNRAS, 264, 25
Birzan L., Rafferty D. A., McNamara B. R., Wise M. W., Nulsen P. E. J., 2004, ApJ, 607, 800
Crawford C. S., Allen S. W., Ebeling H., Edge A. C., Fabian A. C., 1999, MNRAS, 306, 857
Donahue M., Voit G. M., 1991, ApJ, 381, 361
Donahue M., Mack J., Voit G. M., Sparks W., Elston R., Maloney P. R., 2000, ApJ, 545, 670
Dunn R. J. H., Fabian A. C., MNRAS, 373, 959
Edge A. C., 2001, MNRAS, 328, 762
Fabian A. C., Johnstone R. M., Sanders J. S., Conselice C. J., Crawford C. S., Gallagher J. S., Zweibel E., 2008, Nat., 454, 968
Ferland G. J., Fabian A. C., Hatch N. A., Johnstone R. M., Porter R. L., van Hoof P. A. M., Williams R. J. R., 2009, MNRAS, 392, 1475
Groves B. A., 2004, Dust in Photoionized Nebulae, Ph.D. Thesis, Australian National University, Australia
Heckman T. M., Baum S. A., van Breugel W. J., McCarthy, P., 1989, ApJ, 338, 48
Jaffe W., Bremer M.N., Baker K., 2005, MNRAS, 360, 748
Johnstone R. M., Fabian A. C., 1988, MNRAS, 233, 581
Maloney P. R., Hollenbach D. J., Tielens A. G. G. M., 1996, ApJ, 466, 561
McNamara B. R., Wise M., Nulsen P. E. J., David L. P., Sarazin C. L., Bautz M., Markevitch M., Vikhlinin A., Forman W. R., Jones C., Harris, D. E., ApJ, 534, 135
McNamara B. R., Nulsen, P. E. J., 2007, ARA&A, 45, 117
Oonk J. B. R., Jaffe W., Bremer M. N., van Weeren R. J., 2010, MNRAS, 405, 898
Oonk J. B. R., Hatch, N. A., Jaffe W., Bremer M. N., van Weeren R. J., 2011, MNRAS, 414, 2309
Peterson J. R., Fabian A. C., 2006, PhR, 427, 1
Salome P., Combes F., 2003, A&A, 412, 657
Salome P., Combes F., Revaz Y., Downes D., Edge A. C., Fabian A. C., 2011, A&A, 531, 85
Voit G. M., Donahue M., 1997, ApJ, 486, 242
Wrathmall S. A., Gusdorf A., Flower D. R., MNRAS, 2007, 382, 133

Chapter 2

The Distribution and Condition of the Warm Molecular Gas in Abell 2597 and Sersic 159-03

We have used the SINFONI integral field spectrograph to map the near-infrared K-band emission lines of molecular and ionised hydrogen in the central regions of two cool core galaxy clusters, Abell 2597 and Sersic 159-03. Gas is detected out to 20 kpc from the nuclei of the brightest cluster galaxies and found to be distributed in clumps and filaments around it. The ionised and molecular gas phases trace each other closely in extent and dynamical state. Both gas phases show signs of interaction with the active nucleus.

Within the nuclear regions the kinetic luminosity of this gas is found to be somewhat smaller than the current radio luminosity. Outside the nuclear region the gas has a low velocity dispersion and shows smooth velocity gradients. There is no strong correlation between the intensity of the molecular and ionised gas emission and either the radio or X-ray emission.

The molecular gas in Abell 2597 and Sersic 159-03 is well described by a gas in local thermal equilibrium (LTE) with a single excitation temperature $T_{\text{exc}} \sim 2300$ K. The emission line ratios do not vary strongly as function of position, with the exception of the nuclear regions where the ionised to molecular gas ratio is found decrease. These constant line ratios imply a single source of heating and excitation for both gas phases.

MNRAS 405, 898 (2010)

J. B. R. Oonk¹, W. Jaffe¹, M. N. Bremer², R. J. van Weeren¹

¹Leiden Observatory, Leiden University, P.B. 9513, Leiden, 2300 RA, The Netherlands

²Department of Physics, H.H. Wills Physics Laboratory, Bristol University, Tyndall Avenue, Bristol BS8 1TL, United Kingdom

2.1 Introduction

Cool cores are regions at the centre of rich clusters where the hot thermal X-ray emitting gas ($T \sim 10^8$ K) is dense enough to cool radiatively within a Hubble time (see Peterson & Fabian 2006; Fabian et al. 1994, for reviews). Cooling rates of the order of $100 M_{\odot} \text{ yr}^{-1}$ and up to $1000 M_{\odot} \text{ yr}^{-1}$ have been estimated for this hot X-ray gas (e.g., Peres et al. 1998). However, recent *Chandra* and *XMM-Newton* X-ray spectra show that little or no X-ray emitting gas (<10%) cools below one third of the virial temperature (e.g., Kaastra et al. 2001; Peterson & Fabian 2006). The solution most often invoked in the literature is that some form of reheating balances the radiative cooling of the X-ray gas.

Substantial cooler gas and dust components exist in the cores of these galaxy clusters (Edge 2001; Irwin, Stil & Bridges 2001; Salome & Combes 2003; O’Dea et al. 2008). Extended 10^4 K emission-line nebulae are found surrounding Brightest Cluster Galaxies (BCG) (Heckman et al. 1989; Crawford et al. 1999; Jaffe et al. 2005, hereafter J05). These nebulae are observed to extend at least up to 50 kpc from the BCG nuclei (J05). This component at $T \sim 10^4$ K emits far more energy than can be explained by the simple cooling of the intracluster gas through this temperature i.e., additional heating is needed (Fabian et al. 1981; Heckman et al. 1989).

More recently, work in the infrared and mm-wavelengths has shown that there are large quantities of molecular gas at the centre of these clusters with temperatures between 15 and 2500 K extending at least up to 20 kpc from the BCG nuclei (e.g., J05; Jaffe & Bremer 1997; Jaffe, Bremer & van der Werf 2001; Falcke et al. 1998; Edge 2001; Edge et al. 2002; Wilman et al. 2002; Salome & Combes 2003; Hatch et al. 2005; Johnstone et al. 2007; Wilman, Edge & Swinbank 2009). The molecular gas has a cooling time of order years (Lepp & McCray 1983; Black & van Dishoeck 1987; Maloney et al. 1996). Without some form of heating one would expect this gas to collapse rapidly and form stars. Although there is strong evidence that starformation does take place at the centres of cool core galaxy clusters it is not yet observed to match the extended gas nebulae (McNamara & O’Connell 1992; O’Dea et al. 2008, Oonk et al. in prep.).

The heating and cooling of the molecular and ionised gas phases are important elements in the energetics of the cool core region. An energy source comparable to that needed to stop the hot X-ray gas from cooling is necessary to heat these colder phases (J05). The primary source of ionisation and heating of the H_2 and HII must be local to the gas (J05; Johnstone & Fabian 1988), consistent with a stellar photoionising source. However, stars are unable to explain the high temperature of the ionised gas (Voit & Donahue 1997, hereafter VD97). The molecular hydrogen lines are much stronger relative to the ionised hydrogen lines than in other types of extragalactic sources, such as AGN or starburst galaxies (e.g., J05; Davies et al. 2003, 2005).

The ratio of H_2 to HII emission lines (J05; Hatch et al. 2005), as well as detailed analysis of the mid-infrared and optical line ratios (VD97; Johnstone et al. 2007) indicate that to explain both heating and ionisation balance, photons harder than those available from O-stars are needed. However, often very high ionisation lines are missing (e.g., [Ne V] – typical of AGN spectra. If present, the source of these photons is elusive. Alternatively shock heating has been considered, however the characteristic [O III] 4363 Angstrom line is missing (VD97). High energy particles have been invoked to explain this problem (Ferland et al. 2009). It is of great importance to pinpoint the nature of the heating mechanism and include it in models of cooling

flows in galaxy clusters as well as models of galaxy growth and evolution.

Cool core clusters are the low redshift cluster scale analogs of high redshift galaxy scale cooling flows. To understand the formation of massive galaxies at high redshift and the feeding and feedback mechanisms in AGNs it is important to understand the heating of the cool gas in BCGs.

All gas phases observed in the intracluster medium require reheating to avoid catastrophic cooling. A variety of heat sources to counteract this cooling gas have been proposed over the years: AGN feedback (e.g., Churazov et al. 2001; Blanton, Sarazin & McNamara 2003; Dalla Vecchia et al. 2004; McNamara et al. 2001; Birzan et al. 2004), low velocity shock waves (Fabian et al. 2006), conduction (VD97), hot stars (VD97) and energetic particles (Ferland et al. 2009). None of these heat sources have so far been able to match the detailed characteristics of cool core galaxy clusters. Whatever the heat mechanism, the cooling region extends over hundreds of kpc across the cluster core, and heating is unlikely to balance the cooling exactly over such a large region. Some residual cooling will occur and presumably corresponds to the emission line nebulae and star clusters surrounding brightest cluster galaxies (BCG) at the centres of cool core galaxy clusters (J05; Hatch et al. 2005; Rafferty et al. 2006).

The BCGs at centres of cooling clusters fall within a region of the BPT diagram (Baldwin, Phillips & Terlevich 2004; Crawford et al. 1999, VD97) that is occupied by LINERs and AGN. In our previous samples (J05; Jaffe & Bremer 1997; Jaffe et al. 2001) we have focused on the LINER-like BCGs and we continue to do so here. These clusters were originally selected based on their high cooling rates, strong $H\alpha$, H_2 emission and low ionisation radiation. LINER-like BCGs were chosen because we wish to minimise the role that their AGN have on the global radiation field. In the work presented here we focus on two LINER-like BCGs from our previous samples, PGC 071390 in Abell 2597 (hereafter A2597) and ESO 0291-G009 in Sersic 159-03 (hereafter S159). Optical ($[O III]/H\beta$ and $[O I]/H\alpha$, Baker (2005, VD97;)) and mid-infrared spectra ($[Ne III]/[Ne II]$ and $[Ne V]/[Ne II]$, Jaffe & Bremer in prep.) of these BCGs indicate that their ionising spectrum is very soft i.e. they are extreme LINERs (VD97; Baker 2005).

However, these BCGs do contain radio-loud AGN. Their 1.4 GHz radio specific luminosity is, 29.3×10^{31} and 1.6×10^{31} $\text{erg s}^{-1} \text{Hz}^{-1}$ for A2597 and S159 (Birzan et al. 2008) respectively, which are typical for BCGs in cool core galaxy clusters (Quillen et al. 2008). In this work we will concern ourselves with the extended molecular and ionised gas surrounding the BCGs in A2597 and S159.

A2597 and to a lesser extent S159 have been the subject of numerous investigations and have been observed at many wavelengths from radio to X-rays (e.g., J05; VD97; O’Dea et al. 1994, 2004; Clarke et al. 2005). In both clusters ionised and molecular gas was observed to at least 50 kpc and 20 kpc from their BCG nuclei respectively (J05; Heckman et al. 1989). Previous investigations of these objects made use of narrowband imaging and longslit spectra. Using long slit observations we were only able to sample parts of the extended line emission and with narrowband imaging no information on the dynamics of the gas is obtained. Furthermore the emission sampled with longslits in previous observations is often strongly dominated by strong emission from the BCG nucleus. As we will show below, the emission away from the nuclei has very different characteristics.

There are a number of kinematic problems concerning the cooler gas phases in cool core

clusters. In nearby clusters ionised and molecular gas is found in thin, long lived, multi-kpc scale, filamentary structures surrounding the BCG (e.g., Fabian et al. 2008; Hatch et al. 2005; Crawford et al. 2005). These structures show smooth velocity gradients, but no rotation beyond the central few kpc (Wilman, Edge & Swinbank 2006; Hatch, Crawford & Fabian 2007). The molecular clouds in these structures are dense and without kinematic support should fall to the galaxy centre. However, they show no signs of infalling. Velocities barely exceed 100 km s^{-1} (J05; Wilman, Edge & Swinbank 2009, and this work), whereas infall velocities should exceed $\sim 600 \text{ km s}^{-1}$. Magnetic support has been invoked by Fabian et al. (2008) but there is no observational evidence yet for the required ordered magnetic fields in clusters. There has also been speculation whether or not all the molecular and ionised gas is locked up in these dense filaments or if a more diffuse underlying component exists.

2.1.1 This project

Here we present the first deep K-band integral field (IFU) spectroscopic observations of the cluster cores in A2597 and S159, taken with the Spectrograph for INtegral Field Observations in the Near-Infrared (SINFONI) on the Very Large Telescope (VLT). With these observations we sample the molecular and ionised gas phases over a major fraction of each cluster's BCG. Our observations are able to provide information on the distribution, kinematics and temperature of this gas. Using these measurements we can compare in detail the kinematic and thermal structure of the gas with the X-ray and radio structures, which represent respectively the primary source of mass in the environment and the primary source of local energy input. Similar data on three other cool core clusters has recently been presented by Wilman et al. (2009), but we are the first to make a detailed comparison of such data with radio and X-ray observations of cool core clusters

In Section 2 we describe the observations and the data reduction. We discuss the morphology and kinematics of the molecular and ionised gas in A2597 in Sections 3 and 4 and similarly for S159 in Sections 5 and 6. In Section 7 we will discuss the excitation of the molecular gas and in Section 8 we compare the observed gas structure to high resolution X-ray and Radio maps. We summarise our results in Section 9 and present our conclusions in Section 10.

Throughout this paper we will assume the following cosmology; $H_0=72 \text{ km s}^{-1} \text{ Mpc}^{-1}$, $\Omega_m=0.3$ and $\Omega_\Lambda=0.7$. For Abell 2597 at $z=0.0821$ (VD97) this gives a luminosity distance 363 Mpc and angular size scale $1.5 \text{ kpc arcsec}^{-1}$. For Sersic159-03 at $z=0.0564$ (Maia et al. 1987) this gives a luminosity distance 245 Mpc and angular size scale $1.1 \text{ kpc arcsec}^{-1}$.

2.2 Observations and reduction

2.2.1 Near Infrared Data

The near infrared (NIR) observations were performed in the K-band with the integral field spectrograph SINFONI (Eisenhauer et al. 2003; Bonnet et al. 2004) on the Very Large Telescope (VLT). SINFONI is an image slicer, slicing the image into strips before dispersing the light using 32 slitlets. The instrument has a spectral resolving power of $R \approx 4000$ in the K-band. Opting for a $8'' \times 8''$ field of view (FOV) the spatial pixels each cover an area of $0.125'' \times 0.250''$. Each

spectral pixel covers $2.45 \times 10^{-4} \mu\text{m}$ in wavelength, oversampling the resolution by a factor two (i.e. Nyquist sampling). The total on-source exposure time for each source is listed in Table 2.1.

The observations were done in a 'ABBA' pattern (A=source, B=sky) and each set was followed by a pointing observation to keep track of pointing drifts. All observations were done such that the FOV was oriented with north pointing up. The spatial extent of each slitlet is then oriented east-west. Equal amounts of time were spend on the sky and on the source. Each science observation has an exposure time of 600 seconds. Each pointing observation has an exposure time of 60 seconds. The observations were carried out in July and August of 2005 in photometric sky conditions with a typical seeing of about 0.9 arcsec in K-band.

Four fields were observed for A2597 and three fields for S159. These fields were selected to lie within areas known to have extended H α emission (J05). The observed spectral and spatial resolution, as measured from telluric lines and standard star observations, is summarised in Table 2.2.

Initial Reduction and Slit Definition

The reduction of the data was done using a combination of the ESO SINFONI pipeline recipes (*SINFONI pipeline version 1.7.1* and *CPL version 3.6.1*), ECLIPSE (Devillard 2001) and a set of dedicated IDL procedures. From the SINFONI pipeline we obtain a masterdark frame, masterflat frame, hot pixel map and a slit curvature model. Wavelength calibration, hot pixel removal, slit edge detection, distortion correction, sky removal and illumination correction as given by the pipeline were found to be inadequate for our purposes and therefore an additional set of reduction tasks was written in IDL.

The reduction was carried out as follows. Source and sky frames are corrected for dark current and flat fielded using the masterflat and masterdark frames from the SINFONI pipeline. Having estimated the slit edges (by eye) the different slits are defined and cut out of the science frames. Each of these slits is then treated independently in the subsequent reduction steps. CCD artefacts are removed from the data. Hot pixels and those affected by cosmic rays are interpolated over.

We correct for the spatial curvature of the slit optics as imaged on the detector by applying the curvature model obtained by the SINFONI pipeline using the ECLIPSE task *warping* (Devillard 2001). Slit columns which do not contain information across the full wavelength range are removed. This also removes the overlap between different slits as imaged on the CCD.

The spectra are wavelength calibrated using a set of 19 identified telluric OH lines in the wavelength range 1.95-2.30 μm (Rousselot et al. 2000). The output wavelength scale is set to $2.45 \times 10^{-4} \mu\text{m}$ per pixel thereby Nyquist sampling the data.

Sky Removal

The K-band night sky is variable on short time scales. We have rather long exposure times, as compared to the variations in the sky background. This means that there is a complicated relationship between the sky contribution in our source frame and the sky observed in our corresponding sky frame. This is readily observed by subtracting two sky frames taken directly

after each other, and leads to systematic residuals of up to 10% in the peak heights of telluric lines. A scaling between the source and its corresponding sky frame thus needs to be performed in order to decrease these residuals. The standard sky scaling performed by the ESO SINFONI pipeline reduces these residuals to about 5% and the special SINFONI pipeline sky correction utility reduces the residuals further to about 4%. In both cases it was noted that the sky removal suffered from poor wavelength matching between the sky and source frames due to flexure of the instrument.

In our approach we remove the sky emission after detailed wavelength calibration using the telluric lines. We apply a simple scaling function to the sky frame before subtracting it from the source frame. This scaling function consists of a constant and a small, linear, wavelength dependent factor. The constant is determined from the relative heights, above the continuum, of the telluric lines and assumed to hold at $2.1 \mu\text{m}$. The small, linear, wavelength dependent factor is the slope of a linear fit to the ratio of the object spectrum and its corresponding sky spectrum.

The full wavelength dependent behaviour of the sky emission between an object and a sky frame is often more complex than the simple linear function used. Here we are only interested in line emission and as such a small residual gradient in the continuum emission does not affect the analysis performed below. Our method leads to residuals that are $\leq 2\%$ in the peak heights of telluric lines. This is a significant improvement over the other methods mentioned above. In the final analysis of the line emission we checked our results carefully for telluric line residuals and removed wavelength regions affected by these from our analysis.

Illumination Correction

After correcting for any residual distortion we collapse the sky and the sky subtracted source spectra into cubes with pixel size ($0.125''$, $0.125''$, $0.000245 \mu\text{m}$). It is known that SINFONI, after all reduction steps described above, still has a varying illumination across its FOV and that this illumination is a function of wavelength (J. Reunanen priv. comm.). This is mostly due to a difference in the illumination of the various slitlets and most easily observed in the sky cubes. Defining a reference slitlet in the sky cubes we determine the variation in illumination across the FOV for each wavelength. We then correct for this variation in the sky subtracted source cubes. The correction is typically less than 10% and particularly affects wavelengths below $2.1 \mu\text{m}$.

Flux Calibration

Flux calibration is carried out using one or, if available, multiple standard star observations per night. The standard star observations are reduced in the same way as outlined for the object observations above. All standard stars observed were either O or B stars, and brighter than 8th magnitude in the K-band. The atmospheric transmission function was determined by dividing the spatially summed standard star spectrum with a black body spectrum of the appropriate temperature. The absolute flux scale is set by using 2MASS K-band magnitudes, these are accurate to 0.05 magnitude in K-band.

Extracting the line emission

Following flux calibration the source cubes are combined. The northern and southern edges of the exposures for the different fields overlap well. The eastern and western edges overlap

less well leading to a higher noise here. The most northern and southern slitlet have very low signal to noise and were removed from the data. Any remaining telluric emission is removed by defining off-source regions. These are marked by the dotted lines in Figs. 2.1 and 2.2.

Continuum emission is removed by fitting the continuum in the immediate neighbourhood of the science line. The continuum subtracted line feature is fit by a single Gaussian function, using the *mpfitpeak* routine (Markwardt 2009) within IDL. It is observed that a single Gaussian always provides a good description of the observed line profile. The line flux, centre and width are determined from this Gaussian fit. For selected regions line profiles and Gaussian fits to them are shown in Appendix A.3. The errors quoted for the fitted line properties are based on Monte-Carlo simulations.

Constructing the line maps

In order to visualise the surface brightness of the line emission we performed a Gaussian smoothing of four pixels full width at half maximum (FWHM) in both the spatial (4 pixels=0.5'') and the spectral plane (4 pixels= $9.80 \times 10^{-4} \mu\text{m}$). To visualise the kinematics of the line emitting gas a two pixel FWHM Gaussian spatial smoothing and no spectral smoothing was found to be adequate for A2597, whereas for S159 a two pixel FWHM Gaussian smoothing in both the spatial and spectral planes was performed. The degradation of the spatial and spectral resolution as a function of the smoothing kernel used is given in Table 2.2. The corresponding noise is given in Tables 2.3 and 2.4.

Surface brightness maps for all lines that could be mapped on a pixel to pixel basis are shown in Appendix A.1 and A.2. For A2597 the northern field is not shown as the signal to noise here is inadequate to show the emission on the same spatial resolution as the central and southern fields. Velocity and velocity dispersion are shown only for the strongest detected ionised and molecular gas line. We note that the velocity structure observed in all detected emission lines agrees with that shown for these lines.

2.2.2 X-ray Data

Cool core clusters were first discovered by analysing their X-ray emission. These observations lead to the still unresolved cooling flow problem for the hot X-ray gas (e.g. Peterson & Fabian 2006). In this paper we are concerned with the cooler HII and H₂ gas phases and will not focus on the cooling flow problem related to the hot X-ray gas. However, in Section 8 we will investigate whether there is a spatial correlation between the X-ray emitting gas and cooler gas phases. In order to do so we have obtained all available X-ray data from the *CHANDRA* archive. The A2597 image, Fig. 2.1, is a co-add of three separate observations having a combined exposure time of 153.7 ks (project codes 7329; 6934; 922). The S159 image, Fig. 2.2, consists of only one shallow 10.1 ks observation (project code 1668).

CHANDRA data for A2597 and S159 has previously been published by McNamara et al. (2001) and J05. A very notable difference in the X-ray emission for the two clusters is that the peak emission in A2597 is well aligned with the nucleus of the BCG, whereas in S159 the peak emission is about 8'' north of the BCG nucleus.

2.2.3 Radio Data

Out of the many heat sources proposed, AGN feedback has received the most attention in recent years. The observed anti-correlation between X-ray and radio emission, also referred to as *X-ray cavities* and *Radio bubbles*, has led to models in which the AGN outflows interact strongly with its surrounding medium (e.g. Sutherland & Bicknell 2007). The kinetic energy carried by these outflows has been calculated based on these X-ray cavities and recent results show that the mechanical power of the jet that created the X-ray cavities can be orders of magnitude larger than its radio inferred radiative power (Birzan et al. 2004, 2008; Dunn & Fabian 2006). In Section 8 we will compare our SINFONI results with high resolution radio maps to investigate how the current AGN outflows interact with the cooler gas in the cores of A2597 and S159.

A2597: A VLA 8.4 GHz map of A2597 was obtained from C. Sarazin (Sarazin et al. 1995). This map has a beam size of $0.26'' \times 0.21''$. The one sigma noise is $50 \mu\text{Jy beam}^{-1}$. It was noted that there is a significant offset of ~ 0.1 seconds in Right Ascension as compared to the 2MASS position of the BCG. Two more 8.4 GHz maps have been published (Birzan et al. 2008; Donahue et al. 2000). These have a much better agreement with the 2MASS position. We thus conclude that this offset is an error and shift the 8.4 GHz map accordingly. Detailed radio maps at lower frequencies have been published by Clarke et al. (2005) and show that there is more low level radio emission present than apparent from the 8.4 GHz map. However, the 8.4 GHz map does give a good indication of the current AGN outflows. A much higher resolution radio map at 1.3 and 5.0 GHz using very long baseline array (VLBA) interferometry has been published by Taylor et al. (1999). These observations show that the current jet has a position angle (PA) of 70 degrees.

S159: Archival VLA 8.4 GHz observations of S159 (project code: AB1190) were reduced with the NRAO Astronomical Image Processing System (AIPS). The B-configuration observations were taken in single channel continuum mode with two IFs centred at 8435 and 8485 MHz. The total on source time was 103 min. The data was flux calibrated using the primary calibrator 0137+331. We used the Perley & Taylor 1999 extension to the Baars et al. (1977) scale to set the absolute flux scale. Amplitude and phase variations were tracked using the secondary calibrator 2314-449 and applied these to the data. The data was imaged using robust weighting set to 0.5, giving a beam size of $3.26'' \times 0.67''$. The one sigma map noise is $25 \mu\text{Jy beam}^{-1}$. Radio maps of S159 at 1.4, 5.0 and 8.4 GHz were previously published by Birzan et al. (2008).

2.3 Abell 2597 – Gas Distribution

Four $8'' \times 8''$ fields were observed on and surrounding the BCG PGC071390 in A2597, see Fig. 2.1. The integration time for each exposure is 600 seconds. The central field, which includes the nucleus of PGC071390, contains 13 exposures. The south-eastern (SE) and south-western (SW) field contain 8 and 15 exposures respectively. The northern field contains 13 exposures. The overlap region between the central and southern fields is sufficient for the line emission to be mapped without problems. However, the SE and SW fields do not completely overlap everywhere. In various locations along the overlap area there are small gaps between the fields of one to two pixels ($1 \text{ spatial pixel} = 0.125''$). We interpolated these before mapping the emission. Despite this, due to the increased noise at the east, west edges of each field, this overlap region (about 10 pixels in width) between the southern fields has a rather poor signal to

noise. The northern field is offset by about $6''$ from the central field.

A four pixel spatial and spectral smoothing was applied to the data prior to fitting the lines. A single Gaussian function provides a good fit to the observed line profile. Surface brightness maps for all other lines that could be mapped on a pixel to pixel basis are shown in Appendix A.1. The northern field is not shown in these images because the signal to noise here is inadequate to show the emission on the same spatial resolution as the central and southern fields.

2.3.1 Molecular gas

The integrated line fluxes for all lines detected within the observed fields for A2597 are given in Table 2.5. All H_2 1-0 and H_2 2-1 S-transitions redshifted into the K-band ($1.95\text{-}2.40\ \mu\text{m}$) are detected. A flux value for the H_2 2-1 S(4) line has been omitted due to uncertain continuum subtraction. The H_2 2-1 S(5) and the Br δ line are too close in wavelength to be separated by our observations. None of the H_2 3-2 S-transitions were detected. As an example of the fidelity of the data we show the full K-band spectrum of the nuclear region and the south eastern filament in Fig. 2.4.

The H_2 surface brightness maps all show the same structure. As an example of the molecular gas distribution we show the surface brightness map for the H_2 1-0 S(3) line in Fig. 2.6. This map clearly shows that the peak of the molecular gas emission coincides with the stellar nucleus of PGC071390. Two extended gas structures away from the nucleus are observed. One extends north from the nucleus and hence we will refer to this structure as the northern filament. The second structure extends from the north-east to the south-west in the SE field, just south from the nucleus and hence we will refer to this structure as the southern filament.

We observe that the surface brightness of the molecular gas varies rather smoothly within the nuclear region. However, from higher spatial resolution HST imaging by Donahue et al. (2000, hereafter D00) we know, that the molecular and ionised line emission in the central $4''\times 4''$ is concentrated in narrow clumpy, filamentary structures. Here we do not have the resolution to resolve these structures. We do note some enhanced emission features, embedded within the central field, extending to the north and east away from the nucleus which are roughly coincidental with some of structures observed by D00.

The northern filament extends at least up to the northern edge of the central field, i.e., $6''$ (9 kpc) from the nucleus. This is well beyond the region in which molecular emission was detected by D00. Using deep K-band longslit spectra J05 have previously observed that the H_2 emission extends at least up to 20 kpc towards the north from the nucleus. We will see below that molecular gas can still be found in the northern field observed by us, i.e., at a distance of about 22 kpc from the nucleus, thus confirming the J05 results.

The southern filament is clearly detected in the emission of the stronger lines. This southern filament has not been observed in D00, but J05 also find molecular gas south of the nucleus (see their figures 8 and 11). The extent of the northern and southern filaments observed here is bounded by the edges of the observed fields, and it is likely that these continue beyond the regions mapped by us.

2.3.2 Ionised gas

The Pa α line is redshifted into the K-band for both galaxy clusters studied here. The line is redshifted into a region of poor atmospheric transmission, but it is the strongest ionised gas line by far in our spectra and unambiguously detected in both clusters. In A2597 the Pa α emission globally follows the H₂ emission closely, Fig. 2.6. Within the nuclear region enhanced emission is again observed towards the north and east. These features are roughly coincidental with the emission line filaments observed in D00. Beyond the nuclear region the emission extends along the northern and southern filaments, peaking in the same locations as the H₂ emission.

We also detect the Br γ , Br δ and Fe II (1.8100 μm rest wavelength) lines. The Br δ line is blended with H₂ 2-1 S(5) and these cannot be disentangled directly by our observations. In the central field we find that Br γ /Pa α = 0.082. This ratio agrees with the dust-free Case B recombination ratio of these lines for $n_e = 10^2 \text{ cm}^{-3}$ and $T = 10^4 \text{ K}$ (Osterbrock & Ferland 2006). The Case B scenario then implies that Br γ /Br δ = 1.5, and we use this ratio to disentangle the Br δ , H₂ 2-1 S(5) blend. In the nuclear region we find that Br δ and H₂ 1-0 S(5) are of similar strength.

A small dust lane has been observed in the nuclear region of A2597 (D00; Koekemoer et al. 1999). We have investigated whether differential extinction in the K-band may affect our emission line ratios. From the above value for the Br γ /Pa α ratio we find that differential extinction is unimportant in the K-band. This is confirmed by deep optical spectroscopy of A2597 by VD97 and Baker (2005). They find a V-band extinction $A_V \sim 1$ across the nebulousity. Assuming standard galactic dust ($R_V=3.1$) an $A_V \sim 1$ translates in to $A_K \sim 0.1$. This amount of extinction is negligible.

The Fe II (1.81 μm) line is redshifted to the short wavelength edge of our observed spectrum. It is unambiguously detected in the nuclear region. The decrease in the Fe II emission outwards from the nucleus, in both intensity and dispersion, appears to be much faster than for either the HII lines or the H₂ lines. The HII emission drops by a factor of 3 and the H₂ flux drops by a factor 4 from the nuclear region to a region just north of the nucleus. The Fe II emission drops by a factor of 10 for the same regions. If the Fe II emission has a different origin than hydrogen lines, for example if it is preferably coming from the AGN and the associated jet instead of the gaseous filaments, this may explain the difference. Our observations do not have the spatial resolution to investigate this in detail.

We have searched our spectra for the presence of even higher ionisation lines, such as the Si VI (1.9634 μm) line, which one would expect from typical hard AGN spectra. None of these higher ionisation lines were detected. This once more confirms the LINER nature of PGC071390. It may also indicate that the active nucleus is not the main source of ionisation of the gas observed in the core of A2597. Alternatively it would have to have an atypically soft ionising spectrum.

2.4 Abell 2597 – Gas Kinematics

A single Gaussian function gives a good description of the observed line profiles, see Appendix A.3. From the Gaussian fits of these line profiles we obtain information about the kinematical structure of the molecular and ionised gas in A2597. The velocity, with respect to the systemic velocity of PGC071390, and the velocity dispersion of the gas have been derived for all emis-

sion lines. These all show the same global kinematical structure. The velocity and velocity dispersion maps shown below differ from the surface brightness maps in that only a two pixel spatial smoothing has been applied, as supposed to a four pixel spatial and spectral smoothing. This is done to preserve as much of the velocity structure as possible and provides us with a velocity resolution of 38 km s^{-1} .

2.4.1 Molecular gas

The molecular gas in A2597 shows a wealth of small scale kinematical structure. Velocity and velocity dispersion maps were made for all H_2 lines. All show the same kinematical structure on all scales observed. As an example of this structure we have displayed the velocity and velocity dispersion maps for the H_2 1-0 S(3) line in Figs. 2.7 and 2.8. The nuclear region contains a blueshifted and a redshifted gas component at about $\pm 80 \text{ km s}^{-1}$. This is seen more clearly if we place a pseudo slit with a width of $1''$ and a PA of 105.5 degree, centred 1 kpc south of the stellar nucleus. The corresponding position-velocity diagram is shown in Fig. 2.15. The velocity structure observed in Figs. 2.7 and 2.15 is reminiscent of gas rotating around the nucleus and does not appear to be related to an expanding shell or AGN outflows.

The average velocity of gas in the nuclear region is approximately zero with respect to the systemic velocity of PGC071390 ($z=0.0821$, VD97). This shows that the gas here is situated at or near the stellar nucleus. The reason for placing the pseudo slit slightly south of the nucleus is because east of the nucleus there is a small strongly redshifted feature at $+150 \text{ km s}^{-1}$. Whether this feature is part of the global gas flow or a single event is unclear. It shows up prominently in all velocity maps. Projected on to the sky, the feature appears to be coincident with the north-eastern radio jet of PKS2322-12 the radio source in PGC071390, see Fig. 2.7. The filamentary structures extending towards the north and the south from the nucleus show smooth velocity gradients and these will be discussed in more detail below.

The velocity dispersion of the molecular gas also shows interesting structure. Globally the dispersion of the gas decreases with distance from the nucleus. It drops from an average of about 220 km s^{-1} in the nuclear region to about 100 km s^{-1} a few kpc north and the south of the nucleus. The velocity dispersion is very high in two narrow structures extending towards the east and south of the nucleus. The two-dimensional data allows us to determine the area which is disturbed to be an elongated structure of about 2 kpc by 5 kpc oriented at a PA of about 45 degrees.

Projected on to the sky these high dispersion structures appear to run along the inner, South East edge of the curved radio lobes of PKS2322-12, see Fig. 2.8. If we interpret the lobe morphology as a Wide Angle Tail, caused by the relative motion of the AGN and the external medium, then the dispersion map illustrates for the first time the turbulent wake expected from this motion. Alternatively, the region of maximum dispersion, at $\text{PA} \sim 70$ degrees from the nucleus, may represent the interaction of the current, VLBI radio jet with the surrounding medium, as has been seen in Centaurus A (Neumayer et al. 2007). In this picture we must assume that the counter-jet has been deflected near the nucleus to the South, causing the high dispersion region and radio lobe in this direction. There is, however, no evidence for a major kinematic disturbance at the point of deflection.

The highest velocity dispersion is found for the small, strongly red-shifted feature east of the nucleus. This high velocity and dispersion for this feature can be explained if this is gas that

is entrained within the AGN outflow. The feature aligns well with the current, projected jet axis (PA=70 degrees, Taylor et al. 1999).

2.4.2 Ionised gas

Velocity and the velocity dispersion maps for the ionised gas in A2597, as traced by the Pa α line, are shown in Figs. 2.7 and 2.8. We observe two key features when we compare the Pa α and H₂ derived kinematics. Firstly, globally we find that the Pa α derived kinematics follows the H₂ derived kinematics tightly. Secondly, the velocity dispersion of the Pa α emitting gas appears on average to be slightly higher than the H₂ emitting gas, especially in the nuclear region.

It may be possible that on scales below the resolution of our observations the ionised gas has a different distribution than the H₂ emitting gas. This may be especially true in the nuclear region where the active nucleus appears to be strongly interacting with the gas. The position-velocity diagram shown in Fig. 2.15 also shows that the ionised gas, as traced by the Pa α and Fe II lines, reaches slightly higher velocities in the nuclear region. D00 show that within the nuclear region the H₂ and HII gas has a very complicated and disturbed morphology and it is difficult to say how well these two trace each other on small scales here.

The kinematics of the molecular and ionised gas for A2597 derived here agrees well with previous long slit investigations by J05 and Heckman et al. (1989). O’Dea et al. (1994, hereafter O94) detected HI in absorption against the radio continuum source PKS2322-12 in A2597. The absorption observation represents a line of sight of a few arcsec along the central radio source. They find a spatially resolved broad HI component with $\sigma \sim 174 \text{ km s}^{-1}$ and a narrow unresolved HI component with $\sigma \sim 93 \text{ km s}^{-1}$ at the position of the nucleus. The width of the broad component is somewhat smaller than the width observed in HII and H₂. O94 find that the widths are consistent if one takes into account that the HI absorption measurements only sample the gas in front of the radio source, whereas the HII and H₂ measurements sample all of the gas along the line of sight.

As in our data O94 find a narrow and a broad component, but the relative strength of narrow component is much stronger in their observation. We do not see the narrow component on the nucleus. The dominance of the narrow component in the HI observations is probably caused by the $1/T_s$ dependence of the HI absorption, as pointed out by O94. T_s being the spin temperature of the HI gas. In the HI absorption spectra the cold gas at large radii in front of the nucleus is probably over-represented relative to the HII and H₂ emission spectra. We conclude, as do O94, that there is no evidence for a kinematically distinct HI component.

2.4.3 Filaments

In Fig. 2.13 we show the surface brightness, velocity and velocity dispersion along the two filamentary structures we identified in our observations of A2597. The regions used for this investigation are marked by the green and red squares in Fig. 2.3. The black points in Fig. 2.13 correspond to green squares and the red points to the red squares. Following the northern filament from slightly south of the nucleus towards the northern edge of the central field we find that the Pa α /H₂ 1-0 S(3) is approximately equal to 0.75 in the nuclear region and rapidly increases to unity outwards. The northern filament shows a smooth velocity gradient from south

to north across the nucleus, as the velocity decreases from $+50 \text{ km s}^{-1}$ to -50 km s^{-1} $2''$ north of the nucleus. At this point the velocity gradient reverses and the velocity increases again to $+50 \text{ km s}^{-1}$ towards the northern edge of the central field.

Velocity gradients and even reversals for this filament may be explained in terms of bending and stretching of the filament, perhaps due to a combination of its proper motion and gravitational forces. However, it is more likely that we observe multiple filaments, each with its own characteristic motion, along the line of sight. Our data shows that the eastern part of the northern filament is predominantly blue shifted whereas the western part is red shifted. Higher spatial resolution images taken with HST by O’Dea et al. (2004) and Oonk et al. (in prep.) show evidence that the northern filament observed here consists of at least two filamentary structures. We thus favour the latter explanation for the observed velocity structure of the northern filament

This interpretation also agrees with what is observed for more nearby galaxy clusters such as Perseus and Centaurus, where a multitude of long, thin filaments are observed along the line of sight (Fabian et al. 2008; Crawford et al. 2005; Hatch et al. 2005). The narrow spatial and velocity range observed here for the filaments however still suggest that any substructure in it will likely have a common origin. If the gas observed in the northern filament is connected to the gas detected in the northern field its velocity continues to increase to about $+150 \text{ km s}^{-1}$, as also shown by J05. From the J05 observations it appears that the gas in the central field is joined smoothly with that in the northern field, in terms of both surface brightness and dynamics.

The velocity dispersion along the northern filament decreases smoothly from 220 km s^{-1} to 100 km s^{-1} , from the nucleus to the edges of the central field. This decrease is fastest near the nucleus and slows down beyond 3 kpc north of the nucleus. This point may mark a change in the influence of the AGN upon the dynamical state of the gas.

The southern filament has a much lower surface brightness and is hence detected at a lower signal to noise. Variations along this filament are thus more difficult to detect. Following this filament from the north-east (NE) to the south-west (SW) we find that the surface brightness is highest at its NE edge whereafter it decreases slightly and becomes approximately constant. The velocity decreases from $+50 \text{ km s}^{-1}$ to about -40 km s^{-1} . The velocity dispersion remains constant at about 100 km s^{-1} along the filament. We will discuss the stability of the observed filaments in more detail below.

2.5 Sersic 159-03 – Gas Distribution

Three $8'' \times 8''$ fields were observed on and surrounding the BCG ESO291-G009 in S159, Fig. 2.2. The integration time for each exposure is 600s. The south-eastern (SE) and south-western (SW) fields contain 8 and 9 exposures respectively. The northern field contains 8 exposures. The SE field contains the nucleus of ESO 291-G009. There is no overlap between the three fields observed. A four pixel spatial and spectral smoothing was applied to the data prior to fitting the lines. A single Gaussian function provides a good fit to the observed line profiles. Surface brightness maps for all detected emission lines that could be mapped on pixel to pixel basis are shown in Appendix A.2.

2.5.1 Molecular gas

Only two out of five H_2 1-0 S-transition lines redshifted into the K-band are unambiguously detected for S159. These are the H_2 1-0 S(1) and H_2 1-0 S(3) lines. Their resulting integrated line fluxes are given in Table 2.6. The presence of the H_2 1-0 S(2) line can also be confirmed, see also Fig. 2.5. This line cannot be fitted reliably due to a strong telluric line residual in the red wing of the line profile and as such a flux value has been omitted. Tentative evidence is found for the presence of the H_2 1-0 S(0) and H_2 1-0 S(4) lines. However, both lines lie in spectral regions of poor atmospheric transmission and are close to strong telluric features, preventing us from claiming detections. We have searched for the H_2 2-1 S-transitions, but these and higher H_2 transitions remain undetected in our spectra. Except for the above mentioned two H_2 lines only the Pa α line is detected. Full K-band spectra of the nuclear region and the western filament are presented in Fig. 2.5.

The two H_2 surface brightness maps show the same structure and as an example of this we show the map for the H_2 1-0 S(3) line in Fig. 2.9. This map clearly shows that the peak of the H_2 emission is well aligned with the stellar nucleus of ESO0291-G009. A filament of molecular emission extends north-east from the nucleus up to the edge of the SE field. We will refer to this structure as the northern filament. Clumpy emission extends towards the west and the south of the nucleus, up to the edges of the SE field.

The SW field shows a strong filament of gas having an east-west elongation, originally discovered by Crawford & Fabian (1992). We will refer to this structure as the western filament. The northern field shows two features (i) low signal to noise clumpy emission in the southern and central part of the field, and (ii) a stronger, somewhat larger emission feature at the northern edge of the field. Both features are treated in more detail below. Whether the clumpy emission observed in the northern field is part of the northern filament observed in the SE field is not clear from our observations.

The spatial extent of the gas for both the western and northern filament is bounded by the edges of our observed fields and it is likely that these filaments continue beyond the regions mapped here, as seems to be the case from narrowband $H\alpha$ + $[NII]$ imaging by J05 and Hansen et al. (2000).

2.5.2 Ionised gas

Pa α is the only ionised gas line detected in our K-band spectra for S159. It is redshifted into a region of poor atmospheric transmission. Strong Pa α emission is found along the northern and western filaments, Fig. 2.9. We detect Pa α in all places where H_2 emission is detected. A noticeable difference concerns the nuclear region. Almost no Pa α emission appears to be associated with the stellar nucleus. As we will see below, some Pa α emission is found here, but there is a strong decrease of it relative to molecular hydrogen emission. The Pa α / H_2 1-0 S(3) ratio is observed to drop from about 0.7 in the filaments to about 0.2 in the nuclear region. We note that the nuclear region has a rather high spectral noise, due to the strong stellar continuum, which affects our ability to detect emission lines here. The detection of the Pa α line is furthermore complicated by it being in a region of poor atmospheric transmission.

Pa α is also present within the northern field and, like the H_2 gas, appears to be clumpy. The strong emission feature observed in H_2 towards the northern edge of this field is also confirmed

by Pa α emission.

In S159 the Pa α line is the only ionised gas line detected. An estimate of differential extinction within the K-band can thus not be made directly from our observations. Baker (2005) finds little variation from $A_V \sim 1$ across the nebosity. Applying the same arguments to S159 as for A2597, we conclude that differential extinction in the K-band is negligible for this cluster.

2.6 Sersic 159-03 – Gas Kinematics

A single Gaussian function gives a good description of the observed line profiles, see Appendix A.3. The velocity, with respect to the systemic velocity of ESO 0291-G009, and the velocity dispersion of the gas have been derived for all emission lines. These all show the same global kinematical structure. The velocity and velocity dispersion maps shown below differ from the surface brightness maps in that only a two pixel spatial and spectral smoothing has been applied. This is done to preserve as much of the velocity structure as possible and provides us with a velocity resolution of 51 km s^{-1} .

2.6.1 Molecular gas

The kinematical structure observed in the H₂ 1-0 S(1) and H₂ 1-0 S(3) maps is the same. As an example of this structure we show the velocity and velocity dispersion of the H₂ gas as traced by the H₂ 1-0 S(3) line in Figs. 2.10 and 2.11. The nuclear region contains a blue- and redshifted gas component at about $\pm 120 \text{ km s}^{-1}$. This velocity structure is reminiscent of gas rotating around the nucleus. However, the two gas filaments coming in from the north-east and west towards the nucleus may also explain the observed velocity structure. The velocity along the filaments will be treated in more detail below. The gas extending towards the west and south from the nucleus appears to be predominantly blueshifted. The average velocity of the gas in the nuclear region is equal to the systemic velocity of ESO 291-G009 ($z=0.0564$, Maia et al. 1987) showing that the gas is situated at or near the stellar nucleus.

Globally the dispersion of the gas is low and decreases with distance from the nucleus. The dispersion of the gas in the nuclear region is about 230 km s^{-1} , but drops rapidly to about 90 km s^{-1} along the two filaments. This is similar to what is observed in A2597. In projection the high dispersion structure around the nucleus appears coincidental with the radio jets of ESO0291-G009, see Fig. 2.11. The increase in the velocity dispersion here again indicates that the radio jets are stirring up the gas.

From Figs. 2.10 and 2.11 it is difficult to draw conclusions on the average velocity and velocity dispersion of the clumpy low signal to noise emission in the northern field. From the previous investigation by J05 it appears that the gas observed here is connected to the strong filament extending north from the nucleus. Below, we will see that the clumpy emission has velocities varying between -20 and -60 km s^{-1} and a velocity dispersion less than 100 km s^{-1} . If this emission is connected to the filament extending north this implies that the line emission continues to decrease with distance to nucleus as was also shown by J05.

2.6.2 Ionised gas

Velocity and velocity dispersion maps for the ionised gas in S159 as traced by the Pa α line are shown in Figs. 2.10 and 2.11. As for A2597 we find that the Pa α derived kinematics follows that of the H₂ lines closely. The only exception in S159 being the high dispersion nuclear region observed in H₂ emission, which appears to be missed by the Pa α emission. The high noise in the nuclear region of S159 combined with the poor atmospheric transmission in the wavelength range of the Pa α line makes the fit of this line here rather difficult.

2.6.3 Filaments

In Fig. 2.14 we show the surface brightness, velocity and velocity dispersion along the two filaments observed in S159. The regions used for this investigation are marked by the green squares in Fig. 2.3. Following the northern filament from the north-eastern edge in the SE field southwards toward the nucleus and subsequently to the eastern edge of the SE field, we find that the Pa α /H₂ 1-0 S(3) decreases strongly in the nuclear region and is approximately constant outside of it. The filament has a smooth velocity gradient. North-east of the nucleus the velocity decreases very slightly with distance from about +130 km s⁻¹ to about +90 km s⁻¹. Across the nucleus the velocity changes from about +100 km s⁻¹ to -100 km s⁻¹. Whether this velocity reversal is due to rotation or due to the filamentary structure of the gas can not be clearly distinguished.

The velocity dispersion of the gas in the northern filament is low everywhere, except within the nuclear region. All detected lines show an increase in the velocity dispersion near the nucleus, but the increase in the H₂ lines is much higher than for the Pa α line. The decrease in the dispersion east of the nucleus is difficult to measure due to low signal to noise here.

The surface brightness of the western filament has two prominent peaks about 11'' from the nucleus. It has a very smooth velocity gradient along the filament, from about -100 km s⁻¹ to about +20 km s⁻¹. This velocity structure agrees with the possibility that it is connected to the nuclear region. The dispersion of the gas in this filament is low everywhere. All three lines detected show the same flux and velocity structure along the western filament.

2.7 Physical Conditions in the Warm Molecular Gas

Molecular hydrogen emission can be excited by various processes, (1) thermal excitation produced by kinetic energy injection into the gas due to for example shock heating (Hollenbach & McKee 1989), (2) fluorescence by soft-UV photons, i.e. Photo dissociation regions (PDR) (Black & van Dishoeck 1987; Sternberg & Dalgarno 1989), (3) high energy X-ray photons, i.e. X-ray dissociation regions (XDR) (Maloney et al. 1996) and (4) high energy particles (Lepp & McCray 1983; Ferland et al. 2009). If the density of the molecular gas is above the critical density the gas is in local thermal equilibrium (LTE). It is then not possible to distinguish between the various H₂ excitation mechanisms and one would observe a thermal H₂ spectrum where the excitation temperature is equal to the kinetic temperature of this gas. For the photon and particle processes mentioned above the gas can be thermalised, via heating through secondary (suprathermal) electrons.

In order to investigate the H₂ excitation mechanism we have constructed H₂ excitation diagrams for a number of regions in A2597. Seven regions, A1-A7, were selected based on having distinct physical properties in terms of either their emissivity, spatial location or kinematical structure, see Fig. 2.3. Similarly seven regions, B1-B7, were selected in S159, see Fig. 2.3. Excitation diagrams were not made for S159 since we only have reliable detections for two H₂ lines.

All line detections for regions A1-A7 and B1-B7 are presented in Appendix A.3. The line profiles are well described by a single Gaussian function. For the lines detected in these regions their integrated fluxes are given in Tables 2.7 and 2.10. Kinematical information for these regions are presented for the H₂ 1-0 S(3) and Pa α lines only and these are given in Tables 2.8 and 2.11. Gas temperatures and masses for the selected regions are given in Tables 2.9 and 2.12. We will first shortly describe the selected regions below.

2.7.1 A2597: Selected regions

In the central field we have selected four regions, A1, A2, A3 and A6. Region A1 corresponds to the nuclear region, A2 samples the region where the northern filament connects to the nucleus. A3, just north of A2, samples that part of the northern filament that appears to not be influenced (directly) by the nucleus anymore. Lastly, in the central field a clump of strong emission is noted on the western edge of the field, which we selected as region A6. There is tentative evidence for a narrow ridge connecting A6 to the nucleus, but we cannot confirm this with the present observations. The emission in region A6 itself is also uncertain, due to the increased noise at the edge of the field. It is only observed significantly in two H₂ lines and therefore we have not constructed an excitation diagram for this region.

In the south-eastern field we have selected one region, A4, which captures most of the emission in the southern filament. This region was selected such to avoid the noisy overlap region between the SE and SW fields. The strongest emission lines showed weak evidence in their surface brightness maps that the south-eastern filament may extend across the overlap region into the SW field. Region A5 was selected to test this. Significant line emission is found in this region. The kinematical structure of the gas observed in A5 is similar to that measured in A4 and thus a connection between the two regions seems plausible.

The northern field also contains significant emission for the strongest emission lines. A systematic search for line emission in the northern field was performed using various binnings. Region A7 was selected to show that emission does exist at a significant level in the northern field. J05 previously showed that molecular and ionised gas existed out to 20 kpc north from the nucleus using long slit spectra. The H₂ 1-0 S(1), 1-0 S(3) and Pa α lines are all detected at the 3.0 sigma level, and the H₂ 1-0 S(5) line is observed at the 2 sigma level. All four detected lines show the same velocity structure.

The velocity dispersion of the gas in A7 is more difficult to constrain. Of the four lines the H₂ 1-0 S(3) line is observed at the highest significance and has the most reliable fit. This line has a dispersion of about 60 km s⁻¹ using a spatial smoothing of two pixels. The other lines have higher fitted velocity dispersions ranging from 70 to 110 km s⁻¹, however within their large errors (40-60 km s⁻¹) they agree with the H₂ 1-0 S(3) result.

The positive velocity and low velocity dispersion of the gas makes it plausible that the gas in A7 is connected with the northern filament. This interpretation agrees with the J05 results. We

conclude that molecular and ionised gas is present at least up to region A7, i.e. 22.5 kpc from the nucleus, in good agreement with the J05 results. There is tentative evidence from regions investigated north and south of A7 within the northern field that line emission is present there as well.

2.7.2 S159: Selected regions

In the SE field we have selected four regions, B1, B2, B3 and B4. Region B1 corresponds to the nuclear region. B2 samples the tail of the northern filament as it connects to the nucleus. Region B3, just north of B2, is selected to sample the filament where it is no longer (directly) influenced by the nucleus. Lastly, B4 is selected to contain the clump of emission just to the south of the nucleus. Whether this clump is part of a filament or not our observations can not confirm.

As discussed above, the nuclear region B1 is significantly noisier than surrounding regions. The spectral noise is higher here by a factor two to three. The H₂ 1-0 S(1) and 1-0 S(3) lines are still easily detected here. The H₂ 1-0 S(3) line is considerably stronger than the H₂ 1-0 S(1) line in this region as compared to any of the other regions. The Pa α line is detected at a much lower significance and at a much lower flux level. In the SW field we have selected one region, B5, which captures most of the western filament.

We have selected two regions in the the northern field, B6 and B7, to investigate the low level clumpy emission here. Region B7 was selected to capture the strong clump of emission at the northern edge of this field. Region B6 was selected to investigate the remaining emission. The summed spectra clearly show that line emission is present in the northern field. We can thus conclude that molecular and ionised emission is present at least up to 18.0 kpc from the nucleus. Whether the gas in the northern field is directly connected to that in the SE field cannot be confirmed by our observations, although it seems plausible from the J05 results. The velocity and low velocity dispersion of the gas are such that this gas can be connected smoothly to that in the northern filament.

2.7.3 Thermal excitation of the molecular gas

In the case of a gas in LTE, assuming a ortho:para abundance ratio of 3:1, there is a simple relation between the flux F and the temperature T_u corresponding to the energy of the upper state of a line, $F \sim h\nu AN \sim h\nu gA \exp(-T_u/T_{\text{exc}})$, (e.g., J05; Jaffe et al. 2001; Wilman et al. 2002, 2005). Normalising the flux of each H₂ line flux by the flux of the corresponding H₂ 1-0 S(1) line, we find;

$$\ln(F) = \ln\left(\frac{F_i \nu_{S1} A_{S1} g_{S1}}{F_{S1} \nu_i A_i g_i}\right) \quad (2.1)$$

$$= \left(\frac{-1}{T_{\text{exc}}}\right) \times (T_{u,i} - T_{u,S1}) \quad (2.2)$$

Here F is the flux of the line, A its transition probability, ν its frequency and g the statistical weight of the transition. If the molecular gas is in LTE the H_2 emission lines will lie on a straight line in a diagram of $\ln(F)$ vs. T_u . T_{exc} , the reciprocal of the slope, will then be the kinetic temperature of this gas. We have investigated relation (1) for the all regions selected in Abell 2597 in which we have detected at least 3 H_2 lines. We show in Fig. 2.12 that the H_2 lines detected in these regions are well fit by a thermal excitation model, with an average temperature of about 2300 K. The derived excitation temperature for each region is given in Table 2.7.

Besides the best-fitting LTE model for the H_2 line fluxes we plot three additional H_2 models. These models are shown for qualitative comparison purposes only, and are not tuned exactly to our physical conditions, see Fig. 2.12. The best-fitting LTE model is given by the black solid line. The red dotted line is a low-density UV fluorescence model by Black & van Dishoeck (1987) that does not include collisions (their model 14; $n=3\times 10^3$ cm $^{-3}$, a temperature $T=100$ K and a UV intensity $I_{UV}=10^3$ relative to I_{tot}). The blue dotted line is a high-density UV fluorescence model by Sternberg & Dalgarno (1989) which does include collisions (their model 2D; $n=1\times 10^6$ cm $^{-3}$, a temperature $T=1000$ K and $I_{UV}=10^2$ relative to I_{tot}). Lastly the green dotted line is the cosmic ray model by Ferland et al. (2009), which was developed for the gas filaments observed in the Perseus cluster.

The Black & van Dishoeck low-density UV and the Ferland cosmic ray models have distinct features that make them deviate from a thermal model. Low-density UV fluorescence models tend to boost the higher S-transitions (2-1, 3-2,...) relative to the 1-0 S-transitions as compared to a LTE model. The Ferland model is observed to boost the even H_2 1-0 S-transitions relative to uneven H_2 1-0 S-transitions as compared to a LTE model. The high-density UV model by Sternberg & Dalgarno simply shows that at high densities, collisions within the gas will cause it to become thermalised and thus the line ratios also produce a straight line in our excitation diagrams. We thus conclude, qualitatively, that out of the four models investigated here that a LTE model provides the best description of the data.

As the molecular line ratios in A2597 appear to be in LTE this implies that the density of this gas is near its critical density, $n_{H_2,crit} \approx 10^6$ cm $^{-3}$ (Shull & Beckwith 1982) and is dominated by collisional excitation. Information regarding the source of excitation is thus not obtainable from this data set.

There is a trend that on average we find higher LTE temperatures of the molecular gas in the filaments as compared to the nuclear region. We note though that within errors the temperatures agree for all regions, except for A6. Neither the H_2 1-0 nor the H_2 2-1 S-transitions lie exactly on a straight line. If we use only pairs of lines like the H_2 1-0 S(1), 1-0 S(3) line pair or the H_2 1-0 S(3), 1-0 S(5) line pair to determine an excitation temperature, assuming LTE, we find on average a temperature that is a few hundred degrees lower or higher than when all lines are used. Typically the first pair gives a lower temperature and the second pair a higher temperature.

If the H_2 gas observed here is at its critical density then there is a pressure imbalance between the molecular gas $p(H_2) \sim nT = n_{crit}T_{exc} \approx 10^9$ and the ionised gas has $p(HII) \sim nT = 10^2 \times 10^4 = 10^6$. That the molecular and ionised gas are not in pressure equilibrium has previously been suggested by J05 using similar arguments.

For Sersic 159-03 only two H_2 lines were reliably detected in all regions. If we assume that the molecular gas here is in LTE, we can calculate an excitation temperature for this gas. The resulting excitation temperatures for the selected regions are given in Table 2.10. Again we find

an average temperature of about 2300 K for the H₂ gas in the filaments. In the nuclear region the strong increase of the H₂ 1-0 S(3)/H₂ 1-0 S(1) ratio leads to a very uncertain and physically unrealistic temperature above the dissociation temperature for H₂. This either means that our line fits overestimate this ratio or that a different excitation mechanism is at work here.

In this work we have only considered the K-band H₂ lines. These H₂ lines do not show strong deviations from a single temperature thermal model with $T \approx 2000\text{--}2500$ K. From recent Spitzer spectroscopy (Jaffe & Bremer in prep.) we find that another H₂ gas component exists in the nuclear regions of A2597 and S159 with a LTE temperature of about 300 K. The situation in these clusters is thus similar to the situation in the Perseus cluster where multiple temperature LTE components have been invoked to explain the H₂ line ratios (e.g., Wilman et al. 2002, 2005; Johnstone et al. 2007).

Whether the need for multiple LTE components to H₂ line ratios hints at a multiphase gas, a difference in optical depth, or a different excitation mechanism is unclear currently. A more thorough modelling of the molecular gas, including all of the measured of the H₂ lines in the infrared and mid-infrared, for A2597 and S159 will be presented by us in a future paper.

2.7.4 Luminosity of the Warm Molecular Gas

If we assume that the H₂ gas is in LTE and can be described by a single kinetic temperature of about 2000 K, then the H₂ 1-0 S(1) line luminosity represents about 10 percent of the total H₂ luminosity. This is estimated using a list of 312 H₂ lines, corresponding to all H₂ emission lines with an intensity greater than 1 percent of H₂ 1-0 S(1) line flux for $T \leq 4000\text{K}$. From the total integrated H₂ 1-0 S(1) line fluxes in Tables 2.5 and 2.6 we thus find $L(\text{H}_2, \text{A2597}) = 1.1 \times 10^{42} \text{ erg s}^{-1}$ and $L(\text{H}_2, \text{S159}) = 1.2 \times 10^{41} \text{ erg s}^{-1}$ within the fields observed by us.

This is significantly below the total H₂ luminosity estimated by J05, i.e. $L(\text{H}_2) \sim 10^{43\text{--}44} \text{ erg s}^{-1}$. J05 calculate the total H₂ luminosity in the same manner as we do here. The difference follows from two simple arguments. Firstly J05 assumed that the H₂ 1-0 S(1) line luminosity represents only about 1 percent of the total H₂ luminosity. This is true for low-density UV excitation models such as the Black & van Dishoeck models. However, when the gas is in LTE (see above) or in a XDR environment (Draine & Woods 1992) a fraction of 10 percent is found. The J05 results thus need to be corrected down by a factor of 10 as consequence of this. The second argument that J05 made is that the H₂ emission coexists with the H α emission. This argument follows from the HII/H₂ ratio which is observed to remain rather constant over large areas (J05 and this work). J05 detect H α over a much larger area than the fields observed by us. Correcting our results upward for the area covered by the H α map in J05 increases the H₂ luminosity given above by a factor of 10. With these corrections, we find that the H₂ luminosity obtained in this work is in good agreement with the J05 results.

To conclude, upon correcting our results for the area covered by the total extent of the ionised gas nebulae, we find H₂ luminosities $L(\text{H}_2, \text{A2597}) \sim 10^{43} \text{ erg s}^{-1}$ and $L(\text{H}_2, \text{S159}) \sim 10^{42} \text{ erg s}^{-1}$ for our clusters. The analysis performed above relies heavily on the assumption that the H₂ gas is in a single temperature phase. If there is colder H₂ gas present in these clusters, as expected from CO observations by Edge (2001) and mid-infrared spectroscopy (Jaffe & Bremer in prep.) we underestimate the total H₂ luminosity here.

2.7.5 Mass of the Warm Molecular Gas

In the previous section we found that a LTE model provides a good description of the observed H₂ line ratios in A2597 and assumed that the same is true for a S159. Following Scoville et al. (1982) and Storchi-Bergmann et al. (2009) the mass of a H₂ gas in LTE conditions with a single kinetic temperature, can be calculated using the following equation,

$$M_{\text{H}_2} = \frac{2m_p F_{\text{H}_2 1-0\text{S}(1)} 4\pi D^2}{f_{v=1,J=3} A_{\text{H}_2 1-0\text{S}(1)} h\nu} \quad (2.3)$$

$$= (5.08 \times 10^{13}) \left(\frac{F_{\text{H}_2 1-0\text{S}(1)}}{\text{ergs}^{-1} \text{cm}^{-2}} \right) \left(\frac{D}{\text{Mpc}} \right)^2 \quad (2.4)$$

Here m_p is the proton mass, h is the Planck constant and D is the distance to the cluster core. $F_{\text{H}_2 1-0\text{S}(1)}$ is the flux of the H₂ 1-0 S(1) line and $f_{v=1,J=3}$ is its population fraction. $A_{\text{H}_2 1-0\text{S}(1)}$ is the transition probability ($A_{\text{H}_2 1-0\text{S}(1)} = 3.47 \times 10^{-7} \text{ s}^{-1}$) and ν is the frequency of the H₂ 1-0 S(1) line. The right-hand side of equation (2) is obtained by assuming a vibration temperature $T_{\text{vib}} = 2000 \text{ K}$ for the gas, in which case $f_{v=1,J=3} = 1.22 \times 10^{-2}$. In the above formula M_{H_2} is given in units of solar masses.

The resulting H₂ gas masses for the regions investigated here are given in Tables 2.9 and 2.12. The total H₂ gas mass integrated over all observed fields is $4.5 \times 10^4 \pm 4.2 \times 10^2 M_\odot$ for A2597 and $5.2 \times 10^3 \pm 2.9 \times 10^3 M_\odot$ for S159. Since our observations do not cover the entire cluster core these numbers underestimate the total amount of molecular gas present in these clusters. We furthermore note that there is evidence from mid-infrared spectroscopy from Jaffe & Bremer (in prep.) that a colder H₂ phase ($T \sim 300 \text{ K}$) exists in A2597 and S159. If this colder H₂ gas coexists with the warmer H₂ gas observed here this means that we strongly underestimate the H₂ mass present in these clusters. CO observations by Edge (2001) indicate that even colder H₂ gas is present in A2597 at a temperature of a few tens of kelvin. The total molecular gas mass inferred from CO for A2597 is $8 \times 10^9 M_\odot$, although this value relies heavily on the CO to H₂ conversion factor. To our knowledge there is no published CO detection for S159.

2.7.6 Mass of the Ionised Gas

Following Storchi-Bergmann et al. (2009) the mass of the ionised hydrogen gas can be estimated as $M_{\text{HII}} = m_p n_e V_{\text{HII}}$. Here m_p is the proton mass, n_e is the electron density and V_{HII} is the volume of the HII emitting region. Using $j_{\text{H}\beta}/n_e^2 = 9.788 \times 10^{-27} \text{ erg s}^{-1} \text{ cm}^3$ and $j_{\text{Pa}\alpha}/j_{\text{H}\beta} = 0.339$ (Osterbrock & Ferland 2006), for $n_e = 10^2 \text{ cm}^{-3}$ and $T = 10^4 \text{ K}$, we can write $F_{\text{Pa}\alpha} = j_{\text{Pa}\alpha} V_{\text{HII}} D^{-2} = 3.32 \times 10^{-27} \times (n_e^2 V_{\text{HII}} D^{-2})$. Here $F_{\text{Pa}\alpha}$ is the flux of the Pa α line, $j_{\text{Pa}\alpha}$ is the volume emissivity coefficient of Pa α and D is the distance to the cluster core. The HII gas mass can be written as:

$$M_{\text{HII}} = m_p n_e V_{\text{HII}} \quad (2.5)$$

$$= (2.41 \times 10^{18}) \left(\frac{F_{\text{Pa}\alpha}}{\text{ergs}^{-1} \text{cm}^{-2}} \right) \quad (2.6)$$

$$\times \left(\frac{D}{\text{Mpc}} \right)^2 \left(\frac{n_e}{\text{cm}^{-3}} \right)^{-1} \quad (2.7)$$

Using the right-hand side of equation (3) the mass of the HII emitting gas, M_{HII} , is given in units of solar masses. Heckman et al. (1989) finds an electron density, $n_e = 200 \text{ cm}^{-3}$, for the central regions of A2597. Thus assuming an electron density $n_e = 200 \text{ cm}^{-3}$, the mass of the HII emitting gas in the selected regions of Abell 2597 and Sersic 159-03 can be calculated.

The resulting HII gas masses are given in Tables 2.9 and 2.12. The total HII gas mass integrated over all observed fields is $9.7 \times 10^6 \pm 3.2 \times 10^5 M_{\odot}$ for A2597 and $7.6 \times 10^5 \pm 8.4 \times 10^4 M_{\odot}$ for S159. Since our observations do not cover the entire cluster core these numbers underestimate the total amount of ionised gas present in these clusters. The total ionised gas mass to warm molecular gas mass is similar in both clusters; $M_{\text{HII}}/M_{\text{H}_2} \sim 10^2$. The HII gas mass derived here for A2597 agrees well with Heckman et al. (1989) who find $M_{\text{HII}} = 5.8 \times 10^6 M_{\odot}$ for a region with radius 2.5 kpc centered on the BCG nucleus.

2.7.7 Stability of the Filaments

From our observations we see that the ionised and molecular gas is locked up in large scale filamentary structures surrounding the BCG. If the filaments in our the clusters are similar to the ones observed in more nearby clusters, such as Perseus (Fabian et al. 2008), then we do not resolve their true physical thickness. Furthermore if we assume that the filaments observed here are connected to the global distribution of ionised gas in these clusters then its clear that these extent far beyond the distance observed here by us (J05; O’Dea et al. 2004).

This interpretation is strengthened by higher resolution images in for example $\text{H}\alpha$ and $\text{Ly } \alpha$ emission (D00; O’Dea et al. 2004). These show the existence of narrow gas filaments coincidental with the larger scale structures observed here. Considering this, even if these large structures consist of many unresolved filaments it seems plausible that all of these have a similar origin. The currently favoured picture is that these structures are related to past and current AGN outflows. Another explanation may be that these structures arise in regions of these clusters where heating and cooling rates are not balanced and thus that we observe residual cooling here.

Not only is the origin of these structures unclear, there are many other puzzling aspects concerning them. On large scales these structures appear to connect all the way down to the nucleus of the BCG. One may speculate on whether this gas falls in towards the black hole thereby feeding it and sustaining its activity. However, the velocities observed for the filaments studied here or in other clusters (Hatch et al. 2005) does not agree with gas that is freely infalling from distances far away from the potential centre. We observe the gas to be moving at velocities of about 100 km s^{-1} , whereas for freely infalling gas we would expect to observe velocities of about 600 km s^{-1} .

We would expect tidal forces to rip these filaments apart as discussed in Fabian et al. (2008). These authors suggest that magnetic fields may help stabilise these filaments against these gravitational forces. For a typical filament in Perseus, or one of our clusters, the required magnetic field is around a few hundred μG . From equipartition arguments the ICM typically has magnetic field strengths less than $10 \mu\text{G}$. Larger magnetic field strengths, up to about $50 \mu\text{G}$, have been found in the centres of clusters but these are usually related to current AGN outflows (Taylor et al. 2007; Govoni & Feretti 2004). Significantly higher magnetic field strengths in the filaments are necessary to stabilise them against gravitational forces.

Some of the gaseous filaments appear, in projection, to be related to the current AGN outflows, see Fig. 2.6 and 2.9. These outflows maybe be responsible for pushing gas outwards, thereby in fact creating the observed filaments (Hatch et al. 2005). This may explain why some filaments do not show large infall velocities. However, there are also filaments that are not related to current radio outflows. If these filaments were deposited at their current location by previous AGN outflows, then this gas has had a long time to cool and should now be falling back at high velocities towards the potential centre. No signs of high velocity infalling gas is observed in either of our clusters. We will discuss the relation between the filaments and the radio emission in more detail below.

2.8 X-ray and Radio Emission

In the above sections we have shown that there is a strong spatial and dynamical relation between the HII and H_2 gas phases in the cores of A2597 and S159. Below we investigate how these gas phases relate to X-ray and Radio emission.

2.8.1 X-ray emission

We find that globally the H_2 and HII line emission in A2597 appears to match the X-ray emission as imaged by *CHANDRA* rather well, see Fig. 2.1. However, upon examining the detailed distribution, Fig. 2.13, we find that the X-ray brightness profile is considerable shallower than that of the colder gas.

In S159, see Fig. 2.14, we observe that the peak X-ray emission is significantly offset from the BCG nucleus and the peak H_2 , HII emission. One may perhaps argue for a relation between the X-ray and Pa α emission along the northern filament, but Pa α is difficult to detect in the nuclear region. There appears to be no relation between Pa α and X-ray emission along the western filament in S159. This leads us to conclude that is no strong correlation between the X-ray and either the H_2 or HII phase in A2597 and S159.

The total X-ray luminosity is $L_X(\text{A2597}) = 2.1 \times 10^{44} \text{ erg s}^{-1}$ (de Grandi 1999, 0.5-2.0 keV) and $L_X(\text{S159}) = 9.6 \times 10^{43} \text{ erg s}^{-1}$ (de Grandi 1999, 0.5-2.0 keV) in A2597 and S159 respectively. Taking into account the difference in areas between this work and that of J05, the total warm H_2 luminosity for these clusters is a factor 10-100 times less than their X-ray luminosities and not of the same order of magnitude as previously claimed in J05. Adding the colder H_2 gas to this analysis (Jaffe & Bremer in prep.) to obtain a total warm plus cold H_2 luminosity may change this conclusion.

2.8.2 Radio emission

In Figs. 2.6, 2.7, 2.8, 2.9, 2.10 and 2.11, we show VLA 8.4 GHz radio contours on top of the H₂ 1-0 S(3) and Pa α surface brightness, velocity and velocity dispersion maps. The total radio power is 3.1×10^{42} erg s⁻¹ for A2597 and 2.1×10^{41} erg s⁻¹ for S159 (Birzan et al. 2008, integrating the radio spectrum between 10 MHz and 10 GHz).

Our observations of the molecular and ionised gas in A2597 and S159 do not have the spatial resolution to investigate the detailed sub-kpc scale correspondence between the AGN outflows and the gas. On kpc scales we note small enhancements in the HII and H₂ intensity along the lower parts of the projected radio lobes in A2597. Most notably along the northern lobe. D00, using higher resolution HST imaging, have previously shown this in more detail for A2597. Similarly in S159 we observe that on kpc-scales some of the gas appears to lie along the radio lobes. In neither S159 and A2597 is there a clear correlation between the radio emission and the cold gas.

It has been postulated that gas observed on the edges of radio lobes is gas that was uplifted and deposited here through AGN outflows (Hatch et al. 2005). Another possibility in which the AGN outflows may create the observed structures is via pressure driven compression of the in-situ thermal gas by the outward expanding non-thermal plasma. In this latter scenario the pressure driven compression increases the local gas density leading to an increase in the cooling rate here.

That the gas observed along the radio lobes is a purely projectional effect and has nothing to do with the radio outflow seems unlikely. Strong evidence that an AGN interacts with the gas in the nuclear region of a BCG comes, for example, from the flux enhancement and high velocity dispersion structure observed in A2597 here and in D00. These structures coincide with the current radio outflows. Many other observations, mostly done in X-rays, have shown that there is a global correlation between the radio outflows in BCGs and the hot X-ray gas surrounding it (e.g., McNamara et al. 2001; Fabian et al. 2002; Clarke et al. 2005; Birzan et al. 2008). We do caution the reader that even though this global correlation is found in many cool core clusters that there are also cases where one observes similar amounts of gas in structures that appear to have no relation at all to the current radio outflows. One example of this is the western filament in S159.

Alignment of the radio and gas rotation axes ?

In A2597 we note that, in projection, there is a rough alignment between the radio axis and the axis of rotation for the HII and H₂ gas. The same seems to be true for S159 although the evidence for gas rotation is less clear here. Three other clusters, Abell 1664, PKS 0745-19 and A2204, have recently been observed with SINFONI by Wilman et al. (2009). They show that the HII and H₂ gas in PKS 0745-19 rotates. High resolution radio images by Baum & O'Dea (1991) show us that again that the radio axis and gas rotation axis roughly agree. For the other two clusters the situation is unclear. The velocity fields of the gas in Abell 1664 and Abell 2204 do not show clear evidence for gas rotation, and radio images by Govoni et al. (2001) and Sanders Fabian & Taylor (2009) do not allow for a reliable identification of the jet axis. Higher spatial resolution spectroscopy and radio imaging will be required to investigate the possible alignment of the radio axis and the gas rotation axis in more detail.

Kinetic energy of the outflows

It has been proposed in the literature that AGN feedback in the form of radio outflows, jets could deliver the required heat that keeps the gas in cluster cores from cooling (e.g., Birzan et al. 2004; Dunn & Fabian 2006). The kinetic power in the molecular and ionised phases may be a useful indicator for estimating the total energy input into the cluster medium by the current jet. Here we will estimate the kinetic power from the kinetic energy of the disturbed gas and its turbulent dissipation. The kinetic energy E_K and kinetic (turbulent) power P_K may be written as;

$$E_K = \frac{Mv^2}{2} = \frac{3M\sigma^2}{2} \quad (2.8)$$

$$P_K = \frac{Mv^3}{2r} = \frac{E_K \sqrt{3}\sigma}{r} \quad (2.9)$$

Here $v = \sqrt{3}\sigma$ with the σ the velocity dispersion of the gas and r is the thickness of the high dispersion features. We will perform this estimate using region A1 in A2597. This region contains most of the gas whose dispersion is clearly related to the AGN as described in Section 2.4. The mass of the HII gas in A1 is $4.1 \times 10^6 M_\odot$ and its velocity dispersion is 256 km s^{-1} . We use only the HII gas here as this gas component dominates in mass over the warm H_2 gas. We thus find that a total kinetic energy of $E_K(\text{A2597 : A1}) = 8.1 \times 10^{54} \text{ erg}$ and a kinetic energy power $P_K(\text{A2597 : A1}) = 5.8 \times 10^{40} \text{ erg s}^{-1}$, where we used $r = 2 \text{ kpc}$.

For S159 this calculation is more uncertain due to the lower significance of the Pa α line in the nuclear region B1. If we use that the mass of the HII gas in B1 is $5.8 \times 10^4 M_\odot$ and its velocity dispersion is 127 km s^{-1} . We then find that a total kinetic energy of $E_K(\text{S159 : B1}) = 2.8 \times 10^{52} \text{ erg}$ and a kinetic power $P_K(\text{S159 : B1}) = 1.0 \times 10^{38} \text{ erg s}^{-1}$ is injected into stirring up the gas, again using $r = 2 \text{ kpc}$. These numbers are rather low for S159. If we use the H_2 1-0 S(3) velocity dispersion for the Pa α line and increase the Pa α flux such that the Pa α/H_2 1-0 S(3) ratio is the same as in region A1 for A2597 we find that E_K and P_K both increase by about a factor of 10 for S159.

We compare this mechanical power injected into the cool gas to the current radio power. We assume that the stirring of the gas in the nuclei of A2597 and S159 is related to the most recent AGN outburst and thus we look only at the recent radio emission. This is done to avoid the older radio plasma, from previous outbursts, which will dominate the radio power due to its emissivity at low frequencies.

The 8.4 GHz radio emission is a good indicator of recent AGN activity. The synchrotron lifetime of electrons emitting at 8.4 GHz is about 10^{6-7} years, for a magnetic field strength of $30 \mu\text{G}$ (Taylor et al. 2007). The 8.4 GHz specific luminosities L_ν in regions A1 and B1 are $1.75 \times 10^{31} \text{ erg s}^{-1} \text{ Hz}^{-1}$ and $3.88 \times 10^{29} \text{ erg s}^{-1} \text{ Hz}^{-1}$. One can then estimate the total current radio power P_{rad} in these regions by $P_{\text{rad}} = \nu \times L_\nu$, with $\nu = 8.4 \text{ GHz}$. We find $P_{\text{rad}}(\text{A2597 : A1}) = 1.5 \times 10^{41} \text{ erg s}^{-1}$ and $P_{\text{rad}}(\text{S159 : B1}) = 3.3 \times 10^{39} \text{ erg s}^{-1}$.

The kinetic power inserted into the cool gas is thus smaller than the radio power in A2597 by a factor 2-3. For S159 we find that P_K is smaller than P_{rad} by more than an order of magnitude.

If we allow for the higher dispersion and flux as mentioned above then this ratio becomes similar to that observed in A2597. Adding the warm ($T \sim 2300$ K) H_2 gas to the above analysis does not significantly change the derived kinetic powers due to its low mass. We thus find that within the nuclear regions the current radio jets in A2597 and S159 are radiating efficiently with respect to the warm HII and H_2 gas.

The kinetic power deduced here should though be seen as a lower limit to the total kinetic power of the cool ($T \leq 10^4$ K) gas in these clusters since the colder gas phases have not been taken into account. O94 find a kinetic energy $E_K \sim 10^{56}$ erg and a kinetic power $P_K \sim 10^{42}$ ergs $^{-1}$ for the HI gas in a region with radius 2.5 kpc centered on the BCG nucleus in A2597. Similarly the cold ($T \leq 10^3$ K) molecular gas may contain a significant amount of kinetic energy. Studies of X-ray cavities find evidence for inefficiently radiating jets in that the mechanical power of the jet often can be orders of magnitude larger than the radio power. However, when looking at X-ray cavities one may be looking back in time towards an epoch in which the balance between the mechanical and radiative power of the radio source is different from the current one.

Low velocity shocks

The argument that AGN feedback is responsible for reheating the ICM gas in cool core clusters is made purely on the global energetics of the problem and does not consider the microphysics of the energy transfer between the non-thermal radio plasma and thermal ICM plasma, nor does it consider the various scales involved in this energy transfer. Fast shocks ($v \geq 40$ km s $^{-1}$) can be ruled out based on the absence of typical shock tracers like the [O III] 4363 Angstrom line in optical spectra (VD97) and the high H_2 /HII ratios (Donahue et al. 2000). However, another way of delivering the required heat for the cooler gas observed here is via low velocity shocks in a dense gas. Such a model was recently invoked to explain the strong H_2 emission observed in 'Stephan's Quintet' (Guillard et al. 2009). From X-ray observations (e.g. McNamara et al. 2001; Fabian et al. 2006) and jet models (Sutherland & Bicknell 2007, e.g.) it is found that AGN outflows may give rise to low velocity C-type shocks through a turbulent cascade of the expanding jet momentum in an inhomogeneous gas.

We have investigated low velocity C-type shocks by Kristensen et al. (2007) and Flower & Pineau des Forets (2003) to model the molecular ratios in region A1 for A2597. The following parameter range was allowed for, shock velocity $v_S = [15-30]$ km s $^{-1}$, pre-shock density $n_H = [10^4-10^7]$ cm $^{-3}$ and magnetic field strength $B = [0.05-30]$ mG. The best-fitting model to the molecular line ratios is $v_S = 22$ km s $^{-1}$, $n_H = 5 \times 10^6$ cm $^{-3}$ and $B = 5.6$ mG. This model is shown by the purple line in Fig. 2.16. It implies a pre-shock density above the critical density and thus that the gas is already in LTE prior to the shock. This model furthermore implies a very high magnetic field in the molecular gas, something which has not yet been observed in our objects.

2.9 Summary

Warm molecular gas is observed in the central 20 kpc of the A2597 and S159 galaxy clusters. All of the H_2 1-0 S-transitions and H_2 2-1 S-transitions redshifted into the K-band and none of the higher ro-vibrational H_2 transitions are detected in A2597. Ionised gas is observed in

A2597 through the detection of the Pa α , Br γ , Br δ and Fe II (1.81 μm) lines. For S159 only two H₂ 1-0 S-transitions are detected. There is tentative evidence for the presence of the other H₂ 1-0 S-transitions, but these are strongly affected by atmospheric effects. None of the higher ro-vibrational H₂ lines were detected. Ionised gas is observed in S159 through the detection of the Pa α line. Higher ionisation lines, such as [Si IV], are not detected in either S159 or A2597.

Molecular and ionised gas is detected out to 22.5 kpc from the nucleus of PGC071390 in A2597 and 18.0 kpc from the nucleus of ESO291-G009 in S159. The fields observed by us do not cover the entire extent over which molecular and ionised emission has previously been detected in these clusters. Our observations thus miss a significant fraction of the total emission and gas mass. Based on the H α maps in J05 we estimate that we have observed about one tenth of the total HII and H₂ gas present in A2597 and S159.

The gas morphology in A2597 is more diffuse than in S159. In both clusters the ionised and molecular gas is observed to be distributed in clumps and filamentary structures surrounding their BCGs. This observation brings these higher redshift cool core clusters closer to the situation observed in more nearby clusters, such as Perseus and Centaurus, that show a wealth of small scale filamentary structure (e.g. Fabian et al. 2008; Crawford et al. 2005).

In both A2597 and S159 the ionised and molecular gas phases trace each other closely on kpc-scales, in both extent and dynamical state. The H₂ line ratios and the H₂ to HII line ratios only vary slowly as a function of position throughout the investigated regions, with the exception of the nuclear regions. This implies that there is a tight coupling between these gas phases and that there may be a single excitation mechanism responsible for the observed emission.

In both clusters the Pa α to H₂ ratio is found to be lower within their nuclear regions than outside. In A2597 this decrease is small as the Pa α /H₂ 1-0 S(3) ratio decreases from 0.94 ± 0.04 in region A2 to 0.77 ± 0.07 in the nuclear region A1. In S159 the decrease is much larger and we find that the Pa α /H₂ 1-0 S(3) ratio decreases from 0.66 ± 0.12 in region B3 to 0.19 ± 0.08 in the nuclear region B1. This may imply that the physical conditions differ within the nuclear regions as compared to further out.

The velocity structure of the ionised and molecular gas within the nuclear regions of A2597 and S159 is consistent with gas rotating around the nucleus. The data suggests a possible alignment between the axis of rotation and the radio axis. Further high spatial resolution, spectroscopic observations are required to disentangle this rotation from velocity gradients observed along the filamentary gas structures and to confirm the axis of rotation.

The high velocity dispersion of the gas within the nuclear regions clearly shows that the AGNs harboured by these BCGs interact with the molecular and ionised gas situated here. This is especially obvious in A2597 where the observed increase in the velocity dispersion is suggestive of a turbulent wake marking the passage of the radio lobes through the surrounding medium, or of direct acceleration of the dense material by the AGN jet.

We estimate that the mechanical power of the AGN flow is somewhat smaller than its radiative radio power within the nuclear regions of A2597 and S159 with respect to the ionised and warm molecular gas. If we were to include the mechanical energy contained within the colder atomic and molecular gas phases than this situation will reverse.

The velocities observed for the filamentary structures are less than 150 km s^{-1} . This does not agree with freely infalling gas which should have much higher velocities, i.e. $\sim 600 \text{ km s}^{-1}$. The filaments do show smooth velocity gradients. Possible explanations for this are; (i) we

see a single filament that is being stretched and bended by its proper motion and gravitational forces, (ii) we see a blend of a number of unresolved filaments along the line of sight. From observations of nearby clusters such as Perseus the latter explanation appears most likely (e.g. Fabian et al. 2008; Hatch et al. 2005).

The velocity dispersion of the ionised and molecular gas decreases with distance to the nucleus. It drops below 100 km s^{-1} at distances of a few kpc from the nucleus which implies that the gas is kinematically cold outside the nuclear region. The decrease in velocity dispersion is strongest within the first ~ 2 kpc from the nucleus and slows down after that. This point may mark a transition in where the AGN is able to strongly interact with its surrounding medium.

The low velocity and velocity dispersion of the gas in the filamentary structures indicates that the gas here resides in well defined structures. The gas may still be clumpy but individual clumps must have a spread in velocity no larger than the derived dispersion. It also implies that these structures need some form of support, which can not be kinematical, to keep them from plummeting towards the potential centre. A possible source of support are magnetic fields as suggested by Fabian et al. (2008). This requires magnetic field strengths of a few hundred μG . So far there is no observational evidence for the existence of these magnetic fields in galaxy clusters.

The molecular and ionised gas emission observed in A2597 and S159 does not match the observed X-ray emission very well. In S159 there is no match in the observed brightness profiles. In A2597 there is a rough global agreement in the peak emission but the detailed X-ray brightness profiles are significantly shallower than observed for the H_2 and HII gas.

There is no evidence for a strong correlation between either H_2 or HII and the radio emission in A2597 and S159. If the AGN is main source of heating and excitation for these gas phases, then we would expect to find this gas near the current AGN outflows at all times. This is especially important for the H_2 gas since it has a cooling time of order years. One prime example where we find H_2 gas that appears to have no relation to the current outflows is the western filament in S159. The emission line spectra for all regions in S159 are similar. This then implies that the physical process that is heating the gas in these regions is similar and likely not directly related to the current AGN outflows.

In A2597 the H_2 line emitting gas is well described by an LTE model with a single excitation temperature T_{exc} . We find that T_{exc} is about 2300 K for the different regions investigated. We find slightly higher excitation temperatures for the molecular gas in the filaments as compared to the nuclear region.

In S159 we have only been able to reliably measure two H_2 lines. The temperature and excitation of the H_2 gas in this cluster thus remains largely unconstrained. Assuming a single temperature LTE model, we find that T_{exc} is about 2300 K for the different regions investigated. The temperature derived in this way for the nuclear region in S159 is above the dissociation temperature of H_2 and considered unphysical. No clear trends in temperature with distance to the nucleus are observed for S159.

If the molecular gas in A2597 and S159 is in LTE then this implies that the H_2 gas is not in pressure equilibrium with the HII gas, as has previously been pointed out by J05. We find that $M_{\text{HII}}/M_{\text{H}_2} \sim 10^2$ in A2597 and S159. We note that M_{H_2} is likely to be seriously underestimated since only the K-band H_2 lines tracing the warm molecular gas have been considered here.

For a region with radius 2.5 kpc centered on the nucleus of the A2597 BCG we can make an inventory of the cool gas. In agreement with Heckman et al. (1989) we find an ionised gas mass

$M_{\text{HII}} \approx 6 \times 10^6 M_{\odot}$. We find a warm molecular gas mass $M_{\text{H}_2, \text{warm}} \approx 3 \times 10^4 M_{\odot}$. O’Dea et al. (1994) find a neutral hydrogen mass $M_{\text{HI}} \sim 10^8 M_{\odot}$. Using much lower spatial resolution Edge (2001) find a spatially unresolved cold molecular gas mass $M_{\text{H}_2, \text{cold}} = 8 \times 10^9 M_{\odot}$ in the central $22''$ of A2597.

We are able to fit the H_2 line emitting gas by a low velocity shock model. Such a model requires high pre-shock densities and very high magnetic fields. Low velocity shocks may be a viable option for heating the H_2 gas in cool core clusters, but this requires further modelling and observations.

Using recent Spitzer observations we find that another lower temperature H_2 gas component exists at about 300 K in A2597 and S159 (Jaffe & Bremer in prep.). This shows that a single temperature LTE model is not a good description for all of the H_2 gas present in cool core clusters and again brings the situation in our clusters closer to that observed in more nearby cool core clusters (Johnstone et al. 2007). This also implies that we significantly underestimate the total H_2 luminosity and gas mass by using only the H_2 K-band spectrum.

Our K-band spectra of cool core clusters do not resemble typical K-band spectra of other line emitting, extragalactic objects such as Ultraluminous Infrared Galaxies (ULIRG) and AGNs that are not in BCGs. For comparisons we can look at the Br γ and H_2 1-0 S(1) line. In ULIRGs these lines have a similar intensity and width and in AGNs that are not in BCGs the Br δ line usually has a higher intensity and larger width than the H_2 1-0 S(1) line (Davies et al. 2003, 2005). In our spectra for Abell 2597 we find that these lines have similar widths, but the H_2 1-0 S(1) line is more than ten times brighter than the Br γ line.

2.10 Conclusions

Above we have presented the first K-band integral-field spectroscopic observations of the extended molecular and ionised gas distributions in the core regions of the A2597 and S159 galaxy clusters. These observations add one extra dimension to the analysis of the molecular and ionised gas in these clusters as compared to our previous investigation in J05. This allows us to study the distribution, kinematics and thermal structure of this gas over a much larger area than in our previous investigation. The spatial resolution of our observations limit us to studying this gas on kpc-scales. Below we summarise our conclusions.

- Line emission from molecular and ionised gas is found in all observed fields. We confirm the conclusion in J05 that molecular and ionised gas are tightly coupled out to 20 kpc from the BCG nucleus in A2597 and S159.
- The molecular and ionised gas is distributed in filamentary structures surrounding the BCG. The gas morphology is more diffuse in A2597 than in S159.
- In all regions where we have sufficient signal to noise we find that the H_2 gas can be described by an LTE model with a temperature $T \sim 2300$ K. LTE implies a high-density for this gas.
- Kinematically there is a fairly clear separation between the central few kpc, energetically dominated by the AGN, and an area outside where the support of the HII and H_2 gas remains to be explained.

- Within the nuclear region of A2597 and S159 the kinetic luminosity of the HII and warm H₂ gas is somewhat smaller than the current radio luminosity.
- The very high dispersion regions observed in H₂ and HII may represent a turbulent wake of the relative motion of galaxy and surrounding medium, or the interaction of the current jet with this medium.
- A2597 shows a better correlation between the morphology of the cool gas and X-ray emission than S159. The detailed radial brightness profiles of the X-ray and either the H₂ or HII gas do not match in either cluster.
- The high frequency radio emission and cool gas have the same overall scale size. There is no strong correlation between either the H₂ or HII gas and the radio structures, but there are weak enhancements in the surface brightness of this gas along the northern radio lobe in A2597.
- The data suggests that the HII and H₂ gas situated within a few kpc from the nucleus rotates around an axis parallel to the radio jet, this needs further confirmation.

A more detailed investigation into the heating and cooling of the intracluster medium will need to take into account the microphysics of the interaction between the various phases situated within the intracluster medium; the hot X-ray gas, the cool HII, H₂ gas and the radio emitting plasma. Once such a model is in place, the next step will be to compare detailed maps of local heating versus local cooling in cool core clusters. We will follow this work up in the near future with optical integral field spectroscopy (Oonk et al. in prep.) and Spitzer IRS spectroscopy (Jaffe & Bremer in prep.). A more detailed investigation of the excitation mechanisms for the molecular hydrogen gas will also be presented in a future paper.

Acknowledgments

JBRO wishes to thank J. Reunanen and L. Vermaas for useful discussions regarding the reduction of the SINFONI data. We would like to thank Lars Kristensen for use of his large grid of 1D shock models. The SINFONI observations were taken at the Very Large Telescope (VLT) facility of the European Southern Observatory (ESO) as part of project 075.A-0074. The National Radio Astronomy Observatory is a facility of the National Science Foundation operated under cooperative agreement by Associated Universities, Inc.

Bibliography

- Baars J. W. M., Genzel R., Pauliny-Toth I. I. K., Witzel A., *A&A*, 1977, 61, 99
Baker K., Thesis, 2005, Bristol University.
Baldwin J. A., Phillips M. M., Terlevich R., 1981, *PASP*, 93, 5
Baum S. A., O’Dea C. P., 1991, *MNRAS*, 250, 73
Birzan L., Rafferty D. A., McNamara B. R., Wise M. W., Nulsen P. E. J., 2004, *ApJ*, 607, 800
Birzan L., McNamara B. R., Nulsen P. E. J., Carilli C. L., Wise M. W., 2008, *ApJ*, 686, 859

- Black J. H., van Dishoeck E. F., 1987, *ApJ*, 322, 412
- Blanton E. L., Sarazin C. L., McNamara, B. R., 2003, *ApJ*, 585, 227
- Bonnet H., Abuter R., Baker A., Bornemann W., Brown A., Castillo R., Conzelmann R., Damster R., Davies R., Delabre B., Donaldson R., Dumas C., Eisenhauer F., Elswijk E., Fedrigo E., Finger G., Gemperlein H., Genzel R., Gilbert A., Gillet G., Goldbrunner A., Horrobin M., Ter Horst R., Huber S., Hubin N., Iserlohe C., Kaufer A., Kissler-Patig M., Kragt J., Kroes G., Lehnert M., Lieb W., Liske J., Lizon J., Lutz D., Modigliani A., Monnet G., Nesvadba N., Patig J., Pragt J., Reunanen J., Růhrle C., Rossi S., Schmutzer R., Schoemaker T., Schreiber J., Stroebele S., Szeifert T., Tacconi L., Tecza M., Thatte N., Tordo S., van der Werf P., Weisz H., 2004, *The ESO Messenger*, 117, 17
- Churazov E., Brueggen M., Kaiser C. R., Boehringer H., Forman W., 2001, *ApJ*, 554, 261
- Clarke T. E., Sarazin C. L., Blanton E. L., Neumann D. M., Kassim N. E., 2005, *ApJ*, 625, 748
- Crawford C. S., Fabian A. C., 1992, *MNRAS*, 259, 265
- Crawford C. S., Allen S. W., Ebeling H., Edge A. C., Fabian A. C., 1999, *MNRAS*, 306, 857
- Crawford C. S., Hatch N. A., Fabian A. C., Sanders J. S., 2005, *MNRAS*, 363, 216
- Dalla Vecchia C., Bower R. G., Theuns T., Balogh M. L., Mazzotta P., Frenk C. S., 2004, *MNRAS*, 355, 995
- Davies R. I., Sternberg A., Lehnert M., Tacconi-Garman L. E., 2003, *ApJ*, 597, 907
- Davies R. I., Sternberg A., Lehnert M. D., Tacconi-Garman L. E., 2005, *ApJ*, 633, 105
- Devillard N., 1997, *The ESO Messenger*, 87
- Devillard N., 2001, *ASP Conf. Ser.*, 238, 525
- de Grandi S., Böhringer H., Guzzo L., Molendi S., Chincarini G., Collins C., Cruddace R., Neumann D., Schindler S., Schuecker P., Voges W., 1999, *ApJ*, 514, 148
- Donahue M., Mack J., Voit G. M., Sparks W., Elston R., Maloney P. R., 2000, *ApJ*, 545, 670
- Draine B. T., Woods D. T., 1992, *ApJ*, 363, 464
- Dunn R. J. H., Fabian A. C., *MNRAS*, 373, 959
- Edge A. C., 2001, *MNRAS*, 328, 762
- Edge A. C., Wilman R. J., Johnstone R. M., Crawford C. S., Fabian A. C., Allen S. W., 2002, et al., *MNRAS*, 337, 49
- Eisenhauer F., Abuter R., Bickert K., Biancat-Marchet F., Bonnet H., Brynnel J., Conzelmann R. D., Delabre B., Donaldson R., Farinato J., Fedrigo E., Genzel R., Hubin N. N., Iserlohe C., Kasper M. E., Kissler-Patig M., Monnet G. J., Roehrle C., Schreiber J., Stroebele S., Tecza M., Thatte N. A., Weisz H., 2003, *SPIE*, 4841, 1548
- Fabian A. C., Nulsen P. E. J., Stewart G. C., Ku W. H. M., Malin D. F., Mushotzky R. F., 1981, *MNRAS*, 196, 35
- Fabian A. C., Crawford C. S., Edge A. C., Mushotzky R. F., 1994, *MNRAS*, 267, 779
- Fabian A. C., Celotti A., Blundell K. M., Kassim N. E., Perley R. A., *MNRAS*, 331, 369
- Fabian A. C., Sanders J. S., Taylor G. B., Allen S. W., Crawford C. S., Johnstone R. M., Iwasawa K., 2006, *MNRAS*, 366, 417
- Fabian A. C., Johnstone R. M., Sanders J. S., Conselice C. J., Crawford C. S., Gallagher J. S., Zweibel E., 2008, *Nat.*, 454, 968
- Falcke H., Rieke M. J., Rieke G. H., Simpson C., Wilson A. S., 1998, *ApJ*, 494, 155
- Ferland G. J., Fabian A. C., Hatch N. A., Johnstone R. M., Porter R. L., van Hoof P. A. M., Williams R. J. R., 2009, *MNRAS*, 392, 1475
- Flower D. R., Pineau des Forêts G., 2003, *MNRAS*, 343, 390

- Govoni F., Feretti L., Giovannini G., Boehringer H., Reiprich T. H., Murgia M., 2001, *A&A*, 376, 803
- Govoni F., Feretti L., 2004, *IJMPD*, 8, 1549
- Guillard P., Boulanger F., Pineau Des Forêts G., Appleton P. N., 2009, *A&A*, 502, 515
- Hansen L., Joergensen H. E., Noergaard-Nielsen H. U., Pedersen K., Goudfrooij P., Linden-Voerle M. J. D., 2000, *A&A*, 356, 83
- Hatch N. A., Crawford C. S., Fabian A. C., Johnstone R. M., 2005, *MNRAS*, 358, 765
- Hatch N. A., Crawford C. S., Fabian A. C., 2007, *MNRAS*, 380, 33
- Heckman T. M., Baum S. A., van Breugel W. J., McCarthy, P., 1989, *ApJ*, 338, 48
- Hollenbach D., McKee C. F., 1989, *ApJ*, 343, 306
- Irwin J. A., Stil J. M., Bridges T. J., 2001, *MNRAS*, 328, 359
- Jaffe W., Bremer M.N., 1997, *MNRAS*, 284, 1
- Jaffe W., Bremer M.N., van der Werf P.P., 2001, *MNRAS*, 324, 443
- Jaffe W., Bremer M.N., Baker K., 2005, *MNRAS*, 360, 748
- Johnstone R. M., Fabian A. C., 1988, *MNRAS*, 233, 581
- Johnstone R. M., Hatch N. A., Ferland G. J., Fabian A. C., Crawford C. S., Wilman R. J., 2007, *MNRAS*, 382, 1246
- Kaastra J. S., den Boggende A. J., Brinkman A. C., Ferrigno C., den Herder J. W., Mewe R., Tamura T., de Vries C., Cottam J., Kahn S. M., Paerels F. B. S., Peterson J. M., Rasmussen A. P., Branduardi-Raymont G., Sakelliou I., Audard M., Gijdel M., Erd C., 2001, *ASPC*, 234, 351
- Koekemoer A. M., O’Dea C. P., Sarazin C. L., McNamara B. R., Donahue M., Voit G. M., Baum S. A., Gallimore J. F., 1999, *ApJ*, 525, 621
- Kristensen L. E., Ravkilde T. L., Field D., Lemaire J. L., Pineau Des Forêts G., 2007, *A&A*, 469, 561
- Lepp S., McCray R., 1983, *ApJ*, 296, 560
- Maia M. A. G., da Costa L. N., Willmer C., Pellegrini P. S., Rite C., 1987, *AJ*, 93, 546
- Maloney P. R., Hollenbach D. J., Tielens A. G. G. M., 1996, *ApJ*, 466, 561
- Markwardt C. B., 2009, *ASPC*, 411, 251
- McNamara B. R., O’Connell R. W., 1992, *ApJ*, 393, 579
- McNamara B. R., Wise M. W., Nulsen P. E. J., David L. P., Carilli C. L., Sarazin C. L., O’Dea C. P., Houck J., Donahue M., Baum S., Voit M., O’Connell R. W., Koekemoer A., 2001, *ApJ*, 562, 149
- Neumayer N., Cappellari M., Reunanen J., Rix H. W., van der Werf P. P., de Zeeuw P. T., Davies, R. I., 2007, *ApJ*, 671, 1329
- O’Dea C. P., Baum S. A., Gallimore J. F., 1994, *ApJ*, 436, 669
- O’Dea C. P., Baum S. A., Mack J., Koekemoer A. M., Laor A., 2004, *ApJ*, 612, 131
- O’Dea C. P., Baum S. A., Privon G., Noel-Storr J., Quillen A. C., Zufelt N., Park, J., Edge A., Russell H., Fabian A. C., Donahue M., Sarazin C. L., McNamara B., Bregman J. N., Egami E., 2008, *ApJ*, 681, 1035
- Osterbrock D. E., Ferland G. J., 2006, *Astrophysics of Gaseous Nebulae and Active Galactic Nuclei*, University Science Books.
- Peterson J. R., Fabian A. C., 2006, *PhR*, 427, 1
- Peres C. B., Fabian A. C., Edge A. C., Allen S. W., Johnstone R. M., White D. A., 1998, *MNRAS*, 298, 416

Cluster	z	D_L	Θ	L_X	$L_{1.4\text{GHz}}$	t_{obs}
Sersic 159-03	0.0564	245	1.1	2.1	29.3	4.2
Abell 2597	0.0821	363	1.5	1.0	1.6	8.5

Table 2.1 — Targets. Columns 1, 2 give the cluster name and the redshift of its BCG. In column 3 we give the luminosity distance to the BCG in units of Mpc. In column 4 we give the angular size scale at the distance of the BCG, in units of kpc arcsec⁻¹. In column 5 we give the X-ray luminosity, in units of 10⁴⁴ erg s⁻¹, of the cluster in the 0.5-2.0 keV band from de Grandi (1999). In column 6 we give the radio power, in units 10³¹ erg s⁻¹ Hz⁻¹, of the cluster at 1.4 GHz from Birzan et al. (2008) In column 7 we give the on-source integration time in units of hours. An equal amount of time was spend off-source observing the sky.

Resolution	no smoothing	ss20	ss22	ss44
Spatial [arcsec]	0.9	1.0	1.0	1.1
Spectral [km s ⁻¹]	38	38	51	73

Table 2.2 — Spatial and spectral Resolution. Dependence of the spatial and spectral resolution on smoothing. The spatial resolution is given in units of arcsec and the spectral resolution in terms of km s⁻¹. Column 1 gives the type of resolution. Column 2 gives the resolution for no smoothing. Column 3 gives the resolution after smoothing with a two pixel FWHM Gaussian in the spatial domain. Column 4 gives the resolution after smoothing with two pixel FWHM Gaussians in both the spatial and spectral domain. Column 5 gives the resolution after smoothing with four pixel FWHM Gaussians in both the spatial and spectra domain.

- Quillen A. C., Zufelt N., Park J., O’Dea C. P., Baum S. A., Privon G., Noel-Storr J., Edge A., Russell H., Fabian A., Donahue M., Bregman J. N., McNamara B. R., Sarazin C. L., 2008, *ApJS*, 176, 39
- Rafferty D. A., McNamara B. R., Nulsen P. E. J., Wise M. W., 2006, *ApJ*, 652, 216
- Rousselot P., Lidman C., Cuby J. G., Moreels G., Monnet G., 1999, *A&A*, 354, 1134
- Salome P., Combes F., 2003, *A&A*, 412, 657
- Sanders J. S., Fabian A. C., Taylor G. B., 2009, *MNRAS*, 393, 71
- Sarazin C. L., Burns J. O., Roettiger K., McNamara B., 1995, *ApJ*, 447, 559
- Scoville N. Z., Hall D. N. B., Ridgway S. T., Kleinmann S. G., *ApJ*, 253, 136
- Shull J. M., Beckwith S., *A&AR*, 20, 163
- Sternberg A., Dalgarno A., 1989, *ApJ*, 338, 197
- Storchi-Bergmann T., McGregor P. J., Riffel R. A., Simoes Lopes R., Beck T., Dopita M., 2009, *MNRAS*, 394, 1148
- Sutherland R. S., Bicknell G. V., 2007, *ApJS*, 173, 37
- Taylor G. B., O’Dea C. P., Peck A. B., Koekemoer A. M., 1999, *ApJ*, 512, 27
- Taylor G. B., Fabian A. C., Gentile G., Allen S. W., Crawford C., Sanders J. S., 2007, *MNRAS*, 382, 67
- Voit G. M., Donahue M., 1997, *ApJ*, 486, 242
- Wilman R. J., Edge A. C., Johnstone R. M., Fabian A. C., Allen S. W., Crawford C. S., 2002, *MNRAS*, 337, 63
- Wilman R. J., Edge A. C., Johnstone R. M., 2005, *MNRAS*, 371, 755
- Wilman R. J., Edge A. C., Swinbank A. M., 2006, *MNRAS*, 359, 93
- Wilman R. J., Edge A. C., Swinbank A. M., 2009, *MNRAS*, 395, 1355

Field [10^{-17} erg s $^{-1}$ cm $^{-2}$ μ m $^{-1}$]	no smoothing	ss20	ss44
Central	24.9	12.6	3.7
South-East	40.0	19.8	5.4
South-West	25.8	12.9	3.5
North	30.1	15.0	4.0

Table 2.3 — ABELL 2597 Sensitivity. The RMS noise is given in units of 10^{-17} erg s $^{-1}$ cm $^{-2}$ μ m $^{-1}$ for an area of 0.125×0.125 arcsec 2 which is equivalent to one spatial pixel. The RMS noise was calculated in the interval 2.07 - 2.30 μ m with a sampling of 2.45×10^{-4} μ m which is equivalent to one spectral pixel. Column 1 gives the observed field. Column 2 gives the RMS noise for no smoothing. Column 3 gives the RMS noise after smoothing with a two pixel FWHM Gaussian in the spatial domain. Column 4 gives the RMS noise after smoothing with a four pixel FWHM Gaussian in both the spatial and spectral domain. The RMS noise does not vary much across the observed field.

Field [10^{-17} erg s $^{-1}$ cm $^{-2}$ μ m $^{-1}$]	no smoothing	ss22	ss44
South-East	33.1	13.2	9.0
South-West	30.5	10.2	4.3
North	36.7	12.2	5.0

Table 2.4 — SERSIC 159-03 Sensitivity. The RMS noise is given in units of 10^{-17} erg s $^{-1}$ cm $^{-2}$ μ m $^{-1}$ for an area of 0.125×0.125 arcsec 2 which is equivalent to one spatial pixel. The RMS noise was calculated in the interval 2.07 - 2.30 μ m with a sampling of 2.45×10^{-4} μ m which is equivalent to one spectral pixel. Column 1 gives the observed field. Column 2 gives the RMS noise for no smoothing. Column 3 gives the RMS noise after smoothing with two pixel FWHM Gaussians in both the spatial and spectral domain. Column 4 gives the RMS noise after smoothing with four pixel FWHM Gaussian in both the spatial and spectral domain. The RMS noise does not vary much across the observed field.

Line Name	Flux [10^{-17} erg s $^{-1}$ cm $^{-2}$]	Luminosity [10^{39} erg s $^{-1}$]
H $_2$ 1-0 S(0) (2.2235μ m) ¹	121.7 \pm 11.3	19.2 \pm 1.8
H $_2$ 1-0 S(1) (2.1218μ m)	669.0 \pm 14.6	105.5 \pm 2.3
H $_2$ 1-0 S(2) (2.0338μ m)	280.2 \pm 8.4	44.2 \pm 1.3
H $_2$ 1-0 S(3) (1.9576μ m)	732.0 \pm 19.3	115.4 \pm 3.0
H $_2$ 1-0 S(4) (1.8920μ m)	129.7 \pm 7.5	20.5 \pm 1.2
H $_2$ 1-0 S(5) (1.8358μ m)	462.2 \pm 11.7	72.9 \pm 1.8
H $_2$ 2-1 S(2) (2.1542μ m) ²	22.0 \pm 4.1	3.5 \pm 0.6
H $_2$ 2-1 S(3) (2.0735μ m) ¹	38.0 \pm 2.2	6.0 \pm 0.3
H $_2$ 2-1 S(5) (1.9449μ m), Br δ (1.9451μ m) ¹	39.3 \pm 4.2	6.2 \pm 0.7
Br γ (2.1661μ m) ²	30.1 \pm 4.6	4.7 \pm 0.7
Pa α (1.8756μ m)	613.0 \pm 20.3	96.7 \pm 3.2
Fe II (1.8100μ m) ¹	86.5 \pm 5.6	13.6 \pm 0.9

Table 2.5 — ABELL 2597 Integrated line fluxes and luminosities. The integrated line fluxes are obtained by collapsing the data cube into a single spectrum and fitting the lines by a single Gaussian. The data was smoothed by a four pixel FWHM in both the spatial and spectral domain. The results were inspected by eye and the errors were estimated using Monte-Carlo simulations. The spectrum also hints at the presence of the H $_2$ 2-1 S(4) line, but a reliable flux could not be derived for this line. Fluxes are given in units of 10^{-17} erg s $^{-1}$ cm $^{-2}$ and luminosities are given in units of 10^{39} erg s $^{-1}$.

¹ The H $_2$ 1-0 S(0), H $_2$ 2-1 S(3), H $_2$ 2-1 S(5), Br δ and Fe II lines have been integrated over the central field only.

² The H $_2$ 2-1 S(2) and Br γ lines have been integrated over the combined areas A1 and A2 only, see Fig. 2.3.

Line Name	Flux [10^{-17} erg s $^{-1}$ cm $^{-2}$]	Luminosity [10^{39} erg s $^{-1}$]
H ₂ 1-0 S(1) (2.1218 μ m)	171.0 \pm 11.9	12.3 \pm 0.9
H ₂ 1-0 S(3) (1.9576 μ m)	217.9 \pm 18.1	15.7 \pm 1.3
Pa α (1.8756 μ m)	104.4 \pm 11.6	7.5 \pm 0.8

Table 2.6 — SERSIC 159-03 Integrated line fluxes and luminosities. The integrated line fluxes are obtained by collapsing the data cube into a single spectrum and fitting the lines by a single Gaussian. The data was smoothed by a four pixel FWHM in both the spatial and spectral domain. The results were inspected by eye and the errors were estimated using Monte-Carlo simulations. The spectrum also hints at the presence of the H₂ 1-0 S(0), 1-0 S(2) and 1-0 S(4) lines, but reliable fluxes could not be derived for these lines. Fluxes are given in units of 10^{-17} erg s $^{-1}$ cm $^{-2}$ and luminosities are given in units of 10^{39} erg s $^{-1}$.

Line/Area	A1	A2	A3	A4	A5	A6	A7
H ₂ 1-0 S(0)	69.0 \pm 8.5	18.6 \pm 3.0	-	-	-	-	-
H ₂ 1-0 S(1)	332.0 \pm 6.6	84.1 \pm 3.0	4.9 \pm 1.2	21.8 \pm 6.1	4.6 \pm 1.1	12.0 \pm 0.9	3.2 \pm 1.1
H ₂ 1-0 S(2)	129.0 \pm 4.1	31.0 \pm 2.1	(2.1)	14.6 \pm 1.7	-	-	-
H ₂ 1-0 S(3)	335.3 \pm 9.2	85.2 \pm 3.0	6.0 \pm 1.0	32.6 \pm 4.3	4.8 \pm 0.7	10.2 \pm 1.3	2.6 \pm 0.9
H ₂ 1-0 S(4)	69.7 \pm 4.0	21.5 \pm 2.0	1.9 \pm 0.9	10.9 \pm 2.1	-	-	-
H ₂ 1-0 S(5)	223.1 \pm 5.4	53.0 \pm 2.5	3.7 \pm 1.1	25.4 \pm 4.5	3.5 \pm 0.7	-	1.5 \pm 0.7
H ₂ 2-1 S(2)	16.2 \pm 2.4	5.5 \pm 2.2	-	-	-	-	-
H ₂ 2-1 S(3)	26.9 \pm 3.0	7.5 \pm 1.0	-	-	-	-	-
H ₂ 2-1 S(5)	13.7 \pm 4.1	2.8 \pm 1.0	-	-	-	-	-
Br δ	14.1 \pm 4.1	4.3 \pm 1.0	-	-	-	-	-
Br γ	21.1 \pm 2.5	6.5 \pm 2.1	-	-	-	-	-
Pa α	257.9 \pm 8.8	79.7 \pm 3.6	5.3 \pm 1.2	29.0 \pm 7.0	3.6 \pm 0.7	-	2.4 \pm 0.8
Fe II	50.2 \pm 7.2	5.0 \pm 2.1	-	-	-	-	-

Table 2.7 — ABELL 2597 Integrated line fluxes for regions A1-A7. The integrated line fluxes are obtained by collapsing the data cube, within the selected region, into a single spectrum and fitting the lines by a single Gaussian. The smoothing performed for a given line is specified in the caption of the line spectra shown in Appendix A.3. The results were inspected by eye and the errors were estimated using Monte-Carlo simulations. If Br γ is detected the H₂ 2-1 S(5), Br δ complex is disentangled by assuming that the Br γ /Br δ ratio is 1.5 (Osterbrock & Ferland 2006). The uncertain H₂ 1-0 S(2) flux in region A3 could not be fitted well. The H₂ 1-0 S(2) flux given for A3 is based on fixing the width of this line to that of the H₂ 1-0 S(4) line. Fluxes are given in units of 10^{-17} erg s $^{-1}$ cm $^{-2}$.

Line/Area	A1	A2	A3	A4	A5	A6	A7
v(H ₂ 1-0 S(3))	+3 \pm 6	-29 \pm 6	+36 \pm 19	-10 \pm 13	+20 \pm 14	+174 \pm 17	+156 \pm 25
σ (H ₂ 1-0 S(3))	214 \pm 6	146 \pm 6	98 \pm 20	89 \pm 13	103 \pm 15	120 \pm 17	60 \pm 15
v(Pa α)	-21 \pm 8	-59 \pm 8	+59 \pm 27	-4 \pm 29	+22 \pm 22	-	+152 \pm 52
σ (Pa α)	256 \pm 9	177 \pm 8.3	108 \pm 28	118 \pm 29	116 \pm 23	-	109 \pm 56

Table 2.8 — ABELL 2597 Kinematics for regions A1-A7. For each line the top row gives the velocity, with respect to the systemic velocity, and the bottom row gives the velocity dispersion. These are derived from a single Gaussian line fit to the collapsed spectrum for a selected region. Here we present results only for the H₂ 1-0 S(3) and Pa α lines. All other lines follow the behaviour observed in these two lines within errors. The smoothing performed for a given line is specified in the caption of the line spectra shown in Appendix A.3. The results were inspected by eye and the errors were estimated using Monte-Carlo simulations. Velocity and velocity dispersion are both given in units of km s $^{-1}$.

Line/Area	A1	A2	A3	A4	A5	A6	A7
$T_{\text{exc,H}_2}$	2229±38	2141±59	2792±808	2660±481	2678±640	1586±264	1863±592
M_{H_2}	222.2±4.4	56.3±2.0	3.3±0.8	14.6±4.1	3.1±0.7	8.0±0.6	2.1±0.6
M_{HII}	410.0±14.0	126.7±5.7	8.4±1.9	46.1±11.1	5.7±1.1	-	3.8±1.3

Table 2.9 — ABELL 2597 Gas temperatures and masses for regions A1-A7. For each region an excitation temperature, $T_{\text{exc,H}_2}$ in units of Kelvin, is calculated for the H_2 gas. Molecular and ionised gas masses are calculated using the equations in the text. The molecular gas mass M_{H_2} is given in units of $10^2 M_{\odot}$. The ionised gas mass M_{HII} is given in units of $10^4 M_{\odot}$, using $n_e = 200 \text{ cm}^{-3}$ and $T_{\text{HII}} = 10^4 \text{ K}$. The temperature and mass calculations for the H_2 gas assume LTE conditions.

Line/Area	B1	B2	B3	B4	B5	B6	B7
H_2 1-0 S(1)	26.6±2.6	20.4±1.8	16.4±1.7	3.1±0.9	35.7±2.6	12.2±5.6	6.0±1.2
H_2 1-0 S(3)	42.2±5.3	24.1±2.0	18.8±1.4	3.5±0.7	40.2±2.8	12.6±3.3	7.1±0.9
Pa α	8.0±2.4	12.9±1.5	12.4±1.3	3.1±0.8	25.2±3.2	11.4±5.4	5.6±1.2

Table 2.10 — SERSIC 159-03 Integrated line fluxes for regions B1-B7. The integrated line fluxes are obtained by collapsing the data cube, within the selected region, into a single spectrum and fitting the lines by a single Gaussian. The smoothing performed for a given line is specified in the caption of the line spectra shown in Appendix A.3. The results were inspected by eye and the errors were estimated using Monte-Carlo simulations. Fluxes are given in units of $10^{-17} \text{ erg s}^{-1} \text{ cm}^{-2}$.

Line/Area	B1	B2	B3	B4	B5	B6	B7
$v(\text{H}_2$ 1-0 S(3))	-26±29	+109±12	+102±8	-49±17	-23±8	-63±21	-19±9
$\sigma(\text{H}_2$ 1-0 S(3))	250±31	132±13	103±8	78±18	100±8	65±14	62±4
$v(\text{Pa } \alpha)$	-7±40	+121±15	+106±10	-42±35	-28±13	-58±49	-20±21
$\sigma(\text{Pa } \alpha)$	127±40	120±16	95±10	122±36	104±15	98±53	86±20

Table 2.11 — SERSIC 159-03 Kinematics for regions B1-B7. For each line the top row gives the velocity, with respect to the systemic velocity, and the bottom row gives the velocity dispersion. These are derived from a single Gaussian line fit to the collapsed spectrum for a selected region. Here we present results only for the H_2 1-0 S(3) and Pa α lines. All other lines follow the behaviour observed in these two lines within errors. The smoothing performed for a given line is specified in the caption of the line spectra shown in Appendix A.3. The results were inspected by eye and the errors were estimated using Monte-Carlo simulations. Velocity and velocity dispersion are both given in units of km s^{-1} .

Line/Area	B1	B2	B3	B4	B5	B6	B7
$T_{\text{exc,H}_2}$	5655±3632	2520±546	2391±518	2331±1359	2321±385	2032±1550	2527±1073
M_{H_2}	8.0±0.8	6.2±0.5	5.0±0.5	0.9±0.3	10.9±0.8	3.7±1.7	1.8±0.4
M_{HII}	5.8±1.7	9.3±1.1	9.0±0.9	2.2±0.6	18.2±2.3	8.3±3.9	4.1±0.9

Table 2.12 — SERSIC 159-03 H_2 Gas temperatures and masses for regions B1-B7. For each region an excitation temperature, $T_{\text{exc,H}_2}$ in units of Kelvin, is calculated for the H_2 gas. Molecular and ionised gas masses are calculated using the equations in the text. The molecular gas mass M_{H_2} is given in units of $10^2 M_{\odot}$. The ionised gas mass M_{HII} is given in units of $10^4 M_{\odot}$, using $n_e = 200 \text{ cm}^{-3}$ and $T_{\text{HII}} = 10^4 \text{ K}$. The temperature and mass calculations for the H_2 gas assume LTE conditions.

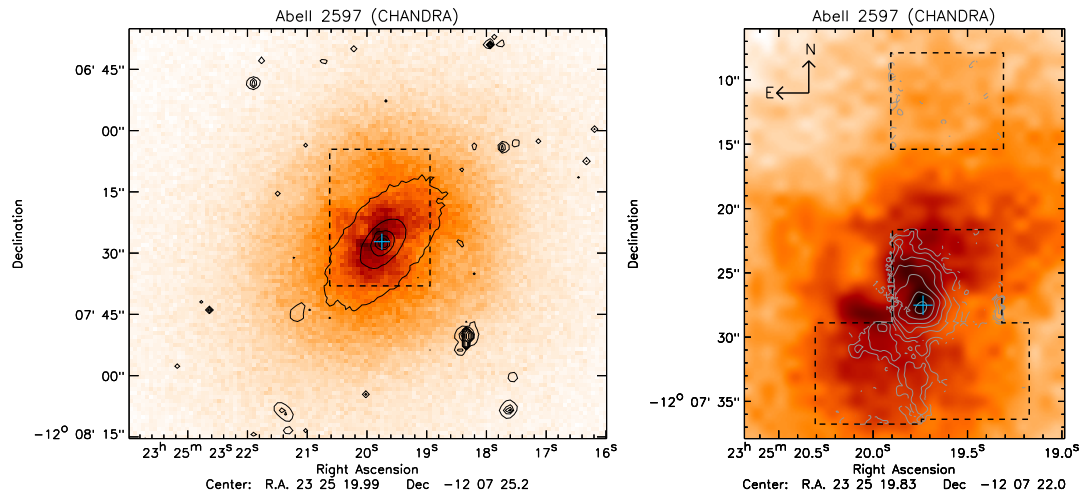


Figure 2.1 — ABELL 2597 Observed fields. (*left*) extent of the X-ray emission in the cluster core as observed by *CHANDRA* (exposure time 153.7 ks). VLT FORS *R*-band contours are overlaid in black (solid line). (*right*) zoom in of the region marked by the black dashed box in the left image. The fields observed by SINFONI are indicated with a dashed line in the right image. H_2 1-0 S(3) contours are overlaid in grey (solid line), drawn starting at $1.5 \times 10^{-17} \text{ erg s}^{-1} \text{ cm}^{-2} \text{ arcsec}^{-2}$ in steps of 2^n with $n=0,1,2,\dots$. The plus sign marks the position of the stellar nucleus.

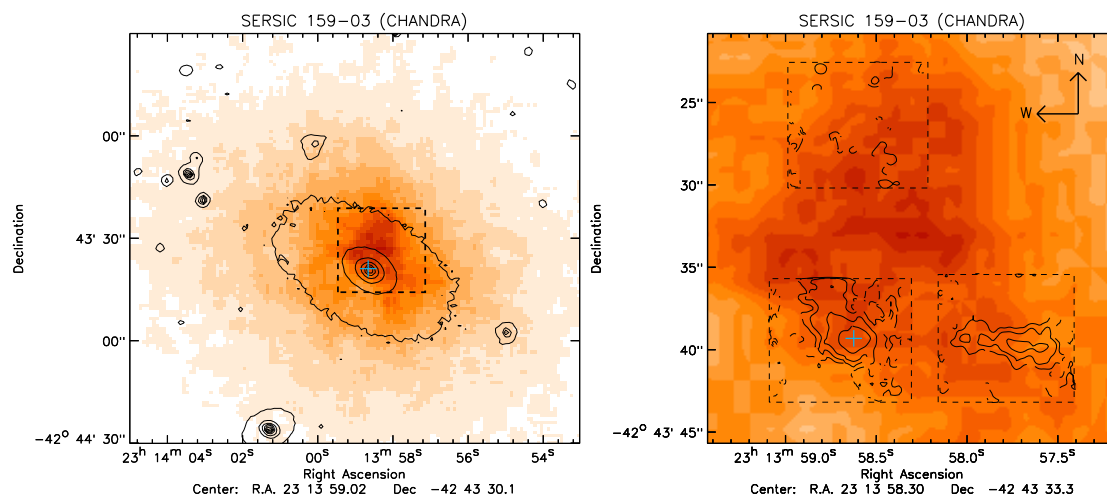


Figure 2.2 — SERSIC 159-03 Observed fields. (*left*) the extent of the X-ray emission in the cluster core as observed by *CHANDRA* (exposure time 10.1 ks), has been smoothed slightly. VLT FORS *R*-band contours are overlaid in black (solid line). (*right*) zoom in of the region marked by the black dashed box in the left image. The fields observed by SINFONI are indicated with a dashed line in the right image. H_2 1-0 S(3) contours are overlaid in black (solid line), drawn starting at $1.5 \times 10^{-17} \text{ erg s}^{-1} \text{ cm}^{-2} \text{ arcsec}^{-2}$ in steps of 2^n with $n=0,1,2,\dots$. The plus sign marks the position of the stellar nucleus.

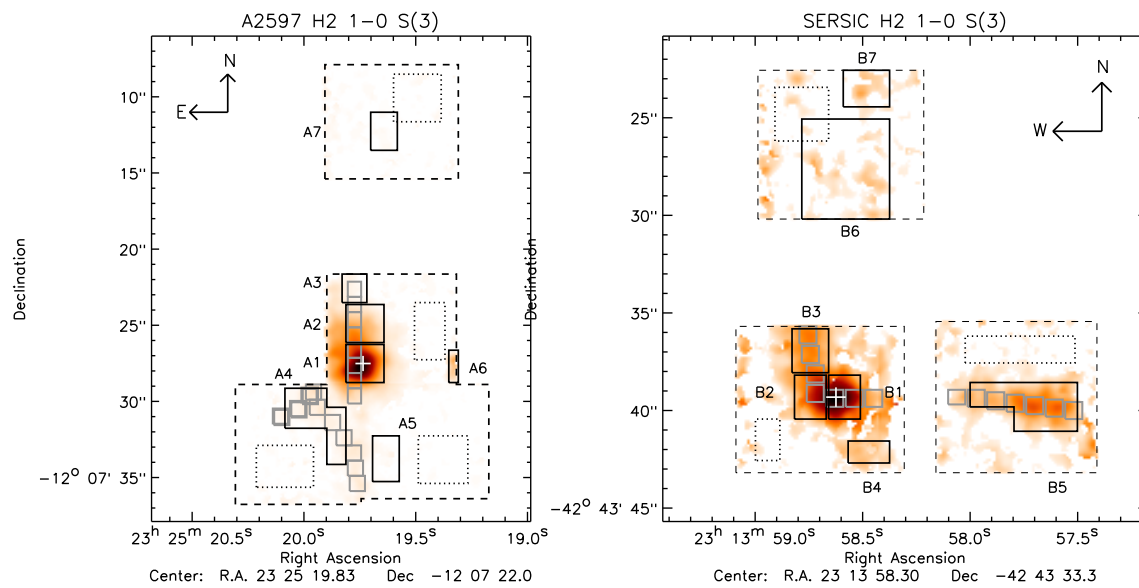


Figure 2.3 — Selected regions in ABELL 2597 and SERSIC 159-03. The regions are shown overlaid on SINFONI H₂ 1-0 S(3) surface brightness maps. The left image shows A2597 and the right image S159. The fields observed by SINFONI are indicated with a dashed black line. The dotted black lines show the regions used for obtaining the off-source spatial median in these fields. The solid black lines show the selected regions A1-A7 for A2597 and B1-B7 for S159, see Sections 2.7.1 and 2.7.2. The small grey squares show the regions investigated along the filaments, see Sections 2.4.3 and 2.6.3. The plus sign marks the position of the stellar nucleus.

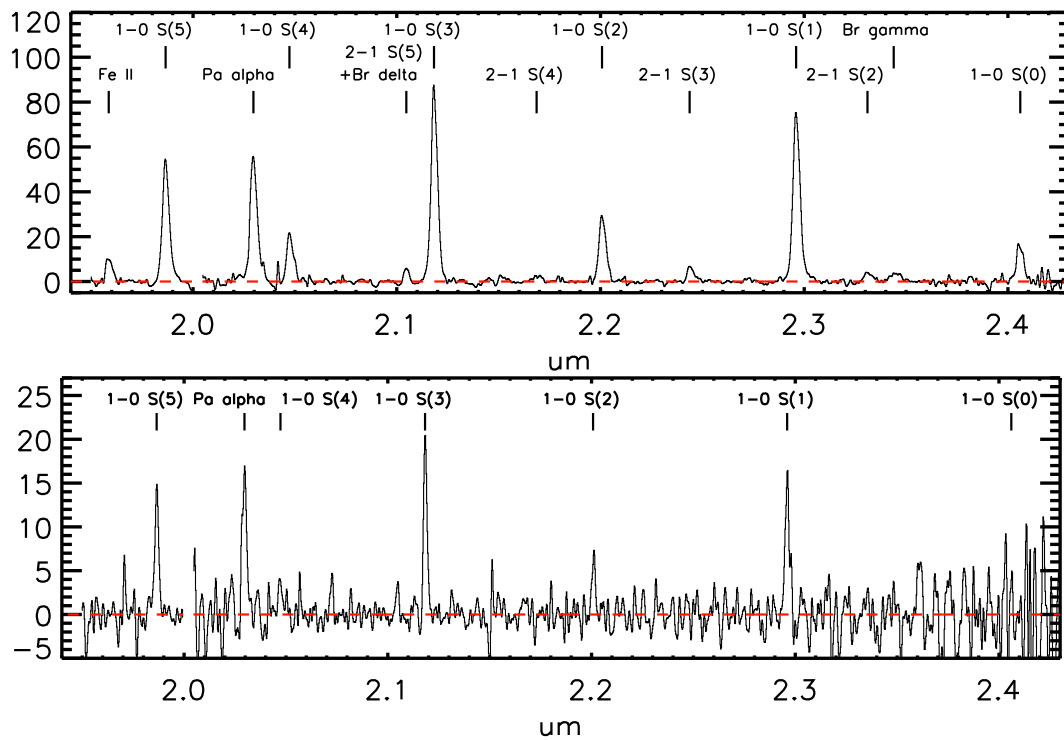


Figure 2.4 — ABELL 2597 full K-band spectra. As an example of the quality of our SINFONI spectra we show full K-band spectra for two regions. The top image shows the spectrum for region A1 and the bottom image shows the spectrum for region A4, see Fig. 2.3 and Section 2.7.1. These spectra were obtained after smoothing the data by four pixels in both the spatial and spectral planes. The horizontal axis is given in units of μm and the vertical axis is given in units of $10^{-14} \text{ erg cm}^{-2} \text{ s}^{-1} \mu\text{m}^{-1}$.

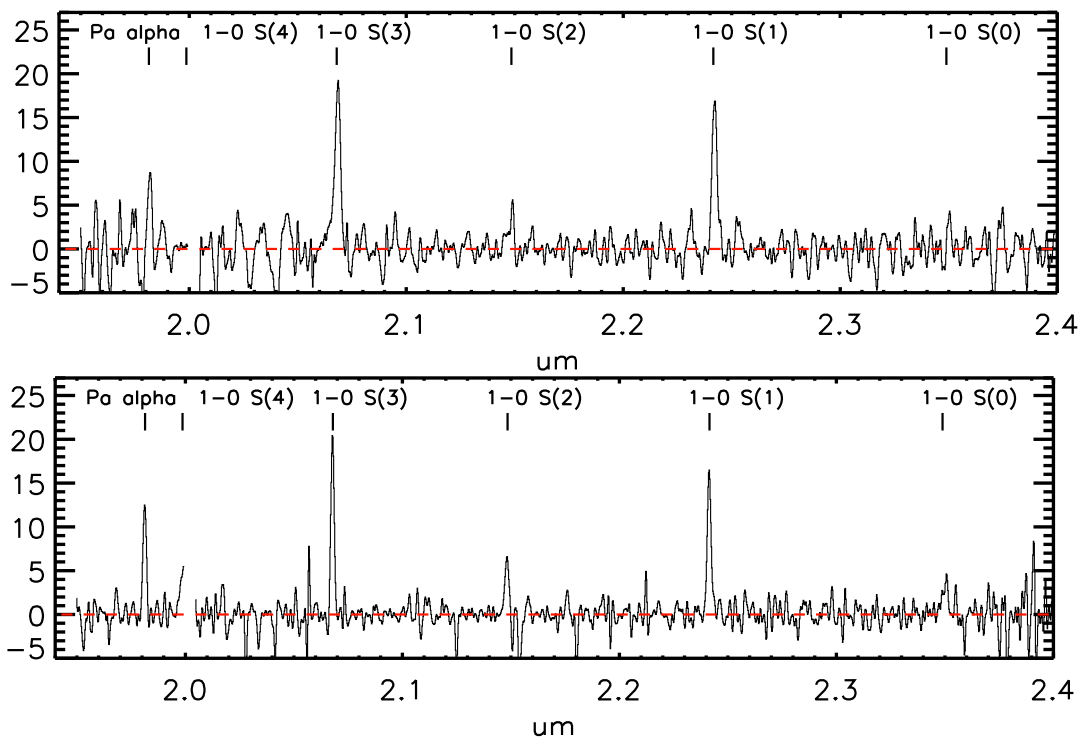


Figure 2.5 — SERSIC159-03 full K-band spectra. As an example of the quality of our SINFONI spectra we show full K-band spectra for two regions. The top image shows the spectrum for the combined regions B1 and B2. The bottom image shows the spectrum for region B5, see Fig. 2.3 and Section 2.7.2. These spectra were obtained after smoothing the data by four pixels in both the spatial and spectral planes. The horizontal axis is given in units of μm and the vertical axis is given in units of $10^{-14} \text{ erg cm}^{-2} \text{ s}^{-1} \mu\text{m}^{-1}$.

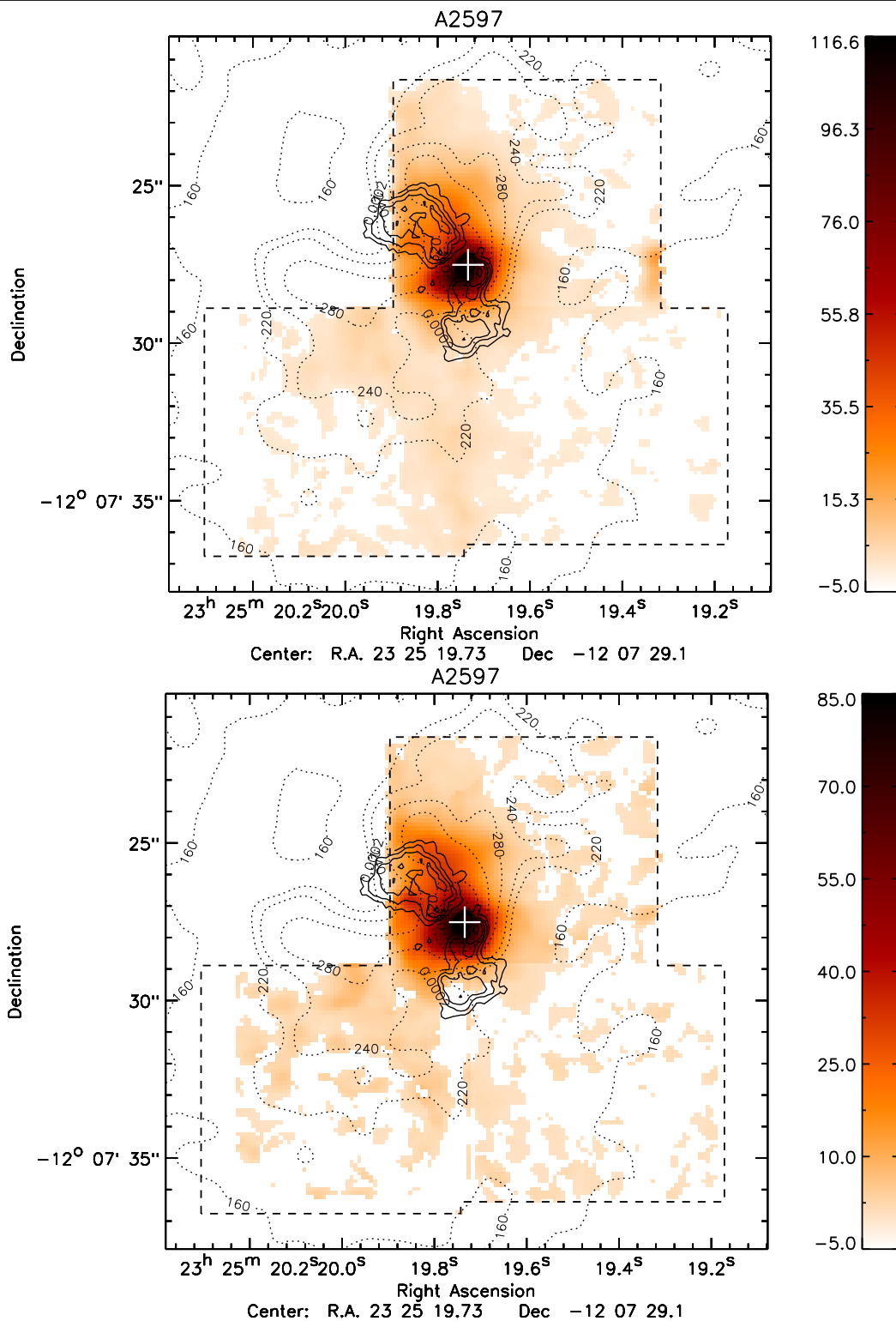


Figure 2.6 — ABELL 2597 Surface brightness. We show surface brightness maps for the H_2 1-0 S(3) (top) and Pa α (bottom) lines in units of $10^{-17} \text{ erg s}^{-1} \text{ cm}^{-2} \text{ arcsec}^{-2}$. The maps are obtained by fitting the spectrum for each spatial pixel in the data cube by a single Gaussian. The data was smoothed by four pixels in both the spatial and spectral planes. The stellar nucleus is indicated by the cross. VLA 8.4 GHz Radio Continuum contours (solid black line, Sarazin et al. 1995) and *CHANDRA* X-ray contours (dotted black line) are overlaid. The Radio contours start at 4σ ($1\sigma = 50 \mu\text{Jy}$). Consecutive Radio and X-ray contours double in value. Surface brightness maps for all detected lines are shown in Appendix A.1. The northern field is not shown.

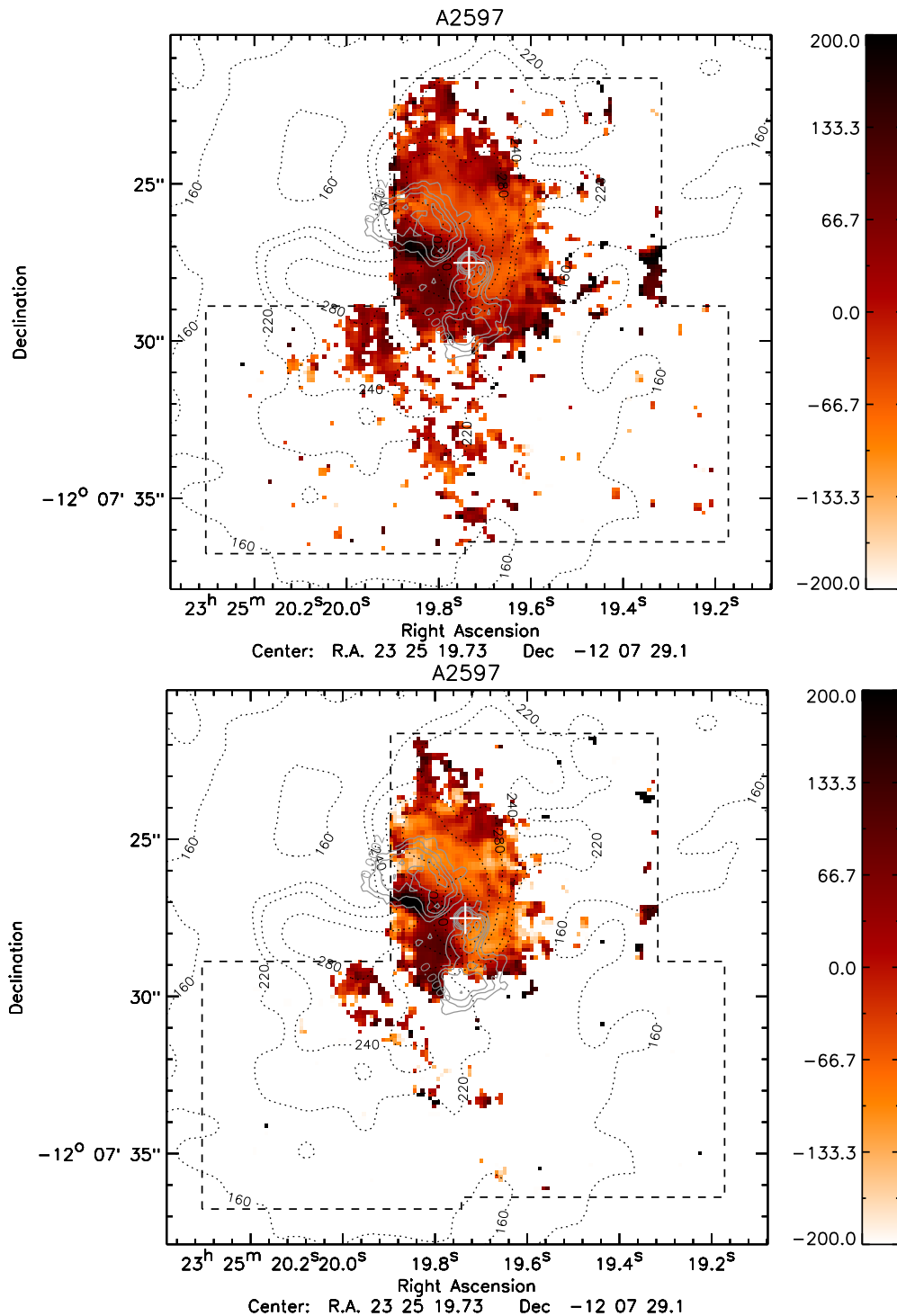


Figure 2.7 — ABELL 2597 Velocity. We show velocity maps for the H_2 1-0 S(3) (top) and $\text{Pa } \alpha$ (bottom) lines in units of km s^{-1} with respect to the systemic velocity of the BCG. The velocity of the gas is derived by fitting the spectrum for each spatial pixel in the data cube by a single Gaussian. The data was smoothed by two pixels in the spatial plane. The stellar nucleus is indicated by the cross. VLA 8.4 GHz Radio Continuum contours (solid grey line, Sarazin et al. 1995) and *CHANDRA* X-ray contours (dotted black line) are overlaid. The Radio contours start at 4σ ($1\sigma = 50 \mu\text{Jy}$). Consecutive Radio and X-ray contours double in value. Velocity maps were made for all detected emission lines. These all show the same structure and are thus not all shown here. The northern field is not shown.

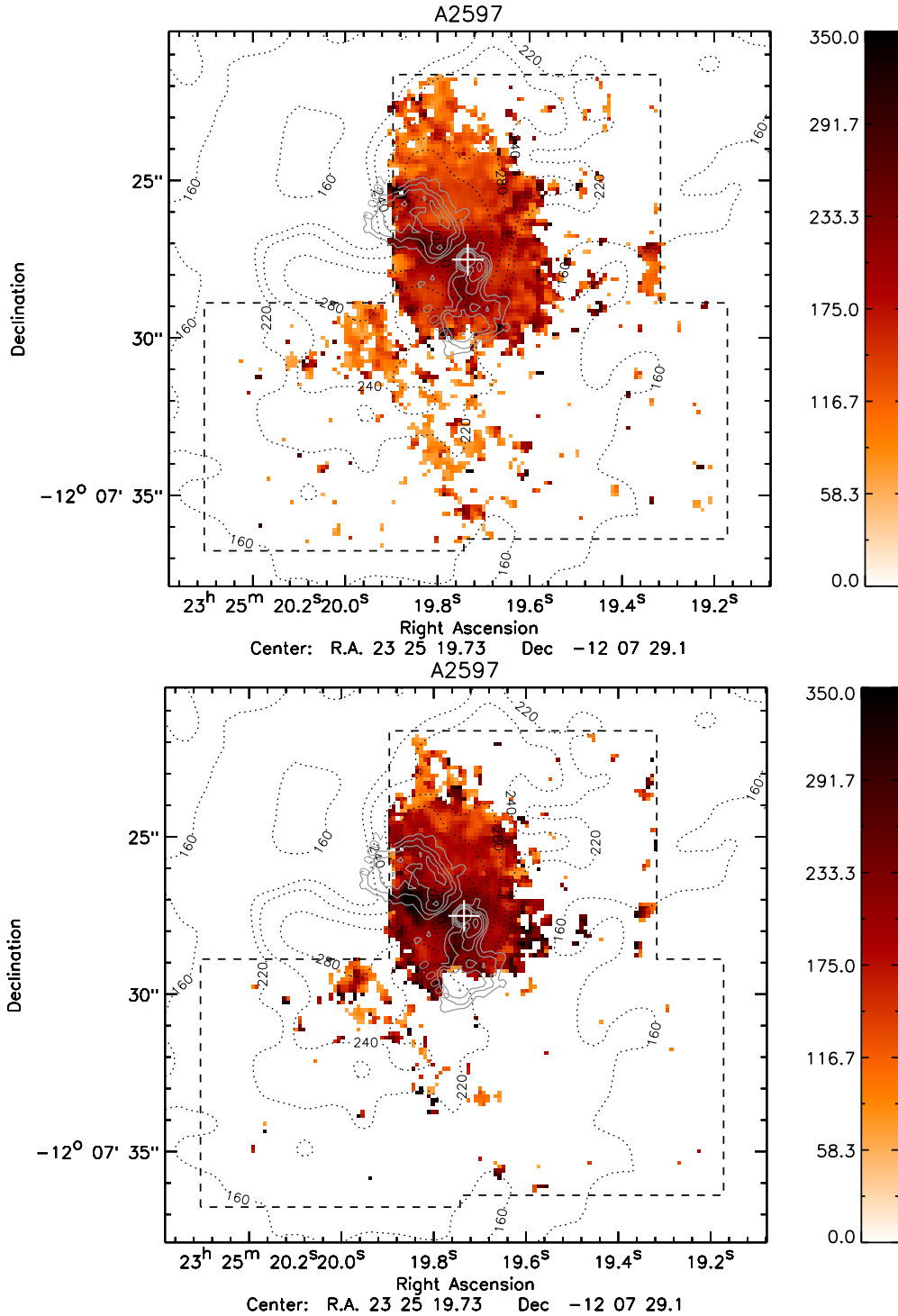


Figure 2.8 — ABELL 2597 Velocity dispersion. We show velocity dispersion maps for the H_2 1-0 S(3) (top) and the Pa α (bottom) lines in units of km s^{-1} . The velocity dispersion σ_v of the gas is derived by fitting the spectrum for each spatial pixel in the data cube by a single Gaussian. The data cube was smoothed by two pixels in the spatial plane. The stellar nucleus is indicated by the cross. VLA 8.4 GHz Radio Continuum contours (solid grey line, Sarazin et al. 1995) and *CHANDRA* X-ray contours (dotted black line) are overlaid on the dispersion maps. The Radio contours start at 4σ ($1\sigma = 50 \mu\text{Jy}$). Consecutive Radio and X-ray contours double in value. Gas dispersion maps were made for all detected emission lines. All show the same structure and are thus not all shown here. The northern field is not shown.

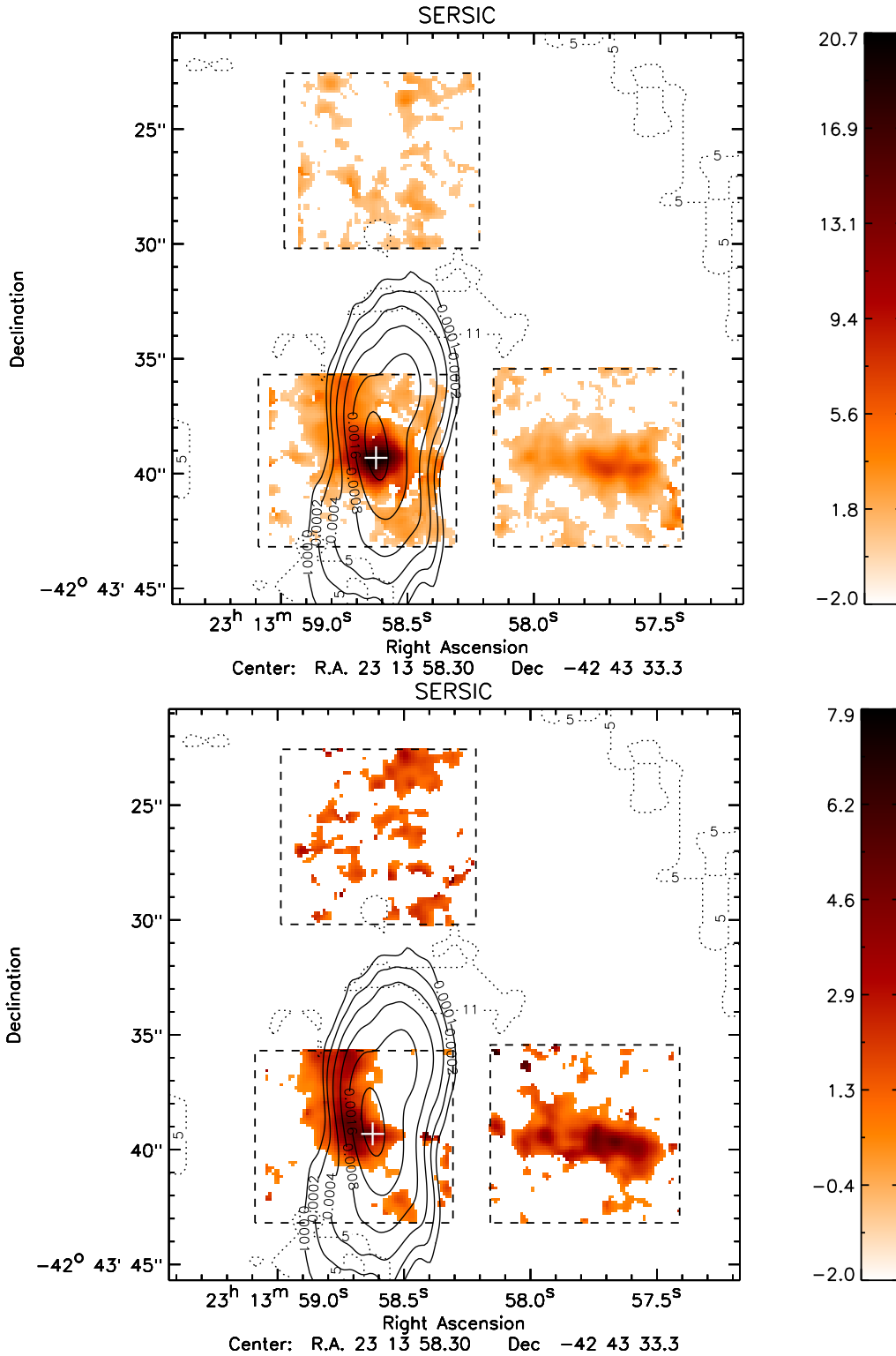


Figure 2.9 — SERSIC 159-03 Surface brightness. We show surface brightness maps for the H_2 1-0 S(3) (top) and $\text{Pa } \alpha$ (bottom) lines in units of $10^{-17} \text{ erg s}^{-1} \text{ cm}^{-2} \text{ arcsec}^{-2}$. The maps are obtained by fitting the spectrum for each spatial pixel in the data cube by a single Gaussian. The data cube was smoothed by four pixels in both the spatial and spectral planes. The stellar nucleus is indicated by the cross. VLA 8.4 GHz Radio Continuum contours (solid black line) and *CHANDRA* X-ray contours (dotted black line) are overlaid. The Radio contours start at 4σ ($1\sigma = 25 \mu\text{Jy}$). Consecutive Radio and X-ray contours double in value. Surface brightness maps for all detected lines are shown in Appendix A.2.

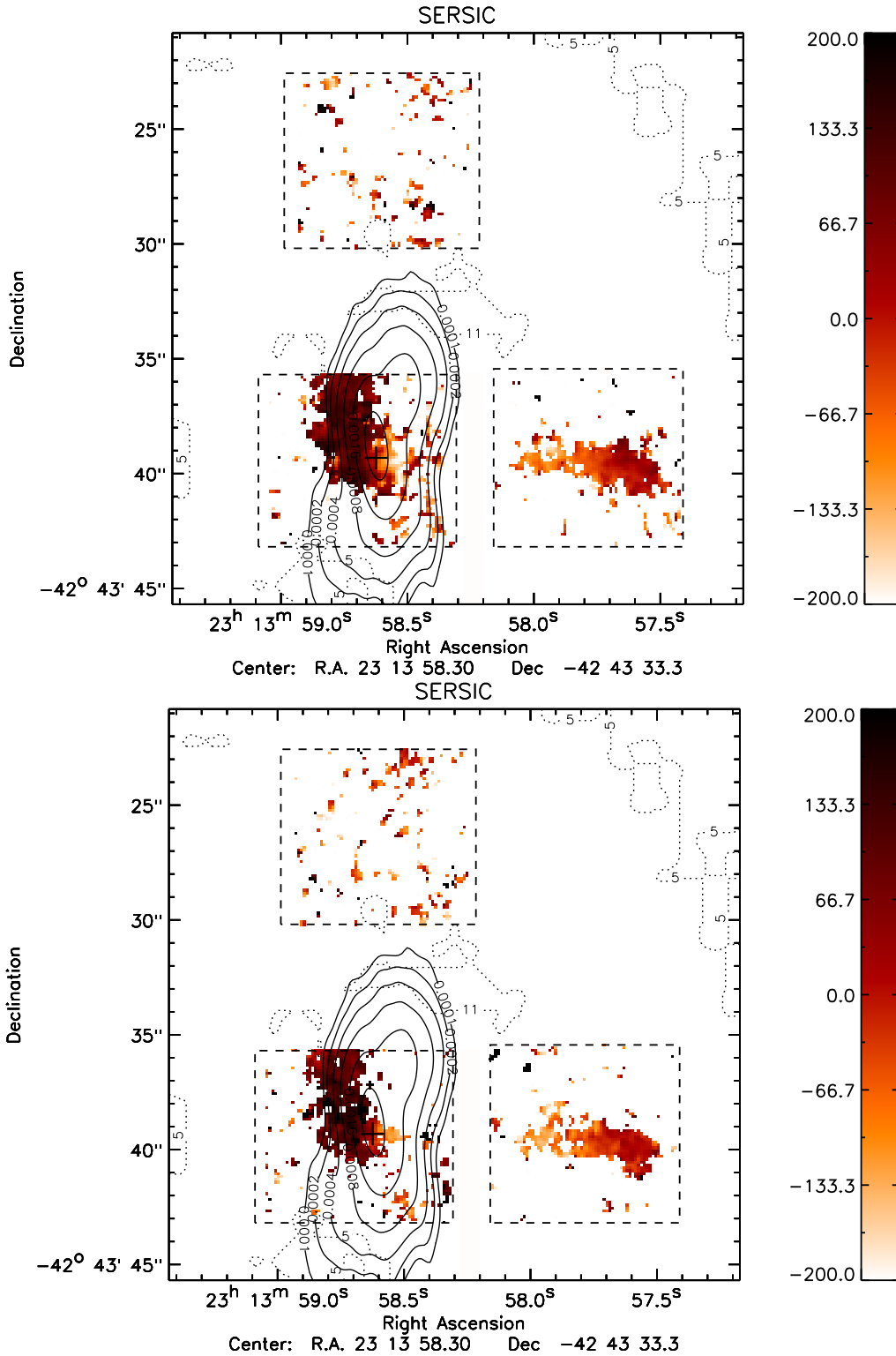


Figure 2.10 — SERSIC 159-03 Velocity. We show velocity maps for the H_2 1-0 S(3) (top) and Pa α (bottom) lines in units of km s^{-1} with respect to the systemic velocity of the BCG. The velocity of the gas is derived by fitting the spectrum for each spatial pixel in the data cube by a single Gaussian. The data was smoothed by two pixels in the spatial plane. The stellar nucleus is indicated by the cross. VLA 8.4 GHz Radio Continuum contours (solid black line) and *CHANDRA* X-ray contours (dotted black line) are overlaid. The Radio contours start at 4σ ($1\sigma = 25 \mu\text{Jy}$). Consecutive Radio and X-ray contours double in value. Velocity maps were made for all detected emission lines. These all show the same structure and are thus not all shown here.

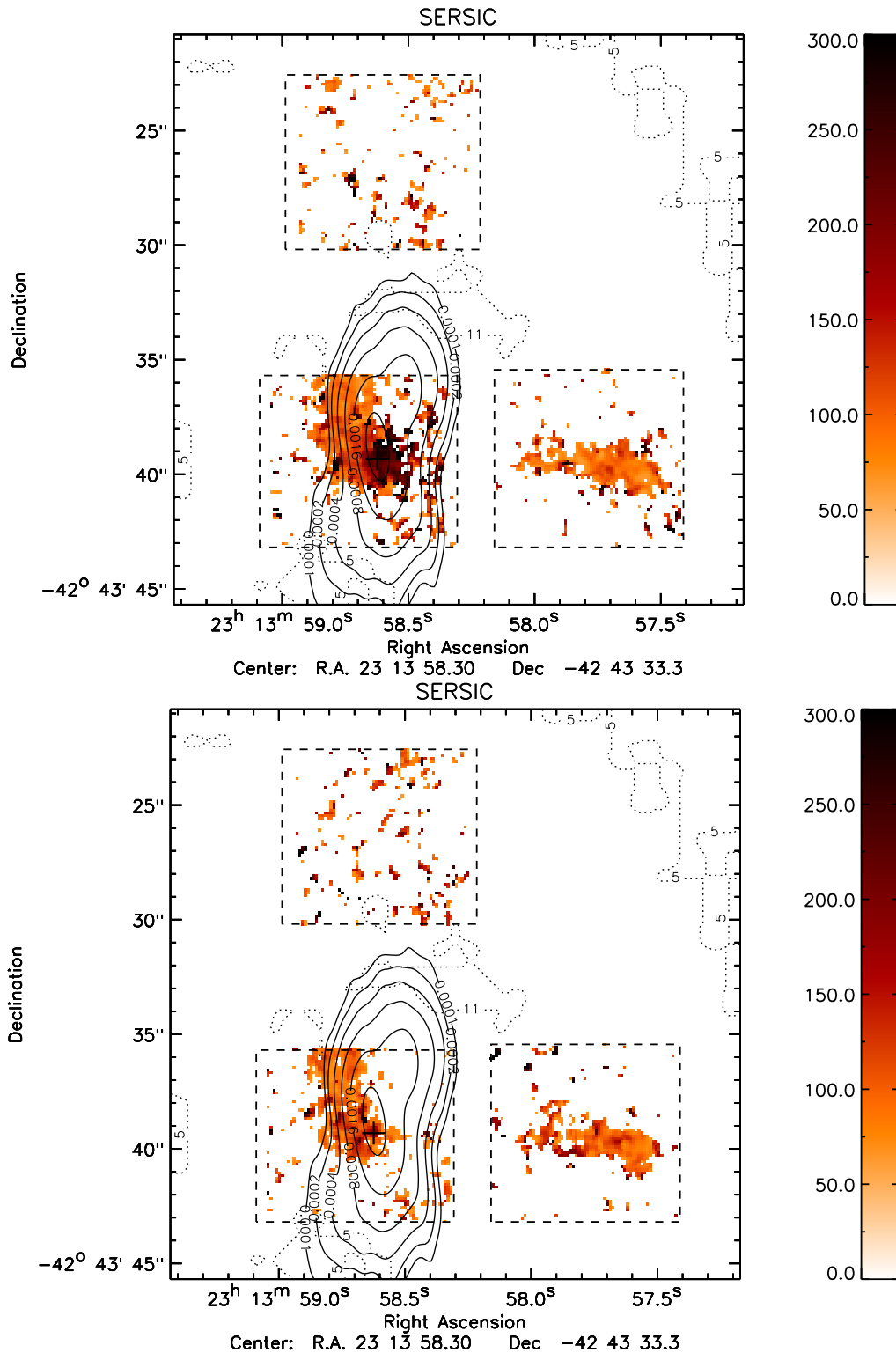


Figure 2.11 — SERSIC 159-03 Velocity dispersion. We show velocity dispersion maps for the H_2 1-0 S(3) (top) and the Pa α (bottom) lines in units of km s^{-1} . The velocity dispersion σ_v of the gas is derived by fitting the spectrum for each spatial pixel in the data cube by a single Gaussian. The data cube was smoothed by two pixels in the spatial plane. The stellar nucleus is indicated by the cross. VLA 8.4 GHz Radio Continuum contours (solid black line) and *CHANDRA* X-ray contours (dotted black line) are overlaid on the dispersion maps. The Radio contours start at 4σ ($1\sigma = 25 \mu\text{Jy}$). Consecutive Radio and X-ray contours double in value. Gas dispersion maps were made for all detected emission lines. All show the same structure and are thus not all shown here.

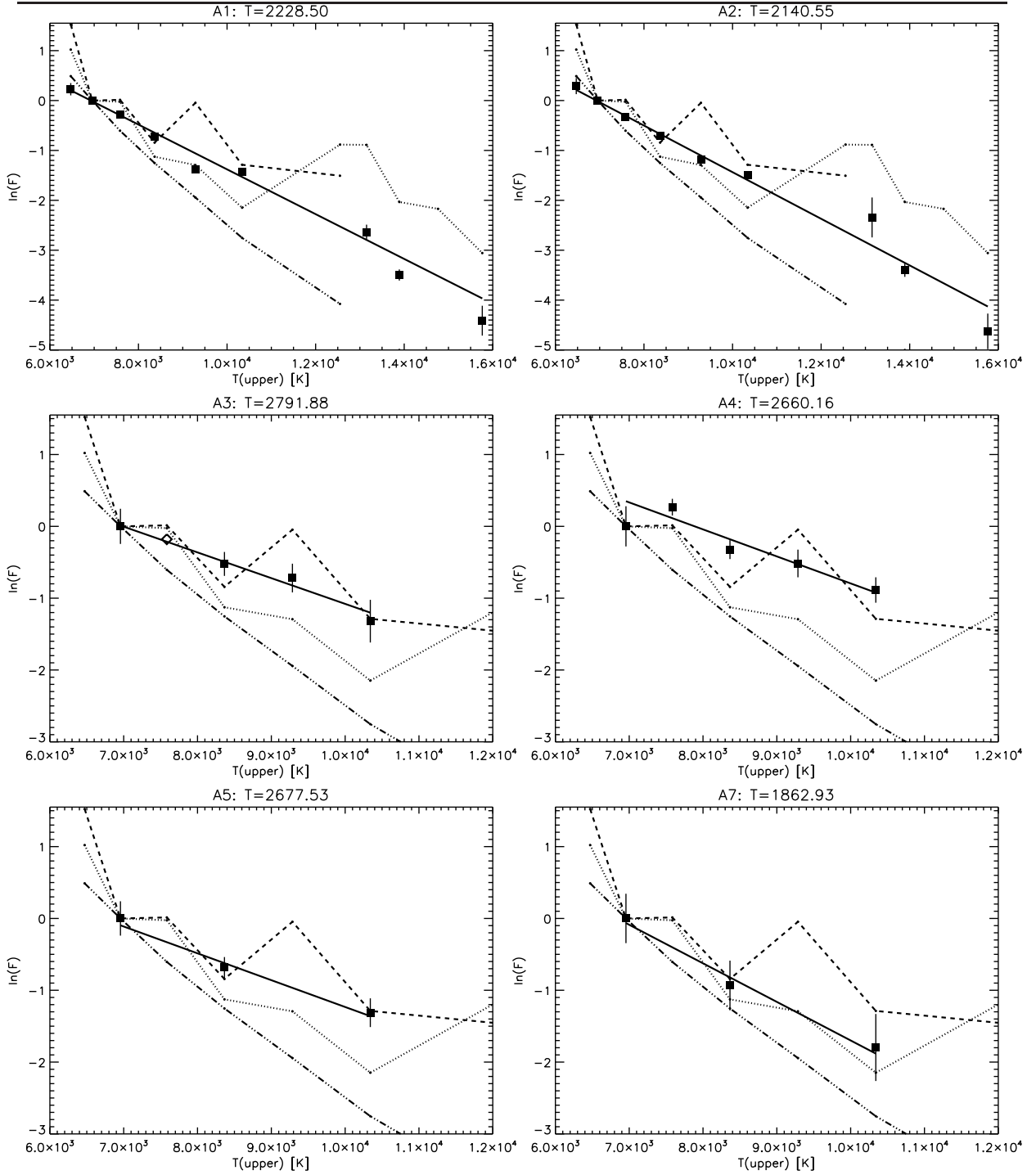


Figure 2.12 — ABELL 2597 Molecular excitation. Excitation diagrams for the H₂ lines in regions A1, A2, A3, A4, A5 and A7. The figures show the natural logarithm of the normalised line flux $\ln(F)$ versus the upper state temperature T_u (squares). The best-fitting LTE model is given by the solid black line. For qualitative comparison reasons we plot three other H₂ excitation models. The dotted line shows a low-density UV fluorescence model by Black and van Dishoeck 1987 (their model 14; $n = 3 \times 10^3 \text{ cm}^{-3}$, $T = 100 \text{ K}$, $I_{\text{UV}} = 1 \times 10^3$ relative to I_{tot}). The dash-dotted line shows a high-density UV fluorescence model by Sternberg & Dalgarno 1989 (their model 2D; $n = 1 \times 10^6 \text{ cm}^{-3}$, $T \sim 1000 \text{ K}$, $I_{\text{UV}} = 1 \times 10^2$ relative to I_{tot}). The dashed line shows the Ferland et al. 2009 cosmic ray model for the Perseus cluster. For region A3 the uncertain H₂ 1-0 S(2) flux value is shown, but it is not used for the fit.

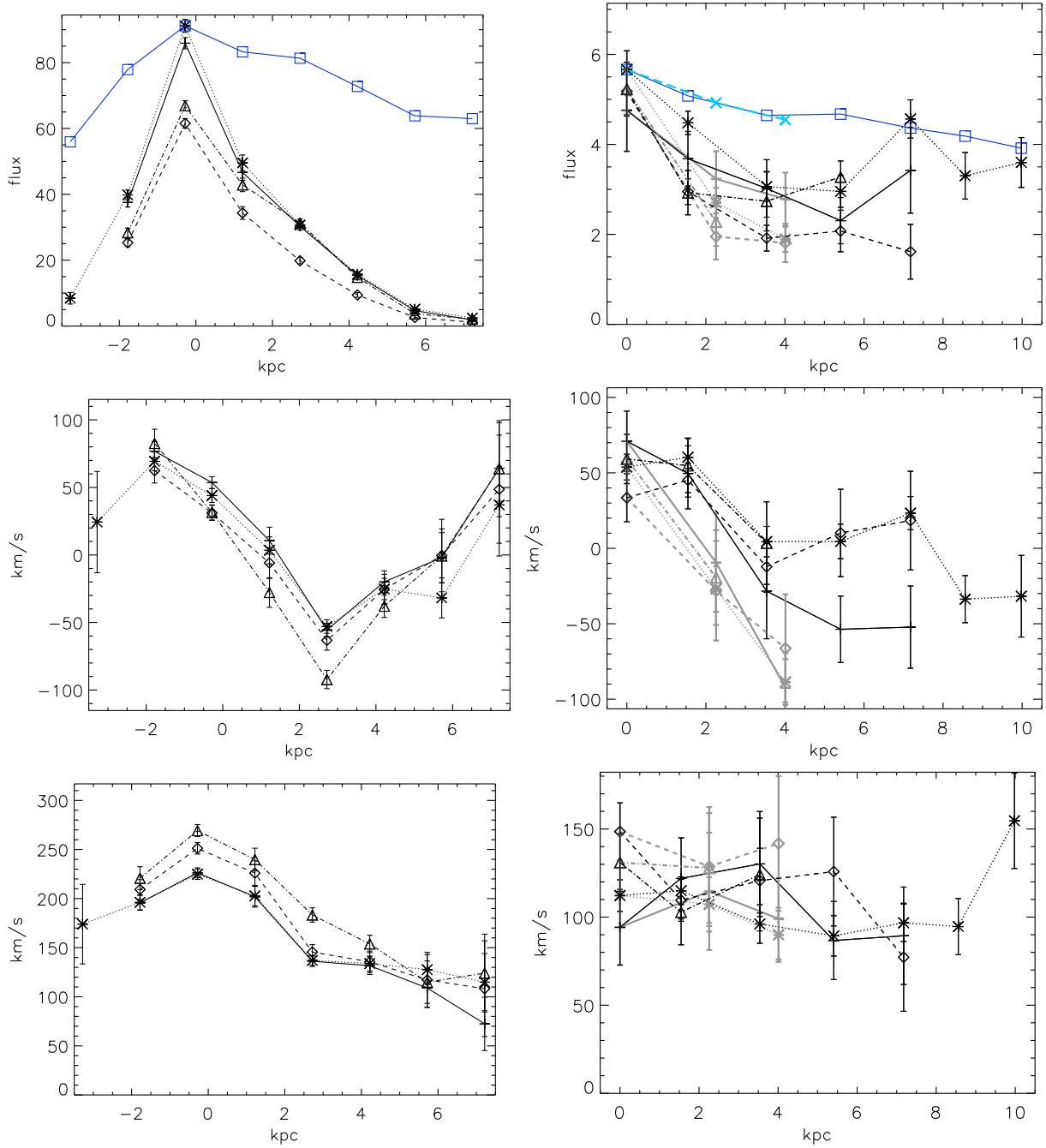


Figure 2.13 — ABELL 2597 Filaments. We show from top to bottom the flux, velocity and velocity dispersion along the filaments in A2597. The left images show the northern filament and the right images the southern filament. Each point shown represents a $1'' \times 1''$ area along a filament. These areas are marked by the grey thin and thick squares in Fig. 2.3. The black points correspond to the thin grey squares and the grey points to the thick grey squares. The distance of the points along the northern filament are given in kpc from the nucleus, here north is positive. The distance of the points along the southern filament are given in kpc from the north-eastern tip of this filament. The black points trace the southern filament from its north-eastern tip towards the south-west. The grey points trace the southern filament from its north-eastern tip towards the south-east. The plus, asterisk, diamond and triangle symbols indicate values obtained for the H_2 1-0 S(1), 1-0 S(3), 1-0 S(5) and the Pa α lines respectively. The solid lines with the open squares indicate values obtained for the X-ray emission as observed by *CHANDRA*. These X-ray points have been normalised with respect to the maximum value of the H_2 1-0 S(3) line.

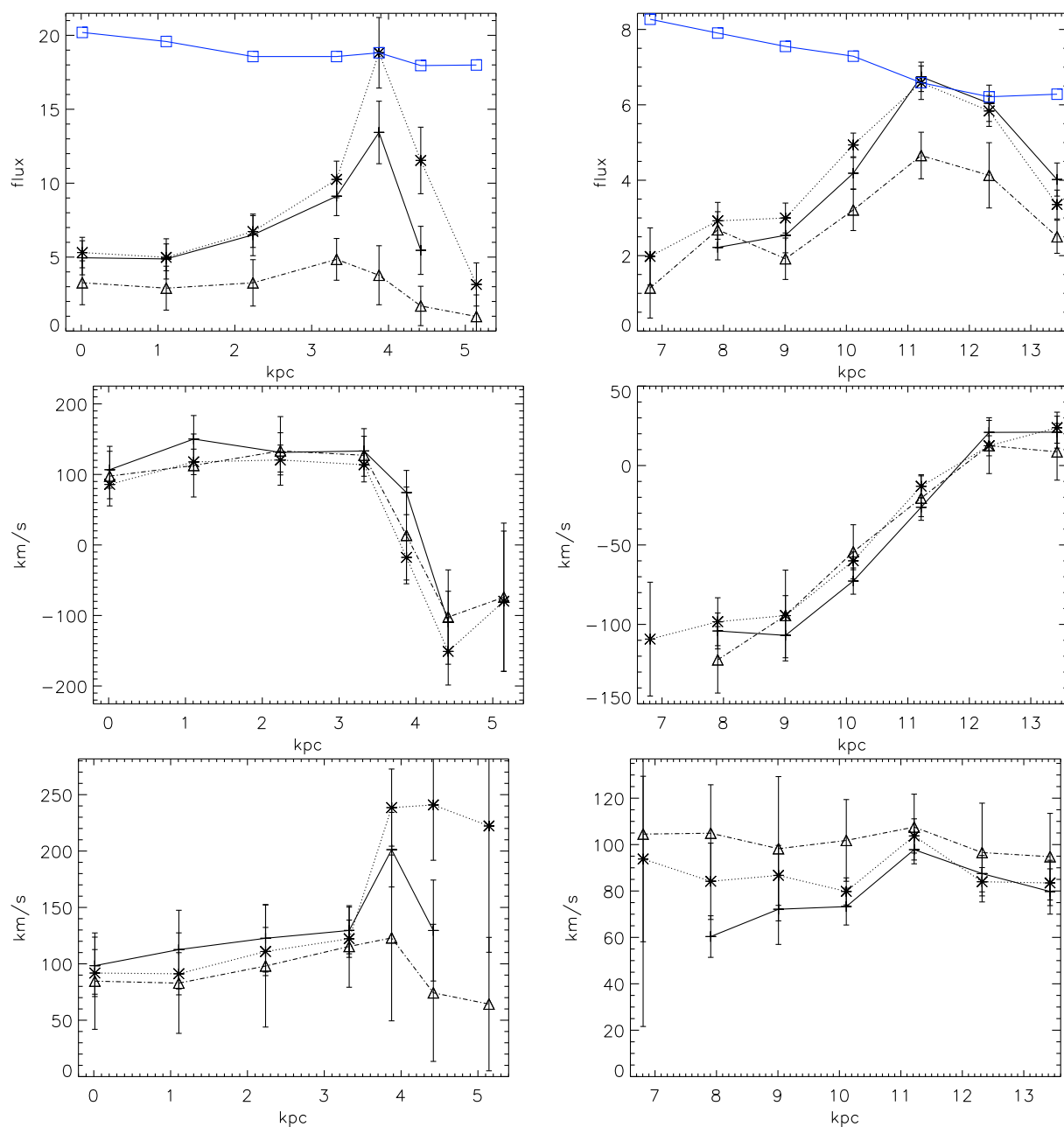


Figure 2.14 — SERSIC 159-03 Filaments. We show from top to bottom the flux, velocity and velocity dispersion along the filaments in S159. The left images show the northern filament and the right images the western filament. Each point shown represents a $1'' \times 1''$ area along a filament. These areas are marked by the grey squares in Fig. 2.3. The distance of the points along the northern filament are given in kpc to the north-eastern tip of this filament. The distance of the points along the western filament are given in kpc from the nucleus. The plus, asterisk and triangle symbols indicate values obtained for the H₂ 1-0 S(1), 1-0 S(3) and the Pa α lines respectively. The solid lines with the open squares indicate values obtained for the X-ray emission as observed by *CHANDRA*. These X-ray points have been normalised with respect to the maximum value of the H₂ 1-0 S(3) line.

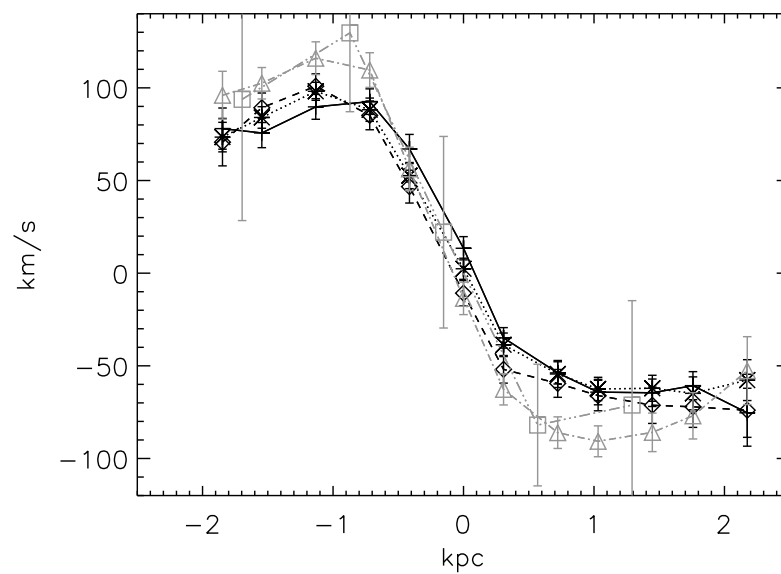


Figure 2.15 — ABELL 2597 Position-Velocity Diagram. Each point shown represents a $0.25'' \times 1.0''$ area along a pseudo long slit with a PA of 105.5 degrees. The slit centre is placed 1 kpc south of the nucleus. This is done to avoid the velocity features just north-east and north-west of the nucleus. The plus, asterisk, diamond, triangle and square symbols indicate values obtained for the H_2 1-0 S(1), 1-0 S(3), 1-0 S(5), Pa α and Fe II lines respectively. The molecular line velocities are shown in black and the ionised line velocities are shown in grey.

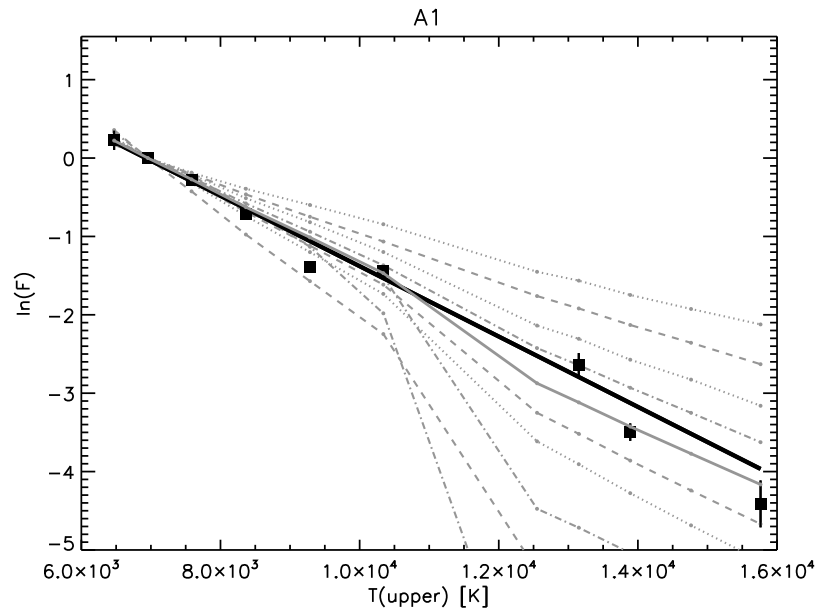


Figure 2.16 — ABELL 2597 Low velocity shock excitation for region A1. The figure shows the natural logarithm of the normalised line flux $\ln(F)$, normalisation with respect to the H_2 1-0 S(1) line, versus the upper state temperature T_u . The best-fitting LTE model is given by the solid black line. The best-fitting low velocity shock model (shock velocity $v_s = 22 \text{ km s}^{-1}$, pre-shock density $n_{\text{H}} = 5 \times 10^6 \text{ cm}^{-3}$ and magnetic field strength $B = 5.6 \text{ mG}$) is shown by the grey solid line. The grey dash-dot lines show what happens to the best-fitting model if we change the pre-shock density. Increasing the pre-shock density from $1 \times 10^5 \text{ cm}^{-3}$, $1 \times 10^6 \text{ cm}^{-3}$ to $1 \times 10^7 \text{ cm}^{-3}$ the model becomes progressively flatter. Similarly increasing the shock velocity from 15 km s^{-1} , 20 km s^{-1} to 30 km s^{-1} , grey dashed lines, flattens the model. However, increasing the magnetic field strength from 1.1 mG , 3.4 mG to 7.8 mG , grey dotted lines, leads to a progressive steepening of the model.

A.1 Abell 2597 Surface Brightness Maps**A.2 Sersic 159-03 Surface Brightness Maps****A.3 Selected Regions: Line Profiles and Gaussian Fits**

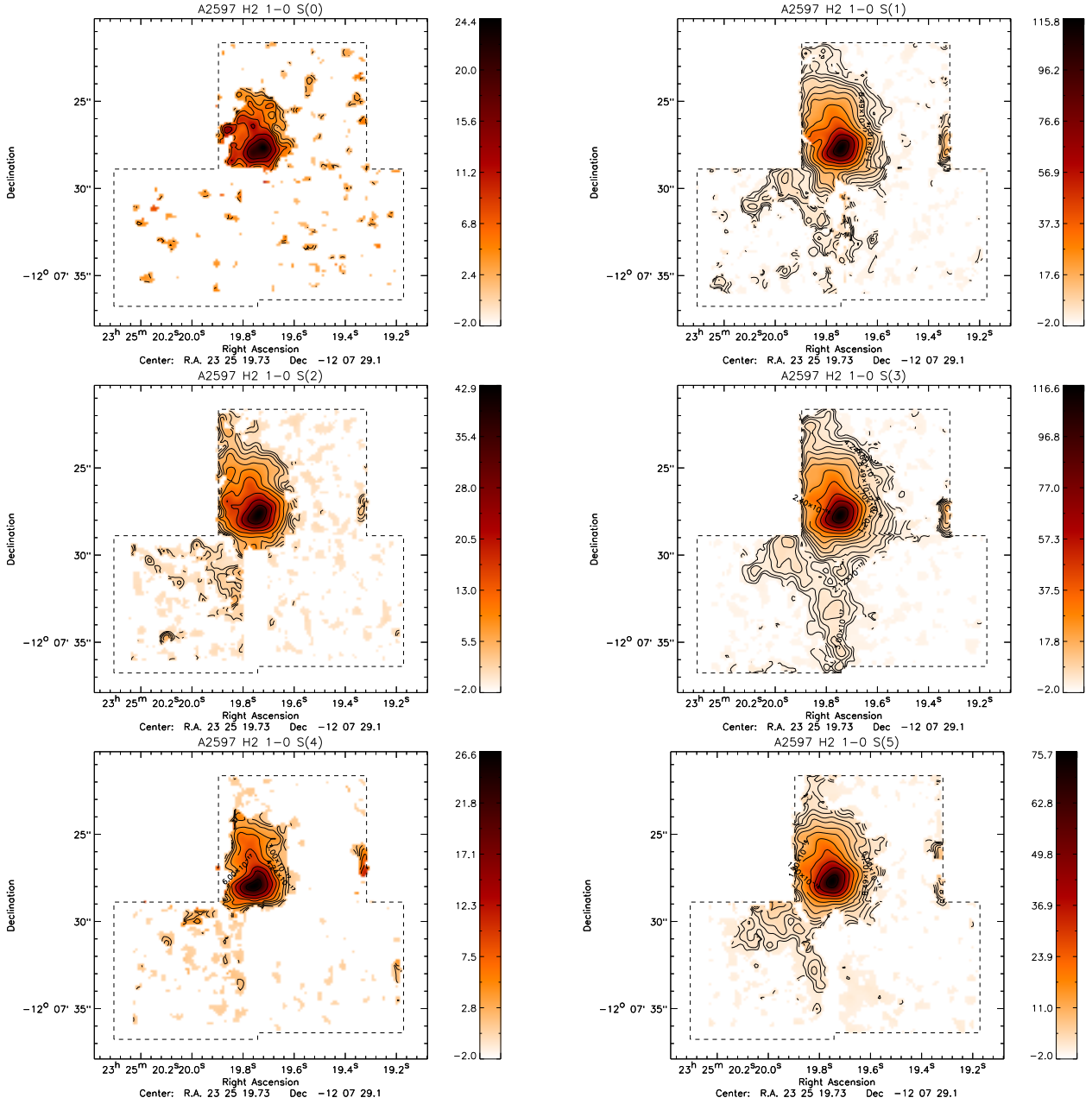
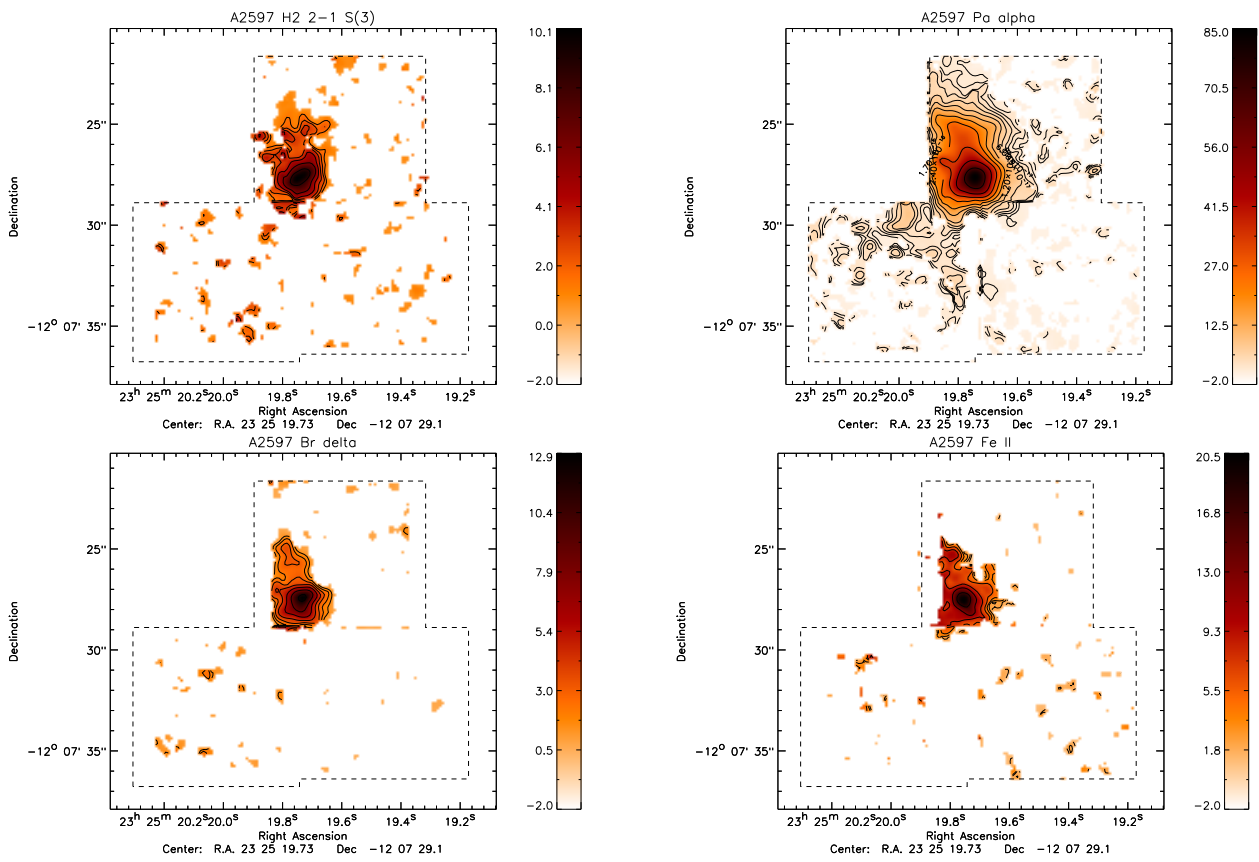


Figure 17 — ABELL 2597 Surface Brightness Maps. We show surface brightness maps for all detected lines that could be mapped on a pixel to pixel basis. The surface brightness is given in units of $10^{-17} \text{ erg s}^{-1} \text{ cm}^{-2} \text{ arcsec}^{-2}$ and contours are drawn starting at $1.5 \times 10^{-17} \text{ erg s}^{-1} \text{ cm}^{-2} \text{ arcsec}^{-2}$ in steps of $2^{n/2}$ with $n=0,1,2,\dots$. The maps are obtained by fitting the spectrum for each spatial pixel in the data cube by a single Gaussian. The data was smoothed by four pixels in both the spatial and spectral planes. Maps are shown for H₂ 1-0 S(0), 1-0 S(1), 1-0 S(2), 1-0 S(3), 1-0 S(4), 1-0 S(5), 2-1 S(3), Pa α , Br δ and Fe II ($1.81 \mu\text{m}$). The Br δ map includes the flux due to H₂ 2-1 S(5). The Br γ , H₂ 2-1 S(2) and H₂ 2-1 S(4) lines are too weak and are thus not shown here. The northern-most observed field is not shown here.

Figure 17 — *continued*

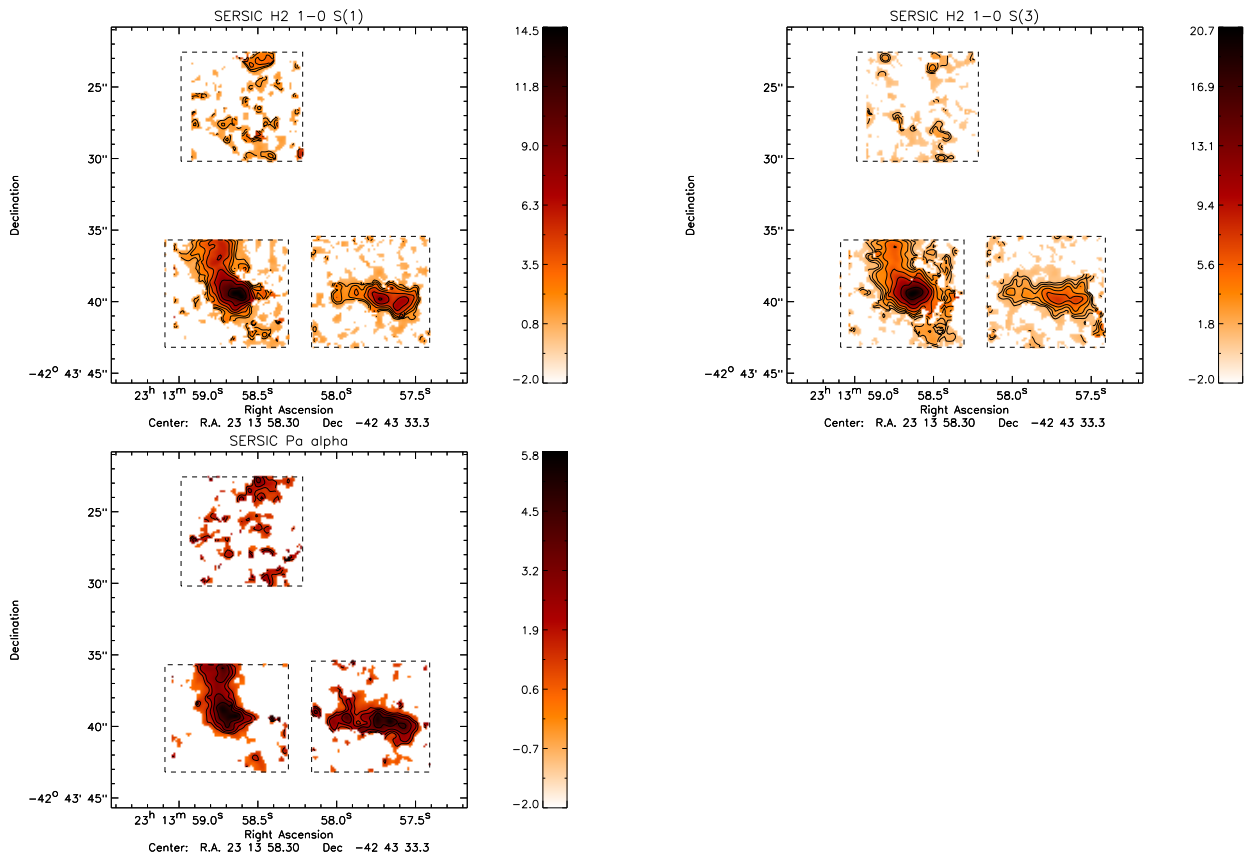


Figure 18 — SERSIC 159-03 Surface Brightness Maps. We show surface brightness maps for all detected lines that could be mapped on a pixel to pixel basis. The surface brightness is given in units of $10^{-17} \text{ erg s}^{-1} \text{ cm}^{-2} \text{ arcsec}^{-2}$ and contours are drawn starting at $1.5 \times 10^{-17} \text{ erg s}^{-1} \text{ cm}^{-2} \text{ arcsec}^{-2}$ in steps of $2^{n/2}$ with $n=0,1,2,\dots$. The maps are obtained by fitting the spectrum for each spatial pixel in the data cube by a single Gaussian. The data was smoothed by four pixels in both the spatial and spectral planes. Maps are shown for H₂ 1-0 S(1) 1-0 S(3) and Pa α .

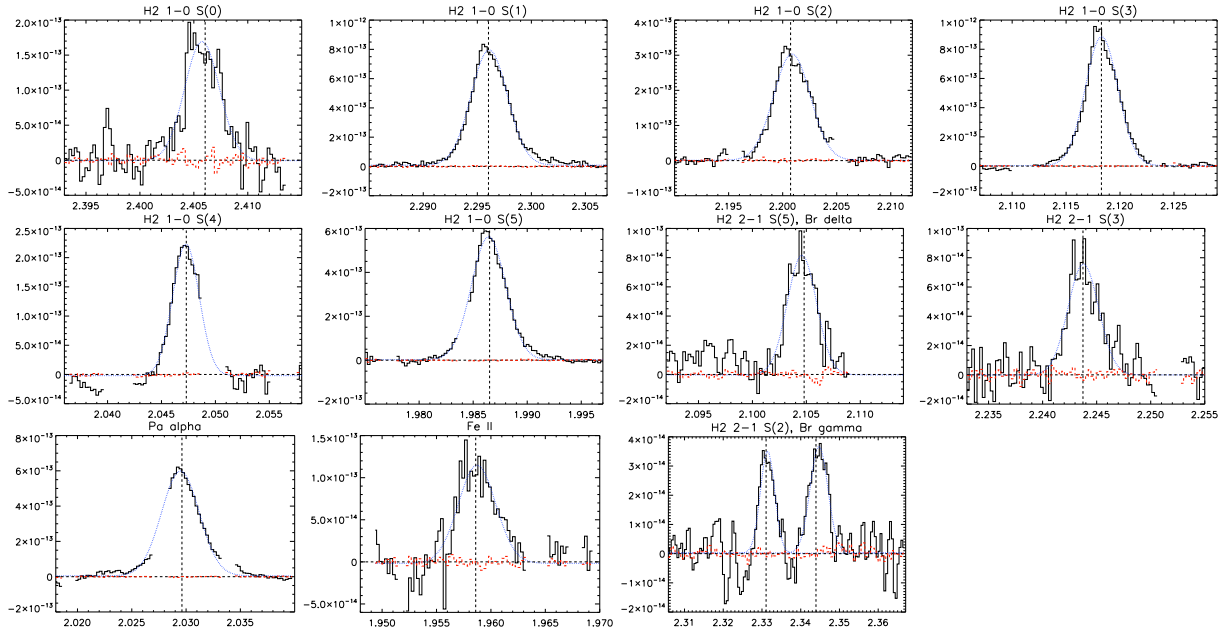


Figure 19 — ABELL 2597 Line Spectra (Region A1). For the Br γ and H₂ 2-1 S(2) lines we used a four pixel spatial and spectral smoothing. For all other lines a two pixel spatial smoothing was used. The solid black line shows the measured line spectrum. The dotted line shows the Gaussian fit to the line profile. The dashed line shows the spectrum from the corresponding spatial median region (this spectrum has been scaled to match the area of the selected region).

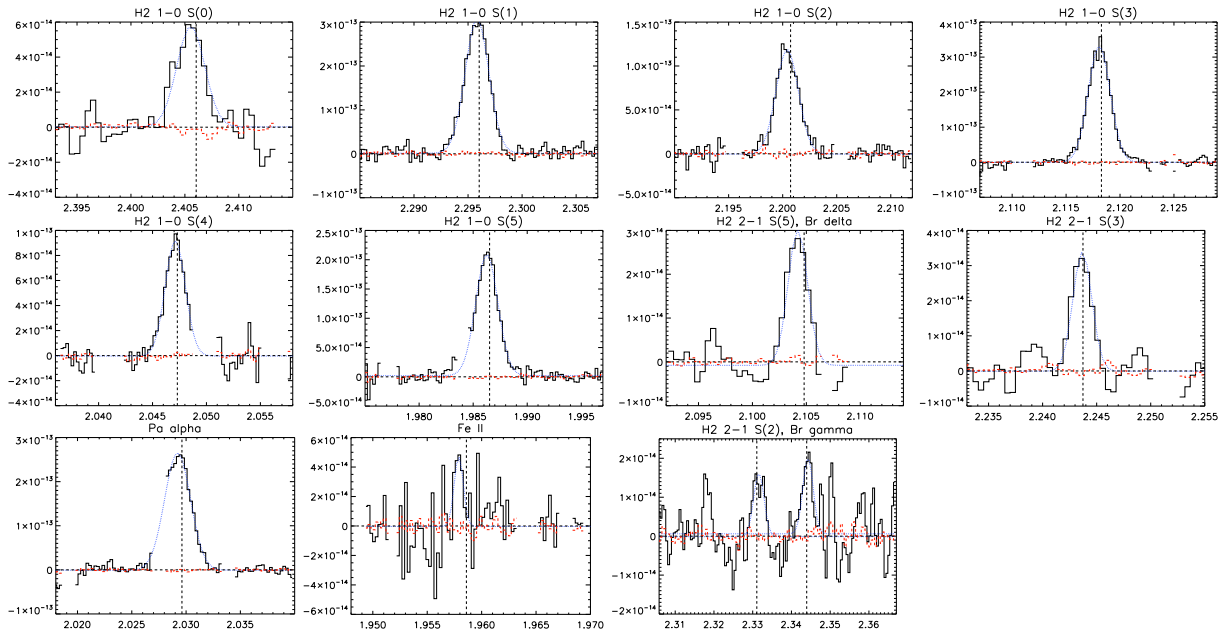


Figure 20 — ABELL 2597 Line Spectra (Region A2). For H₂ 1-0 S(0), 2-1 S(3), 2-1 S(2), Br γ , Br δ we used a four pixel spatial and spectral smoothing. For all other lines a two pixel spatial smoothing was used. The lines and symbols used are the same as in Fig. 19.

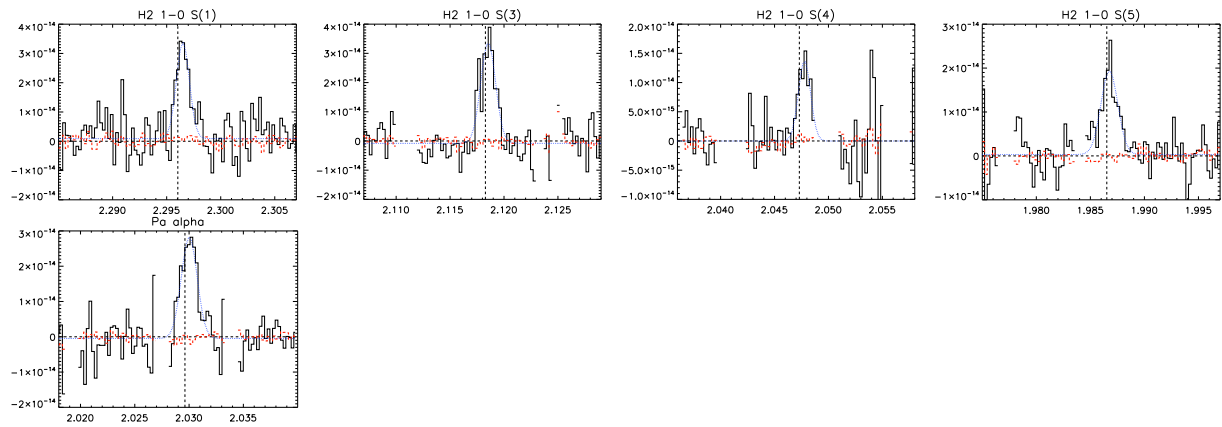


Figure 21 — ABELL 2597 Line Spectra (Region A3). For all lines we used a two pixel spatial smoothing. The lines and symbols used are the same as in Fig. 19.

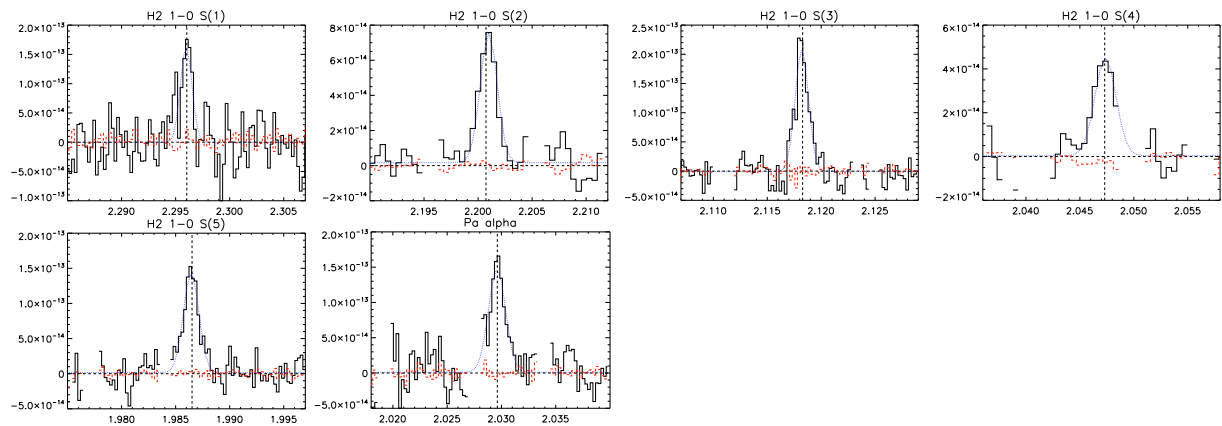


Figure 22 — ABELL 2597 Line Spectra (Region A4). For H_2 1-0 S(2) and 1-0 S(4) we used a four pixel spatial and spectral smoothing. For all other lines a two pixel spatial smoothing is used. The lines and symbols used are the same as in Fig. 19.

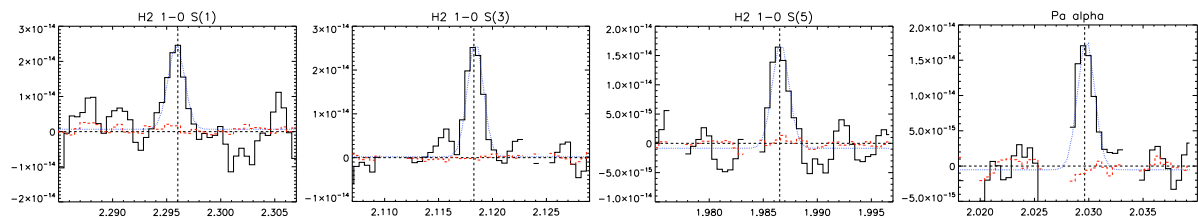


Figure 23 — ABELL 2597 Line Spectra (Region A5). For all lines we used a four pixel spatial and spectral smoothing. The lines and symbols used are the same as in Fig. 19.

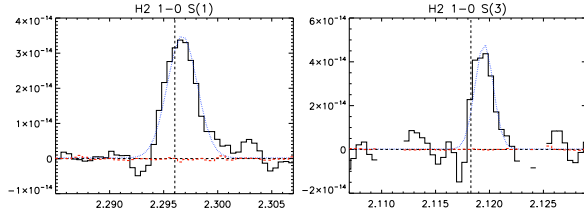


Figure 24 — ABELL 2597 Line Spectra (Region A6). For all lines we used a four pixel spatial and spectral smoothing. The lines and symbols used are the same as in Fig. 19.

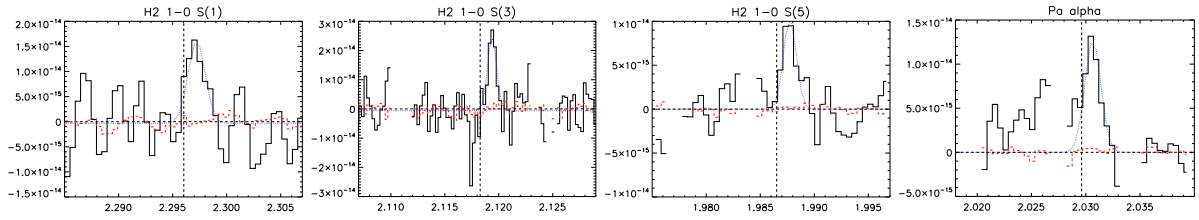


Figure 25 — ABELL 2597 Line Spectra (Region A7). For the H₂ 1-0 S(3) we used a two pixel spatial smoothing. For all other lines a four pixel spatial and spectral smoothing was used. The lines and symbols used are the same as in Fig. 19.

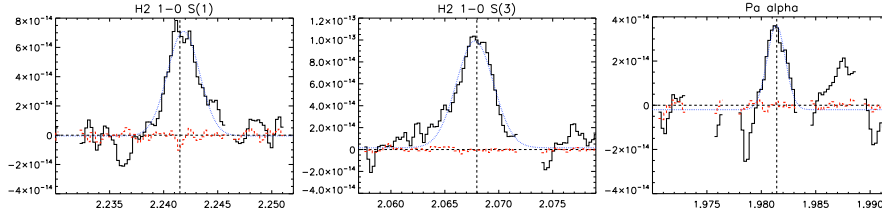


Figure 26 — SERSIC 159-03 Line Spectra (Region B1). For all lines a two pixel spatial and spectral smoothing was used. The solid black line shows the measured line spectrum. The dotted line shows the Gaussian fit to the line profile. The dashed line shows the spectrum from the corresponding spatial median region (this spectrum has been scaled to match the area of the selected region).

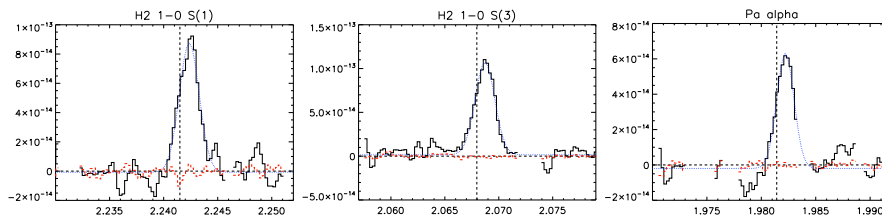


Figure 27 — SERSIC 159-03 Line Spectra (Region B2). For all lines a two pixel spatial and spectral smoothing was used. The lines and symbols used are the same as in Fig. 26.

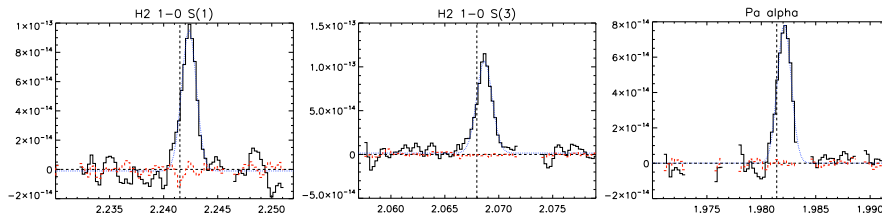


Figure 28 — SERSIC 159-03 Line Spectra (Region B3). For all lines a two pixel spatial and spectral smoothing was used. The lines and symbols used are the same as in Fig. 26.

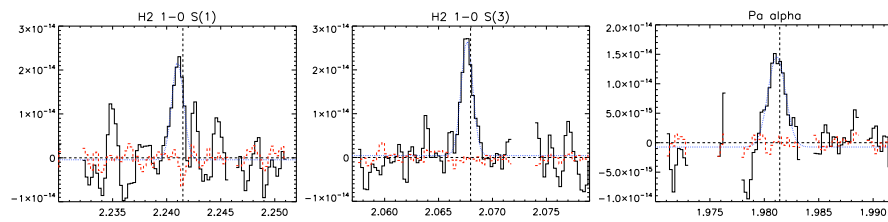


Figure 29 — SERSIC 159-03 Line Spectra (Region B4). For all lines a two pixel spatial and spectral smoothing was used. The lines and symbols used are the same as in Fig. 26.

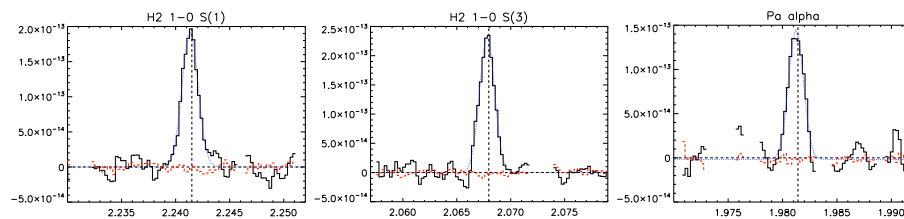


Figure 30 — SERSIC 159-03 Line Spectra (Region B5). For all lines a two pixel spatial and spectral smoothing was used. The lines and symbols used are the same as in Fig. 26.

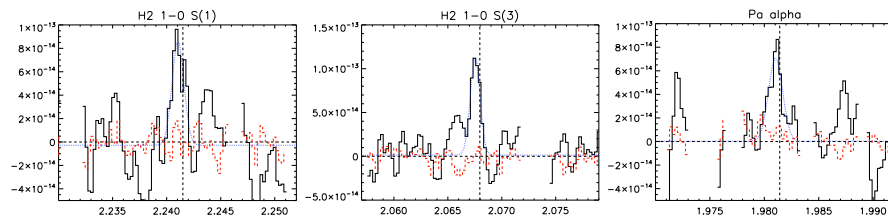


Figure 31 — SERSIC 159-03 Line Spectra (Region B6). For all lines a two pixel spatial and spectral smoothing was used. The lines and symbols used are the same as in Fig. 26.

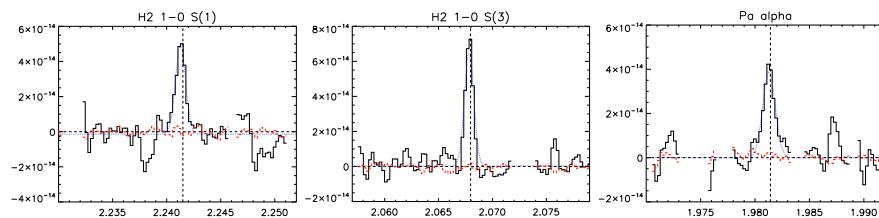


Figure 32 — SERSIC 159-03 Line Spectra (Region B7). For all lines a two pixel spatial and spectral smoothing was used. The lines and symbols used are the same as in Fig. 26.

Chapter 3

Far Ultraviolet Emission in the A2597 and A2204 Brightest Cluster Galaxies.

We use the Hubble Space Telescope ACS/SBC and Very Large Telescope FORS cameras to observe the Brightest Cluster Galaxies in Abell 2597 and Abell 2204 in the far-ultraviolet (FUV) F150LP and optical U, B, V, R, I Bessel filters.

The FUV and U band emission is enhanced in bright, filamentary structures surrounding the BCG nuclei. These filaments can be traced out to 20 kpc from the nuclei in the FUV. Excess FUV and U band light is determined by removing emission due to the underlying old stellar population and mapped with 1 arcsec spatial resolution over the central 20 kpc regions of both galaxies.

We find the FUV and U excess emission to be spatially coincident and a stellar interpretation requires the existence of a significant amount of 10000-50000 K stars. Correcting for nebular continuum emission dust intrinsic to the BCG further increases the FUV to U band emission ratio and implies that stars alone may not suffice to explain the observations. However, lack of detailed information on the gas and dust distribution and extinction law in these systems prevents us from ruling out a purely stellar origin.

Non-stellar processes, such as the central AGN, Scattering, Synchrotron and Bremsstrahlung emission are investigated and found to not be able to explain the FUV and U band measurements in A2597. Contributions from non-thermal processes not treated here should be investigated.

Comparing the FUV emission to the optical H α line emitting nebula shows good agreement on kpc-scales in both A2597 and A2204. In concordance with an earlier investigation by O'Dea et al. (2004) we find that O-stars can account for the ionising photons necessary to explain the observed H α line emission.

MNRAS 405, 898 (2010)

J. B. R. Oonk¹, N.A. Hatch², W. Jaffe¹, M. N. Bremer³, R. J. van Weeren¹

¹Leiden Observatory, Leiden University, P.B. 9513, Leiden, 2300 RA, The Netherlands

²School of Physics and Astronomy, University of Nottingham, University Park, Nottingham NG7 2RD

³Department of Physics, H.H. Wills Physics Laboratory, Bristol University, Tyndall Avenue, Bristol BS8 1TL, United Kingdom

3.1 Introduction

Regions at the centre of rich clusters where the hot $T \sim 10^8$ K, thermal X-ray emitting gas is dense enough to cool radiatively within a Hubble time are called cool-cores. Cooling rates of the order of $10^{2-3} M_{\odot} \text{ yr}^{-1}$ in the central few hundred kpc of the cluster have been estimated from X-ray imaging for this hot gas (e.g., Peres et al. 1998). However, X-ray spectroscopy implies that at most 10 per-cent of the X-ray emitting gas cools below one third of the virial temperature of a system, see (Peterson & Fabian 2006) for a review. The solution most often invoked in the literature is that some form of heating balances the radiative cooling of the X-ray gas.

At the heart of these cool-core clusters lie their Brightest Cluster Galaxies (BCG). These cD type galaxies are the most massive galaxies in the universe and peculiar in many ways. They contain substantial, cool ($T \sim 10^{1-4}$ K) gas and dust components within about 30 kpc from their nucleus (e.g., Jaffe & Bremer 1997; Edge 2001; Irwin, Stil & Bridges 2001; Jaffe, Bremer & van der Werf 2001; Edge et al. 2002; Wilman et al. 2002; Salome & Combes 2003; Hatch et al. 2005; Jaffe, Bremer & Baker 2005; Wilman, Edge & Swinbank 2006; Johnstone et al. 2007; O’Dea et al. 2008; Wilman, Edge & Swinbank 2009; Oonk et al. 2010). Whether this cool gas is the product of the cooling process in these clusters or has an alternative origin, such as minor mergers, is unclear. However, statistically speaking these cooler gas nebulae exist only in and around BCGs situated in cool-core clusters (e.g., Heckman et al. 1989).

These gas components at $T \sim 10^{1-4}$ K in BCGs emit far more energy than can be explained by the simple cooling of the intracluster gas through these temperatures and some form of heating is required (e.g., Fabian et al. 1981; Heckman et al. 1989; Jaffe et al. 2005; Oonk et al. 2010). Detailed investigations show that the primary source of ionisation and heating of the cool gas must be local to the gas (Johnstone & Fabian 1988; Jaffe et al. 2005; Oonk et al. 2010). This requirement combined with the observation that BCGs in cool-core clusters have significantly bluer colors in the ultraviolet (UV) to optical regime than their peers in non-cool-core clusters and in the field supports a young stellar origin for the ionizing photons (Donahue et al. 2010, and references therein).

Previous studies agree that the UV to optical emission is consistent with young stars (Crawford & Fabian 1993; Pipino et al. 2009; Hicks, Mushotzky & Donahue 2010). However, these studies suffer from poor spatial resolution, as the UV part of their datasets is based on observations with the International Ultraviolet Explorer (IUE) and GALEX.

A number of recent papers, using high resolution FUV imaging with the Hubble Space Telescope (HST), have shown that BCGs in cool-core clusters contain clumpy, asymmetric FUV emission on scales up to ~ 30 kpc from the nucleus (O’Dea et al. 2010; Oonk et al. 2010). This is consistent with the scales on which cool gas has been detected in BCGs (e.g. Edge 2001; Salome & Combes 2003; Jaffe et al. 2005; Wilman et al. 2009; Oonk et al. 2010). The clumpy, extended morphology of the FUV emission is consistent with a local stellar origin and comparison with radio imaging disfavors a direct relation with the central active galactic nucleus (AGN) or its outflows (O’Dea et al. 2010).

Based on FUV morphology O’Dea et al. (2010) and O’Dea et al. (2004) argue that the FUV emission is due to young stars and that the clumpiness may be related to the absence of gas rotation on large scales (Wilman et al. 2009; Oonk et al. 2010). In this picture the FUV lumi-

nosities indicate a minimum star formation rate (SFR) of the order of $1\text{-}10 M_{\odot} \text{ yr}^{-1}$ in BCGs. Deriving the true SFRs is highly dependent on very uncertain extinction corrections and as we will discuss below this uncertainty limits our interpretation of the observations.

O’Dea et al. (2010) and O’Dea et al. (2004) show that FUV continuum and the $\text{Ly}\alpha$ emission cover the same area, with the FUV continuum emission being clumpier than the $\text{Ly}\alpha$ emission. They find evidence for significant dust extinction from the high $\text{H}\alpha/\text{H}\beta$ ratios observed towards their BCGs. They also state that they find variations in the $\text{Ly}\alpha/\text{H}\alpha$ ratio, which may be attributed to a non-uniform dust distribution.

3.1.1 This project

Here we present deep far-ultraviolet (FUV) and optical imaging for the BCGs PGC 071390 in Abell 2597 (hereafter A2597) and ABELL 2204_13:0742 (LARCS catalog by Pimbblet et al. (2006) in Abell 2204 (hereafter A2204). We perform the first spatially resolved investigation into the FUV to optical emission ratio in the central 20 kpc regions of these BCGs.

The two BCGs studied here are part of our previous sample of BCGs in cool core clusters (Jaffe & Bremer 1997; Jaffe et al. 2001, 2005; Oonk et al. 2010). The objects were selected based on their high cooling rates, strong $\text{H}\alpha$, H_2 emission and low ionisation radiation in order to minimise the role that their AGN have on the global radiation field. A2597 and A2204 have been the subject of numerous investigations in the past and have been observed at wavelengths from radio to X-rays (e.g. Heckman et al. 1989; Voit & Donahue 1997; Koekemoer et al. 1999; Donahue et al. 2000; O’Dea et al. 2004; Jaffe et al. 2005; Wilman et al. 2006, 2009; Oonk et al. 2010).

This paper has two main goals: (1) To establish the morphology of the FUV emission from two BCGs and compare it to the emission structures at other wavelengths (2) To establish the nature of the stars responsible for the FUV emission (if indeed it arises from stars). For this second purpose we compare quantitatively the FUV emission with optical emission in other bands, particularly U-band. For this comparison there are two important intermediate steps: correction of the longer wavelength (i.e. U-band) fluxes for emission from the old stellar population of the galaxy, and correction of the U- and FUV- band fluxes for dust extinction. This last procedure in particular requires considerable discussion here.

For the above purposes we present in Section 2 descriptions of the methods and reductions of our observations with the HST ACS-SBC and the VLT FORS, and of archival data: radio data from the VLA and X-ray data from Chandra. In Section 3 we present the direct qualitative and quantitative results of the reductions in the form of images, graphs, and tables. In Section 4 we make a preliminary analysis of the FUV to optical colors by interpreting, somewhat naively, the FUV/U ratio on the basis of models of starburst spectra. In Section 5 we present a more sophisticated analysis of the spectra including the removal of U-band emission of old stars and different dust scenarios. In Section 6 we discuss the star formation implied by the FUV emission and its relation to the ionised gas in these systems.

Because the FUV/U ratio in the purely stellar scenario is uncomfortably large, in Section 7 we consider the possibility that some of this emission is from conventional non-stellar sources. Finally in Section 8 we compare our results with those of other ultraviolet observations, and discuss in detail the possibility that the high value of the extinction corrected FUV/U ratio is the result of unconventional extinction behaviour of the dust in the UV. Section 9 contains our

conclusions.

Throughout this paper we will assume the following cosmology; $H_0=72 \text{ km s}^{-1} \text{ Mpc}^{-1}$, $\Omega_m=0.3$ and $\Omega_\Lambda=0.7$. For Abell 2597 at $z=0.0821$ (Voit & Donahue 1997) this gives a luminosity distance 363 Mpc and angular size scale $1.5 \text{ kpc arcsec}^{-1}$. For Abell 2204 at $z=0.1517$ (Pimblet et al. 2006) this gives a luminosity distance 702 Mpc and angular size scale $2.6 \text{ kpc arcsec}^{-1}$.

3.2 Observations and Reduction

We have observed the central BCG in the two cool-core clusters A2597 and A2204 with ACS/SBC on the HST and with FORS on the VLT. The observations are summarised in Tables 3.1 and 3.2. Similar, but less deep, FUV and optical data for A2597 has previously been presented by Voit & Donahue (1997); Koekemoer et al. (1999); Donahue et al. (2000); O’Dea et al. (2004). Similar data for A2204 has not been published before. We complement this data set with archival radio and X-ray observations from the Very Large Array (VLA) and Chandra. The data reduction is described below.

3.2.1 HST ACS-SBC imaging

Hubble Space telescope (HST) FUV images were obtained with the Solar Blind Channel (SBC) of the Advanced Camera for Surveys (ACS) in the F150LP (1612 \AA) filter (effective wavelength 1612 \AA). The filter was selected to sample the FUV continuum emission and not include the $\text{Ly}\alpha$ line. Five pointings were performed for the A2204 field, with a total an exposure time of 3.76 hours. Five pointings were also performed for the A2597 field. Two of the five A2597 pointings were found to be contaminated by a non-uniform dark current glow. These two pointings were excluded from further analysis. The total exposure time for the three remaining pointings on A2597 is 2.26 hours. No dark current glows were found in any of the A2204 pointings.

Flat-fielded and dark-subtracted single exposure frames were obtained from the *HST* archive. Dither offsets were calculated for the exposures of each target using image cross-correlation and then the exposures were drizzled and combined using the STSDAS package MULTIDRIZZLE. Optical distortions were automatically corrected by MULTIDRIZZLE during the image stacking, but no cosmic ray correction was applied since the MAMA detectors are not affected by cosmic rays.

The combined images are convolved to an output spatial resolution of a Gaussian with 1 arcsec full width at half maximum (FWHM), in order to match the optical images. These images are then re-gridded and aligned to the optical images by using the northern star and the two companion galaxies for A2204. The FUV images of A2597 do not contain any sources that can be used to align it to the optical images. We aligned these by comparing the nuclear structures in the ACS/SBC image to the FORS U-band image. We convert the ACS/SBC units elec s^{-1} to AB magnitude by applying the *ABmag* zeropoint (ACS instrument handbook) and we convert this to flux in units of $\text{erg s}^{-1} \text{ cm}^{-2} \text{ Hz}^{-1} \text{ arcsec}^{-2}$ by applying the zeropoint for the AB system.

3.2.2 Optical data

VLT FORS Imaging

A2597 and A2204 were observed with the Focal Reducer/low dispersion Spectrograph (FORS) in imaging mode on the Very Large Telescope (VLT) in 2001 and 2002. Images were taken in the U, B, V, R and I Bessel filters under photometric conditions with a seeing better than 1 arcsec. The reduction was performed using IRAF and a number of dedicated IDL routines. The frames are dark and flat corrected. Hot pixels, cosmics and artefacts are identified and interpolated over. A linear plane is fitted to the sky background and subtracted from the data.

All images are convolved to a common output spatial resolution of a Gaussian with 1 arcsec FWHM. The point spread function (PSF) was measured using about 20 stars in each frame, 10 of these stars are common to all observed frames. The zeropoints are determined by correcting the Landolt standard star magnitudes for the color difference between the Johnson (Landolt) and Bessel (FORS) filter systems. Multiple standard stars are available in each Landolt field and the uncertainty given for the zeropoint is taken as the maximum deviation in the zeropoints obtained from all standard stars within a given field. Only frames obtained in photometric conditions are kept in the subsequent analysis. The results are given in Tables 3.1 and 3.2.

Using bright stars near the BCGs that are visible in all bands we align the FORS images to the 2MASS World Coordinate System (WCS). The FORS Bessel magnitudes are converted to AB magnitudes. The conversion factor ($FORS_AB$)_{conv} is calculated using the FORS Bessel filter curves and the HYPERZ program (Bolzonella, Miralles & Pello 2000, ; H. Hildebrandt priv. comm.). The results are listed in Table 3.3. We then convert AB magnitude to flux in units of $\text{erg s}^{-1} \text{cm}^{-2} \text{Hz}^{-1} \text{arcsec}^{-2}$ by applying the zeropoint for the AB system.

VLT FORS Spectroscopy

A2597 and A2204 were observed with FORS in a 2 arcsec wide, long-slit spectroscopy mode on the VLT in 1999 and 2002. The A2597 observations were taken along minor axis of the BCG and the A2204 observations were taken along an axis running the north-south. Both set of observations intercepted the nucleus of the BCG. The data will presented in a forthcoming paper (Oonk et al. in prep.). For the purposes of this paper we will only use spatially integrated spectra. In the case of A2597 we summed the spectrum over a $16 \times 2 \text{ arcsec}^2$ region and for A2204 we summed the spectrum over a $12.5 \times 2 \text{ arcsec}^2$ region. Within these regions the lines ratios do not vary strongly as a function of position.

Here we use these spectra to investigate (i) the contamination of the U, B, V, R and I Bessel filters by line emission and (ii) the extinction using the Balmer decrements. The spectra were reduced using a set of dedicated IDL scripts. Emission line fluxes were measured using Gaussian fitting. Broadband fluxes were obtained by convolving the spectra with FORS Bessel filter curves. The contribution of the line emission to the broadband flux is given in Table 3.4 and the measured Balmer decrements are given in Table 3.5.

3.2.3 Radio data

A2597: Archival VLA 5 GHz observations of A2597 (project code: AC742) were reduced with the NRAO Astronomical Image Processing System (AIPS). The A-configuration observations

were taken in single channel continuum mode with two 50 MHz wide IFs centred around 4850 MHz. The total on source time was 405 min. The data was flux calibrated using the primary calibrator 0137+331. We used the Perley & Taylor (1999) extension to the Baars et al. (1977) scale to set the absolute flux scale. Amplitude and phase variations were tracked using the secondary calibrator 2246-121 and applied to the data. The data was imaged using robust weighting set to 0.5, giving a beam size of 0.64 arcsec by 0.49 arcsec. The one sigma map noise is $20 \mu\text{Jy beam}^{-1}$. Radio maps of A2597 at 0.33, 1.4, and 8.4 GHz were previously published by (Birzan et al. 2008; Clarke et al. 2005; Sarazin et al. 1995).

A2204: Archival VLA 5 and 8 GHz observations of A2204 (project code: AT211) were reduced with the NRAO Astronomical Image Processing System (AIPS). The 5 GHz observations were taken in A-configuration in single channel continuum mode with two 50 MHz wide IFs centred around 4850 MHz. The 8 GHz observations were taken in B- and C-configuration in single channel continuum mode with two 50 MHz wide IFs centred around 8115 MHz. The total on source time was 31 min and 113 min for the 5 and 8 GHz observations respectively. The data was flux calibrated using the primary calibrator 1331+305. Amplitude and phase variations were tracked using the secondary calibrator 1651+014 and applied to the data. The data was imaged using robust weighting set to 0.0. This gives a 0.44 arcsec by 0.41 arcsec beam size and one sigma noise of $60 \mu\text{Jy beam}^{-1}$ at 5 GHz observations and a 0.97 arcsec by 0.86 arcsec beam size and one sigma noise of $20 \mu\text{Jy beam}^{-1}$ at 8 GHz. Observations of A2204 at 1.4, 4.8 and 8 GHz were previously published by (Sanders et al. 2009).

3.2.4 X-ray data

We have retrieved all publicly available X-ray data from the *CHANDRA* archive. For A2597 we combined three separate observations having a total exposure time of 153.7 ks (project codes 7329; 6934; 922). For A2204 we combined three separate observations having a total exposure time of 98.1 ks (project codes 7940; 6104; 499). *CHANDRA* data for A2597 and A2204 has previously been published by (McNamara et al. 2001; Clarke et al. 2005; Jaffe et al. 2005; Sanders et al. 2009).

3.3 Results

3.3.1 FUV: A2597 and A2204.

The combined F150LP images of A2597 and A2204 show FUV continuum emission out to 20 kpc from their respective BCG nuclei, see Figs. 3.1, 3.2, 3.3 and 3.4. This emission is observed to originate in knots that are part of narrow, kpc-scale filaments. These knots and filaments are embedded in lower-level, diffuse FUV emission centered on the BCG nucleus. The most prominent knots identified by us are given in Fig. 19 and Tables 10 and 11 in Appendix B.1.

In A2597 the filaments appear to be winding around the BCG nucleus in a spiral-like manner, perhaps indicative of ongoing gas in- and outflows. There are three main filamentary structures extending towards the north-east (NE), the south-east (SE) and the south-west (SW) from the nucleus. With the exception of the SE filament the FUV emission extends mostly along the

projected minor axis of the A2597 BCG. The optical nucleus lies along the SW filament.

The central knots observed in the our ACS-SBC FUV continuum map of A2597 match those seen in the lower signal to noise HST-STIS FUV continuum image by O’Dea et al. (2004). The central FUV structures observed here also match the observed optical and near-infrared line emission observed with HST by Koekemoer et al. (1999) and Donahue et al. (2000). The extension of the SW filament towards $(\alpha, \delta)=(23:25:19.5, -12:07:30)$ is marginally visible in the Ly α +FUV continuum image by O’Dea et al. (2004), but it is not visible in the Koekemoer et al. (1999) and Donahue et al. (2000) images.

Convolving the FUV emission to match the resolution of the deep, ground-based H α map by Jaffe et al. (2005) we find that there is good agreement between H α and FUV continuum emission in the central 40×40 kpc² in A2597, see Fig. 3.2.

There have been no earlier investigations of A2204 in the FUV at the resolution of HST. There are many small clumps and filaments extending mostly radially away from the nucleus. There are two main filamentary structures. The first filament runs south-east to north-west along the major axis of the BCG. The second filament runs from the south to the north. Both filaments pass through the nucleus.

Convolving the FUV emission to match the resolution of the H α map by Jaffe et al. (2005) shows that also in this object there is good agreement between H α and FUV continuum emission in the central 40×40 kpc², see Fig. 3.4.

3.3.2 Optical: A2597 and A2204

The combined optical images of A2597 show that the BCG has a blue core, see Fig. 3.5. In Section 3.4 we show that this core consists of three blue filamentary structures extending outwards from the nucleus towards the north-east, south-east and south-west. These structures closely follow the morphology of the FUV emission. The optical images are not as deep as the FUV image and only allow us to trace these filaments out to about 10 kpc from the nucleus.

The combined optical images of A2204 show that this BCG also has a blue core, see Fig. 3.5. In Section 3.4 we show that there are two blue filamentary structures intersecting the nucleus along an axis running north-south and an axis running south-east to north-west. This is in good agreement with the FUV emission. The quality of the optical imaging again only allows us to trace these filaments out to about 10 kpc from nucleus.

The optical images furthermore show that the A2204 cluster is a strongly lensing system. Many blue, lensed galaxies are observed and these become even more pronounced if the B-band data is added (not shown here). The lensed galaxy ($z=1.06$, Wilman et al. (2006)) 8 arcsec north-east shows up prominently in the U-band image but it is not visible in the FUV image.

3.3.3 Radio and X-ray emission

The radio source in the A2597 BCG is known as PKS 2322-12. We show a very deep 5 GHz radio map of A2597 in Fig. 3.2. The radio structures are in good agreement with the previously published deep, but lower resolution, 1.3 GHz map by Clarke et al. (2005). We now clearly see that besides the well known northern and southern radio lobes a much weaker double lobe-like structure appears at a roughly orthogonal position angle. Whether this structure is due to an older outflow or perhaps a backflow from the current jets can not be clarified from this data

alone. Clarke et al. (2005) show that more extended radio emission is present in A2597 at lower frequencies.

Previous investigations of A2597 claim a correlation between the radio emission, the UV-optical excess emission and the central emission line gas (McNamara & O’Connell 1993; Koekemoer et al. 1999; Donahue et al. 2000; O’Dea et al. 2004). In particular they show that the U-band excess light follows the radio lobes in the central 10 kpc, and that some of the FUV and emission line filaments trace parts of the radio lobes.

In Oonk et al. (2010) we found a strong dynamical interaction between the emission line gas and the current radio jet in the central few kpc of A2597. Outside of this central region there was no sign of a causal relation between the two. The FUV observations presented here are consistent with this picture. We find that the peak of the FUV emission agrees with the radio core in A2597 and that the central FUV filaments overlap with the radio structures. This is most evident for the brightest parts of the northern and southern filaments that appear to curve along the inner edges of the radio lobes. A new feature observed here is that the south-eastern FUV filament is oriented along the low surface brightness double lobe-like radio structure.

The radio source in A2204 is known as VLSS J1632.7+0534. Fig. 3.4 shows that the 5 GHz radio emission extends to the north and south of the nucleus. This double lobe structure is confirmed by the very deep 8 GHz observations shown in in Fig. 3.6. In the 8 GHz map we find two new radio features at the 3 sigma level. The first feature is about 4 arcsec north of the nucleus and, in projection, coincides with the bright northern FUV knot. It is discussed further in Section 3.6.2. The second feature is a narrow arc about 3 arcsec south-west of the nucleus. This arc does not coincide with any known structures at other wavelengths. Both features are low signal-to-noise and need to be confirmed by future observations.

The relation between the FUV and radio emission in A2204 is similar to A2597. In A2204 we find that the peak of the FUV emission agrees with the radio core and that the north-south FUV filament is aligned with the radio lobes. Wilman et al. (2009) show that the emission line gas in the central few kpc of A2204 has a high velocity dispersion. It is likely that the gas here is stirred up by the AGN, in the same manner as in A2597, but this needs to be confirmed by observations a higher spatial resolution.

The observations presented here for A2597 and A2204 are consistent with the idea of a strong interaction between the radio source and its immediate surroundings in the central few kpc of the BCG. However, outside of this region the FUV emission, and the emission line gas, does not show an obvious causal relation with the current radio outflows and as such remain to be explained.

The general relation between FUV and radio emission, if any exists, is currently not clear for cool-core BCGs as a class of objects. O’Dea et al. (2010) present FUV and radio observations for a sample of 7 BCGs. All of their sources show FUV and radio emission, but only half of them show enhanced FUV continuum emission at the location of the radio source. In our observations, as well as in those by O’Dea et al. (2010), it is found that in almost all BCGs the current radio outflows are active on scales less than 10 kpc whereas the FUV emission is present on scales of about 30 kpc. More and deeper observations, in particular in the radio, are necessary to investigate the relation between the FUV emission and the radio outflows in these objects further.

The radio images of A2597 and A2204 presented here show that previously unknown or unresolved radio structures become visible when imaging the BCGs to ever-greater depths. At

present it is difficult to determine the details of these structures as matched multi-frequency observations at sufficient depth and spatial resolution are lacking. At 5 GHz the radio emission traces young relativistic electrons with a synchrotron lifetime $\sim 10^7$ yr for a magnetic field strength of $30 \mu\text{G}$.

The X-ray emission in both clusters is centered on the BCG. The peak of the X-ray emission agrees with the peak emission observed in the radio, FUV and optical images. The X-ray emission in these clusters is discussed in detail in Sanders et al. (2009) and Clarke et al. (2005); McNamara et al. (2001).

3.3.4 Surface brightness profiles

In Fig. 3.7 we compare the FUV, $\text{H}\alpha$, V-band, X-ray emission and 5 GHz radio continuum with each other along 2 arcsec wide pseudo-slits centred on the nuclei of the BCGs. The V-band emission traces the older stellar population in both BCGs. The $\text{H}\alpha$ emission is taken from Jaffe et al. (2005) and shown superimposed on the smoothed FUV emission in Figs. 3.2 and 3.4. The surface brightness profiles obtained from these pseudo-slits have been normalised at the position of the optical nucleus and have been computed after convolving all images to a common spatial output resolution of 1 arcsec FWHM.

In A2597 the slits are placed along the projected major (PA=-40 degrees) and minor (PA=+50 degrees) optical axis of the BCG. Along the major axis of the BCG the FUV and $\text{H}\alpha$ and radio emission are more centrally concentrated than the stellar V-band and thermal X-ray emission. Northwards along the minor axis, excess FUV, $\text{H}\alpha$ and radio emission is observed relative to the V-band stellar emission. No excess emission relative to the V-band stellar light is observed south along the minor axis. Overall, the 5 GHz radio emission is more and the X-ray emission is less centrally concentrated than the FUV, $\text{H}\alpha$ and V-band light. The FUV and $\text{H}\alpha$ emission trace each other better than the stellar V-band light. The sharp decrease in radio emission outside of the nucleus is in part due to our focus on the 5 GHz radio emission alone. Clarke et al. (2005) show that the radio source is significantly larger at lower radio frequencies. To properly account for the non-thermal, relativistic, electron component in BCGs matched multi-frequency radio imaging needs to be performed.

In A2204 the slits are placed along an axis running east-west and an axis running north-south. There are no regions with both strong FUV and $\text{H}\alpha$ excesses observed relative to the stellar light along these slits. The $\text{H}\alpha$ emission appears to be in excess relative to the FUV and stellar V-band light. This is unlikely to be physical. A possible explanation follows from the filters used by Jaffe et al. (2005) to measure $\text{H}\alpha$. These filters are so narrow that part of the broad $\text{H}\alpha$ line wings at the nucleus are not included. This will then lead to an artificially broadened $\text{H}\alpha$ profile. For A2204 we also find that the radio emission is more and the X-ray emission is less centrally concentrated than the FUV, $\text{H}\alpha$ and stellar light. The northern radio lobe is largely missed by our north-south slit, this explains the steep drop in the radio surface brightness profile here. The radio source in A2204 is observed to be more extended at lower frequencies (Sanders et al. 2009).

3.4 Total FUV/U emission

BCGs in cool-core clusters are well known to have large extended ionised gas nebulae and bluer continuum colors than non-cool-core cD galaxies (e.g. McNamara & O’Connell 1992; Bildfell et al. 2008).

Johnstone & Fabian (1988) find that to explain the observed distribution of $H\alpha$ line emission in NGC 1275, the BCG in the Perseus galaxy cluster, that one needs a source of heating and excitation which is local to the gas. The same is true for other BCGs (e.g. Heckman et al. 1989). A natural explanation for these observations would be that hot, young stars are forming in BCGs (Crawford & Fabian 1993; Pipino et al. 2009; Hicks et al. 2010).

In the previous section we showed that the ionised gas emission in A2597 and A2204 on large scales matches the FUV emission. In this section we will show that the central 20 kpc regions of the BCGs in these clusters are very blue by investigating the FUV_{ν}/U_{ν} flux ratio and by, somewhat naively, comparing it to single stellar population (SSP) models from Bruzual & Charlot (2003). We use the FUV_{ν}/U_{ν} ratio as these are the only bands that are free of contamination by line emission. In Section 3.5 we will investigate in more detail what kind of stars are required in order to reproduce the observed FUV to optical colors. In Section 3.6 we will study the relation between these stars and the ionised gas in these systems.

Prior to computing the FUV_{ν}/U_{ν} ratio we remove the background emission from the FUV images using the background regions shown in Fig. 3.5. For consistency we use the same regions to define and remove a zero-level from the optical images. In the optical images these background regions still lie within regions of stellar emission, but the optical colors are not affected by selecting the background in this way.

3.4.1 Bruzual & Charlot 2003 SSP models

In Fig. 3.8 and 3.9 we model the total observed FUV to U band emission with the emission ratio expected from a single stellar population (SSP). The aim of this SSP investigation is not to determine what the exact stellar population is, but simply to show that the emission in the filamentary structures in the cores of the BCGs is blue and indicative of a young stellar population.

The SSPs used in this investigation are a set of solar metallicity template spectra published by Tremonti et al. (2003) that are based on the models by Bruzual & Charlot (2003). The ages of these populations vary from 5 Myr to 11 Gyr. We have calculated the FUV_{ν}/U_{ν} ratio for these models as function of SSP age using different amounts of extinction for A2597 and A2204. The results are shown in Fig. 3.9.

If we take into account extinction due to the MW foreground only we find that the central 10 kpc emission in A2597 and A2204 can be explained with SSPs models that have SSP ages less than 100 Myr, see Fig. 3.8. In this analysis most of the blue knots in A2597 and A2204 have SSP ages less than 30 Myr. The most extreme knots, i.e. the eastern knot in the south-eastern filament in A2597 and northern knot in the north-south filament in A2204, have SSP ages less than 5 Myr.

We note here that the SSPs are double-valued in terms of the FUV_{ν}/U_{ν} ratio for ages older than 640 Myr in A2597 and 290 Myr in A2204. This behaviour of the FUV_{ν}/U_{ν} ratio is due to the UV-upturn for stellar populations with ages above a 1 Gyr. For all FUV_{ν}/U_{ν} ratios in the range where the SSP models are double valued we have set the SSP age in Fig. 3.8 to the

youngest value allowed in this range.

Allowing for additional extinction intrinsic to the BCG further lowers the allowed SSP ages for the regions observed. In Fig. 3.8 we present the FUV_{ν}/U_{ν} ratio for SSPs reddened by different amounts of dust. If all of the extinction attributed to the BCG were to lie in front of the filaments then all of the filamentary emission in the central 10 kpc of both A2597 and A2204 would require an SSP age less than 5 Myr. We will discuss the presence of the dust and to correct for it in more detail in Section 3.5.5.

We conclude here that the observations are marginally consistent with the existence of a very young stellar population. Modelling the filamentary emission with a SSP is not very realistic as there is a considerable underlying older stellar population in the BCGs. Any contribution to the FUV and U band light from the underlying old stellar population will lead to a lower FUV_{ν}/U_{ν} ratio and hence to an overestimate of the age of the young stellar component. Trying to distinguish multiple stellar populations using our current set of broadband data, with only two line emission free bands, is a highly degenerate process for these complex systems and we will not pursue it here. Instead we will attempt to further constrain the nature of the blue filaments by removing the old stellar population and investigating only the FUV_{ν}/U_{ν} ratio of the excess emission in terms of simple stellar and non-stellar models.

3.5 Excess FUV/U: Stellar Origin ?

In this section we will investigate whether young stars can account for the observed colors in A2597 and A2204. We do this by obtaining the excess $FUV_{\nu,exc}/U_{\nu,exc}$ continuum emission ratio and compare it with main sequence stellar models by Kurucz (1993) (hereafter K93). The K93 stellar models will allow us to assign stellar temperatures to the stars necessary to explain the observed emission. In this work we focus on stars, however we also present results for blackbody (BB) models. These BB models can be used to describe optically thick emission processes and are given for comparison purposes.

The FUV to U-band ratio is a good discriminator of stellar temperature, because (i) the ratio increases strongly with increasing temperature and (ii) it is single valued in terms of temperature. We show this in the context of BB models in Fig. 3.10 and this is equally true for the K93 stellar models. We have verified that the stellar temperatures derived via our broad band method are consistent with the stellar temperatures derived from FUV spectroscopy for a number of main sequence in the nearby HII region NGC 604 in M33, see Appendix B.2.

In order to obtain the excess ratio we will first investigate line contamination of our images and then remove emission due to the old stellar population from our FUV and U-band images. Having obtained the excess ratio we calculate the stellar temperatures necessary to explain the observations. We then end this section by discussing the implications of nebular continuum emission and dust intrinsic to the BCG.

3.5.1 Contamination by line emission

BCGs contain a significant amount of gas at a large range of temperatures. Emission from this gas is usually dominated by line emission and not by the underlying nebular continuum. This

emission may contribute the observed F_{UV_V}/U_V ratio. In this section we will discuss the line emission and in Section 3.5.4 we will discuss the nebular continuum.

Optical to millimetre spectroscopy shows prominent line emission from gas at temperatures $T \sim 10^{1-4}$ K (e.g. Voit & Donahue 1997; Edge 2001; Jaffe et al. 2005). We have taken optical spectra of A2597 and A2204 with FORS on the VLT (Oonk et al. in prep.). These spectra show that the [OII] 3727 Å line is redshifted out of the U-band for both A2597 and A2204, see Fig. 3.11. No other known strong emission lines are present that could contaminate the U-band images. Contamination of the continuum by line emission does affect the V, R and I-band images. The fraction of line to continuum emission, as measured from our FORS spectra, is summarised in Table 3.4.

The FUV F150LP images of A2597 and A2204 are not affected by $Ly\alpha$ emission. However, the images could be affected by other emission lines such as CIV at 1549 Å. After $Ly\alpha$ this CIV line is usually the most prominent emission line in the FUV regime. This line is typically observed in regions where gas is heated to temperatures $T \sim 10^5$ K. Regions near powerful AGN or heated by strong shocks are examples in which CIV at 1549 Å is seen in emission. Below we elaborate on why we believe that there is no contamination by line emission in the FUV band.

CIV emission in A2597 and A2204

CIV 1549 Å line emission was recently suggested by Sparks et al. (2009) to explain the FUV emission of the south-eastern filaments in M87. If strong line emission is present in our FUV images this means that our method will overestimate the stellar temperatures in A2597 and A2204.

In the case of A2597 an off-nuclear FUV spectrum is presented in O’Dea et al. (2004). This spectrum shows no evidence for line emission in the wavelength range sampled by our F150LP images. We can calculate what the strength of the CIV 1549 Å line would have to be in the O’Dea et al. (2004) spectrum if the FUV emission observed by us in this region is solely due to this line. From our F150LP image we find $F_\lambda \sim 10^{-17}$ erg s⁻¹ cm⁻² Å⁻¹ arcsec⁻². This is in good agreement with O’Dea et al. (2004). The width of the F150LP filter is 113 Å and thus the integrated F150LP flux is $F \sim 10^{-15}$ erg s⁻¹ cm⁻² arcsec⁻².

If we assume that the line has the same FWHM as the $Ly\alpha$ line measured by O’Dea et al. (2004) then the peak flux of this line would be $F_{peak} \sim 10^{-16}$ erg s⁻¹ cm⁻² Å⁻¹ arcsec⁻². This would be comparable to the $Ly\alpha$ line and should easily have been visible in the FUV spectrum presented by O’Dea et al. (2004). These authors calculate the $F(Ly\alpha)/F(CIV) \leq 0.07$ in their spectrum.

We thus conclude that the CIV 1549 Å line or any other line in the wavelength range sampled by the F150LP filter can not be responsible for a significant part of the FUV flux observed by us in A2597. For A2204 there is no measured FUV spectra with sufficient quality to investigate the presence of line emission.

In order to further assess the presence of line emission in our FUV band we have re-processed the M87 FUV images from Sparks et al. (2009). We find that CIV emission is not a necessary requirement. Normal main sequence stars with stellar temperatures $T \sim 10000$ K are able to explain the observations, see Appendix B.3. We thus conclude, by extension of the A2597 and M87 results, that it is unlikely that a significant part of the FUV emission observed in A2204 would be due to line emission.

3.5.2 Removing the old stellar population

BCGs are complex stellar systems. The U band and to a smaller degree the FUV band emission do not just come from young stars. Older stars, such as K-giants, contribute to the observed emission. In order to determine whether a young stellar population is consistent with the observed FUV_v/U_v ratio we need to first remove the older population.

We do this by identifying regions in our images that are dominated by old stars. These regions are indicated by the blue squares in Fig. 3.5 or equivalently by the black squares in Figs. 3.12 and 3.13. The area in which we can find reliable old-star regions is limited by the field of view of the FUV observations.

In the case of A2204 there is a companion elliptical galaxy to the south-west of the BCG. This elliptical is part of the galaxy cluster and shows low-level diffuse FUV emission expected from an old stellar population. We will refer to this old elliptical as A2204-SW. The other elliptical companion north of the A2204 BCG contains a bright FUV point-source associated with its nucleus. This is not consistent with an old stellar population and hence we do not use it.

In the case of A2597 there is no elliptical companion galaxy within the field of view of the FUV observations. Instead we use two regions within the outer regions of the BCG itself to identify old stellar regions. We will refer to the average of these two regions as A2597-OFF.

Having identified the old stellar regions in our observations, we can determine their FUV/V and U/V ratios and use the V image to remove the emission coming from the underlying old stellar population in our FUV and U images. We use the V band image, instead of the R or I band image, because the line contamination in this band is small and well determined from our spectroscopic observations.

However, first we perform a cross-check of the old stellar regions defined by us. We do this by comparing the U/V ratios determined here with the U/V ratio for a number of nearby elliptical galaxies using the larger field of view of the optical images. The nearby ellipticals selected are indicated by the red squares in Fig. 3.5. We will refer to this sample of nearby ellipticals as A2597-COMP and A2204-COMP and we find that their average U/V ratio agrees well with that of A2597-OFF and A2204-SW, see Tables 3.6 and 3.7.

Next we need to consider line contamination of the FORS V band image. The V band line contamination is due to $H\beta$ and OIII emission. The deep narrow-band $H\alpha$ images by Jaffe et al. (2005) show that the old stellar regions selected by us do not contain significant line emission, see also Fig. 3.2. Similarly from off-nuclear FORS spectroscopy (not shown here) we know that the line contamination of the V band decreases sharply along the major-axis of the BCG, see also Fig. 3.7. We thus conclude that the U/V and the FUV/V ratios determined in the old-star regions are not contaminated by line emission.

We then assume that the line contamination within the FUV, U-band bright filamentary regions is independent of location and well described by the average value quoted in Table 3.4. This assumption is supported by our $H\alpha$ images and FORS spectra. These show that the line contamination in the central 20 kpc region along the minor axis of the galaxy does not vary significantly on the scales relevant to this investigation, i.e. ~ 1 arcsec, see also Fig. 3.2.

We thus subtract the emission fraction due to line contamination from our V band images and use these line subtracted V-band images to compute the FUV and U excess images, see Figs. 3.12 and 3.13. We note that the line contamination correction of the V-band has a small

but systematic effect on the $FUV_{v,exc}/U_{v,exc}$ excess emission ratio in that it lowers this ratio about 5 per-cent. This is easily explained by noting that the old stellar population contributes more to the U than to the FUV emission. From here on we will denote the total light images as $FUV_{v,tot}$ and $U_{v,tot}$ and the excess light images as $FUV_{v,exc}$ and $U_{v,exc}$.

In Table 3.8 we give the FUV and U band fluxes integrated over large 18 kpc radial apertures for (i) the total light, (ii) the excess light, (iii) the nebular continuum and (iv) the $H\alpha$ flux in A2597 and A2204. We see that on large scales only about 20 percent of the total observed FUV flux can be accounted for by the old stellar population in both targets. Similarly we find that about 80 percent of the U flux in A2597 and about 60 percent of the U flux in A2204 can be accounted for by the old stellar population.

3.5.3 The $FUV_{v,exc}/U_{v,exc}$ excess ratio

Having subtracted the emission contributed by the old stellar population from the FUV_{tot} and U_{tot} images we obtained the two excess images FUV_{exc} and U_{exc} , see Figures 3.14 and 3.15. These images show that excess FUV and U band light trace each other very well in the central 20 kpc regions of A2597 and A2204.

We will now investigate whether the observed $FUV_{v,exc}/U_{v,exc}$ ratio is consistent with the emission ratio expected for young stars by comparing it to K93 stellar models. A2597 and A2204 are at redshifts $z=0.0821$ and $z=0.1517$ respectively. We redshift the K93 stellar models by these amounts and compute the FUV_v/U_v ratio by convolving the model spectra with the F150LP and U Bessel filters. For comparison reasons we also compute the FUV_v/U_v ratio for a set of BB models. The results for both models are given in Fig. 3.16.

To improve the signal to noise we have re-binned the FUV_{exc} and U_{exc} images for A2597 and A2204 by a factor 3 so that one pixel now corresponds to 0.6×0.6 arcsec². We find in the central region region of A2597 that the observed $FUV_{v,exc}/U_{v,exc}$ ratio is between 1.7 and 2.6. Comparing with the K93 stellar models and invoking extinction by MW foreground dust only, we find that a $FUV_{v,exc}/U_{v,exc}$ ratio between 1.7 and 2.6 corresponds to main-sequence stars with temperatures between 28000 and 50000 K.

We have plotted the observed $FUV_{v,exc}/U_{v,exc}$ ratio, its corresponding K93 stellar temperature, and their uncertainties in Fig. 3.14. The uncertainty in the ratio takes into account the absolute flux uncertainty and the poissonian noise for all involved images. The uncertainty in the ratio and in the temperature are non-linear. For the maps presented here we have chosen to represent the uncertainty by the average of the one sigma upper and lower deviation. The K93 models allow for stellar temperatures in range 0-50000 K. If either the lower or the upper deviation falls outside of this range, then the uncertainty given is set to the deviation that does fall within the allowed range.

There are a number of pixels that have a ratio greater than 2.6 and thus a best-fit temperature above the value allowed for normal main-sequence O-stars. These pixels have a low signal-to-noise mainly because of their low U band flux. The corresponding large error on these pixels allows us to reconcile them with a stellar origin. There is not much sub-structure in the temperature map of A2597. One can argue that there is a small decrease in temperature beyond the central 10×10 kpc² but the low statistics and higher noise here do not allow for strong statements.

In A2204 we find that the observed $FUV_{v,exc}/U_{v,exc}$ ratio is between 1 and 1.8. Comparing

with the K93 stellar models, taking into account extinction by MW foreground dust only, this corresponds to main-sequence stars with temperatures between 20000 and 40000 K. The results are plotted in Fig. 3.15. The temperatures derived for the FUV and U excess emission in A2204 are bit lower than for A2597. The A2204 temperature map does show some substructure in that the knots west and north of the nucleus have the highest temperatures being at 30000 to 40000 K. The remaining parts of the central region in A2204 have a temperature corresponding to 20000 to 30000 K.

Interpreting the observed $FUV_{v,exc}/U_{v,exc}$ ratio terms of BB models requires temperatures above 35000 K in A2597 and above 30000 K in A2204, if extinction by MW foreground dust only is taken into account.

3.5.4 Nebular continuum emission

Figs. 3.2 and 3.4 show that the ionised gas, as traced by the $H\alpha$ recombination line, is co-spatial with the FUV emission on kpc-scales. This ionised gas has a temperature $T \sim 10^4$ K and will emit continuum emission in the FUV-optical wavelength range. The amount of nebular continuum emission depends not only on the temperature and density of this gas but also on whether the gas is ionisation or density bounded.

The maximum amount of nebular continuum is produced when the gas is ionisation bounded. We have estimated the contribution of nebular continuum to the FUV flux in this case based on the $H\alpha$ measurements by Jaffe et al. (2005) using the *NEBCONT* program (Howarth et al. 2004). As our input we use an electron temperature $T_e = 10^4$ K, electron density $n_e = 10^2 \text{ cm}^{-3}$, 10% He abundance and the total extinction estimated from the Balmer decrements measured in our FORS spectra. The results for 18 kpc radial apertures are presented in Table 3.8.

We find that 5% and 11% of the total FUV band flux in A2597 and A2204 respectively is due to nebular continuum emission. This percentage increases to 6% and 13% if we consider only the excess FUV emission. The contribution of nebular emission to the total U band flux is 6% and 15% for A2597 and A2204 respectively. This increases to 38% and 39% if we consider only the excess U emission.

Removing the nebular continuum emission increases the $FUV_{v,exc}/U_{v,exc}$ ratio by a factor 1.5 and 1.4 for A2597 and A2204 respectively. Increasing the observed $FUV_{v,exc}/U_{v,exc}$ ratio by a factor 1.5 means that most of the central 20 kpc emission in A2597 can no longer be explained by stars. In the case of A2204 removing the nebular continuum means that the FUV bright clumps north and north-west of the nucleus can no be explained by stars, but most of the remaining emission in the central 20 kpc can still be reconciled with a stellar origin.

Above we have calculated the maximum contribution coming from the ionised gas in the form of nebular continuum emission. We note that currently it is not clear if the gas is ionisation or density bounded. In the latter case the continuum emission contributed to the FUV and U-bands by the ionised gas could be lower. O’Dea et al. (1994) argue that the $H\alpha$ emission arises from the ionised skins on HI clouds and that as such the gas nebula in A2597 is ionisation bounded. This picture is consistent with low spatial resolution measurements of $H\alpha$, HI and OI 6300 Å. Recent high spatial resolution HST measurements of NGC 1275, the nearby BCG in the Perseus galaxy cluster, show that the $H\alpha$ emission line filaments are very thin, i.e. they have pc-scale widths (Fabian et al. 2008). Such very thin filaments may allow for a density bounded

state of the gas in NGC 1275 and by extension in A2597 and A2204. Further observations are necessary to investigate the condition of this gas.

3.5.5 Dust intrinsic to the BCG

Our FORS optical images of A2597 and A2204 do not show strong evidence for dust in these systems. However, archival optical images from HST do show that these BCGs are morphologically disturbed at their centres, see Fig. 3.17. This patchy morphology is indicative of obscuration by dust in these systems.

This is confirmed by measurements of the Balmer decrements in our FORS spectra, see Table 3.5. These decrements deviate strongly from case B recombination and can be described by dust extinguishing light according to an average Milky Way (MW) type extinction law, such as described by Cardelli, Clayton & Mathis (1989) (hereafter C89).

Results by Voit & Donahue (1997) confirm that in the optical regime the dust in A2597 can be described by an average MW type extinction law with $A_V \sim 1$. For A2204 our Balmer decrements imply a higher extinction than would be obtained from the measurements presented in Crawford et al. (1999). Contrary to Crawford et al. (1999) we measure the Balmer ratios within the same slit which is why we prefer our measurement for A2204. Interestingly we note that our spectra do not show strong changes in the Balmer decrements over the central ~ 15 kpc regions in A2597 and A2204. A disturbed morphology and Balmer decrements that deviate strongly from case B recombination are typical for cool-core BCGs as a class of objects (e.g. Crawford et al. 1999; O’Dea et al. 2010).

The C89 extinction law aims to reproduce the global extinction properties for the diffuse interstellar medium in our galaxy. It is parametrized from 0.125 to 3.5 μm covering the range in wavelengths important to us. Although there is no reason to a priori assume that the dust properties in the BCGs is the same as in the MW, there is no evidence from either optical spectroscopy or the far-infrared spectral energy distributions (Voit & Donahue 1997; Edge et al. 2010, Oonk et al. in prep.) that the dust in BCGs is different.

Below we will investigate how extinction by dust affects the FUV and U band fluxes. In order to do so we will always use the C89 extinction law to describe the total extinction as being due to two components; (i) foreground MW dust and (ii) dust intrinsic to the BCG. The extinction due to the MW towards A2597 and A2204 is $A_{V,MW}=0.1$ and $A_{V,MW}=0.3$ respectively (Schlegel et al. 1998). In order to explain the observed Balmer decrements we require the dust component intrinsic to the BCG to be $A_{V,BCG}=1.3$ for A2597 and $A_{V,BCG}=1.6$ for A2204, see Table 3.5. These values have been calculated by invoking the C89 extinction law and by taking redshift effects into account.

Up to this point we have considered extinction due to MW foreground dust only. In Fig. 3.16 we plot the FUV_{ν}/U_{ν} ratio for varying amounts of extinction. Dust has a dramatic effect upon the FUV_{ν}/U_{ν} ratio. The highest ratio values observed in A2597 and A2204 can be reconciled with the K93 stellar models in the case where the only dust in front of these regions is the MW foreground. The average ratio value observed in the central 10 kpc of A2597 is about 2.1 and about 1.1 in A2204. If half of the dust intrinsic to the BCG or more is front of the emitting regions then normal main sequence stars as described by the K93 models can no longer explain the observed emission ratio.

This leads to the following possible explanations; (i) There is little to no dust in front of

the high FUV_{*v,exc*}/U_{*v,exc*} areas and their emission is due to hot main-sequence stars. (ii) The emission is due to exotic stars, such as Wolf-Rayet stars or White Dwarfs, with temperatures above 50000 K. (iii) A non-stellar source contributes to the observed wavelength regime or alternatively this source affects the Balmer decrement measurements. (iv) A MW type extinction law, although consistent with the optical Balmer decrements, is not applicable to the FUV wavelength range studied here.

Explanations (ii-iv) will be discussed in Sections 3.7 and 3.8. Here we will shortly discuss explanation (i). A clumpy, dusty medium, such as observed in A2597 and A2204, may give rise to a selection effect in that we preferentially observe FUV emission coming from regions with low extinction along the line of sight. There are two ways in which this could arise, (a) the sightlines along these regions have intrinsically very low extinction, or (b) the Balmer decrements trace the dust over a longer column than the observed FUV emission i.e. we only observe the FUV emission coming from the front part of the line of sight.

Our optical spectra sample a small, but representative part of the FUV bright regions. Here we can rule out option (a) because we do not observe any regions with low extinction. Option (b) seems unlikely because the FUV to H α ratio would vary significantly if background HII regions exist where high Balmer decrements are observed but the FUV emission is highly extinguished. Some spread is observed in the FUV to H α emission, but generally they are found to be well correlated, see O'Dea et al. (2004) and Figs. 3.2, 3.4 and 3.7.

While selection bias may have favored regions with low extinction in determining the FUV to U ratio, the FUV to H α ratio seems to indicate that this is not crucial in our analysis. Our optical spectra, ofcourse, only sample a subset of the regime where we have measured the FUV to U ratio. Two dimensional integral field observations of the relation between H α /H β versus FUV/H α could clarify this issue.

3.6 Star formation

In the previous section we showed that very hot O-stars are able to explain to observed FUV and U emission. In this section we investigate whether these stars can power the ionised gas nebulae observed in H α line emission and what the FUV and H α implied star formation rates are.

3.6.1 The H α nebula

Optical emission line nebulae, usually observed in H α emission, are typical for cool-core clusters (e.g. Heckman et al. 1989; Crawford et al. 1999). Jaffe et al. (2005) show that both A2597 and A2204 contain large H α nebulae. Higher spatial resolution observations of the central few kpc in A2597 by Koekemoer et al. (1999) and Donahue et al. (2000) show that the central ionised gas nebula is very clumpy and filamentary. If we assume that the FUV light has a stellar origin then we can ask ourselves whether the observed H α emission is quantitatively consistent with the same stellar origin.

The total FUV fluxes in 18 kpc radial apertures for A2597 and A2204 are given in Table 3.8. Upon correcting for Milky Way foreground dust and distance we find luminosities $L(\text{FUV}, \text{A2597}) = 2.5 \times 10^{28} \text{ erg s}^{-1} \text{ Hz}^{-1}$ and $L(\text{FUV}, \text{A2204}) = 7.2 \times 10^{28} \text{ erg s}^{-1} \text{ Hz}^{-1}$. We

then assume that the stars responsible for the FUV emission are on average hot O-stars and calculate their FUV flux. Here we will perform this calculation for an O3 star with a stellar radius $15 R_{\odot}$. Such a star has a FUV flux $F(\text{F150LP}, \text{O3}) \approx 0.064 \text{ erg s}^{-1} \text{ cm}^{-2} \text{ Hz}^{-1}$ in the F150LP band which then corresponds to a luminosity $L(\text{F150LP}, \text{O3}) \approx 8.74 \times 10^{23} \text{ erg s}^{-1} \text{ Hz}^{-1}$. The observed FUV luminosities thus require about 30000 O3 stars for A2597 and about 80000 O3 stars for A2204.

Following Beckman, Zurita & Rozas (2001) and Vacca, Garmany & Shull (1996) the total Lyman continuum (Lyc) flux of an O3 main sequence star is $F(\text{Lyc}) = 10^{49.87}$ photons s^{-1} or equivalently a luminosity $L(\text{Lyc}) = 10^{39.17} \text{ erg s}^{-1}$. Assuming Case B downward conversion this yields $L(\text{H}\alpha) = 10^{38} \text{ erg s}^{-1}$. The O3 stars in A2597 and A2204 thus produce a $\text{H}\alpha$ luminosities $L(\text{O3-H}\alpha, \text{A2597}) = 3 \times 10^{42} \text{ erg s}^{-1}$ and $L(\text{O3-H}\alpha, \text{A2204}) = 8 \times 10^{42} \text{ erg s}^{-1}$.

This is consistent with the $\text{H}\alpha$ luminosities measured by Jaffe et al. (2005) for A2597 and A2204, i.e. $L(\text{H}\alpha, \text{A2597}) = 0.9 \times 10^{42} \text{ erg s}^{-1}$ and $L(\text{H}\alpha, \text{A2204}) = 2.8 \times 10^{42} \text{ erg s}^{-1}$. We conclude that if all the FUV light is due to hot O-stars, then the overall photon budget of these stars is sufficient to produce the observed $\text{H}\alpha$ emission. For A2597 this result is in agreement with earlier results by O’Dea et al. (2004).

Only the Milky Way foreground extinction was taken into account in the above calculation. Dust extinction intrinsic to the BCGs is discussed in more detail in Sect. 3.5.5. Increasing the amount of dust will increase the amount of extinguished FUV emission relative to $\text{H}\alpha$ emission and thus even more O-stars will be available to produce ionising photons. Not all of the total FUV flux can be attributed to young stars. Below we show that about 20 per cent of the FUV flux in F150LP is due to the old stellar population in A2597 and A2204. Such a small old star contribution to the FUV flux does not affect the above conclusion.

3.6.2 FUV and $\text{H}\alpha$ star formation rates

The extinction uncertainty translates to a large uncertainty for the derived star formation rates (SFR) in these systems. In the case of A2597, using the C89 extinction law with a two component dust analysis, we find that the maximum fractional extinction at the wavelength of the FUV F150LP filter ($\lambda = 1612 \text{ \AA}$) and the $\text{H}\alpha$ line ($\lambda = 6563 \text{ \AA}$) is 28.7 and 2.9 in flux respectively. The minimum fractional extinction due to the Milky Way foreground is only 1.3 and 1.1 at the FUV and $\text{H}\alpha$ wavelengths respectively.

Thus depending on how much of the dust is actually in front of the FUV and $\text{H}\alpha$ emitting structures means that the FUV derived star formation rate is $\text{SFR}(\text{FUV}, \text{A2597}) = 3.5\text{--}77.5 \text{ M}_{\odot} \text{ yr}^{-1}$ and the $\text{H}\alpha$ derived star formation rate is $\text{SFR}(\text{H}\alpha, \text{A2597}) = 7.0\text{--}18.6 \text{ M}_{\odot} \text{ yr}^{-1}$. Here we invoked the SFR relations discussed in Ball & Kennicutt (2001). Similarly, for A2204 we find $\text{SFR}(\text{FUV}, \text{A2204}) = 10.2\text{--}476.9 \text{ M}_{\odot} \text{ yr}^{-1}$ and $\text{SFR}(\text{H}\alpha, \text{A2204}) = 22.1\text{--}75.4 \text{ M}_{\odot} \text{ yr}^{-1}$.

The $\text{H}\alpha$ SFR range falls within the corresponding FUV SFR range, but both are poorly constrained due to the uncertainty in the dust distribution. Previous SFR estimates range from $4\text{--}12 \text{ M}_{\odot} \text{ yr}^{-1}$ for A2597 (McNamara & O’Connell 1993; O’Dea et al. 2004; Donahue et al. 2007) and $15 \text{ M}_{\odot} \text{ yr}^{-1}$ for A2204 (O’Dea et al. 2008). SFRs deduced by different methods are not expected to agree as they trace different physical processes, regions and timescales in the overall star formation scheme. A recent overview of the different star formation rates estimated for A2597 and a discussion of them can be found in O’Dea et al. (2008).

In Section 3.3.3 we showed deep radio maps of our BCGs revealing interesting new struc-

tures. Here we will briefly discuss the northern 3 sigma feature in the 8 GHz observations of A2204. Although it is possible that this feature is simply related to a background radio source it is interesting that its location agrees with the bright northern FUV knot. Assuming for now that the radio emission in this knot is due to synchrotron emission from supernova explosions we can estimate a SFR by invoking the far-infrared radio correlation (Condon, Anderson & Helou 1991) and the SFR relations discussed in Ball & Kennicutt (2001).

The peak emission of the radio feature is $82 \pm 20 \mu\text{Jy}$ and it has an integrated flux of $110 \pm 42 \mu\text{Jy}$ at 8 GHz. Assigning a spectral index $\alpha = -0.5$ ($F \sim \nu^\alpha$) to this synchrotron emission we find a 1.49 GHz radio luminosity $1.4 \times 10^{22} \text{ W Hz}^{-1}$. Applying the above mentioned relations this translates to a $\text{SFR}(\text{radio}, \text{n-knot}) = 5.8 \text{ M}_\odot \text{ yr}^{-1}$. This is much higher than the FUV implied SFR i.e. $\text{SFR}(\text{FUV}) = 0.2 \text{ M}_\odot \text{ yr}^{-1}$. This difference can be accounted for by extinction if most of the dust lies in front of the emitting area. The radio emission can not be associated with free-free emission from young O-stars as this would require far too many of such stars.

3.6.3 Dust and gas mass estimates from A_V

Under the assumption of MW type dust, case B recombination and that the dust is optically thin everywhere we can derive rough gas and dust mass estimates from the amount of visual A_V extinction. In the diffuse interstellar medium of the Milky Way (Bohlin, Savage & Drake 1978) find $N(\text{H})/A_V = 1.9 \times 10^{21} \text{ atoms cm}^{-2} \text{ mag}^{-1}$ where $N(\text{H}) = N(\text{HI} + \text{H}_2)$ is the number of nucleons.

We find $A_{V, \text{BCG}} = 1.3$ for $A_{V, \text{BCG}} = 1.6$ over the central $10 \times 10 \text{ kpc}^2$ regions in A2597 and A2204 respectively. Integrating $N(\text{H})$ over this region and multiplying by two to account for the dust on the far side of the galaxy we find $M(\text{H}, \text{A2597}) = 4.0 \times 10^9 \text{ M}_\odot$ and $M(\text{H}, \text{A2204}) = 4.8 \times 10^9 \text{ M}_\odot$. Our total gas mass estimates for the central region of A2597 are about an order of magnitude higher than the atomic gas mass estimated by O'Dea et al. (1994) for this region. Edge (2001) indeed find a much higher molecular gas mass ($M(\text{H}_2, \text{A2597}) \sim 10^{10} \text{ M}_\odot$), but the lower spatial resolution of this measurement means that it probes a much larger region and makes it difficult to compare it to the other measurements above. All these gas mass estimates suffer from systematic uncertainties and further observational constraints are necessary to refine them. There are no cold gas mass measurements published for A2204.

Edge et al. (2010) show that the global gas to dust ratio for BCGs is similar to the MW average i.e. $M(\text{H})/M(\text{dust}) = 140$. This would imply that $M(\text{dust}, \text{A2597}) = 1.4 \times 10^7 \text{ M}_\odot$ and $M(\text{dust}, \text{A2204}) = 1.7 \times 10^7 \text{ M}_\odot$. For A2597 this dust mass estimate is in good agreement with the value deduced from far-infrared emission by Edge et al. (2010). If the dust is optically thick in some places in the BCG then the above calculated masses are lower limits for the true gas and dust masses. There are no dust mass measurements published for A2204.

If we assume constant star formation at a rate of $10^{1-2} \text{ M}_\odot \text{ yr}^{-1}$ then the gas masses calculated by us above imply a gas depletion time of about 10^{7-8} yr . The (residual) mass deposition rates allowed for by X-ray spectroscopy is similar to the range in star formation rates observed here and may thus be able to sustain star formation over longer time scales (e.g. Peterson & Fabian 2006; Peres et al. 1998).

3.7 Excess FUV/U: Non-stellar Origin ?

In the previous sections we have showed that young, hot stars can explain the observations, but only if the dust content and nebular continuum emission is low enough. Especially in A2597 it is difficult, but not impossible, to reconcile the observed $F_{\text{UV}}/U_{\text{V}}$ ratio with stars alone. Below we show that the common non-stellar processes that are known to take place in cool-core clusters can not provide an alternative explanation for the observations. Stars thus remain as the only evident option.

3.7.1 Active Galactic Nuclei

Using models by Nagao et al. (2001) we have investigated the $F_{\text{UV}}/U_{\text{V}}$ ratio for AGN emission. These models correspond to $F_{\nu} \sim \nu^{-0.5}$ in FUV-Optical wavelength range. This means that this model predicts a $F_{\text{UV}}/U_{\text{V}}$ ratio which is always less than unity. Adding the additional blackbody, infrared and X-ray terms in equation (2) by Nagao et al. (2001) does not change this. We thus conclude that the observed $F_{\text{UV}_{v,exc}}/U_{v,exc}$ ratio in A2597 and A2204 can not be explained by an AGN.

3.7.2 Non-thermal processes

A significant contribution to the U band excess light by synchrotron emission and/or scattering of light by dust or hot electrons is ruled out by McNamara et al. (1999) using U-band polarisation studies. Since the FUV and U excess light trace each other well we conclude that neither synchrotron emission nor scattering contributes significantly to the excess FUV and U emission.

Bremsstrahlung is also ruled out because under optically thin conditions it produces a spectrum that is flat or decreases slowly in flux with increasing frequency in the FUV to optical wavelength range. Only in optically thick conditions can bremsstrahlung produce a spectrum that increases with frequency. In this case the emergent intensity will obey the Rayleigh-Jeans limit of the Planck black body function i.e. $F_{\nu} \propto \nu^2$. However, this can also be ruled out as the integrated bremsstrahlung flux measured with ROSAT (0.1-2.4 keV) for A2597 and A2204 is an order of magnitude below the measured FUV fluxes here (Brinkmann et al. 1994; Ebeling 1998).

3.8 Discussion

Below we will shortly discuss our results. In the first two sections we will compare our results to two previous investigations into the FUV to optical excess emission in cool-core BCGs. In the third section we discuss the extinction law and in the final section we compare the results for A2597 and A2204.

3.8.1 Crawford & Fabian 1993

First we will discuss the CF93 results. They use measurements from the International Ultraviolet Explorer (IUE) and combine it with optical spectroscopy to study the excess emission

from 1300-5000 Å in 4 BCGs. Their spectral coverage of the blue emission in BCGs is wider and better sampled than our investigation. However, they do not have spatial information, being limited by the 10×20 arcsec² IUE aperture. Their analysis is similar to ours in that dust, the old stellar population and line emission is taken into account. For the dust correction they use the Seaton (1979) average MW extinction curve, which is similar to the C89 curve used by us (see Fig. 4 in C89). Their correction for the old stellar population is based on a template model derived from optical spectroscopy of the Abell 4059 BCG and extending it into the UV.

Their main result is that they find that the excess blue emission in BCGs, even if they allow for reddening by dust, can be explained with star formation dominated by B5 stars i.e. ~ 15000 K. Their results are based on the Kurucz 1979 stellar models which are identical to the Kurucz 1993 models used by us.

Considering an aperture with 7 arcsec radius centered on the A2597 BCG we compute the $FUV_{v,tot}/U_{v,tot}$ ratio from our data and correct it only for foreground MW dust. We then find $FUV_{v,tot}/U_{v,tot} \approx 0.7$. This corresponds to a K93 stellar model temperature of 14000 K. This means that at low dust extinction we are in reasonable agreement with the CF93 result for A2597. However, our results are no longer consistent with CF93 after correcting for the dust intrinsic to the BCG and the emission contributed by old stars. There are a number of reasons for this difference.

First CF93 assume an extinction of $A_{V,BCG}=0.3$ based on $Ly\alpha/H\alpha$ results by Hu (1992). We use $A_{V,BCG}=1.3$ based on optical spectroscopy of the Balmer decrements. An additional magnitude of intrinsic extinction at visual wavelength as shown above has dramatic effects on the FUV/U ratio. We will discuss the extinction law in more detail below. The second important difference concerns the ratio of excess to total emission in the U-band. CF93 find that this ratio is 0.55 at 3500 Å, whereas we find that this ratio is 0.17 in the U-band (3600 Å). This is a large difference and means that either; (i) the old stellar population in A2597 differs significantly from the old stellar population template used by CF93, or (ii) there is significant excess emission contributing to the total light in our V-band observations.

To test the second option we have also computed the $FUV_{v,exc}/U_{v,exc}$ ratio by using the R and I band data, which should contain less excess emission as compared to the V-band. Contamination due to line emission was set to 12 per-cent and 7 per-cent for the R and I band respectively. In these numbers we have included contamination due to the SII 6716 Å and 6731 Å lines that were not included in our spectra, but were measured by Voit & Donahue (1997). We find no significant difference in the FUV_v/U_v ratio when either the V, R or I band is used to remove the old stellar population, see Fig. 3.18. We thus conclude the old stellar population in A2597 is different from the template used by CF93.

A further uncertainty in the CF93 work concerns the large aperture mismatch between their optical and UV data which requires them to invoke large, uncertain, scaling factors that can affect their results. We also note that their 1600 Å FUV value for A2597 is about 25 per-cent larger than predicted by their B5 model value. The CF93 FUV 1600 Å value would thus allow for higher stellar temperatures than B5 as indicated by our result. Taking into account the differences due to the dust, old stellar population model and their FUV 1600 Å flux value then our results are in rough agreement with CF93.

CF93 discuss that the blue excess emission can be equivalently well described by a power-law $F_\nu \sim \nu^\alpha$ with $\alpha=[-0.5:0.5]$. As noted by CF93 this is no surprise because hot stars can be approximated by a power law with this slope in the FUV-optical regime. McNamara & O'Connell

(1993) showed evidence for the blue excess emission to be correlated with the AGN radio lobes in two objects a.o. A2597. From our higher resolution data we find that although the FUV emission is roughly extended along the radio axis, that there is no detailed correlation between the radio and the FUV for A2597. In Sections 3.7.1 and 3.7.2 we already discussed that the AGN and non-thermal processes can be ruled out for our observations of blue excess emission in A2597. Stars thus remain as the most plausible option.

3.8.2 Hicks et al. 2010

Hicks et al. (2010) (hereafter H10) recently presented a BCG sample observed with GALEX in the FUV ($\sim 1500 \text{ \AA}$) and the NUV ($\sim 2500 \text{ \AA}$). In their Table 2 they give FUV and NUV photometry for 16 BCGs within 7 arcsec radial apertures centered on the BCG nuclei. These numbers have been corrected for foreground MW extinction but not for the dust intrinsic to the BCG or for emission due to the old stellar population. These apertures correspond on average to the central $\sim 10 \text{ kpc}$ of the BCG which is similar to the area investigated by us.

We have computed the temperature corresponding to tabulated $FUV_{v,tot}/NUV_{v,tot}$ ratio in H10 in the same way as done above for our FUV_v/U_v ratios using the K93 stellar models. The results are given in Table 3.9. Contamination of the FUV band by $Ly\alpha$ emission for systems with $z>0.1$ has not been taken into account and if present would lead to an overestimate of the stellar temperature estimated by us.

The $Ly\alpha$ line is not a problem for A2597 and the H10 $FUV_{v,tot}/NUV_{v,tot}$ ratio implies a K93 stellar temperature 14000 K. This value, being uncorrected for intrinsic dust and the old stellar population, is in good agreement with our results and the results by CF93, see Section 3.8.1.

H10 also perform a correction for emission contributed by the old stellar population. This correction is based on the average UV-J band colors measured for a control sample of elliptical galaxies measured in the same bands with GALEX. The corrected FUV, NUV excess emission is tabulated in their table 7. Interestingly the excess $FUV_{v,exc}/NUV_{v,exc}$ ratios do not increase significantly with respect their corresponding total $FUV_{v,tot}/NUV_{v,tot}$ ratios for most BCGs in their sample, including A2597.

We do find a significant increase in the $FUV_{v,exc}/U_{v,exc}$ ratio as compared to the $FUV_{v,tot}/U_{v,tot}$ ratio which appears to be in disagreement with H10 result for this particular system. We believe that our results are correct because (i) we obtain the correction for the old stellar population from the BCG itself and (ii) the correction does not depend on which band (V, R or I) is used, see Section 3.8.1 and Fig. 3.18. This would indicate that the old stellar population in A2597 differs from the template used in H10. The average old star correction performed by H10 is uncertain for individual systems because the UV-J colors of BCGs have a significant scatter, particularly in the FUV band (priv. comm. A. Hicks, M. Donahue).

3.8.3 The extinction law in BCGs

An average MW type extinction law certainly does not apply to all galaxies. Detailed observations of (i) different sightlines within the Milky Way, (ii) local group galaxies and (iii) luminous infrared galaxies show significant variations in the extinction law (e.g. C89; Calzetti et al. 2000). This is particularly true for emission in the UV regime. Currently we do not know what the detailed shape of the extinction law in BCGs is. This lack of information is the most severe

limitation in interpreting the FUV-optical excess emission presented here. However, even without knowing the exact shape of the extinction law we have obtained interesting limits on the origin of this emission in the previous sections. In this section we will discuss the information that we have on the extinction law in BCGs in a bit more detail.

In this work we have used deep, optical $\sim 3500\text{-}7500$ Å long-slit spectroscopy to determine the amount of extinction and the shape of the extinction law from the Balmer decrements. The reason for using this data set is because of the large wavelength coverage and thus being able to measure the Balmer ratios under the same observing conditions and within the same slit observation. We have shown that these ratios can be described by an average MW type extinction law such as described by C89, with an $A_V \sim 1\text{-}2$, for A2597 and A2204.

The Balmer lines are optically thin and thus we do not know how much of the dust implied by these lines is in front of our line of sight to the FUV and U emitting regions. Star formation is usually accompanied by dust. Thus if young stars are responsible for the observed excess emission then a significant amount of the total extinction should be associated with these stars, see also the discussion in Section 3.5.5.

Including MW type dust in our analysis of the excess emission in these BCGs has profound effects on the nature of this emission. If at least half of the dust is in front of the emitting regions, then stellar temperatures above 50000 K are required to explain the observed excess emission in the central 20 kpc regions of A2597 and A2204. Such high temperatures can not be accounted for by normal O-stars. It is unlikely that exotic, hotter stars such as Wolf-Rayet stars are present in sufficient amounts to dominate the observed excess emission over such large areas. White dwarfs are an option but these will be distributed in the same way as the old stellar population and as such should not contribute to the excess emission.

Measurements of the Ly α to H α ratio appear to contradict the dust properties inferred from the optical Balmer ratios. Hu (1992) and O’Dea et al. (2004) find Ly α /H α ~ 6 for A2597. A simple calculation for A2597 based on eq. 7.4 and the standard R=3.1 MW extinction law tabulated in Table 7.1 in Osterbrock & Ferland (2006) shows that this can not be in agreement with our optical Balmer results. Invoking our measured value of H α /H β =4.5 in A2597 and assuming that the un-extincted value of this ratio is 2.87 we find that the constant c in eq. 7.4 is 0.56. Applying this value of c and the R=3.1 MW extinction law to the dust-free Ly α /H α ≈ 13 ratio Ferland & Osterbrock (1986) we find that the measured value of this ratio in A2597 should be 0.4. This strongly disagrees with the measurements by O’Dea et al. (2004), which by itself would imply $c \approx 0.125$ for a R=3.1 MW extinction law.

The C89 extinction law used in the work above corresponds to the standard R=3.1 MW extinction law. It would seem that applying this extinction law in the manner described above overestimates the Ly α /H α ratio by a factor 15. However, there are a number of possible explanations for this discrepancy.

It is possible that there is a selection effect in that the observed Ly α emission is weighted towards regions of lower extinction. We have discussed a similar case of this selection effect, involving the FUV emission and the Balmer lines, in Section 3.5.5. The same arguments apply here, (i) our optical spectroscopy does not show evidence for inhomogeneous extinction, and (ii) there is a good correlation between Ly α and H α emission (O’Dea et al. 2004). This indicates to us that both come from the same regions and are subject to the same extinction.

Another option to explain the observed Ly α /H α ratio is that the shape of the extinction curve for the dust intrinsic to the BCG is different from the average MW curve. We experimented

with a much flatter $R=5.5$ extinction curve, such as observed along the line of sight towards Orion nebula (e.g. Osterbrock & Ferland 2006). This curve, with $c \approx 0.56$, is able to explain the observed $\text{Ly } \alpha / \text{H}\alpha$ ratio and also gives a reasonable fit for all Balmer ratios except $\text{H}\alpha / \text{H}\beta$ which would have to be 3.9 instead of the measured 4.5.

The standard $R=3.1$ MW type extinction law, with $c=0.56$ i.e. assuming all dust is in front of the emitting regions, implies that the extinction in the FUV(1600 Å) band is a factor 4 and 10 higher than in the U(3600 Å) and $\text{H}\alpha$ (6563 Å) bands respectively. However, a $R=5.5$ extinction law with the same amount of extinction (i.e. $c=0.56$) would imply that the extinction for the FUV(1600 Å) and U(3600 Å) bands are practically the same and that the FUV(1600 Å) would be a factor 2 more extinguished than the $\text{H}\alpha$ emission. Lowering the relative extinction between the FUV and U band also means that it is possible to reconcile the observed excess emission with normal stars and that the range in allowed star formation rates decreases.

Finally it is well known that stars alone are not able to explain all the details of the emission spectra observed from BCGs in cool-core clusters (e.g. Voit & Donahue 1997; Jaffe et al. 2005). In particular the strong neutral atomic lines (e.g. OI 6300 Å) in combination with the weak high excitation lines (e.g. OIII 5007 Å) are a problem (Oonk et al. in prep.). A strong source of heating with modest ionisation is required, but the details of this process are currently not understood. Lyman and Balmer line ratios are known to be affected by non-stellar heating processes such as strong shocks and AGN (Osterbrock & Ferland 2006). Our BCGs are not dominated by either of these processes. Alternative non-thermal models such low velocity shocks and/or heating by energetic particles have been proposed and may play a role (Fabian et al. 2006; Ferland et al. 2009). It is possible that these processes could also influence the line ratios, but this requires further investigation in the future.

A detailed investigation taking into account both the continuum and line emission over a broad wavelength regime is needed to investigate the shape of the extinction curve in BCGs and to clarify which of the above explanations for the Lyman and Balmer lines is appropriate. Such an investigation is beyond the scope of this paper.

3.8.4 A2597 versus A2204

The BCGs in A2597 and A2204 are in many ways typical for the class of nearby ($z \sim 0.1$) BCGs in massive cool-core clusters. They have blue FUV-optical colors, strong optical line emission and Balmer decrements implying significant dust obscuration. The peak fluxes of the emission processes discussed here, i.e. X-ray, FUV, optical and radio emission, all agree and line up with the BCG nucleus. In both A2597 and A2204 the FUV morphology consists of a clumpy, filamentary part and a more diffuse part. Each of these accounts for about half of the total FUV flux. The FUV morphology for A2597 differs from A2204 in that A2597 has a more spiral-like filamentary structure as opposed to the more radially extending filaments in A2204.

The total FUV to U emission ratio, i.e. prior to any corrections for emission contributed by old stars, peaks in FUV bright clumps and is indicative of very young star formation. Correcting for emission contributed to the U-band by old stars shows that the old stellar component in A2597 is responsible for a larger part of the total U-band emission than is the case in A2204. In neither object does the old stellar population contribute significantly to the total FUV emission. Excess FUV and U-band emission is defined by correcting the total observed emission for the emission due to the underlying older stellar population. In both cases the location of the

maximum amount of excess FUV and U-band emission corresponds with the BCG nucleus.

The excess FUV to U emission ratio is found to be significantly higher in A2597 than in A2204. It also has less spatial sub-structure in A2597 as compared to A2204. The maximum ratio of the excess FUV to U emission is found to be located in off-nuclear regions in both objects. In A2204 this ratio peaks in the bright knots north and north-west of the nucleus. In A2597 this ratio is high across most of the central region with small increases to the south and south-east of the nucleus.

Interpreting the excess FUV to U ratio in terms of main-sequence stars, taking into account only Milky Way foreground extinction, we find that we require stellar temperatures up to 40000 K for the bright knots in A2204 and up to the 50000 K for the central region in A2597. Correcting for emission contributed by the nebular continuum and/or additional extinction by dust intrinsic to the BCG means that the regions with highest ratio of excess FUV to U emission can no longer be explained by normal stars. Contributions from non-thermal processes that have not been treated in this work should be investigated.

3.9 Conclusion

Using new, deep FUV imaging with HST and optical imaging and spectroscopy with FORS on the VLT we present the first two dimensional analysis of the FUV-optical colors at 1 arcsec spatial resolution in the A2597 and A2204 BCGs.

- We have mapped the FUV continuum emission with HST ACS/SBC in the F150LP (1612 Å) filter in 30×30 arcsec² regions centered on the BCGs in A2597 and A2204. The FUV continuum emission is distributed in clumpy, filamentary structures and is observed out to 20 kpc from the BCG nuclei.
- The total FUV to U-band emission ratio shows that the A2597 and A2204 BCG have blue cores typical of BCGs in cool-core clusters.
- The excess FUV and U emission, obtained by removing emission due to the old stellar population, is mapped at 1 arcsec resolution throughout the central ~20 kpc regions of the BCGs. The FUV and U excesses are shown to trace each other well on kpc-scales.
- Taking only Milky Way foreground extinction into account the excess FUV to U band emission ratio ranges between 0.6-3.0 in A2597 and 0.7-1.8 A2204 respectively. Interpreting this in terms of K93 main-sequence stellar models we find that stellar temperatures between 10000 K and 50000 K in A2597 and 15000 K and 40000 K in A2204 are required to explain the observations.
- Most of the central 20 kpc regions in A2597 and A2204 have an excess FUV to U band ratio greater than 1. This implies that the AGN and non-thermal emission processes, such as synchrotron emission or bremsstrahlung can not account for the observations.
- The morphology of the excess FUV and U band emission, as well the polarisation limits deduced for A2597 by McNamara et al. (1999), rule out scattering of light coming from the AGN. Stars thus remain as the most plausible explanation for the observed excess emission.

- Spectroscopy shows that the FUV and U-band emission observed by us for A2597 is not contaminated by line emission. Recent claims of significant CIV 1549 Å line emission in M87 are investigated and found not to be necessary in order to explain the observations. By extension of these results we believe that our FUV and U-band observations of A2204 are also free from line emission.
- Nebular continuum emission can account for up to 10 per-cent of the excess FUV flux and up to 40 per-cent of the U flux in A2597 and A2204. Correcting for the maximum amount of allowed nebular continuum means that most of the central 20 kpc excess emission in A2597 and the brightest excess knots in A2204 can no longer be explained by stars.
- Optical Balmer line ratios indicate an average Milky Way extinction law with $A_V=1.3$ for A2597 and $A_V=1.6$ for A2204. Extending the extinction law to the FUV regime means that the observed $FUV_{v,exc}/U_{v,exc}$ ratio in the central 20 kpc regions of A2597 and A2204 can no longer be explained by K93 stellar models, if half or more of this dust is in front of the excess regions.
- The FUV continuum emission matches the morphology of the extended $H\alpha$ nebula in A2597 and A2204 on large scales. If the FUV emission is attributed to hot O-stars then these stars are able to account for the observed $H\alpha$ emission in both systems. For A2597 this is in agreement with earlier results by (O’Dea et al. 2004).
- The minimum star formation rate deduced from the FUV continuum is $3.5 M_\odot \text{ yr}^{-1}$ for A2597 and $10.2 M_\odot \text{ yr}^{-1}$ for A2204. The maximum star formation rate depends strongly on the unknown dust distribution and extinction law.
- Assuming optically thin dust with Milky Way properties we estimate the gas and dust masses of the BCGs based on their measured A_V . We find $M_{gas} \sim 10^9 M_\odot$ and $M_{dust} \sim 10^7 M_\odot$ for the central $10 \times 10 \text{ kpc}^2$ regions in both A2597 and A2204.

This investigation shows that under special conditions on the nebular continuum emission and the dust obscuration it is possible to reconcile the FUV to optical colors with a stellar origin. The conditions are especially stringent for A2597 and in this regard contributions from non-thermal processes not treated here should be investigated in more detail.

A more detailed investigation of the possible stellar origin for the individual knots observed at the intrinsic spatial resolution of HST requires further imaging with HST in line-free bands. Also careful investigation into the dust properties and the shape of the extinction law will need to be carried out in order to resolve the uncertainties in determining the exact nature of the FUV to optical excess emission in BCGs.

We note with interest that detailed observations of the morphology of the FUV continuum, the excess FUV to U band ratio as well as the properties of the cool $T < 10^4 \text{ K}$ gas in BCGs, do not imply a strong interaction with the central AGN or its outflows on scales larger than the central few kpc (e.g. Pipino et al. 2009; O’Dea et al. 2010; Wilman et al. 2009; Oonk et al. 2010). A minor merger or ICM cooling scenario may be more appropriate to explain the extended 30 kpc-scale star formation, cool gas and dust properties in these objects.

If the origin of the cool gas at the centres of BCGs is the (residual) cooling of the hot ICM then the interaction between this hot gas and the AGN outflows, thought to regulate the

cooling process of this hot phase, may still be indirectly responsible for the observations at lower temperatures.

Acknowledgements

JBRO wishes to thank J. Brinchmann, B. A. Groves, G. R. Tremblay and C. P. O’Dea for useful discussions. NAH acknowledges support from STFC, and the University of Nottingham through the Anne McLaren Fellowship.

This research has made use of NASA’s Astrophysics Data System. The FORS observations were taken at the Very Large Telescope (VLT) facility of the European Southern Observatory (ESO) as part of projects 69.A-0444, 67.A-0597 and 63.N-0485. The ACS/SBC observations were taken as part of project 11131 with the NASA/ESA Hubble Space Telescope which is operated by AURA, Inc., under NASA contract NAS 5-26555.

The National Radio Astronomy Observatory is a facility of the National Science Foundation operated under cooperative agreement by Associated Universities, Inc. The Chandra X-ray Observatory Center, which is operated by the Smithsonian Astrophysical Observatory on behalf of the National Aeronautics and Space Administration under contract NAS 8-03060.

Bibliography

- Baars J. W. M., Genzel R., Pauliny-Toth I. I. K., Witzel A., *A&A*, 1977, 61, 99
Beckman J. E., Zurita A, Rozas M., 2001, *ApSSS*, 277, 397
Bell E. F., Kennicutt R. C. Jr, *ApJ*, 548, 681
Bildfell C., Hoekstra H., Babul A., Mahdavi A., 2008, *MNRAS*, 389, 1637
Birzan L., McNamara B. R., Nulsen P. E. J., Carilli C. L., Wise M. W., 2008, *ApJ*, 686, 859
Bohlin R. C., Savage B. D., Drake J. F., 1978, *ApJ*, 224, 132
Bolzonella M., Miralles J.-M., Pello R., 2000, *A&A*, 363, 476
Brinkmann W., Siebert J., Boller Th., 1994, *A&A*, 288, 433
Bruhweiler F. C., Miskey C. L., Smith Neubig M., 2003, *AJ*, 125, 3082
Bruzual A.G., Charlot S., 2003, *MNRAS*, 344, 1000
Calzetti D, Armus L., Bohlin R. C., Kinney A. L., Koornneef Jan, Storchi-Bergmann T., 2000, *ApJ*, 533, 682
Cardelli J. A., Clayton G. C., Mathis J. S., 1989, *ApJ*, 345, 245
Clarke T. E., Sarazin C. L., Blanton E. L., Neumann D. M., Kassim N. E., 2005, *ApJ*, 625, 748
Condon J. J., Anderson M. L., Helou G., 1991, *ApJ*, 376, 95
Crawford C. S., Fabian A. C., 1993, *MNRAS*, 265, 431
Crawford C. S., Allen S. W., Ebeling H., Edge A. C., Fabian A. C., 1999, *MNRAS*, 306, 857
Donahue M., Mack J., Voit G. M., Sparks W., Elston R., Maloney P. R., 2000, *ApJ*, 545, 670
Donahue M., Jordan A., Baum S. A., Cote P., Ferrarese L., Goudfrooij P., Macchetto D., Malhotra S., O’Dea C. P., Pringle J. E., Rhoads J. E., Sparks W. B., Voit, G. M., 2007, *ApJ*, 670, 231
Donahue M., Bruch S., Wang E., Voit G. M., Hicks A. K., Haarsma D. B., Croston J. H., Pratt G. W., Pierini D., O’Connell R. W., Böhringer H., *ApJ*, 715, 881

- Ebeling H., Edge A. C., Bohringer H., Allen S. W., Crawford C. S., Fabian A. C., Voges W., Huchra J. P., 1998, *MNRAS*, 301, 881
- Edge A. C., 2001, *MNRAS*, 328, 762
- Edge A. C., Wilman R. J., Johnstone R. M., Crawford C. S., Fabian A. C., Allen S. W., 2002, et al., *MNRAS*, 337, 49
- Edge A. C., Oonk J. B. R., Mittal R., Allen S. W., Baum S. A., Böhringer H., Bregman J. N., Bremer M. N., Combes F., Crawford C. S., Donahue M., Egami E., Fabian A. C., Ferland G. J., Hamer S. L., Hatch N. A., Jaffe W., Johnstone R. M., McNamara B. R., O’Dea C. P., Popesso P., Quillen A. C., Salome P., Sarazin C. L., Voit G. M., Wilman R. J., Wise M. W., 2010, *A&A*, 518, 47
- Fabian A. C., Nulsen P. E. J., Stewart G. C., Ku W. H. M., Malin D. F., Mushotzky R. F., 1981, *MNRAS*, 196, 35
- Fabian A. C., Sanders J. S., Taylor G. B., Allen S. W., Crawford C. S., Johnstone R. M., Iwasawa K., 2006, *MNRAS*, 366, 417
- Fabian A. C., Johnstone R. M., Sanders J. S., Conselice C. J., Crawford C. S., Gallagher J. S., Zweibel E., 2008, *Nat.*, 454, 968
- Ferland G. J., Osterbrock D. E., 1986, *ApJ*, 300, 658
- Ferland G. J., Fabian A. C., Hatch N. A., Johnstone R. M., Porter R. L., van Hoof P. A. M., Williams R. J. R., 2009, *MNRAS*, 392, 1475
- Hatch N. A., Crawford C. S., Fabian A. C., Johnstone R. M., 2005, *MNRAS*, 358, 765
- Heckman T. M., Baum S. A., van Breugel W. J., McCarthy P., 1989, *ApJ*, 338, 48
- Howarth I. D., Murray J., Mills D., Berry D. S., 2004, *Starlink User Note 50.24*, Council for the Central Laboratory of the Research Councils
- Hicks A. K., Mushotzky R., Donahue M., 2010, *ApJ*, 719, 1844
- Hu E. M., 1992, *ApJ*, 391, 608
- Irwin J. A., Stil J. M., Bridges T. J., 2001, *MNRAS*, 328, 359
- Jaffe W., Bremer M.N., 1997, *MNRAS*, 284, 1
- Jaffe W., Bremer M.N., van der Werf P.P., 2001, *MNRAS*, 324, 443
- Jaffe W., Bremer M.N., Baker K., 2005, *MNRAS*, 360, 748
- Johnstone R. M., Fabian A. C., 1988, *MNRAS*, 233, 581
- Johnstone R. M., Hatch N. A., Ferland G. J., Fabian A. C., Crawford C. S., Wilman R. J., 2007, *MNRAS*, 382, 1246
- Koekemoer A. M., O’Dea C. P., Sarazin C. L., McNamara B. R., Donahue M., Voit G. M., Baum S. A., Gallimore J. F., 1999, *ApJ*, 525, 621
- Kurucz R. L., 1993, *VizieR On-line Data Catalog: VI/39* (Originally published in: 1979, *ApJS*, 40, 1)
- Mack J., Gilliland R., van der Marel R., Bohlin R., 2005, *Instrument Science Report ACS 2005-13*, The Association of Universities for Research in astronomy
- McNamara B. R., O’Connell R. W., 1992, *ApJ*, 393, 579
- McNamara B. R., O’Connell R. W., 1993, *AJ*, 105, 417
- McNamara B. R., Jannuzi B. T., Sarazin C. L., Elston R., Wise M., 1999, *ApJ*, 518, 167
- McNamara B. R., Wise M. W., Nulsen P. E. J., David L. P., Carilli C. L., Sarazin C. L., O’Dea C. P., Houck J., Donahue M., Baum S., Voit M., O’Connell R. W., Koekemoer A., 2001, *ApJ*, 562, 149
- Nagao T., Murayama T., Taniguchi Y., 2001, *ApJ*, 546, 744

- O'Dea C. P., Baum S. A., Gallimore J. F., 1994, *ApJ*, 436, 669
- O'Dea C. P., Baum S. A., Mack J., Koekemoer A. M., Laor A., 2004, *ApJ*, 612, 131
- O'Dea C. P., Baum S. A., Privon G., Noel-Storr J., Quillen A. C., Zufelt N., Park, J., Edge A., Russell H., Fabian A. C., Donahue M., Sarazin C. L., McNamara B., Bregman J. N., Egami E., 2008, *ApJ*, 681, 1035
- O'Dea K. P., Quillen A. C., O'Dea C. P., Tremblay G. R., Snios B. T., Baum S. A., Christiansen K., Noel-Storr J., Edge A. C., Donahue M., Voit G. M., 2010, *ApJ*, 719, 1619
- Onk J. B. R., Jaffe W., Bremer M. N., Hatch N., 2010, *IAUS*, 267, 463
- Onk J. B. R., Jaffe W., Bremer M. N., van Weeren R. J., 2010, *MNRAS*, 405, 898
- Osterbrock D. E., Ferland G. J., 2006, *Astrophysics of Gaseous Nebulae and Active Galactic Nuclei*, University Science Books.
- Peres C. B., Fabian A. C., Edge A. C., Allen S. W., Johnstone R. M., White D. A., 1998, *MNRAS*, 298, 416
- Perley, R. T., Taylor, G. B. 1999, *VLA Calibrator Manual*, Tech. Rep., NRAO
- Peterson J. R., Fabian A. C., 2006, *PhR*, 427, 1
- Pimblet K. A., Smail I., Edge A. C., O'Hely E., Couch W. J., Zabludoff A. I., 2006, *MNRAS* 366, 645
- Pipino A., Kaviraj S., Bildfell C., Babul A., Hoekstra H., Silk J., 2009, *MNRAS* 395, 462
- Salome P., Combes F., 2003, *A&A*, 412, 657
- Sanders J. S., Fabian A. C., Taylor G. B., 2009, *MNRAS*, 393, 71
- Sarazin C. L., Burns J. O., Roettiger K., McNamara B., 1995, *ApJ*, 447, 559
- Schlegel D. J., Finkbeiner D. P., Davis M., 1998, *ApJ*, 500, 525
- Seaton M. J., 1979, *MNRAS*, 187, 73
- Sparks W. B., Pringle J. E., Donahue M., Carswell R., Voit M., Cracraft M., Martin R. G., 2009, *ApJ*, 704, 20
- Taylor G. B., O'Dea C. P., Peck A. B., Koekemoer A. M., 1999, *ApJ*, 512, 27
- Tremonti C., Ph.D. thesis, 2003, John Hopkins University.
- Vacca W. D., Garmany C. D., Shull J. M., 1996, *ApJ*, 460, 914
- Voit G. M., Donahue M., 1997, *ApJ*, 486, 242
- Wilman R. J., Edge A. C., Johnstone R. M., Fabian A. C., Allen S. W., Crawford C. S., 2002, *MNRAS*, 337, 63
- Wilman R. J., Edge A. C., Swinbank A. M., 2006, *MNRAS*, 359, 93
- Wilman R. J., Edge A. C., Swinbank A. M., 2009, *MNRAS*, 395, 1355

Date	Filter	Exptime	Zeropoint
2008-07-21	F150LP	8141	22.4484
2008-06-23	F150LP	5419 ^a	22.4484
2002-06-16	U_Bessel	1320	23.4824±0.0530
2002-06-16	B_Bessel	1080	26.4815±0.0503
2001-07-26	V_Bessel	330	27.2367±0.0129
2001-07-26	R_Bessel	330	27.2484±0.0185
2001-07-26	I_Bessel	330	26.4829±0.0133

Table 3.1 — A2597 observations log. Column 1 lists the date of the observation in YYYY-MM-DD. Column 2 lists the filter name. Column 3 lists the exposure time in units of seconds. Column 4 lists the FORS Bessel system zeropoint in units of magnitudes. The zeropoint is based upon the average of at least 3 Landolt standard stars within each observation. The uncertainty in the zeropoint is taken as the maximum deviation of these standard stars have with respect to the quoted average zeropoint. The SBC F150LP zeropoint is taken from the ACS handbook and given in AB magnitudes. The photometric uncertainty according to the most recent investigation is 2% for the F150LP filter (Mack et al. 2005). All observations listed here were taken in photometric observing conditions.

^a this data set is affected by low level background glow and has been dropped from further analysis.)

Date	Filter	Exptime	Zeropoint
2008-04-30	F150LP	8126	22.4484
2008-04-22	F150LP	5409	22.4484
2002-06-10	U_Bessel	1440	23.5860±0.0197
2002-06-10	B_Bessel	780	26.5420±0.0627
2002-06-10	R_Bessel	400	27.1567±0.0329
2001-04-19	V_Bessel	330	27.2315±0.0158
2001-04-19	R_Bessel	330	27.2503±0.0218
2001-04-19	I_Bessel	330	26.5046±0.0087

Table 3.2 — A2204 observations log. The column headers are the same as in Table 3.1.

Filter	(FORS_AB) _{conv}
U_Bessel	0.931
B_Bessel	-0.042
V_Bessel	0.060
R_Bessel	0.258
I_Bessel	0.458

Table 3.3 — FORS Bessel to AB magnitude conversion factors. Column 1 lists the filter name. Column 2 lists the FORS Bessel to AB conversion factor in units of magnitude. It converts the FORS Bessel magnitudes to AB magnitudes. This conversion factor is calculated for FORS Bessel filter curves with the HYPERZ program (Bolzonella et al. 2000, ; priv. comm. H. Hildebrandt)

Name	U_Bessel	B_Bessel	V_Bessel	R_Bessel	I_Bessel
A2597	-	0.185	0.050	>0.101	>0.034
A2204	-	0.253	0.067	>0.115	>0.239

Table 3.4 — Line contamination of the FORS Bessel images. Column 1 list the target name. Columns 2-6 list the fraction of the total emission in the filter which is due to line emission. This line contamination fraction is calculated using the FORS spectra described in Section 3.2.2. None of the spectral lines probed by our spectra fall in the U filter, see also Fig. 3.11. The spectra do not probe the SII lines at 6716 Å and 6731 Å and thus we can only provide a lower limit to the line contamination fraction of the R and I Bessel filters.

Name	$A_{V,MW}$	$A_{V,BCG}$	$H\delta/H\beta$	$H\gamma/H\beta$	$H\alpha/H\beta$
A2597	0.1	1.3	0.18 (0.19)	0.37 (0.40)	4.52 (4.52)
A2204	0.3	1.6	0.16 (0.15)	0.34 (0.38)	5.27 (5.29)

Table 3.5 — Visual extinction A_V and Balmer decrements. Column 1 lists the target name. Column 2 lists the extinction in the V-band for the MW foreground to (Schlegel et al. 1998). Column 3 lists the extinction in the V-band intrinsic to the BCG. This value is calculated by decomposing the Balmer decrements observed in the FORS spectra (Section 3.2.2) into two dust components, one related to the BCG and one related to the MW foreground. Describing both components by the C89 extinction law allows us to derive $A_{V,BCG}$. The intrinsic dust-free Balmer decrements were set to their stellar case B recombination values i.e. $H\delta/H\beta=0.26$, $H\gamma/H\beta=0.47$ and $H\alpha/H\beta=2.87$ (Osterbrock & Ferland 2006). Columns 4, 5 and 6 list the reddened Balmer decrement values obtained from this two component dust analysis for $A_{V,MW}$ and $A_{V,BCG}$ given in columns 2 and 3. The Balmer decrements calculated in this manner agree well with the measured decrements from our FORS spectra. The latter are given in the parentheses in columns 4, 5 and 6.

Name	$FUV_{v,tot}/U_{v,tot}$	$FUV_{v,tot}/V_{v,tot}$	$FUV_{v,tot}/R_{v,tot}$	$FUV_{v,tot}/I_{v,tot}$
A2597-OFF	0.1564	0.0153	0.0102	0.0068
A2204-SW	0.1526	0.0105	0.0066	0.0043

Table 3.6 — FUV flux ratios for old star regions. Column 1 gives the name of the region, see Section 3.5.2. Columns 2-5 lists the flux ratios. The subscript *tot* refers to the total flux observed in this region.

Name	$U_{v,tot}/V_{v,tot}$	$U_{v,tot}/R_{v,tot}$	$U_{v,tot}/I_{v,tot}$
A2597-OFF	0.0988	0.0654	0.0439
A2597-COMP	0.0969	0.0664	0.0470
A2204 SW	0.0706	0.0437	0.0281
A2204-COMP	0.0710	0.0452	0.0297

Table 3.7 — U flux ratios for old star regions. The column headers are the same as in Table 3.6.

Name	$F(FUV)_{v,tot}$	$F(FUV)_{v,exc}$	$F(FUV)_{v,NC}$	$F(U)_{v,tot}$	$F(U)_{v,exc}$	$F(U)_{v,NC}$	$F(H\alpha)_v$
A2597	12.04	9.60	0.57	21.20	3.60	1.36	41.5
A2204	6.16	5.20	0.67	10.50	4.00	1.57	48.5

Table 3.8 — FUV, U and $H\alpha$ fluxes. These fluxes are integrated over 18 kpc radial apertures centered on the BCG and given in units 10^{-28} erg s^{-1} cm^{-2} Hz^{-1} . Columns 1-3 give the FUV F150LP fluxes. Columns 4-6 give the U_Bessel fluxes. The subscripts *tot*, *exc* and *NC* correspond respectively to the total flux, the excess flux and the flux expected from the nebular continuum. The latter is calculated using the NEBCONT program (Howarth et al. 2004), see also Section 3.5.4. Column 7 gives the $H\alpha$ flux in units 10^{-15} erg s^{-1} cm^{-2} (Jaffe et al. 2005).

name	z	$FUV_{v,tot}/NUV_{v,tot}$	T_{K93}
A85	0.0557	0.60	10656
A1204	0.1706	1.12	23226
A2029	0.0779	0.61	10973
A2052	0.0345	0.54	10000
A2142	0.0904	0.63	11273
A2597	0.0830	0.85	13771
A3112	0.0761	0.74	11858
HercA	0.1540	0.73	14069
HydrA	0.0549	0.77	11876
MKW3s	0.0453	0.67	11083
MKW4	0.0196	0.67	10870
MS0839	0.1980	0.90	17951
MS1358	0.3272	0.91	20747
MS1455	0.2578	1.13	26313
RX1347	0.4500	0.76	21622
Zw3146	0.2906	1.33	37883

Table 3.9 — Hicks et al. (2010) GALEX BCG sample. Column 1 lists the cluster name for the BCG observed. Column 2 lists the redshift as given in Hicks et al. (2010). Column 3 lists the $FUV_{v,tot}/NUV_{v,tot}$ ratio corresponding to the observed 7 arcsec radial apertures and have been corrected for foreground MW extinction only. Column 4 lists the K93 stellar temperatures corresponding to the flux ratio given in column 3. The $z > 0.1$ BCGs are potentially affected by $Ly\alpha$ emission, see also Section 3.8.2.

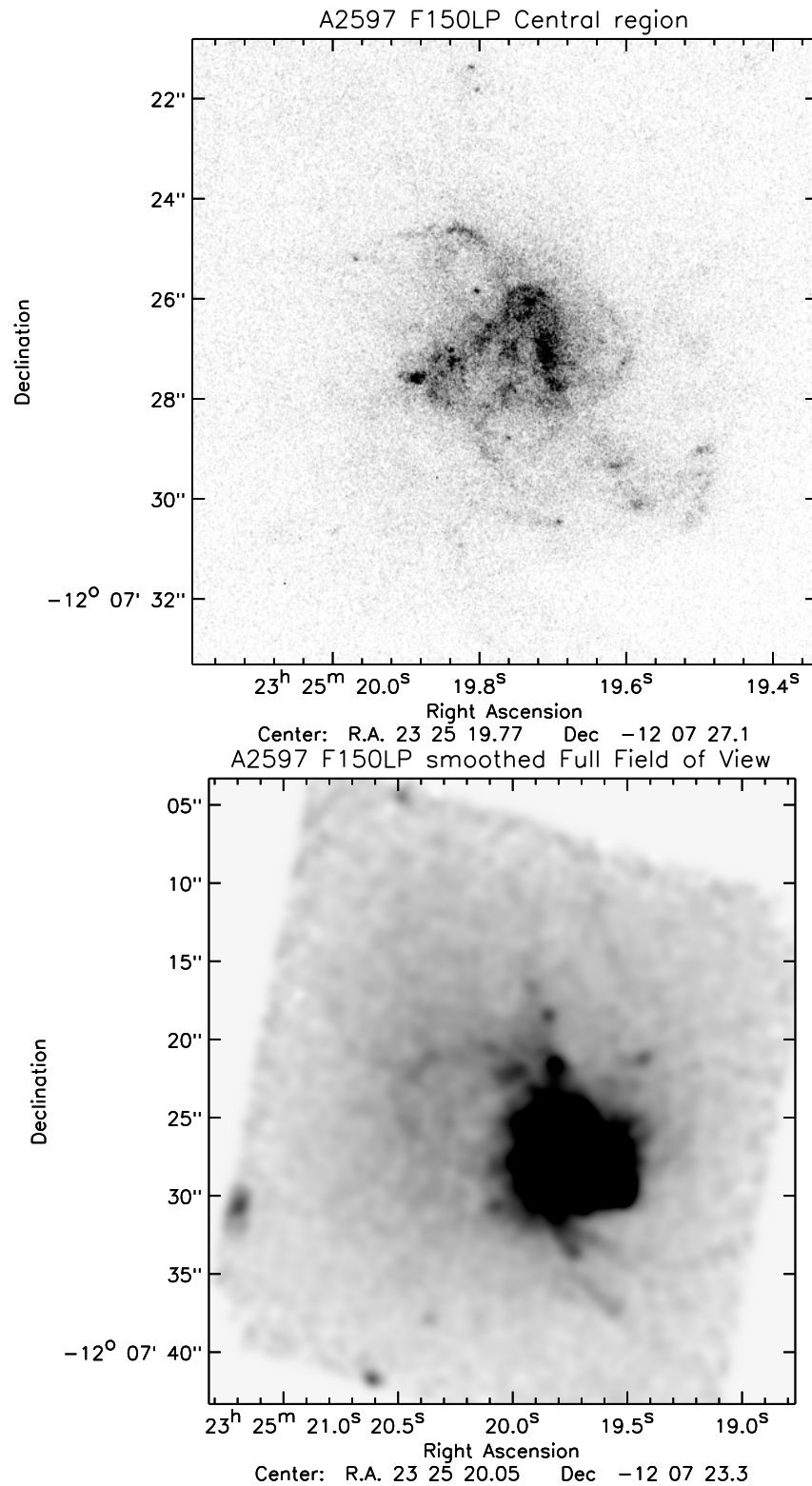


Figure 3.1 — ABELL 2597 FUV F150LP emission. (*Top*) Central bright FUV continuum emission at the intrinsic resolution of HST. (*Bottom*) FUV continuum emission convolved to an output spatial resolution of 1 arcsec FWHM and scaled to enhance the low surface brightness structures. The BCG nucleus is at $(\alpha; \delta) = (23\ 25\ 19.719; -12\ 07\ 26.83)$ (J2000).

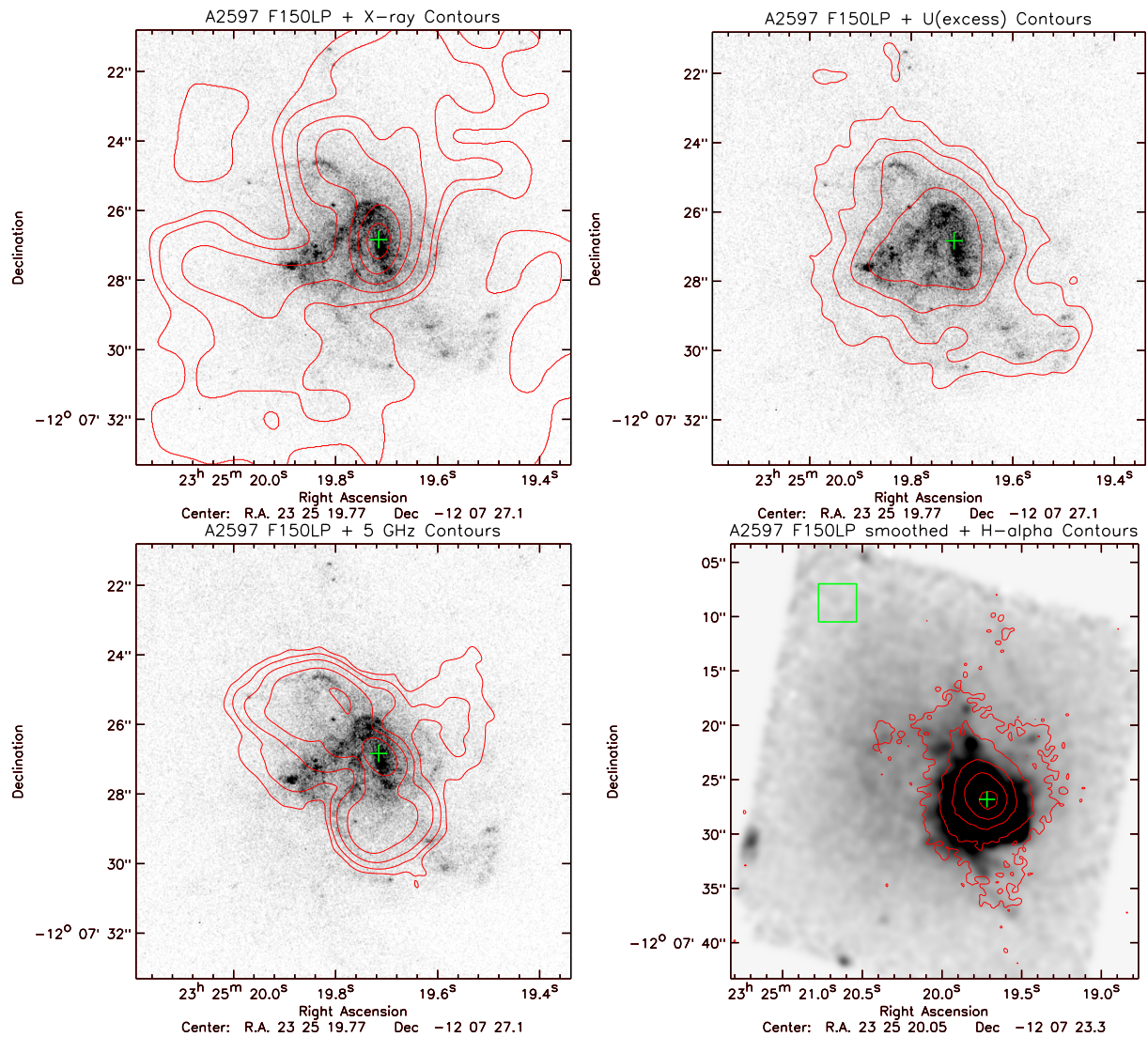


Figure 3.2 — ABELL 2597 FUV F150LP overlays. (*Top-Left*) CHANDRA X-ray contours on top of the FUV emission. (*Top-Right*) FORS U band excess contours on top of FUV emission. (*Bottom-Left*) VLA 5 GHz contours at $[1,4,16,64,256] \times 10^{-4}$ Jy/beam on top of the FUV emission. (*Bottom-Right*) H α contours from Jaffe et al. (2005) on top of the convolved FUV emission. The BCG nucleus is indicated by the cross. The region used for background subtraction is indicated by the rectangle.

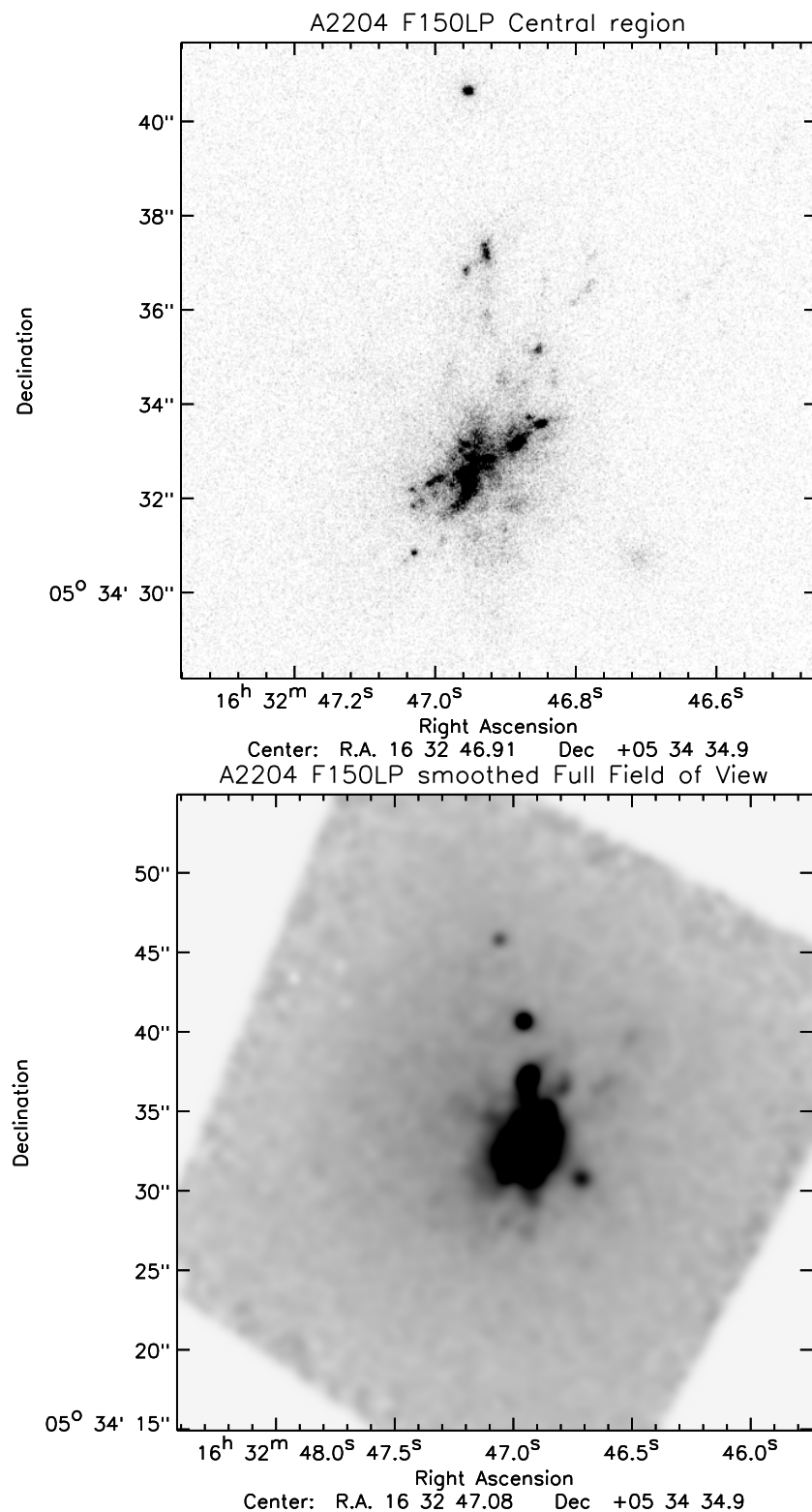


Figure 3.3 — ABELL 2204 FUV F150LP emission. (*Top*) Central bright FUV continuum emission at the intrinsic resolution of HST. (*Bottom*) FUV continuum emission convolved to an output spatial resolution of 1 arcsec FWHM and scaled to enhance the low surface brightness structures. The BCG nucleus is at $(\alpha; \delta) = (16\ 32\ 46.938 ; +05\ 34\ 32.81)$ (J2000).

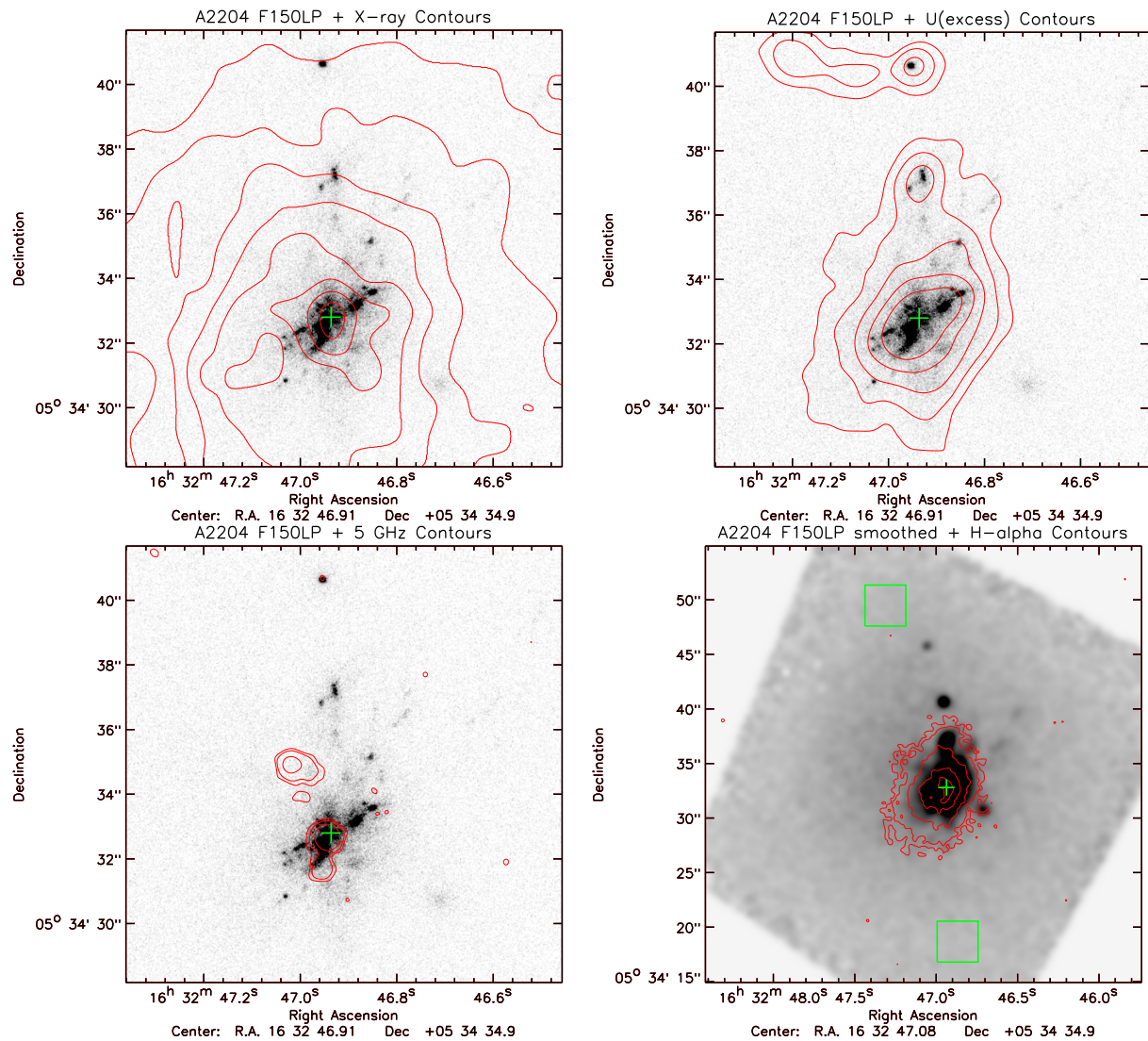


Figure 3.4 — ABELL 2204 FUV F150LP overlays. (*Top-Left*) CHANDRA X-ray contours on top of the FUV emission. (*Top-Right*) FORS U band excess contours on top of FUV emission. (*Bottom-Left*) VLA 5 GHz contours at $[2,4,16,256] \times 10^{-4}$ Jy/beam on top of the FUV emission. (*Bottom-Right*) H α contours from Jaffe et al. (2005) on top of the convolved FUV emission. The BCG nucleus is indicated by the cross. The regions used for background subtraction are indicated by the rectangles. The lensed galaxy north-east of the BCG (e.g. Wilman et al. 2006) is visible in the U-band but not in the FUV band.

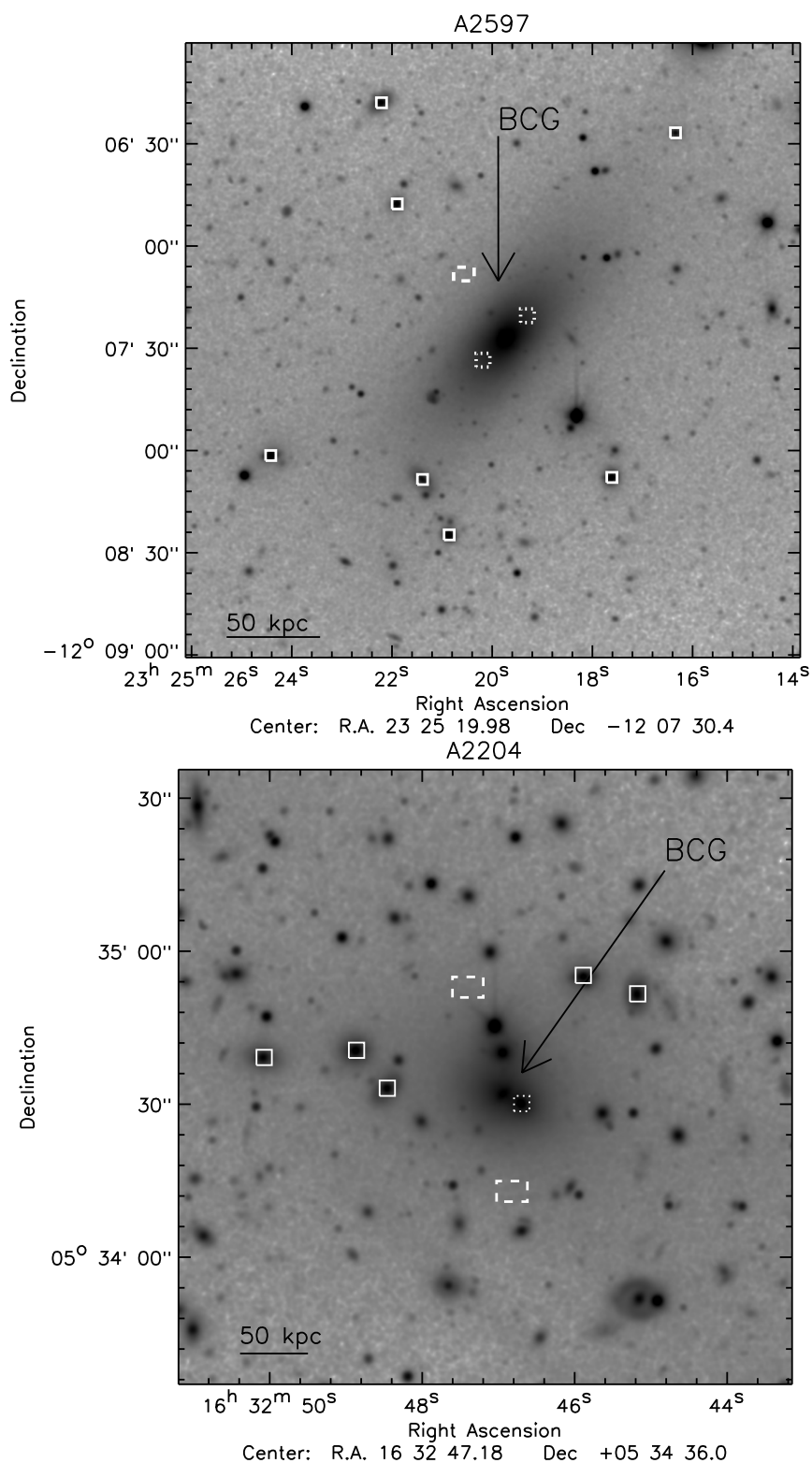


Figure 3.5 — FORS V band images (the UVR 3-color images can be found in the online version). ABELL 2597 (*Top*) and ABELL 2204 (*Bottom*). The dotted squares indicate the old star regions where we estimated the FUV/V and U/V ratios. The solid squares indicate the nearby cluster ellipticals that were used as comparison sample for the U/V ratios determined in the blue squares. The dashed squares show regions used for determining the background in the FUV and optical images. The many distorted galaxies in the A2204 image show that this cluster is a strongly lensing system.

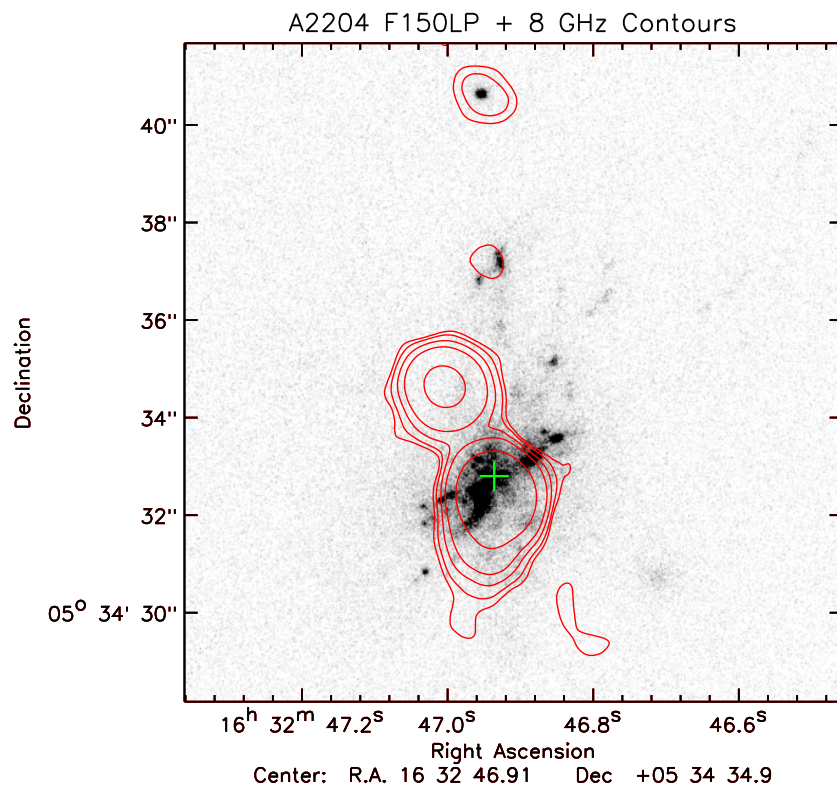


Figure 3.6 — A2204 VLA 8 GHz radio continuum emission. Radio contours are given at $[0.6, 1, 2, 4, 16, 256] \times 10^{-4}$ Jy/beam on top of FUV emission. The one sigma map noise is 0.2×10^{-4} Jy/beam. This dataset is significantly deeper than the 5 GHz data presented in Fig. 3.4.

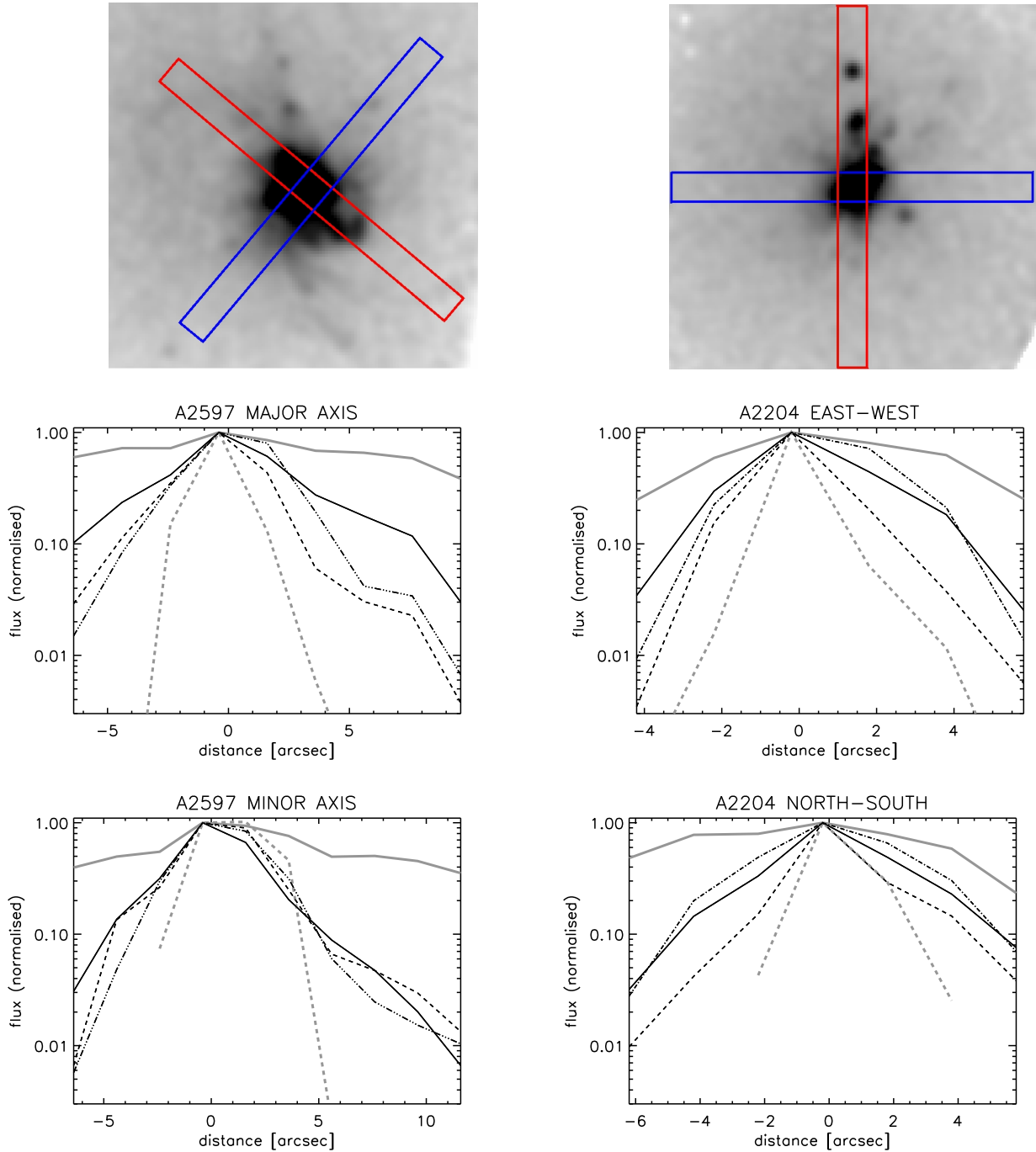


Figure 3.7 — Surface brightness profiles for A2597 (*Left*) and A2204 (*Right*). (*Top-Left*) Position of pseudo slits on A2597. The image is 25 arcsec on a side and the slits drawn are 25 arcsec long and 2 arcsec wide (north is up and east is to the left). (*Top-Right*) Position of pseudo slits on A2204. The image and slit sizes are the same as for A2597. The surface brightness profiles are determined along drawn pseudo slits in 2 arcsec steps along these slits. The solid black line is FORS V band emission. The dashed black line is the background subtracted F150LP FUV emission. The black dot-dash line is $H\alpha$ emission from Jaffe et al. (2005). The thick grey solid line is CHANDRA X-ray emission and the thick grey dashed line is VLA 5 GHz radio emission. (*Middle-Left*) A2597 pseudo slit along the major axis of the BCG (SE-NW slit). Positive distances are north-west of the BCG nucleus. (*Middle-Right*) A2204 pseudo slit along an axis running east-west through the BCG (EW slit). Positive distances are east of the BCG nucleus. (*Bottom-Left*) A2597 pseudo slit along the minor axis of the BCG (NE-SW slit). Positive distances are north-east of the BCG nucleus. (*Bottom-Right*) A2204 pseudo slit along an axis running north-south through the BCG (NS slit). Positive distances are north of the BCG nucleus. All profiles have been extracted from images convolved to a common spatial resolution of 1 arcsec FWHM.

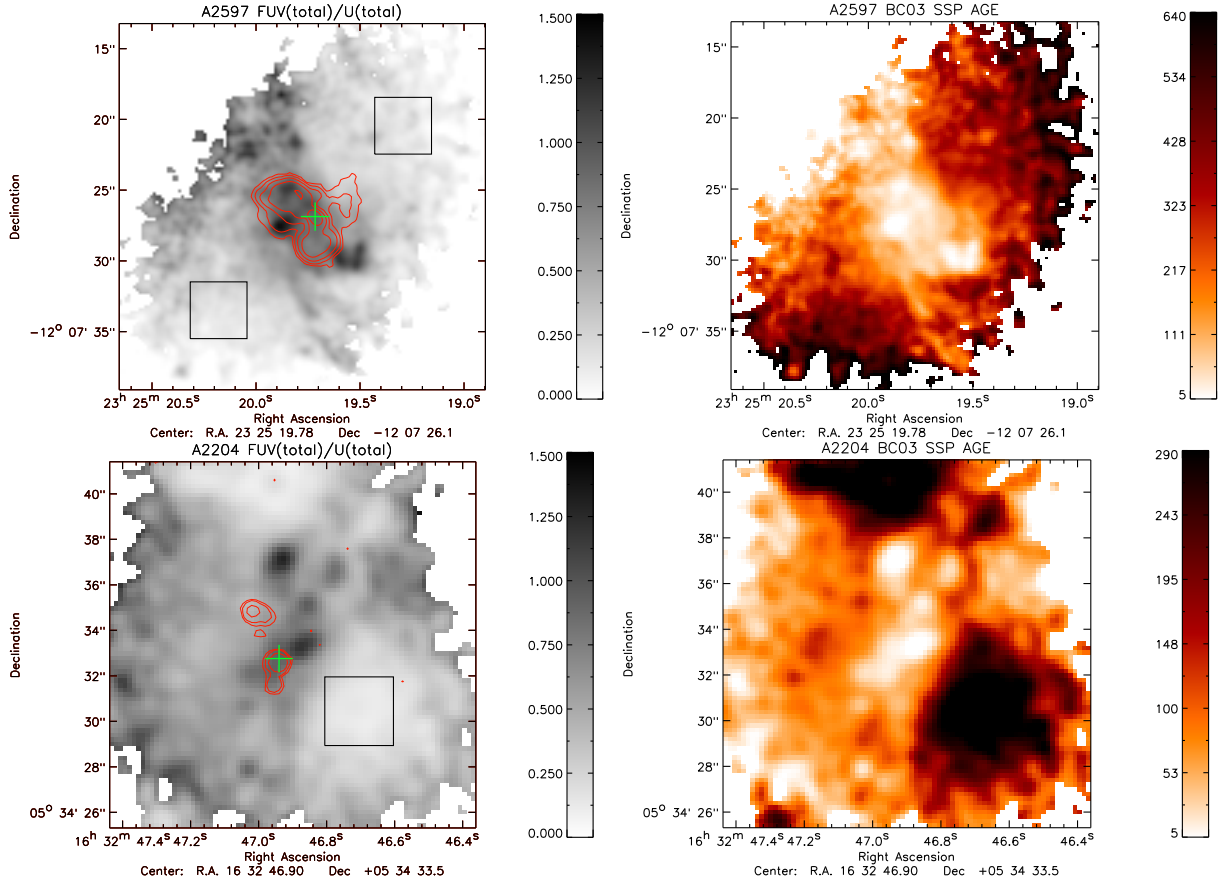


Figure 3.8 — The $FUV_{v,tot}/U_{v,tot}$ ratio and corresponding SSP age for A2597 and A2204. (*Top-Left*) A2597 observed $FUV_{v,tot}/U_{v,tot}$. (*Top-Right*) A2597 SSP age in units of Myr. (*Bottom-Left*) A2204 observed $FUV_{v,tot}/U_{v,tot}$. (*Bottom-Right*) A2204 SSP age in units of Myr. In computing the SSP age we have taken extinction due to the MW foreground only into account, see Fig. 3.9. The SSP age vs $FUV_{v,tot}/U_{v,tot}$ ratio is double valued for ages greater than 640 and 290 Myr in A2597 and A2204 respectively. This is due to the UV upturn for a stellar population older than 1 Gyr. For any flux ratios in the range where the corresponding SSP age is double valued we have set the SSP age to the youngest age possible in this range. The crosses indicate the BCG nuclei. The black squares indicate the regions where the U/V and FUV/V ratios for the old stellar population have been determined. Contours show the 5 GHz radio continuum emission. The contours levels are the same as in Figs. 3.2 and 3.4.

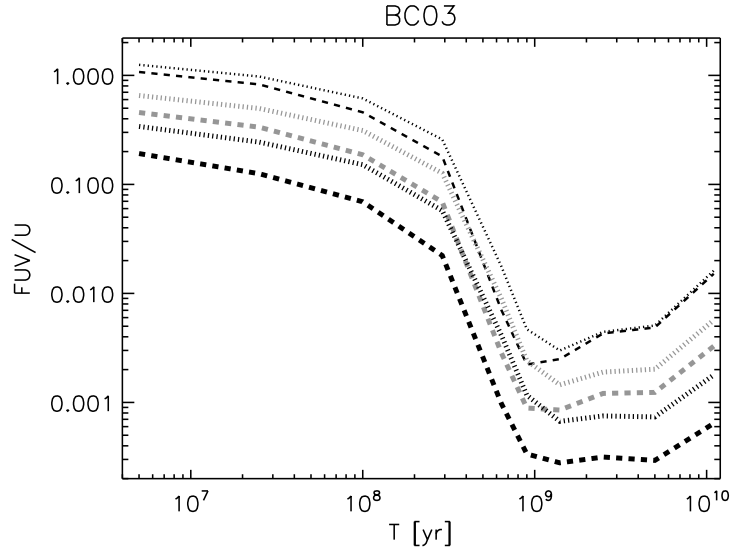


Figure 3.9 — The FUV_v/U_v ratio as a function of SSP age for Bruzual & Charlot (2003) SSP models. Curves are shown for two redshifts and three different amounts of extinction. The dotted and dashed curves correspond to $z=0.0821$ (A2597) and $z=0.1517$ (A2204) respectively. The thin black curves correspond to MW foreground extinction only. The thick black curves assume that all of the extinction intrinsic to the BCG is in front of the FUV and U emitting regions. The thick grey curves assume that only half of the extinction intrinsic to the BCG is in front of the FUV and U emitting regions. Dust extinction has been computed using the C89 extinction law for both the MW and the BCG component. The model ratios are computed for the HST-ACS/SBC F150LP and VLT-FORS U_Bessel filters.

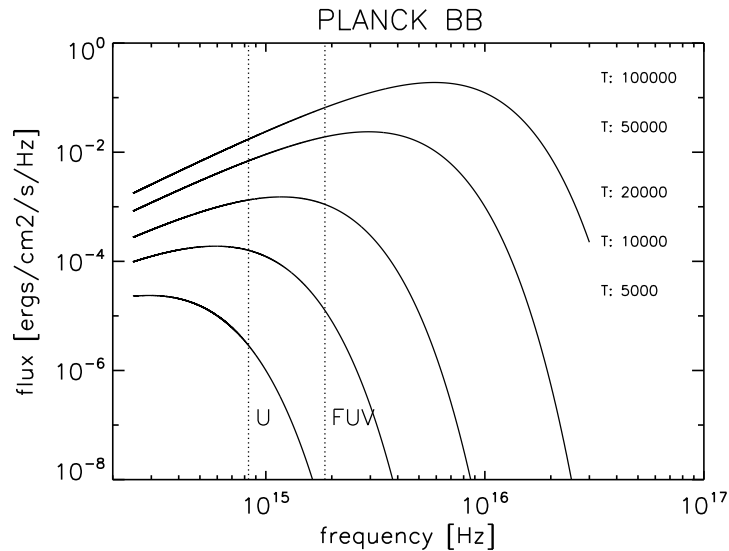


Figure 3.10 — Blackbody (BB) models in the FUV - Optical regime. The dashed lines show the peak transmission wavelengths of the U (U_Bessel) and FUV (F150LP) filters. This image illustrates how the FUV flux changes relative to the U flux as we increase the temperature for a BB model. The fast change in their relative ratio as a function of temperature shows that it is a good discriminator of temperature. We note that the K93 stellar models as function of stellar temperature qualitatively show the same behaviour in the FUV to optical regime as the BB models. The FUV to U band ratio is thus a good discriminator for these models too.

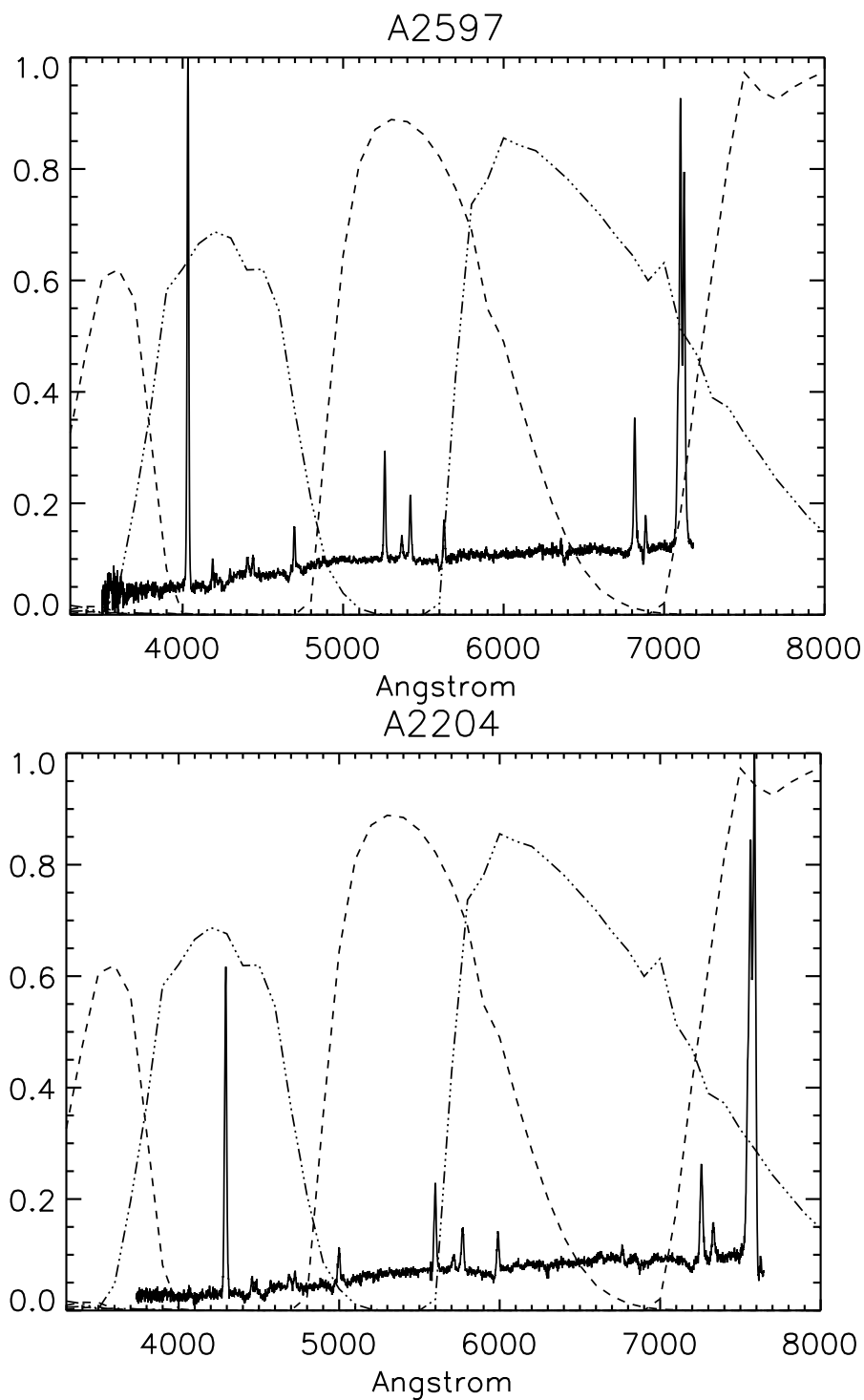


Figure 3.11 — Line Contamination of the FORS U, B, V, R and I Bessel filters. (*Top*) Spatially integrated ($16 \times 2 \text{ arcsec}^2$) spectrum of A2597. (*Bottom*) Spatially integrated ($12.5 \times 2 \text{ arcsec}^2$) spectrum of A2204. Both spectra are centred on their respective BCG nucleus. The dashed and dot-dash curves show the shape of FORS U, B, V, R and I Bessel filters.

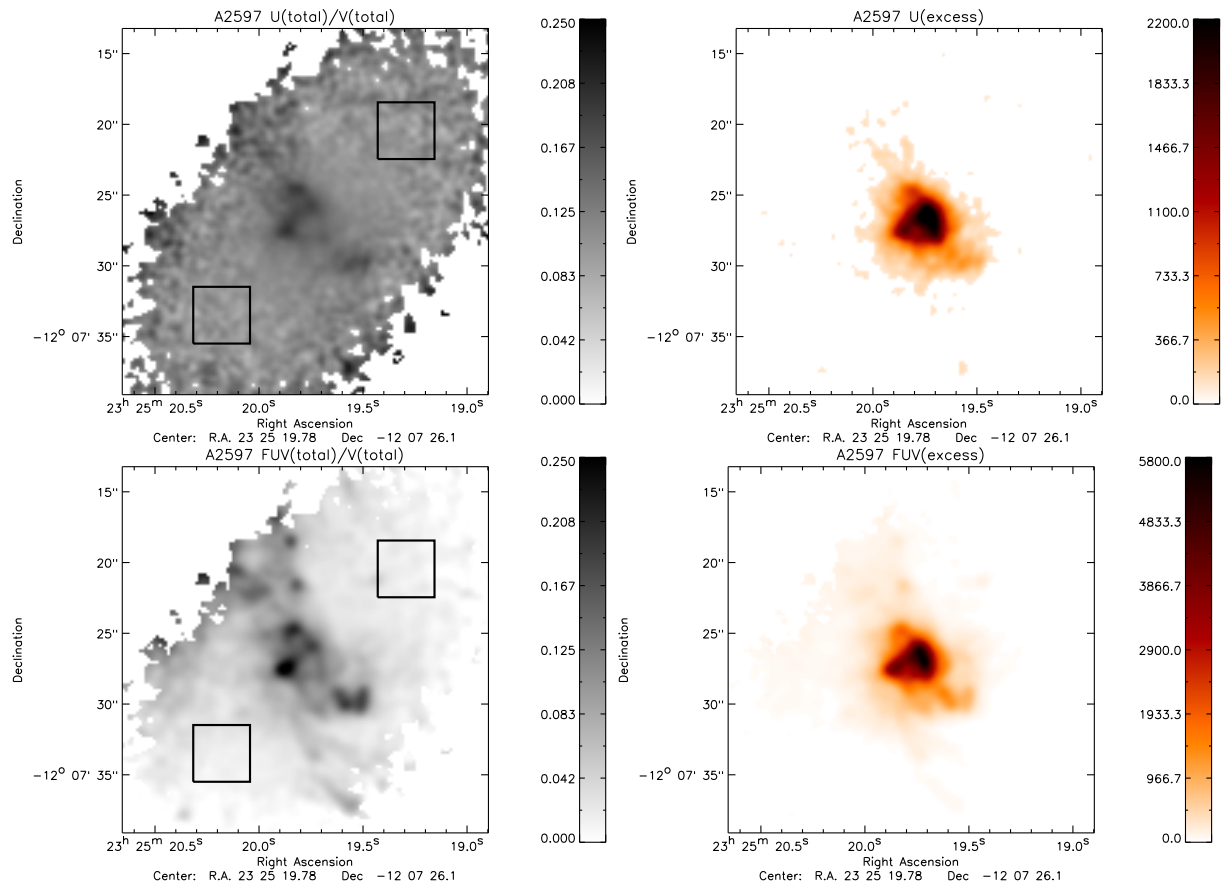


Figure 3.12 — Excess emission in A2597. (*Top-Left*) $U_{v,tot}/V_{v,tot}$ ratio. (*Top-Right*) Excess $U_{v,exc}$ band emission after removal of the old stellar population. (*Bottom-Left*) $FUV_{v,tot}/V_{v,tot}$ ratio. (*Bottom-Right*) Excess $FUV_{v,exc}$ emission after removal of the old stellar population. These images have been corrected for background emission and line contamination. The black squares indicate the regions where the $U_{v,tot}/V_{v,tot}$ and $FUV_{v,tot}/V_{v,tot}$ ratios for the old stellar population have been determined.

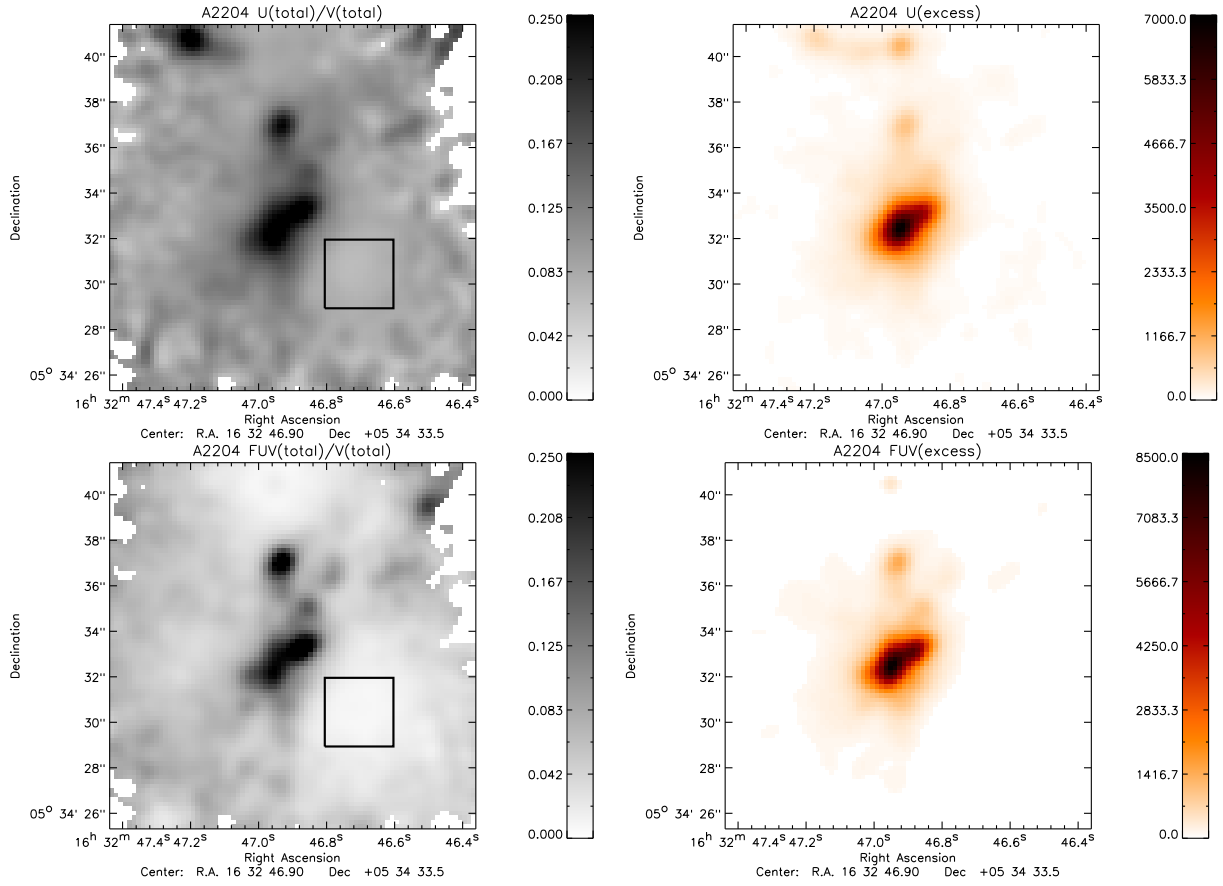


Figure 3.13 — Excess emission in A2204: (*Top-Left*) $U_{v,tot}/V_{v,tot}$ ratio. (*Top-Right*) Excess $U_{v,exc}$ emission after removal of the old stellar population. (*Bottom-Left*) $FUV_{v,tot}/V_{v,tot}$ ratio. (*Bottom-Right*) Excess $FUV_{v,exc}$ emission after removal of the old stellar population. The images have been corrected for background emission and line contamination. The black squares indicate the regions where the $U_{v,tot}/V_{v,tot}$ and $FUV_{v,tot}/V_{v,tot}$ ratios for the old stellar population have been determined.

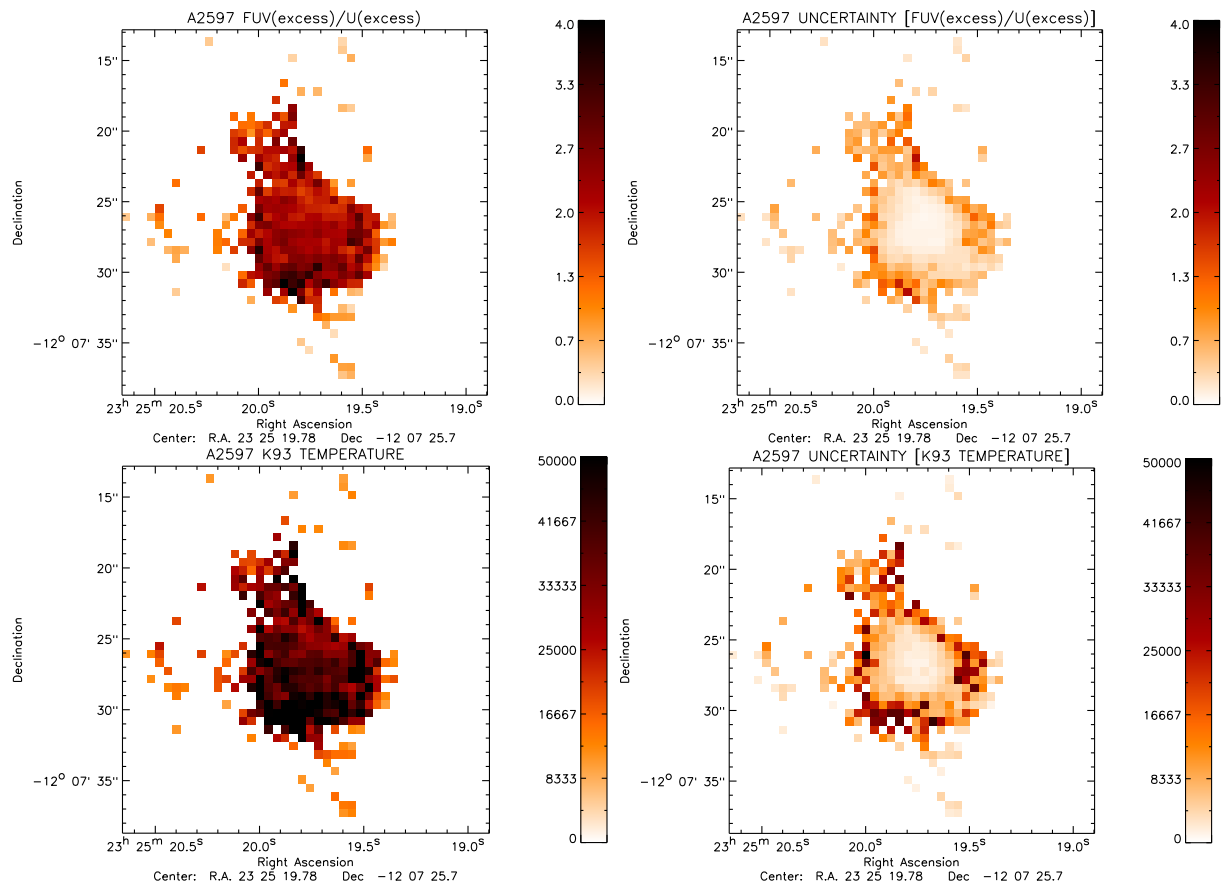


Figure 3.14 — FUV_{v,exc}/U_{v,exc} ratio and K93 stellar temperature maps for A2597. (Top-Left) FUV_{v,exc}/U_{v,exc} ratio. (Top-Right) Uncertainty in the FUV_{v,exc}/U_{v,exc} ratio. (Bottom-Left) K93 stellar temperature corresponding to the FUV_{v,exc}/U_{v,exc} ratio. (Bottom-Right) Uncertainty in K93 derived stellar temperature. Note that in calculating the K93 stellar temperature shown here we have only taken extinction due to the MW foreground into account, see Fig. 3.16. The data shown has been re-binned to 0.6×0.6 arcsec² pixels.

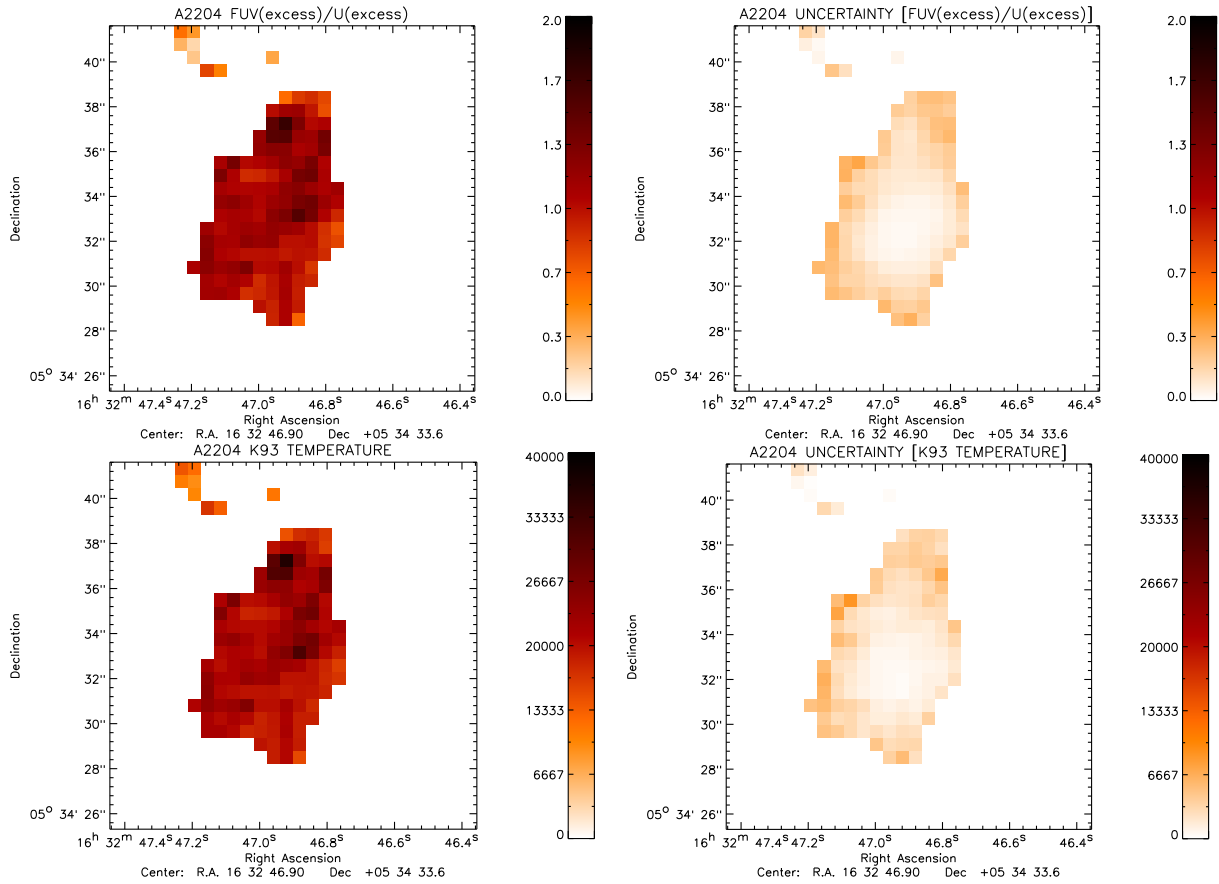


Figure 3.15 — FUV_{v,exc}/U_{v,exc} ratio and K93 stellar temperature maps for A2204. (Top-Left) FUV_{v,exc}/U_{v,exc} ratio. (Top-Right) Uncertainty in the FUV_{v,exc}/U_{v,exc} ratio. (Bottom-Left) K93 stellar temperature corresponding to the FUV_{v,exc}/U_{v,exc} ratio. (Bottom-Right) Uncertainty in K93 derived stellar temperature. Note that in calculating the K93 stellar temperature shown here we have only taken extinction due to the MW foreground into account, see Fig. 3.16. The data shown has been re-binned to 0.6×0.6 arcsec² pixels.

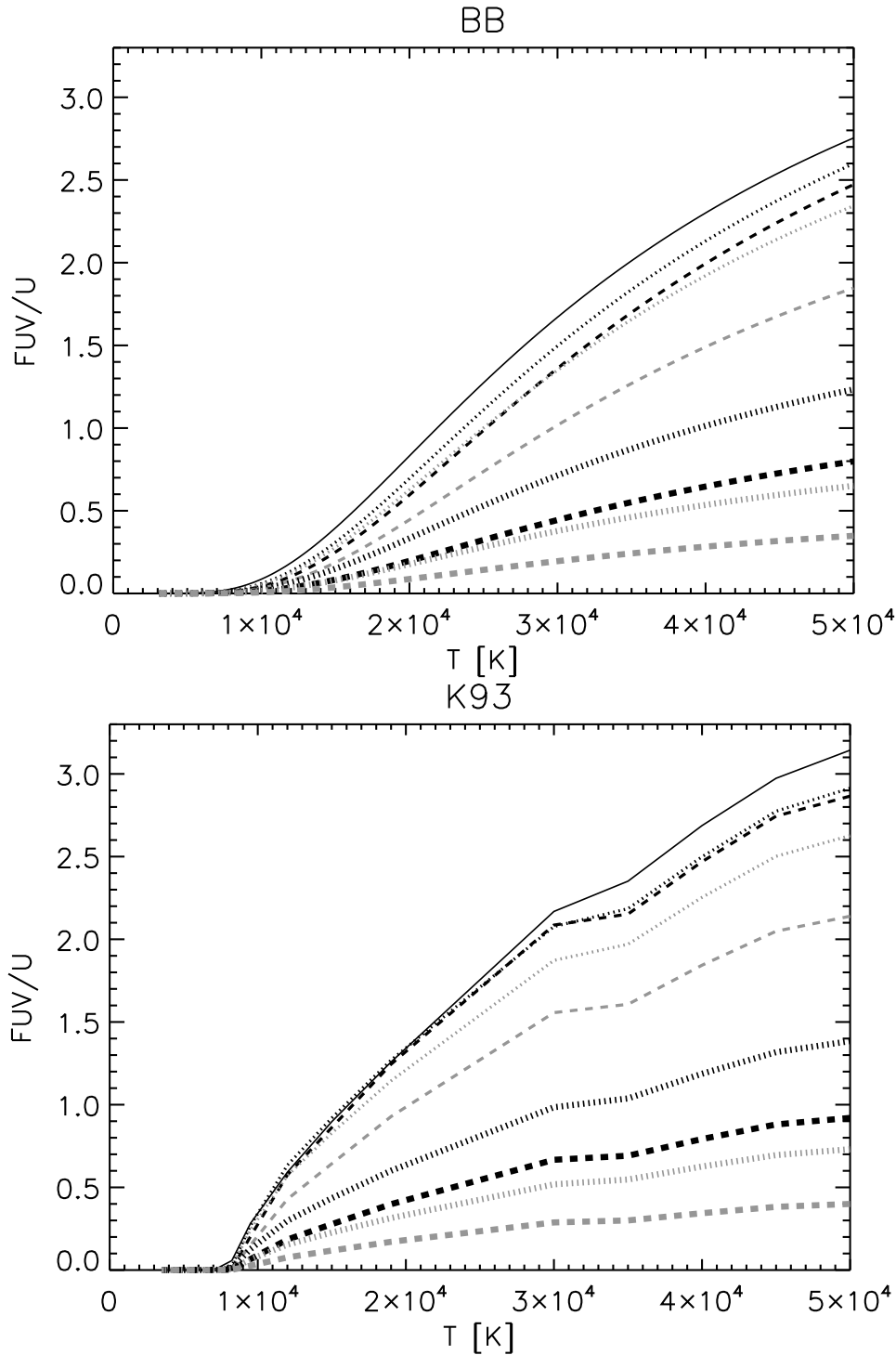


Figure 3.16 — F_{UV_v}/U_v ratio models for A2597 and A2204. Shown are BB models (*top*) and K93 stellar models (*bottom*). Curves are given for three redshifts $z=0$ (solid line), $z=0.0821$ (dotted line) and $z=0.1517$ (dashed line). For the latter two redshifts, corresponding to A2597 and A2204, we computed this flux ratio for varying amounts of extinction. The thin black curves refer to a dust-free environment. The thin grey curves correspond to extinction by the MW foreground only. The thick grey curves assume that all of the extinction intrinsic to the BCG is in front of the FUV and U emitting regions. The thick black curves assume that only half of the extinction intrinsic to the BCG is in front of the FUV and U emitting regions. Dust extinction has been computed using the C89 extinction law for both the MW and the BCG component. The model ratios are computed for the HST-ACS/SBC F150LP and VLT-FORS U_Bessel filters.

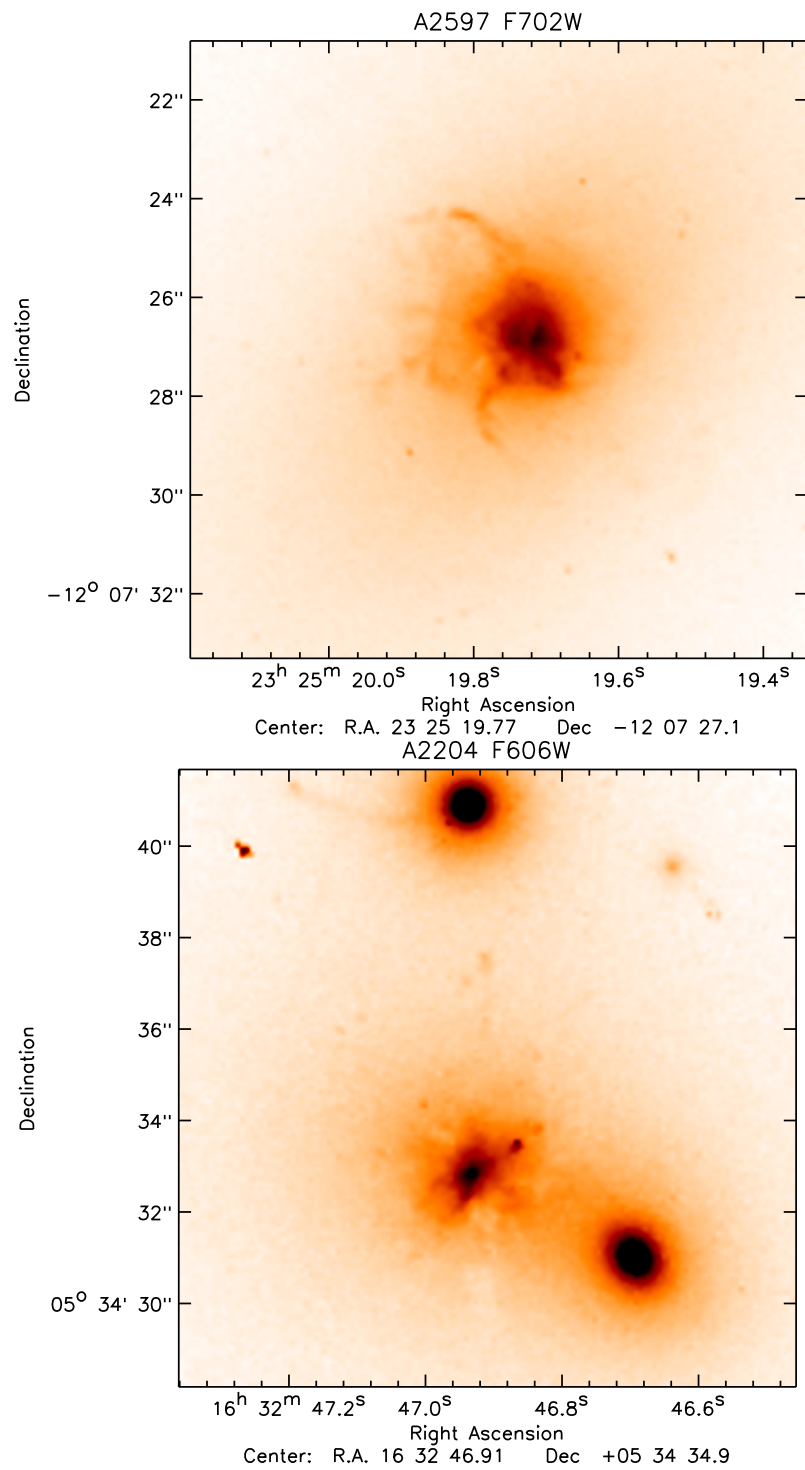


Figure 3.17 — HST optical imaging. A2597 WFPC2 F702W image (*Top*). A2204 WFPC2 F606W image (*Bottom*). These images show that the BCGs have a disturbed morphology indicative of dust obscuration. Contamination by line emission also contributes to observed structures.

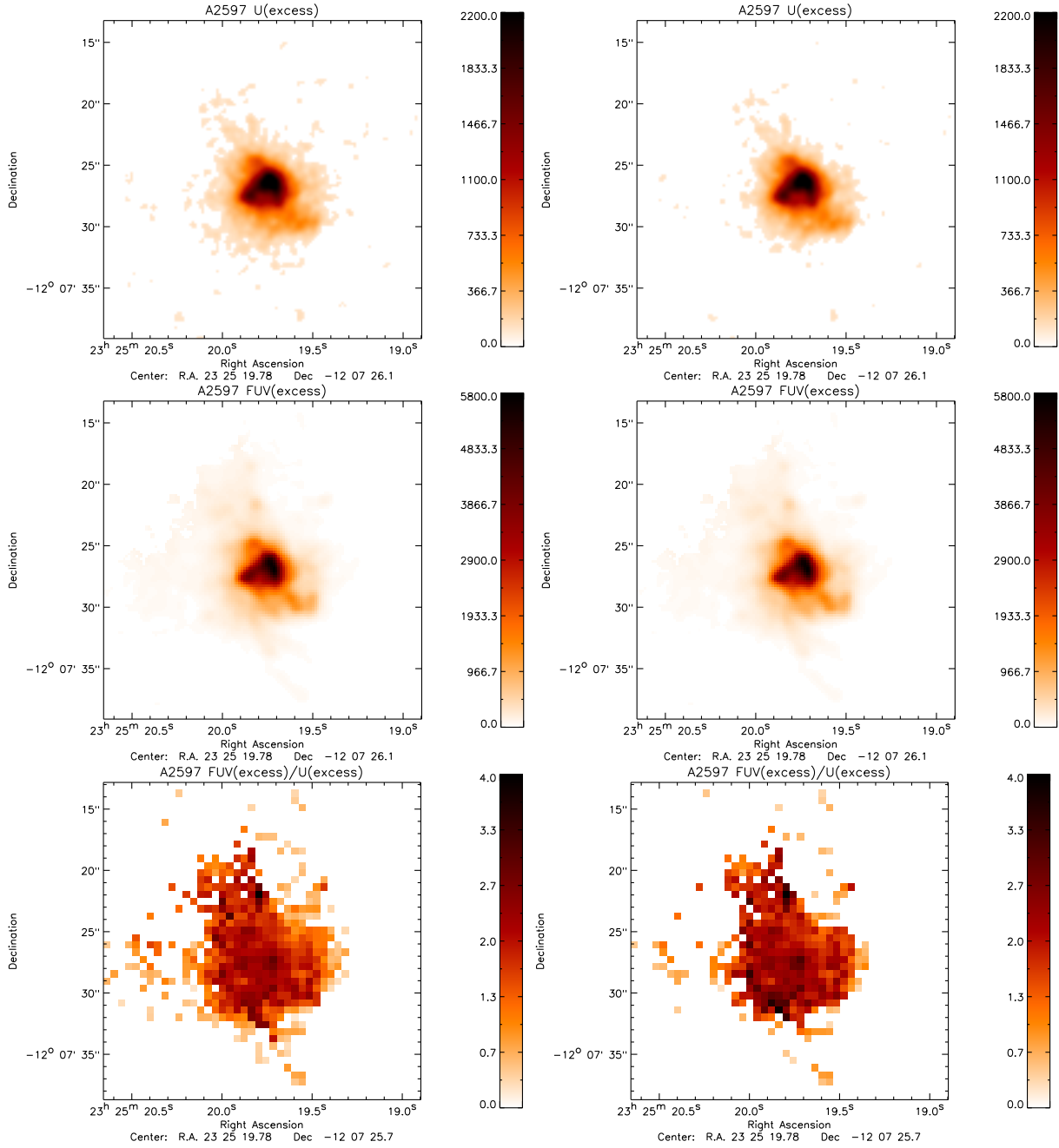


Figure 3.18 — Using the R (*Left*) and I (*Right*) band images to remove the old stellar population in A2597. (*Top-Left*) Excess $U_{v,exc}$ emission when using the R band image to remove emission from old stars. (*Top-Right*) Excess $U_{v,exc}$ emission when using the I band image to remove emission from old stars. (*Middle-Left*) Excess $FUV_{v,exc}$ emission when using the R band image to remove emission from old stars. (*Middle-Right*) Excess $FUV_{v,exc}$ emission when using the I band image to remove emission from old stars. (*Bottom-Left*) $FUV_{v,exc}/U_{v,exc}$ ratio when the R band image is used to remove the old stellar population. (*Bottom-Right*) $FUV_{v,exc}/U_{v,exc}$ ratio when the I band image is used to remove the old stellar population. The bottom images show that the final FUV to U excess ratio does not depend on whether the V, R or I band image is used to remove the old stellar population. This shows that neither of these bands contains a significant contribution by excess emission and that all three are an adequate representation of the old stellar population.

No.	α (J2000)	δ (J2000)	Area	$F_{F150LP,tot}$
0	23:25:19.890	-12:07:18.26	21×21	0.0341735
1	23:25:19.864	-12:07:21.11	21×21	0.0499983
2	23:25:19.781	-12:07:25.81	41×41	1.58047
3	23:25:19.745	-12:07:30.23	21×21	0.0772838
4	23:25:19.637	-12:07:29.88	21×21	0.130110
5	23:25:19.668	-12:07:29.11	21×21	0.147277
6	23:25:19.547	-12:07:28.81	21×21	0.0955810
7	23:25:19.550	-12:07:29.83	21×21	0.0730317
8	23:25:19.762	-12:07:26.73	41×41	1.72703
9	23:25:19.743	-12:07:27.56	41×41	1.20056
10	23:25:19.941	-12:07:27.36	41×41	0.903357
11	23:25:19.885	-12:07:26.93	41×41	1.21367
12	23:25:19.833	-12:07:26.36	41×41	1.39439
13	23:25:19.873	-12:07:24.48	41×41	0.551081
14	23:25:20.021	-12:07:24.93	21×21	0.0503924
15	23:25:19.815	-12:07:27.58	41×41	0.998714
16	23:25:19.656	-12:07:27.06	21×21	0.136095
17	23:25:19.777	-12:07:33.46	15×15	0.0155612
18	23:25:19.842	-12:07:32.58	15×15	0.0138937
19	23:25:19.885	-12:07:30.53	21×21	0.0607091
20	23:25:19.486	-12:07:20.98	15×15	0.0148215
21	23:25:20.050	-12:07:30.41	15×15	0.0139930
22	23:25:19.856	-12:07:25.61	21×21	0.166120
23	23:25:19.552	-12:07:26.68	21×21	0.0585360
24	23:25:19.549	-12:07:25.18	21×21	0.0363437
25	23:25:19.840	-12:07:28.86	21×21	0.146558
26	23:25:19.854	-12:07:21.58	21×21	0.0433445

Table 10 — A2597 FUV continuum knots as measured in the ACS/SBC F150LP filter. Column 1 lists the knot number, see Fig. 19. Column 2 lists the right ascension coordinate. Column 3 lists the declination coordinate. Column 4 lists the aperture used in units of pixels (one pixel has a length of 0.025 arcsec). Column 5 lists the flux integrated over the aperture in units $\text{elec } s^{-1}$.

B.1 A2597, A2204 FUV continuum knots.

The FUV emission in A2597 and A2204 is observed to consist of two components, a filamentary component and a more diffuse component. To estimate the contribution to the total FUV flux from each component we assign pixels belonging to the filamentary component as those pixels having values at least twice the mean flux calculated within a 5 arcsec aperture centered on the BCG. We find that the filamentary component contributes about half of the total FUV flux in our objects. This agrees with the FUV observations by O’Dea et al. (2010) for a sample of BCGs.

Below we have identified knots within the filamentary component. These knots have been selected by eye and are required to have a mean flux per pixel within the specified aperture of at least twice the root-mean-square (RMS) background level.

No.	α (J2000)	δ (J2000)	Area	$F_{F150LP,tot}$
0 ^a	16:32:47.076	+05:34:45.97	21×21	0.0488258
1 ^b	16:32:46.973	+05:34:40.87	21×21	0.1734531
2	16:32:46.801	+05:34:36.72	21×21	0.0399950
3	16:32:46.948	+05:34:37.42	21×21	0.209281
4	16:32:46.977	+05:34:37.05	21×21	0.0986732
5	16:32:46.873	+05:34:35.35	21×21	0.116265
6	16:32:46.945	+05:34:36.07	21×21	0.0687493
7 ^c	16:32:46.731	+05:34:30.95	21×21	0.0598593
8	16:32:47.049	+05:34:31.10	21×21	0.0863461
9	16:32:47.044	+05:34:32.05	21×21	0.172684
10	16:32:47.020	+05:34:32.55	21×21	0.337899
11	16:32:46.977	+05:34:33.37	21×21	0.455177
12	16:32:46.943	+05:34:33.05	21×21	0.664247
13	16:32:46.903	+05:34:33.37	21×21	0.849183
14	16:32:46.868	+05:34:33.80	21×21	0.358830
15	16:32:46.970	+05:34:32.40	41×41	2.00912
16	16:32:46.908	+05:34:32.07	21×21	0.164597
17	16:32:46.967	+05:34:31.32	21×21	0.107333
18	16:32:46.997	+05:34:34.87	21×21	0.0610536
19	16:32:46.937	+05:34:29.75	21×21	0.0322799
20	16:32:46.798	+05:34:37.30	15×15	0.0166241
21	16:32:47.082	+05:34:34.67	21×21	0.0338256
22	16:32:47.054	+05:34:32.45	21×21	0.145208
23	16:32:46.851	+05:34:34.75	21×21	0.0631433
24	16:32:46.923	+05:34:34.75	21×21	0.103866
25	16:32:47.009	+05:34:31.30	21×21	0.0626998
26	16:32:46.862	+05:34:36.80	15×15	0.0146095

Table 11 — A2204 FUV continuum knots as measured in the ACS/SBC F150LP filter. The columns headers are the same as in Table 10.

^a this is a star.

^b this is an elliptical galaxy with a bright FUV point source.

^c this is an elliptical galaxy with diffuse FUV emission.

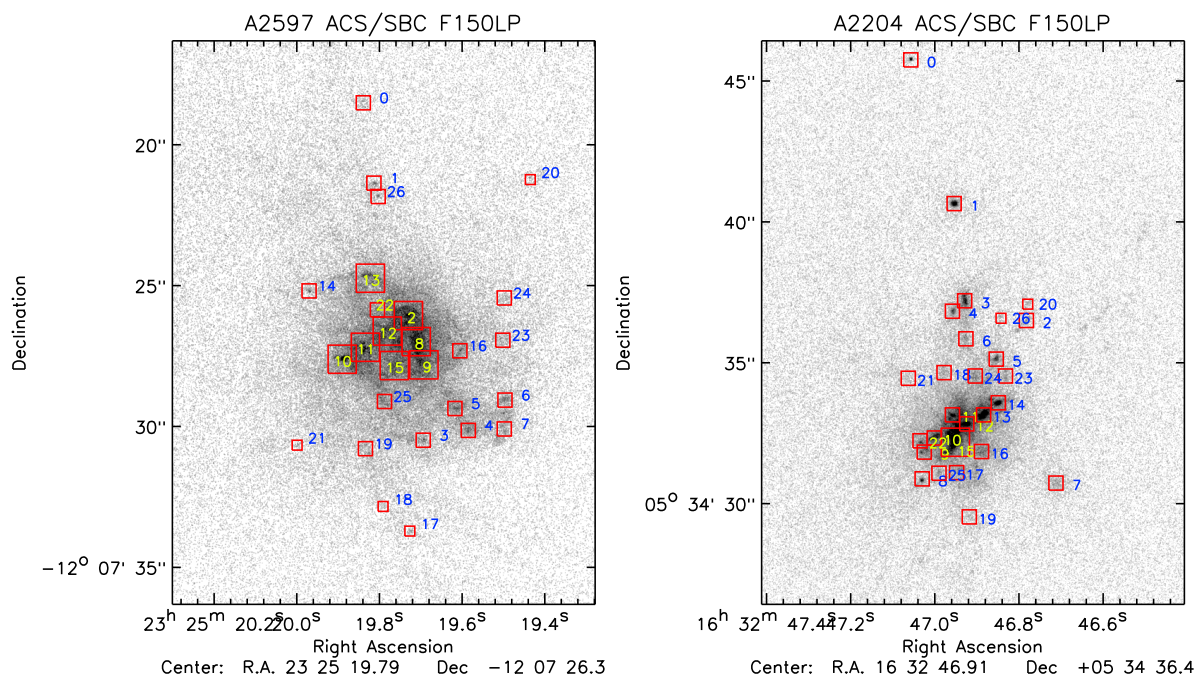


Figure 19 — FUV continuum knots for A2597 (*Top*) and A2204 (*Bottom*) as measured in the ACS/SBC F150LP filter. The squares show the apertures used to extract the knot fluxes. The knots are labelled according to the numbers written next to these apertures and the extracted fluxes are given in Tables 10 and 11.

Name	Type	FUV_v/U_v	$A_{V,tot}$	T_{BB}	T_{K93}	T_{B03}
446A	O7V	1.70	0.461	52000	42700	40100
446B	O8V	1.79	0.384	51000	41900	38000
508A	O7V	1.82	0.306	47400	40200	38000
508B	O6V	1.94	0.229	46900	39900	40100

Table 12 — Stellar Temperatures for main-sequence stars in NGC 604. Column 1 and 2 give the name and type of the star (Bruhweiler et al. 2003). Column 3 lists the FUV_v/U_v ratio as measured for each star. Column 4 lists the total visual extinction in magnitudes towards each star. Columns 5 and 6 list the stellar temperatures derived from BB and K93 stellar models. Column 7 lists the spectroscopic temperatures derived by Bruhweiler et al. (2003).

B.2 NGC 604 a Test Case

In Section 3.5 we have shown that the FUV/U broad band ratio is a good discriminator of stellar temperature. In order to verify that the temperatures derived from the broad band ratio are consistent with spectroscopically derived temperatures we have tested our method on a few main sequence stars in the nearby giant HII region NGC 604 in M33. We retrieved archival HST/ACS SBC-F150LP and HRC-F330W observations of this object. We note that the F330W filter shape is similar to that of our FORS U_Bessel filter and that it does not contain any line emission.

We selected four, isolated, main-sequence stars for which FUV spectroscopic temperatures have been determined by Bruhweiler et al. (2003), see Fig. 20. The FUV_v/U_v ratio derived for these stars, takes into account corrections for the background, the difference in point spread function between the two filters. The stellar temperature is then derived by comparing the measured FUV_v/U_v ratio to the ratio determined for BB and K93 stellar models. The extinction towards each star is taken into account when computing the models. The results for NGC 604 are shown in Fig. 21 and Table 12.

We find that the K93 temperatures derived by our broad band method are consistent with the spectroscopic temperatures determined by Bruhweiler et al. (2003). This is expected as these authors also use the K93 stellar models to derive their temperatures. This thus shows the equivalence of the two methods and that there are no spectral features unaccounted for when using the broad band approach. However, this investigation by no means verifies the K93 models as an adequate model for real stars.

Interpreting the measured FUV_v/U_v ratio in terms of BB models leads to much higher temperatures for the stars investigated. The difference of the slope in FUV to U-band regime means that above 10^4 K the BB inferred temperatures are systematically below the K93 inferred temperatures whereas below 10^4 K they are systematically above the K93 inferred temperatures.

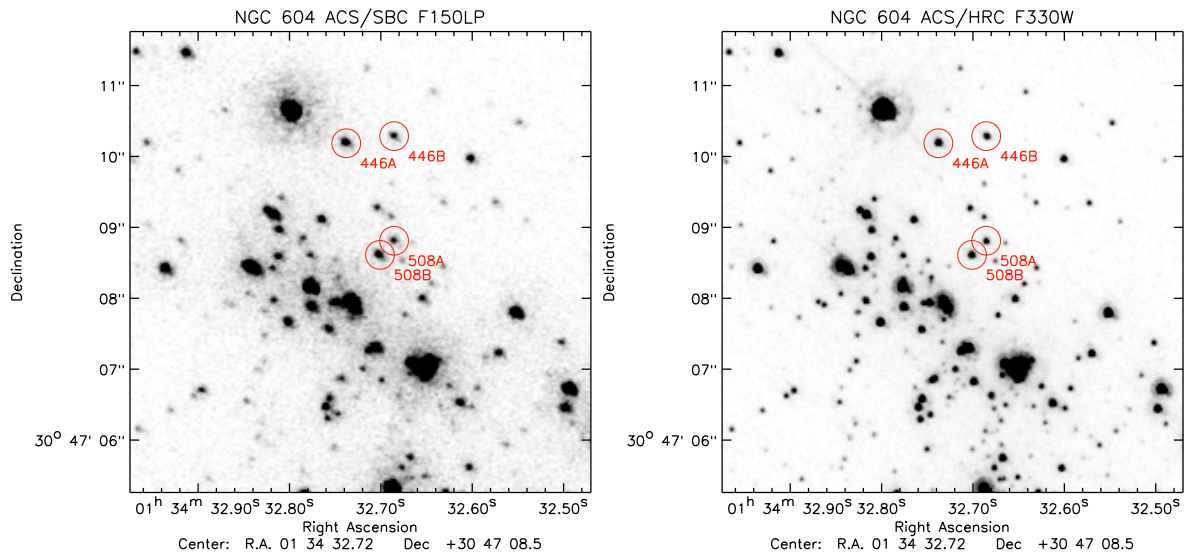


Figure 20 — HST ACS/SBC imaging of NGC 604. (Top) F150LP. (Bottom) F330W. Selected main-sequence stars are marked by the circles.

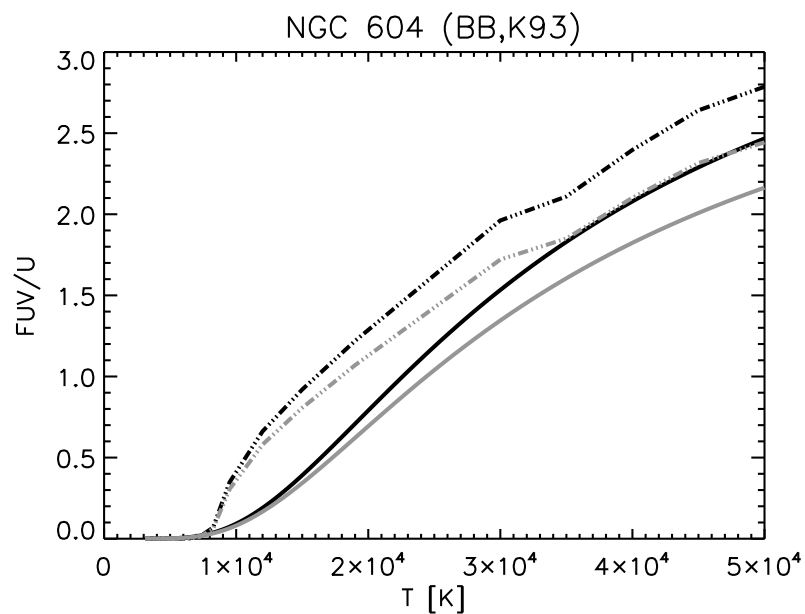


Figure 21 — NGC 604 FUV_v/U_v ratio models. Black Body models (solid line) and the K93 stellar models (dash-dot line) are shown. Black lines refer to a dust-free environment. Grey lines refer to models reddened by MW foreground dust only.

B.3 M87 filaments.

Line emission from [CIV] 1549 Å is claimed by Sparks et al. (2009) to represent the bulk of the FUV emission observed from the south-eastern filaments in M87. They present HST FUV imaging using the F150LP and F165LP filters. Based on the apparent absence of these filaments in the F165LP image they suggest that the bulk of the filamentary FUV emission is due to the CIV line at 1549 Å.

We have re-processed their images (project code 11681) and come to a different conclusion. Both the throughput and the exposure time of the F165LP image is lower than for the F150LP image. This means that the sensitivity of the F165LP image is significantly lower than the F150LP image. After re-binning the pixels by a factor four on each side and smoothing the data with a 30 pixel FWHM Gaussian kernel we do detect the south-eastern filament in both images. The filament is indicated by the dashed square region in Fig. 22.

We find $F_{150LP_\nu}/F_{165LP_\nu}=0.80\pm 0.04$ for the integrated flux in the dotted, 6 arcsec by 6 arcsec region shown in Fig. 22. This region contains the brightest part of the south-east filament. We computed the $F_{150LP_\nu}/F_{165LP_\nu}$ ratio for BB and K93 stellar models, see Fig. 22. We find that the observed ratio is consistent with $T\approx 10000$ K stars in the context of the K93 stellar models. We thus conclude that [CIV] emission is possible, but the observed FUV emission can also be explained by normal stars.

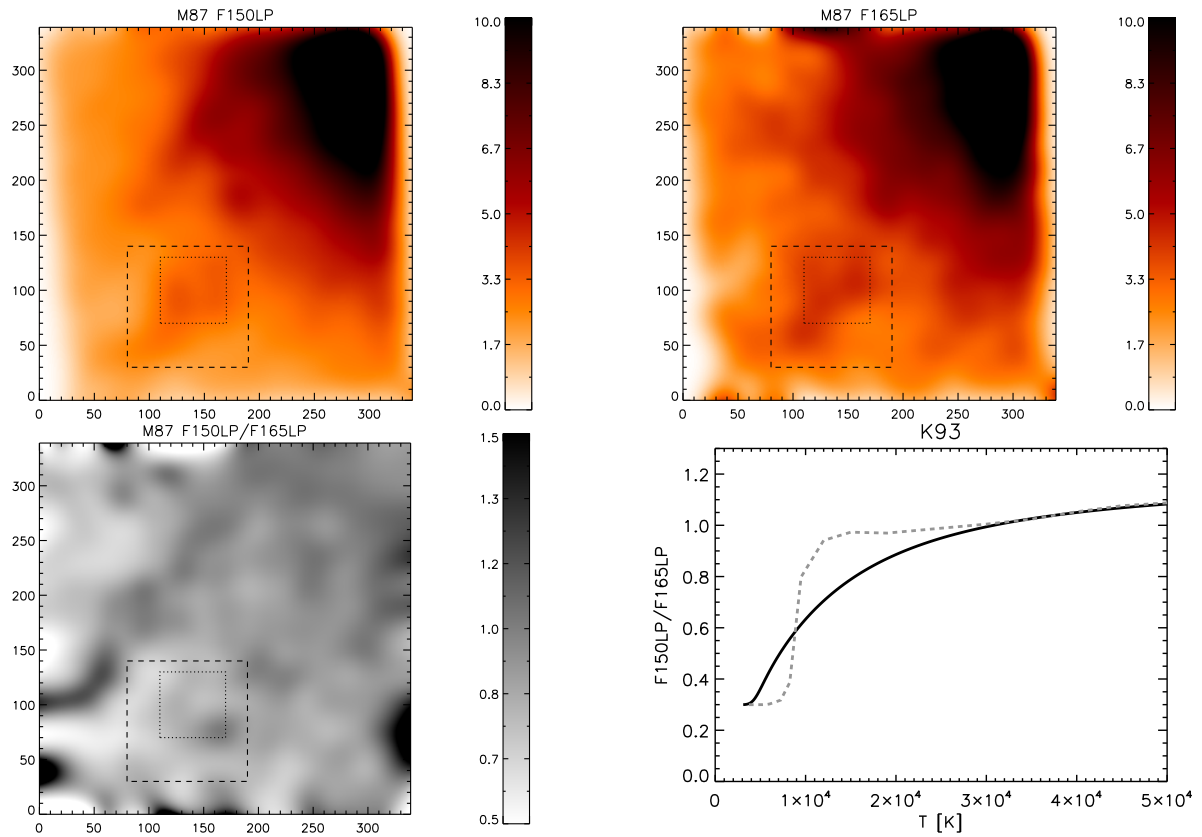


Figure 22 — M87 south-east. (*Top-left*) Re-binned and smoothed F150LP image. (*Top-right*) Re-binned and smoothed F165LP image. (*Bottom-left*) F_{150LP_v}/F_{165LP_v} ratio image. (*Bottom-right*) BB models (black solid line) and K93 stellar models (grey dashed line) showing the F_{150LP_v}/F_{165LP_v} ratio versus temperature. The dashed rectangle shows the location of the filament and the dotted rectangle shows the region used by us to calculate the stellar temperature. The units on the x and y axes are re-binned pixels with each pixel having a projected size on the sky of 0.1 arcsec.

Chapter 4

The dust destruction timescales in the cores of clusters of galaxies are relatively short given their high central gas densities. However, substantial mid-infrared and sub-mm emission has been detected in many brightest cluster galaxies. In this letter we present *Herschel* PACS and SPIRE photometry of the brightest cluster galaxy in three strong cooling flow clusters, A1068, A2597 and Zw3146. This photometry indicates that a substantial mass of cold dust is present ($> 3 \times 10^7 M_{\odot}$) at temperatures significantly lower (20–28 K) than previously thought based on limited MIR and/or sub-mm results. The mass and temperature of the dust appear to match those of the cold gas traced by CO with a gas-to-dust ratio of 80–120.

A&A 518, L47 (2010)

A. C. Edge¹, J. B. R. Oonk², R. Mittal³, S. W. Allen⁴, S. A. Baum³, H. Böhringer⁵, J. N. Bregman⁶, M. N. Bremer⁷, F. Combes⁸, C. S. Crawford⁹, M. Donahue¹⁰, E. Egami¹¹, A. C. Fabian⁹, G. J. Ferland¹², S. L. Hamer¹, N. A. Hatch¹³, W. Jaffe², R. M. Johnstone⁹, B. R. McNamara¹⁴, C. P. O’Dea¹⁵, P. Popesso⁵, A. C. Quillen¹⁶, P. Salomé⁸, C. L. Sarazin¹⁷, G. M. Voit¹⁰, R. J. Wilman¹⁸, M. W. Wise¹⁹

¹ Institute for Computational Cosmology, Department of Physics, Durham University, Durham, DH1 3LE, UK

² Leiden Observatory, Leiden University, P.B. 9513, Leiden 2300 RA, The Netherlands

³ Chester F. Carlson Center for Imaging Science, Rochester Institute of Technology, Rochester, NY 14623, USA

⁴ Kavli Institute for Particle Astrophysics and Cosmology, Stanford University, 452 Lomita Mall, Stanford, CA 94305-4085, USA

⁵ Max-Planck-Institut für extraterrestrische Physik, 85748 Garching, Germany

⁶ University of Michigan, Dept. of Astronomy, Ann Arbor, MI 48109, USA

⁷ H H Wills Physics Laboratory, Tyndall Avenue, Bristol BS8 1TL, UK

⁸ Observatoire de Paris, LERMA, CNRS, 61 Av. de l’Observatoire, 75014 Paris, France

⁹ Institute of Astronomy, Madingley Rd., Cambridge, CB3 0HA, UK

¹⁰ Michigan State University, Physics and Astronomy Dept., East Lansing, MI 48824-2320, USA

¹¹ Steward Observatory, University of Arizona, 933 N. Cherry Avenue, Tucson, AZ 85721, USA

¹² Department of Physics, University of Kentucky, Lexington KY 40506 USA

¹³ School of Physics and Astronomy, University of Nottingham, University Park, Nottingham NG7 2RD, UK

¹⁴ Department of Physics & Astronomy, University of Waterloo, 200 University Avenue West, Waterloo, Ontario, Canada N2L 3G1

¹⁵ Department of Physics, Rochester Institute of Technology, 84 Lomb Memorial Drive, Rochester, NY 14623-5603, USA

¹⁶ Department of Physics and Astronomy, University of Rochester, Rochester, NY 14627, USA

¹⁷ Department of Astronomy, University of Virginia, P.O. Box 400325, Charlottesville, VA 22904-4325, USA

¹⁸ School of Physics, University of Melbourne, Victoria 3010, Australia

¹⁹ ASTRON, Netherlands Institute for Radio Astronomy, P.O. Box 2, 7990 AA Dwingeloo, The Netherlands

4.1 Introduction

The cores of cluster of galaxies are very energetic regions with a high X-ray emissivity, particle density, cosmic ray flux, stellar density and AGN radiation. In this very hostile environment any dust grains are unlikely to survive for more than a few million years due to the action of collisional sputtering (Dwek & Arendt 1992) unless they are shielded (Fabian et al. 1994). It is therefore somewhat surprising to find that dust continuum emission from the brightest cluster galaxies in the most rapidly cooling clusters being detected at sub-mm and MIR wavelengths (Edge et al. 1999, Egami et al. 2006, O’Dea et al. 2008). The presence of cold molecular gas (Edge 2001, Salomé & Combes 2003) and dust absorption in HST imaging (McNamara et al 1996) implies that the dust continuum traces a substantial, cold component to the ISM in these massive elliptical galaxies. However, the origin of the dust and how it is shielded are still poorly understood.

The limitations with the current observations of dust emission make it difficult to establish an unambiguous dust mass as they do not sample over the peak of the dust emission in the FIR. The unprecedented sensitivity of *Herschel* (Pilbratt et al. 2010) to FIR continuum offers the opportunity to accurately constrain the full FIR spectrum of the dust emission in cluster cores. The authors were awarded 140 hours of time in an Open Time Key Project (PI Edge) to investigate the FIR line and continuum properties of a sample of 11 brightest cluster galaxies (BCGs) in well-studied cooling flow clusters selected on the basis of optical emission line and X-ray properties. The full goals of the project are to observe at least five atomic cooling lines for each object that cover a range in density and temperature behaviour and obtain a fully sampled FIR spectral energy distribution. In this paper we present the Photodetector Array Camera & Spectrometer (PACS, Poglitsch et al. 2010) and Spectral and Photometric Imaging REceiver (SPIRE, Griffin et al. 2010) photometry for the three targets observed in the Science Demonstration Phase (SDP), Abell 1068 ($z = 0.1386$), Abell 2597 ($z = 0.0821$) and Zw3146 ($z = 0.2906$). In a parallel paper (Edge et al. 2010), we present the FIR spectroscopy for the first two of these clusters.

The three clusters observed have quite contrasting multiwavelength properties. Abell 1068 and Zw3146 both have strong MIR emission (O’Dea et al. 2008, Egami et al. 2006) with a relatively bright CO detection (Edge 2001) and a weak central radio source (McNamara et al. 2004). A1068 lies just below the luminosity threshold of a ULIRG ($10^{12} L_{\odot}$) and exhibits some contribution from an AGN (Crawford et al. 1999, O’Dea et al. 2008). On the other hand, Abell 2597 is a relatively weak MIR source (Donahue et al. 2007) with a weak CO detection (Salome, priv. comm.) and a powerful central radio source (Sarazin et al. 1995). The implied FIR luminosity of A2597 is a factor of around 30 below that of A1068 and, in addition, the fractional contribution from an AGN in the MIR is also lower in A2597.

4.2 Observations

We performed photometric imaging of A1068, A2597 and Zw3146 with PACS and SPIRE. The data were reduced with the *Herschel* Interactive Processing Environment (HIPE) software version 2.3.1436 (Ott 2010). We used for both PACS and SPIRE the official scripts as presented by the PACS and SPIRE ICC teams during the *Herschel* SDP data processing workshop in

December 2009.

4.2.1 PACS Data

The PACS photometric observations were taken in LargeScanMapping mode in all three bands of the photometer, BS (70 μm), BL (100 μm) and R (160 μm) using the medium scan speed ($20''\text{s}^{-1}$). The scan maps comprised 18 scan line legs of $4'$ length and cross-scan step of $15''$. Each observation had a “scan” and an orthogonal “cross-scan” direction and we calibrated the corresponding data separately before combining them into a single map of $9' \times 9'$. The resulting maps have a resolution of $5.2''$, $7.7''$ and $12''$ at 70, 100 and 160 μm , respectively and are presented in the electronic version of this paper. The PACS photometer performs dual-band imaging such that the BS and BL bands each have simultaneous observations in the R band so we have two sets of scans in the R band.

We adopted the PACS Data Reduction Guideline to process the raw level-0 data to calibrated level 2 products and used the official script for PACS ScanMapping mode but with particular attention to the high pass filtering to remove “ $1/\sqrt{f}$ ” noise. We choose to use the *HighPassFilter* method with a filter of 20 readouts which will remove structure on all scales above $82''$. The target BCG and other bright sources in the field were masked prior to applying the filter. The size of the mask was chosen to be less than the filter size so as to minimize any left-over low-frequency artefacts under the masks. We used masks with a radius of $15''$ for our sources. We tried varying the size for the filter from 10 to 30 readouts and the mask radius from 10– $30''$ and found our results to not change significantly for these ranges in values. Finally the task ‘photProject’, was used to project the calibrated data onto a map on the sky in units of Jy pixel^{-1} . The “scan” and “cross-scan” maps were then averaged to produce the final coadded map. The PACS and SPIRE images are included in the electronic version of the paper. The spatial flux distribution and flux densities of our target sources were investigated using cumulative flux curves. The spatial flux distribution for each of our three sources is consistent with that expected from a point source. Flux densities in the BS, BL and R band were extracted using a $33''$ by $33''$ aperture centered on the BCG. Small aperture corrections were applied as outlined in the PACS Scan Map release note (PICC-ME-TN-035). Care was taken to calibrate these derived flux densities to account for the known flux overestimation in the used HIPE version by factors 1.05, 1.09 and 1.29 in BS, BL and R bands respectively. The absolute flux accuracy is within 10 % for BS and BL, and better than 20 % for R. These uncertainties are not believed to be correlated due to the BS and BL bands being taken at different times and the R band using a different detector.

4.2.2 SPIRE Data

The SPIRE photometry was performed in the LargeScanMap mode with cross-linked scans in two orthogonal scan directions. The photometer has a field of view of $4' \times 8'$, which is observed simultaneously in three spectral bands, PSW (250 μm), PMW (350 μm) and PLW (500 μm) with a resolution of about $18''$, $25''$ and $36''$, respectively. The resulting maps measure $12' \times 12'$ in size and are presented in the electronic version of this paper.

We used the standard HIPE pipeline for the LargeScanMap observing mode and the naïve map-maker. The pre-processed raw telemetry data were first subject to engineering conversion

wherein the raw timeline data were converted to meaningful units, the SPIRE pointing product was created, deglitching and temperature drift correction were performed, and maps were created, the units of which were Jy beam^{-1} . Our targets are unresolved at the spatial resolution of SPIRE. We derived their flux densities by fitting the sources with the SPIRE point source response function. Care was taken to de-blend our target from other nearby sources at the longer wavelengths, where the sources are most likely to be background to the cluster. We account for the known flux calibration offset in the used version of HIPE by applying the following multiplicative calibration factors 1.02, 1.05 and 0.94 to the derived flux densities in the PSW, PMW and PLW bands respectively (see Griffin et al. 2010, Swinyard et al. 2010). We also performed aperture photometry using the HIPE point-source extraction (PSE) tool but this method gives accurate results only for isolated point sources. At $350\ \mu\text{m}$ and $500\ \mu\text{m}$, the BCGs in A2597 and Zw3146 are close to the detection limit and at the confusion limit of SPIRE making the PSE method of determining the fluxes unsuccessful. A1068 has a relatively strong compact BCG in far infrared and so we performed the PSE to find that the flux estimates using AIPS and HIPE agree with each other to better than 5%.

4.3 Results

In the PACS photometry, A1068, A2597 and Zw3146 have been detected in all three bands. For A1068, 70 and $100\ \mu\text{m}$ values are slightly less than the *IRAS* 60 and $100\ \mu\text{m}$ measurements. This could be due to nearby sources that cannot be separated from the BCG in the much lower resolution *IRAS* observations but no sufficiently bright source is visible in our PACS imaging. There is a large difference between the *Spitzer* MIPS $70\ \mu\text{m}$ flux (Quillen et al. 2008) and our PACS $70\ \mu\text{m}$ flux, the PACS flux being a factor 1.7 lower than the MIPS flux. In the case of Zw3146 the MIPS and PACS $70\ \mu\text{m}$ fluxes also differ with the PACS value being a factor 1.4 larger than the MIPS value (Egami et al. 2006). For A2597 the PACS fluxes differ from the *Spitzer* 70 and $160\ \mu\text{m}$ fluxes reported by Donahue et al. (2007). Part of this difference was resolved when the MIPS $70\ \mu\text{m}$ data were re-analysed and found to be a factor of two too high (Donahue, priv. comm.). The differences observed between the PACS and *Spitzer* fluxes require further investigation. In the SPIRE photometry, A1068 is detected in all three SPIRE bands. A2597 and Zw3146, while clearly detected in PSW and PMW bands, have a $1-2\ \sigma$ detection in the PLW band. Table 1 gives the photometric results for the three galaxies, with 2σ upper-limit for A2597 and Zw3146 in PLW. Figure 1 presents the radio to optical spectral energy distributions (SEDs) for the three targets. These plots show the significant variation in the relative radio-FIR-optical contributions for each of our galaxies. Here we focus on the sub-mm/MIR dust emission as sampled by PACS and SPIRE photometry, complemented by published *Spitzer* and *IRAS* measurements.

We fit the SEDs of the dust emission using black bodies modified with a dust emissivity index, β . The FIR-MIR slopes of our sources require the presence of at least two dust components. Previous studies of star-forming galaxies have indeed established that a single modified black body (MBB) is inadequate to account for the observed dust emission (Wiklind 2003). Hence, our model for the SEDs consists of two MBBs with the dust emissivity index for each fixed to $\beta=2$ and a mass absorption coefficient, κ_{dv} , of $2.5\ \text{m}^2\ \text{kg}^{-1}$ at $100\ \mu\text{m}$.

For A1068 we fit the $24-850\ \mu\text{m}$ emission. For A2597 and Zw3146 the SCUBA $850\ \mu\text{m}$

Table 4.1 — Log of *Herschel* Observations. The *Spitzer* data are from Quillen et al. (2008), Donahue et al. (2007, priv. comm.) and Egami et al. (2006). The SCUBA data are from Edge (priv. comm.), Zemcov et al. (2007) and Chapman et al. (2002).

Cluster	z	Instrument	λ (μm)	Obsid	Flux (mJy)
A1068	0.1386	PACS	70	1342187051	542 \pm 6
		PACS	100	1342187053	757 \pm 6
		PACS	160		769 \pm 4
		SPIRE	250	1342187321	376 \pm 6
		SPIRE	350		135 \pm 6
		SPIRE	500		56 \pm 8
		SCUBA	450		39 \pm 13
		SCUBA	850		5.3 \pm 1.1
		<i>Spitzer</i>	24		74.5 \pm 2.0
		<i>Spitzer</i>	70		941 \pm 30
		<i>IRAS</i>	60		577 \pm 52
<i>IRAS</i>	100		958 \pm 144		
A2597	0.0821	PACS	70	1342187118	57 \pm 5
		PACS	100	1342187120	67 \pm 7
		PACS	160		86 \pm 4
		SPIRE	250	1342187329	30 \pm 6
		SPIRE	350		15 \pm 6
		SPIRE	500		< 16
		SCUBA	850		14.5 \pm 2.3
		<i>Spitzer</i>	24		2.1 \pm 0.2
		<i>Spitzer</i>	70		49 \pm 6
		<i>Spitzer</i>	160		52 \pm 3
Zw3146	0.2906	PACS	70	1342187043	94 \pm 6
		PACS	100	1342187045	150 \pm 6
		PACS	160		139 \pm 5
		SPIRE	250	1342187326	81 \pm 6
		SPIRE	350		30 \pm 6
		SPIRE	500		< 16
		SCUBA	450		<48
		SCUBA	850		6.6 \pm 2.6
		<i>Spitzer</i>	24		4.1 \pm 0.4
		<i>Spitzer</i>	70		68 \pm 14
		<i>Spitzer</i>	160		157 \pm 35

detections have been removed and we fit only the 24–350 μm range. In the case of A2597, this is due to the unknown amount of radio contamination at 850 μm . In the case of Zw3146 the BCG is blended with strong background source at 850 μm (Chapman et al. 2002). The data are weighted in the fit inversely to the square of their error. The resulting fits are shown in Figure 1. The derived dust temperatures and total FIR luminosities for each source are listed in Table 2.

The results in Table 2 indicate that at least two dust components, one at 20–25 K and one at 50–60 K, are present in all three sources. The FIR emission is much stronger relative to the optical in A1068 and Zw3146 as compared to A2597. The SEDs of A1068 and Zw3146 resemble those of strongly star-forming systems and, based on the total FIR luminosity derived here, we find star formation rates (SFR) of 60 and 44 $M_{\odot} \text{ yr}^{-1}$ in these two systems using the Kennicutt (1998) conversion factor. For A2597 a much more modest SFR of 2 $M_{\odot} \text{ yr}^{-1}$ is inferred. These values are comparable to SFRs derived from $H\alpha$ line and/or UV continuum emission given the uncertainties of these tracers. However, the SFR values derived from *Spitzer* data are higher for A1068 and Zw3146. The difference for A1068 is the most pronounced and can be directly attributed to the stronger AGN contribution in this object (Quillen et al. 2008) which boosts the 24 μ flux compared other comparable sources. Therefore, when the total FIR luminosity is derived from the 15 μm flux inferred from *Spitzer* it will be overestimated. The value for Zw3146 from Egami et al. (2006) is higher than ours as their fit includes the SCUBA 850 μm point from Chapman et al. (2002) which appears to be overestimated on the basis of our SPIRE data.

The gas to dust ratio is found to be between 80 and 140 (see Table 2). Gas temperatures can be inferred from CO measurements (Edge 2001, Salome & Combes 2003). These estimates infer gas temperatures of 25–40 K thus implying that the gas and dust share a common environment and are potentially co-located in the denser regions of cold, molecular gas clouds. We have attempted to determine how much extended emission is present from our highest spatial resolution PACS 70 μm image but we find no evidence for more than 10% additional flux beyond a point source. Clearly these limits will improve with a better characterisation of the instrument but we believe that we can conclude that the dust emission in our targets has an extent comparable to that the bulk of the CO emitting gas and optical emission lines ($< 5''$ or 5–20 kpc).

4.4 Discussion and conclusions

Our initial *Herschel* results confirm the presence of the striking dust emission peak expected from the observations at sub-mm (Edge et al. 1999, Chapman et al. 2002) and MIR (Egami et al. 2006, O’Dea et al. 2008).

The star formation rates derived from the full-sampled FIR SED are comparable to those derived from *Spitzer* 24 μm fluxes apart from A1068, which has the strongest contribution from an AGN so hot dust dominates to the 24 μm flux. However, in the sub-mm the contribution from the radio continuum from an active nucleus must be correctly accounted for before any dust mass can be estimated from the 850 μm flux. In the case of A2597 here and A2390 in Edge et al. (1999), the presence of a powerful radio source appears to contribute to the SCUBA 850 μm flux.

Table 4.2 — Summary of results and other cluster properties. The *Spitzer* SFR values are from O’Dea et al. (2008), Donahue et al. (2007) and Egami et al. (2006). The Optical/UV SFR values are from McNamara et al. (2004), Donahue et al. (2007) and Egami et al. (2006). The CO gas masses are from Edge (2001) and Salomé (priv. comm.) and the H α slit luminosities are from Crawford et al. (1999).

Cluster	A1068	A2597	Zw3146
Dust Temperatures	24 \pm 4K 57 $^{+12}_{-4}$ K	21 \pm 6K 48 $^{+17}_{-5}$ K	23 \pm 5K 53 $^{+22}_{-6}$ K
Cold Dust Mass	5.1 \times 10 ⁸ M $_{\odot}$	2.3 \times 10 ⁷ M $_{\odot}$	5.4 \times 10 ⁸ M $_{\odot}$
Warm Dust Mass	3.9 \times 10 ⁶ M $_{\odot}$	2.9 \times 10 ⁵ M $_{\odot}$	1.9 \times 10 ⁶ M $_{\odot}$
Total FIR Luminosity	3.5 \times 10 ¹¹ L $_{\odot}$	8.8 \times 10 ⁹ L $_{\odot}$	2.5 \times 10 ¹¹ L $_{\odot}$
Star Formation Rate	60 \pm 20 M $_{\odot}$ yr $^{-1}$	2 \pm 1 M $_{\odot}$ yr $^{-1}$	44 \pm 14 M $_{\odot}$ yr $^{-1}$
SFR <i>Spitzer</i>	188 M $_{\odot}$ yr $^{-1}$	4 M $_{\odot}$ yr $^{-1}$	70 \pm 14 M $_{\odot}$ yr $^{-1}$
SFR <i>optical/UV</i>	20–70 M $_{\odot}$ yr $^{-1}$	10–15 M $_{\odot}$ yr $^{-1}$	47 \pm 5 M $_{\odot}$ yr $^{-1}$
CO gas mass	4.1 \times 10 ¹⁰ M $_{\odot}$	2.0 \times 10 ⁹ M $_{\odot}$	7.7 \times 10 ¹⁰ M $_{\odot}$
H α Slit Luminosity	8 \times 10 ⁴¹ erg s $^{-1}$	3 \times 10 ⁴¹ erg s $^{-1}$	3 \times 10 ⁴² erg s $^{-1}$

While it is difficult to draw any general conclusions from just three BCGs, we note with interest that the ratio of dust mass to CO-derived gas mass is consistent for all three within a factor of five. If the dust were mostly generated through dust ejection from evolved stars then the dust mass should closely correlate with the total stellar mass. However, our three galaxies have very similar optical/NIR absolute magnitudes. So, unless the ejected dust were “captured” by the cold gas clouds protecting it from X-ray sputtering, this suggests that the apparent correlation between the molecular gas and dust masses arises from a direct connection between the gas reservoir and star formation.

These results are a limited example of those to come in the very near future from *Herschel* as there are two other Open Time Key Projects (PI Egami and Smith) that are targeting a total of 70 clusters that cover a broad range of BCG properties so the wider context of these initial observations can be determined. In particular, the amount of dust present in more quiescent BCGs and other massive cluster ellipticals will be important in assessing how much of the dust seen in cool core BCGs originates from the underlying stellar population.

4.5 Acknowledgements

We would like to thank the *Herschel* Observatory and instrument teams for the extraordinary dedication they have shown to deliver such a powerful telescope. We would like to thank the HSC and NHSC consortium for help with data reduction pipelines. J.B.R.O. thanks HSC, the *Herschel* Helpdesk and the PACS group at MPE for useful discussions. R. M. thanks the NHSC for the HIPE tutorials.

Bibliography

- Chapman, S. C., Scott, D., Borys, C., et al. 2002, MNRAS, 330, 92
Crawford, C. S., Allen, S. W., Ebeling, H., et al. 1999, MNRAS, 306, 857

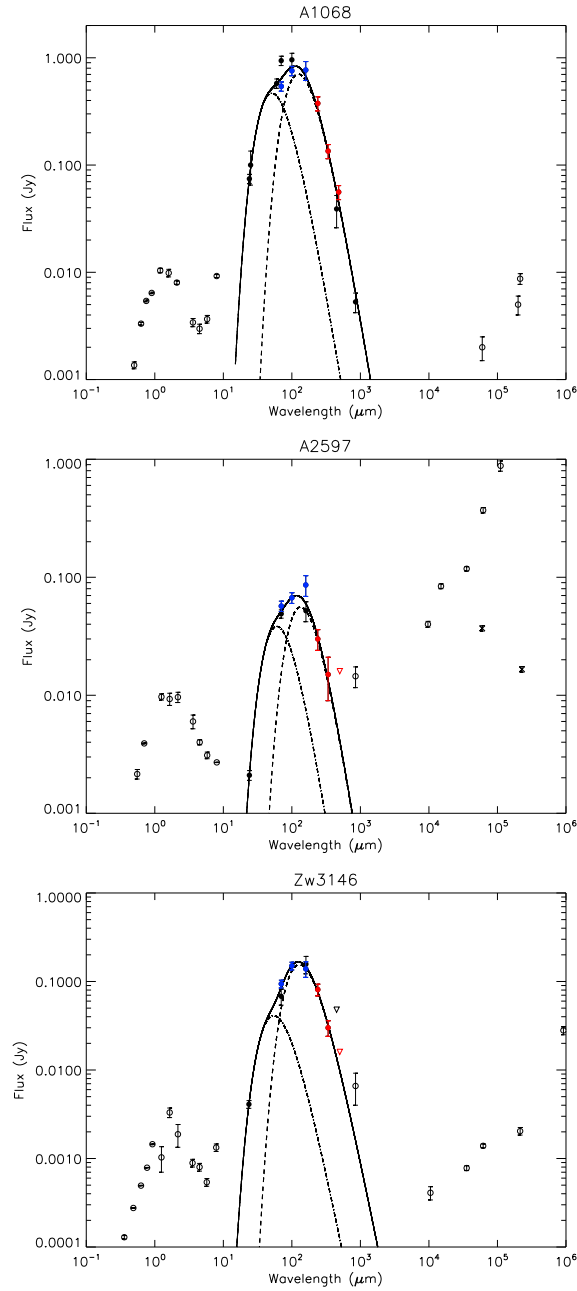


Figure 4.1 — Spectral energy distributions for A1068 (top), A2597 (middle) and Zw3146 (bottom) including *Herschel* PACS/SPIRE, *Spitzer*, Radio, NIR photometry from 2MASS and optical photometry from SDSS. To account for absolute flux uncertainties we have set the following errors on the fluxes derived from the various instruments (unless the quoted error is larger than this); PACS BS/BL 10%, PACS R 20%, SPIRE 15%, *Spitzer* 10%, SCUBA 450 μm 30% and SCUBA 850 μm 20%. The model fit to the sub-mm/FIR/MIR data is shown by the black solid line. Only filled symbols have been used in the fit. The two modified blackbodies making up the model are shown by the black long dash and dash-dot lines. For A2597 we also show two VLBI measurements (black crosses) of the BCG core at 1.3 and 5 GHz (Taylor et al. 1999). These points show that the BCG has a strong, inverted radio core.

- Donahue, M., Jordán, A., Baum, S. A., et al. 2007, *ApJ*, 670, 231
- Dwek, E., & Arendt, R. G., 1992, *ARA&A*, 30, 11
- Edge, A. C., Ivison, R. J., Smail, I. R., et al., 1999, *MNRAS*, 306, 599
- Edge, A. C., 2001, *MNRAS*, 328, 762
- Edge, A. C., Oonk, J. B. R., Mittal, R., et al. 2010, *A&A*, this volume
- Egami, E., Misslet, K. A., Rieke, G. H., et al. 2006, *ApJ*, 647, 922
- Fabian, A. C., Johnstone, R. M., & Daines, S. J., 1994, *MNRAS*, 271, 737
- Griffin, M., Abergel, A., Abreu, A., et al. 2010, this volume
- Kennicutt, R. C. 1998, *ARA&A*, 36, 189
- McNamara, B. R., Wise, M. W., Sarazin, C. L., et al. 1996, *ApJ* 466, L9
- McNamara, B. R., Wise, M. W., & Murray, S. S., 2004, *ApJ*, 601, 173
- O’Dea, C. P., Baum, S. A., Privon, G., et al. 2008, *ApJ*, 681, 1035
- Ott, S. 2010 in *ASP Conference Series, Astronomical Data Analysis Software and Systems XIX*, Y. Mizumoto, K. I. Morita, and M. Ohishi, eds., in press
- Pilbratt, G., et al. 2010, *A&A*, this volume
- Poglitsch, A., et al. 2010, *A&A*, this volume
- Quillen, A. C., Zufelt, N., Park, J., et al. 2008, *ApJS*, 176, 39
- Salomé, P., & Combes, F. 2003, *A&A*, 412, 657
- Sarazin, C. L., Burns, J. O., Roettiger, K., et al. 1995, *ApJ*, 447, 559
- Swinyard, B., Griffin, M., Ade, P., et al. 2010, *A&A*, this volume
- Taylor, G. B., O’Dea, C. P., Peck, A. B., et al. 1999, *ApJ* 512, L27
- Wiklind, T. 2003, *ApJ*, 588, 736
- Zemcov, M., Borys, C., Halpern, M., et al. 2007, *MNRAS*, 376, 1073

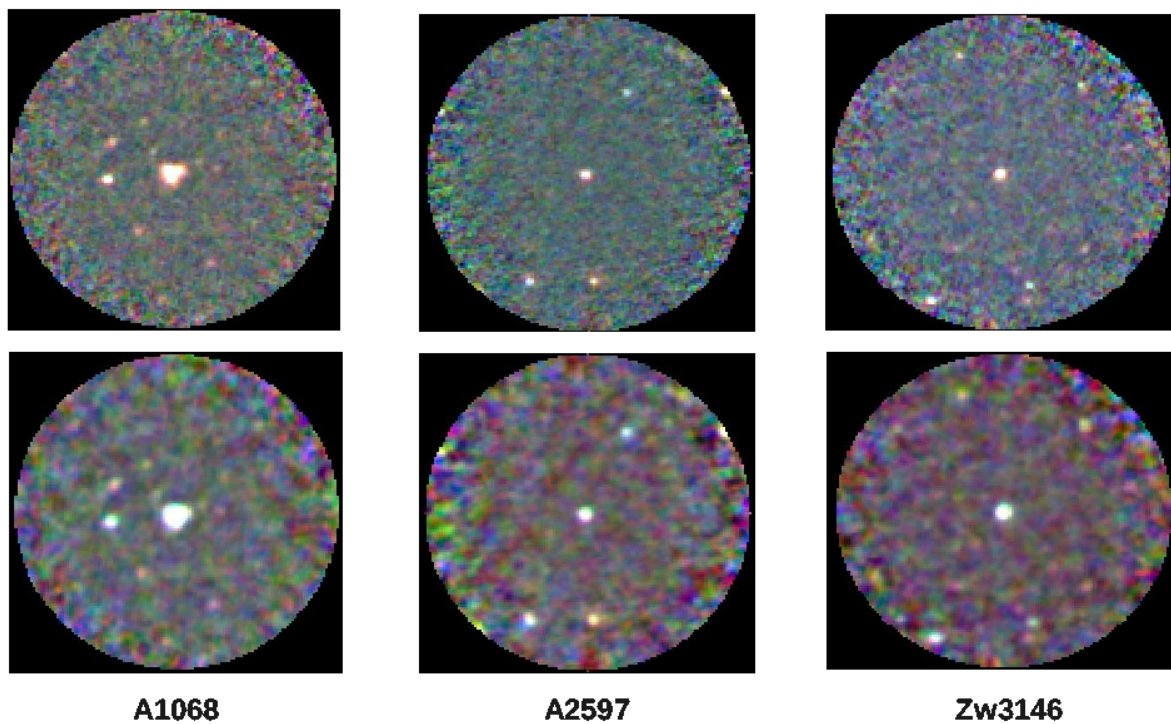


Figure 4.2 — Combined images from the three PACS bands (BS, BL and R in the blue, green and red channels) for the three clusters within radius of $2.5'$ of the BCG. The top row are images combined in their original resolution and the bottom row are the images combined with a common smoothing of $12''$ to match resolution. The images are only available in colour in the online version.

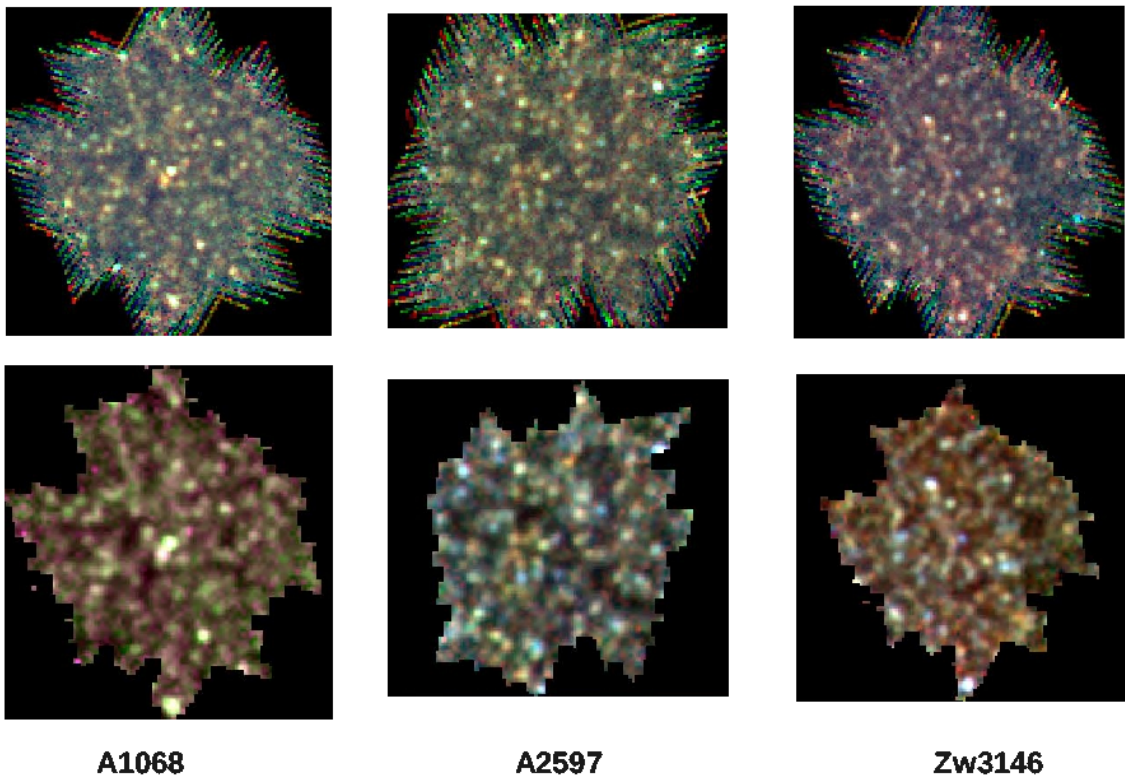


Figure 4.3 — Combined images from the three SPIRE bands (PSW, PMW and PLW in the blue, green and red channels) for full field covered for the three clusters covering approximately $12' \times 12'$. The top row are images combined in their original resolution and the bottom row are the images combined with a common smoothing of $36''$ to match resolution and clipped to remove areas of low exposure. The BCG is at the centre of the image and in A2597 and Zw3146 is the bluest object present (see text). The images are only available in colour in the online version.

Chapter 5

The question of how much gas cools in the cores of clusters of galaxies has been the focus of many, multiwavelength studies in the past 30 years. In this letter we present the first detections of the strongest atomic cooling lines, [CII], [OI] and [NII] in two strong cooling flow clusters, A1068 and A2597, using *Herschel* PACS. These spectra indicate that the substantial mass of cold molecular gas ($> 10^9 M_{\odot}$) known to be present in these systems is being irradiated by intense UV radiation, most probably from young stars. The line widths of these FIR lines indicate that they share dynamics similar but not identical to other ionised and molecular gas traced by optical, near-infrared and CO lines. The relative brightness of the FIR lines compared to CO and FIR luminosity is consistent with other star-forming galaxies indicating that the properties of the molecular gas clouds in cluster cores and the stars they form are not unusual. These results provide additional evidence for a reservoir of cold gas that is fed by the cooling of gas in the cores of the most compact clusters and provide important diagnostics of the temperature and density of the dense clouds this gas resides in.

A&A 518, L47 (2010)

A. C. Edge¹, J. B. R. Oonk², R. Mittal³, S. W. Allen⁴, S. A. Baum³, H. Böhringer⁵, J. N. Bregman⁶, M. N. Bremer⁷, F. Combes⁸, C. S. Crawford⁹, M. Donahue¹⁰, E. Egami¹¹, A. C. Fabian⁹, G. J. Ferland¹², S. L. Hamer¹, N. A. Hatch¹³, W. Jaffe², R. M. Johnstone⁹, B. R. McNamara¹⁴, C. P. O’Dea¹⁵, P. Popesso⁵, A. C. Quillen¹⁶, P. Salomé⁸, C. L. Sarazin¹⁷, G. M. Voit¹⁰, R. J. Wilman¹⁸, M. W. Wise¹⁹

¹ Institute for Computational Cosmology, Department of Physics, Durham University, Durham, DH1 3LE, UK

² Leiden Observatory, Leiden University, P.B. 9513, Leiden 2300 RA, The Netherlands

³ Chester F. Carlson Center for Imaging Science, Rochester Institute of Technology, Rochester, NY 14623, USA

⁴ Kavli Institute for Particle Astrophysics and Cosmology, Stanford University, 452 Lomita Mall, Stanford, CA 94305-4085, USA

⁵ Max-Planck-Institut für extraterrestrische Physik, 85748 Garching, Germany

⁶ University of Michigan, Dept. of Astronomy, Ann Arbor, MI 48109, USA

⁷ H H Wills Physics Laboratory, Tyndall Avenue, Bristol BS8 1TL, UK

⁸ Observatoire de Paris, LERMA, CNRS, 61 Av. de l’Observatoire, 75014 Paris, France

⁹ Institute of Astronomy, Madingley Rd., Cambridge, CB3 0HA, UK

¹⁰ Michigan State University, Physics and Astronomy Dept., East Lansing, MI 48824-2320, USA

¹¹ Steward Observatory, University of Arizona, 933 N. Cherry Avenue, Tucson, AZ 85721, USA

¹² Department of Physics, University of Kentucky, Lexington KY 40506 USA

¹³ School of Physics and Astronomy, University of Nottingham, University Park, Nottingham NG7 2RD, UK

¹⁴ Department of Physics & Astronomy, University of Waterloo, 200 University Avenue West, Waterloo, Ontario, Canada N2L 3G1

¹⁵ Department of Physics, Rochester Institute of Technology, 84 Lomb Memorial Drive, Rochester, NY 14623-5603, USA

¹⁶ Department of Physics and Astronomy, University of Rochester, Rochester, NY 14627, USA

¹⁷ Department of Astronomy, University of Virginia, P.O. Box 400325, Charlottesville, VA 22904-4325, USA

¹⁸ School of Physics, University of Melbourne, Victoria 3010, Australia

¹⁹ ASTRON, Netherlands Institute for Radio Astronomy, P.O. Box 2, 7990 AA Dwingeloo, The Netherlands

5.1 Introduction

The cooling process at the cores of galaxy clusters is highly complex: recent *XMM-Newton* and *Chandra* observations indicate that the cooling rates are reduced by an order of magnitude below the simple cooling flow models at temperatures below $\sim 2 \times 10^7$ K (Peterson & Fabian 2006). These X-ray observations, when linked with the detection of radio jet inflated bubbles in the cores of many of the strongest cooling flows (see McNamara & Nulsen 2007 for a review), suggest that the strong suppression of gas cooling is related to energy injection into the intracluster medium by the action of jets and related AGN activity.

The detection of substantial masses of molecular gas in the cores of the most rapidly cooling clusters through CO lines (Edge 2001, Salomé & Combes 2003) and warm H₂ molecular lines in the NIR and MIR (Jaffe & Bremer 1997, Egami et al. 2006) indicates that not all cooling is suppressed and this cooled gas may provide the fuel for future AGN activity. These tracers of molecular gas appear to correlate with the strength of optical lines from ionised gas (Crawford et al. 1999, Edge 2001) and the dust continuum at MIR and sub-mm wavelengths (O’Dea et al. 2008). However, the excitation of these various emission lines and the relative importance of energy input from star formation, AGN, cosmic rays and/or the intracluster medium is poorly constrained (Ferland et al. 2009).

One as yet unexplored diagnostic of the properties of the cold gas are the atomic cooling lines found in the FIR, [CII], [OI] and [NII]. The unprecedented sensitivity of *Herschel* (Pilbratt et al. 2010) to FIR line emission offers the opportunity to assess the ionisation and density of the colder gas for the first time with the [CII] line and two principle [OI] lines. The authors were awarded 140 hours of time in an Open Time Key Project (PI Edge) to investigate the FIR line and continuum properties of a sample of 11 brightest cluster galaxies (BCGs) in well-studied cooling flow clusters selected on the basis of optical emission line and X-ray properties. The full goals of the project are to observe at least five atomic cooling lines for each object that cover a range in density and temperature behaviour and obtain a fully sampled FIR spectral energy distribution for systems where significant star formation is expected. In this paper we present the Photodetector Array Camera & Spectrometer (PACS, Poglitsch et al. 2010) spectroscopy for the two targets observed in the Science Demonstration Phase (SDP), Abell 1068 ($z = 0.1386$) and Abell 2597 ($z = 0.0821$). In a parallel paper (Edge et al. 2010), we present the FIR photometry for these clusters.

The two clusters observed have quite contrasting multiwavelength properties. A1068 is a strong MIR source (O’Dea et al 2008) with a bright CO detection (Edge 2001) but a weak radio source (McNamara et al 2004). A1068 lies just below the luminosity threshold of a ULIRG ($10^{12} L_{\odot}$) and exhibits some contribution from an AGN (Crawford et al. 1999, O’Dea et al. 2008). On the other hand, A2597 is a relatively weak MIR source (Donahue et al. 2007) with a weak CO detection (Salomé, priv. comm.) but a powerful radio source (Sarazin et al. 1995). The implied FIR luminosity of A2597 of $8.8 \times 10^9 L_{\odot}$ is a factor of around 30 below that of A1068 ($3.5 \times 10^{11} L_{\odot}$) and, in addition, the fractional contribution from an AGN in the MIR is also lower.

Table 5.1 — Log of *Herschel*PACS observations

Cluster	Redshift	Line	Wavelength (μm)	Obsid	Bandwidth (km s^{-1})	Resolution (km s^{-1})	Beam Size
A1068	0.1386	[CII]	179.61	1342186308	1200	201	13.5''/33 kpc
		[OI]	71.94	1342186307	600	55	5.4''/13 kpc
A2597	0.0821	[CII]	170.78	1342187125	1100	218	12.8''/20 kpc
		[OI]	68.41	1342187124	550	68	5.1''/7.8 kpc
		[NII]	131.94	1342188942	1200	281	9.9''/15 kpc
		[OIb]	157.56	1342188704	1200	241	11.8''/18 kpc
		[OIII]	95.61	1342188703		108	7.2''/11 kpc

5.2 Observations

We have observed the [CII] and [OI] lines at $157.74\mu\text{m}$ and $63.18\mu\text{m}$ for A1068 and A2597 with the PACS spectrometer on *Herschel*. These are the primary cooling lines of the cold gas at a temperature $T < 40$ K (Kaufman et al. 1999). In addition for A2597 we observed the [NII], [OI] and [OIII] lines at $121.90\mu\text{m}$, $145.52\mu\text{m}$ and $88.36\mu\text{m}$. These lines are used to constrain the excitation and temperature of this gas. Table 1 gives a summary of the observations.

All spectral line observations were taken in *PACS chopped line scan (standard faint line)* mode with chopping-nodding. The *simple pointed observations* mode was used for all observations. The data were reduced following the PACS data reduction guide (PDRG) using the PACS Line Spectroscopy script for Point Source Chop/Nod Mode as presented by the PACS ICC team during the *Herschel* science demonstration phase data processing workshop at ESAC in december 2009. The reduction was performed within the *Herschel* Interactive Processing Environment (HIPE) version 2.0.0 (Ott 2010), build RC 3. We have processed the data from level 0 (raw channel data) to level 2 (calibrated spectra) in a number of steps as outlined in the PDRG. Level 0 to 1.0 processing removes the telescope specific structures from the data. The slopes of the raw channel data are fitted and removed. The signal is converted from data units to volts per second. Sky coordinate information is added and bad pixels and glitches are removed from data. The data is flatfielded and flux calibrated by applying the ground based nominal response function as recommended in the PACS spectroscopy performance and calibration (PSPC) document. This ground based response calibration is known to yield overestimated fluxes and following the PSPC we divide our fluxes by 1.3 and 1.1 in the blue and red bands. The accuracy of this flux calibration for the PACS spectrometer, at the time of writing, is about 50 percent within a given spectral band (PSPC).

During the final stage of the reduction, level 1.0 to 2.0, the data are spectrally and spatially rebinned into a $5 \times 5 \times \lambda$ cube. Using the standard 5×5 spatial rebinning each spatial pixel (spaxel) has a projected size of $9.4'' \times 9.4''$ on the sky. The spectral rebinning is performed using the recommended weak line density i.e. oversamp=1 and upsamp=4. Values between 1 and 10 were tried for the upsamp and oversamp parameters to test the robustness of the line profiles. We find that the line profiles do not change significantly for this range in values.

Table 5.2 — Spectral line results for *Herschel*PACS observations

Cluster	Redshift	Line	Integrated Line Flux (10^{-18} W m $^{-2}$)	Velocity offset (km s $^{-1}$)	measured FWHM (km s $^{-1}$)	intrinsic FWHM (km s $^{-1}$)
A1068	0.1386	[CII]	104.7 \pm 1.8	+25 \pm 55	378 \pm 40	320 \pm 55
		[OI]	64.8 \pm 0.2	+25 \pm 50	356 \pm 40	352 \pm 55
A2597	0.0821	[CII]	58.5 \pm 1.9	+15 \pm 60	463 \pm 40	408 \pm 55
		[OI]	54.7 \pm 0.2	+40 \pm 55	411 \pm 40	405 \pm 55
		[NII]	3.8 \pm 1.3	+30 \pm 60	578 \pm 90	505 \pm 110
		[Ob]	3.3 \pm 1.3	-57 \pm 65	484 \pm 90	420 \pm 110
		[OIII]	< 2.9	-	-	-

5.3 Results

The [CII] 157 μ m and [OI] 63 μ m lines are detected at a signal to noise greater than 30 for both A1068 and A2597. The much weaker [NII] 122 μ m and [Ob] 145 μ m lines are detected at the 3–5 σ level for A2597. The [OIII] 88 μ m line was not detected in A2597, an upper limit for this line is given in Table 2.

The line spectra are fitted by a model consisting of; (i) a linear function to determine the continuum flux, and (ii) a single gaussian function to determine the line flux. Continuum subtracted line spectra are shown for the central spaxel in Fig. 1 for A1068 and Fig. 2 for A2597. The fitted line centers agree well with the redshift of CO in the BCG and the fitted FWHM line widths indicate gas with velocities of 300–500 km s $^{-1}$.

The [CII] and [NII] lines in the central spaxel of both objects are well described by a single gaussian. However, the [OI] 63 μ m lines, where the PACS spectral resolution is best, have profiles indicative of weak (2–3 σ) deviations from a single gaussian function. The [OI] line in A1068 hints at a two-component structure in the form of a narrow core component on top of a broad underlying component comparable to the CO(2-1) profile in Edge (2001). Both [OI] lines observed in A2597 appear to have their dominant flux component at the systemic redshift of the BCG and a weaker component offset by about +250 km s $^{-1}$ which is also seen in the CO data (Salomé, priv. comm). We attribute the shared structure of these atomic and molecular lines to gas kinematics rather than self-absorption as the observed emission is from a large number of clouds that have much narrower intrinsic line width.

The resolution of PACS at the observed wavelengths varies from about 5'' for the [OI] 63 μ m line to about 14'' for the [CII] 157 μ m line. We have investigated line emission in all 25 spaxels of the PACS FoV. In all cases the line flux is dominated by the central spaxel. Summing up the flux in all 25 spectra and comparing it to the flux in the central spaxel shows no evidence of excess line flux as compared to what is expected from a point source. In order to properly recover the full beam line fluxes we have applied point source corrections (appendix A of the PSPC document) to the central spaxel integrated line fluxes. The results are listed in Table 2. This spatial resolution matches the best sub-mm interferometry results for CO (Edge & Frayer 2003; Salomé & Combes 2004) which implies that most of the emission is on scales < 5'' so we believe our PACS line fluxes can be compared to literature values without large beam corrections.

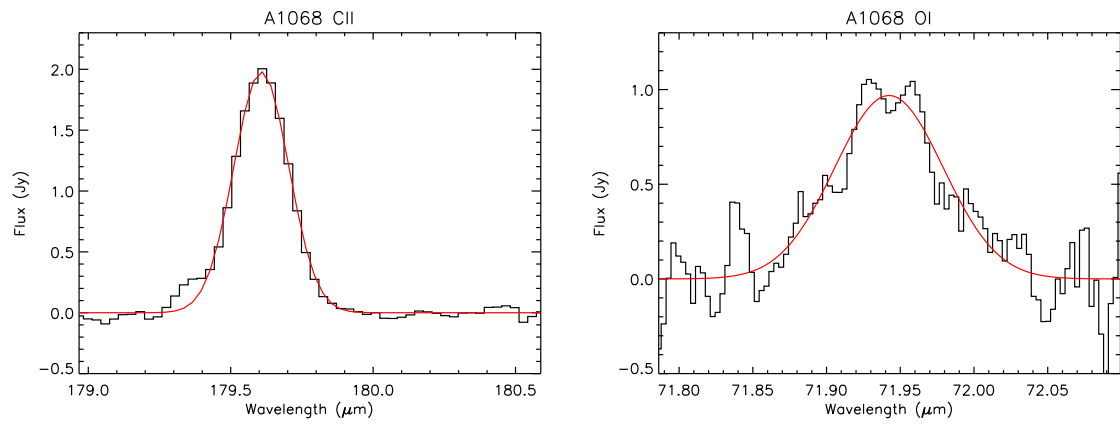


Figure 5.1 — *Herschel* PACS spectra of [CII] and [OI] in A1068

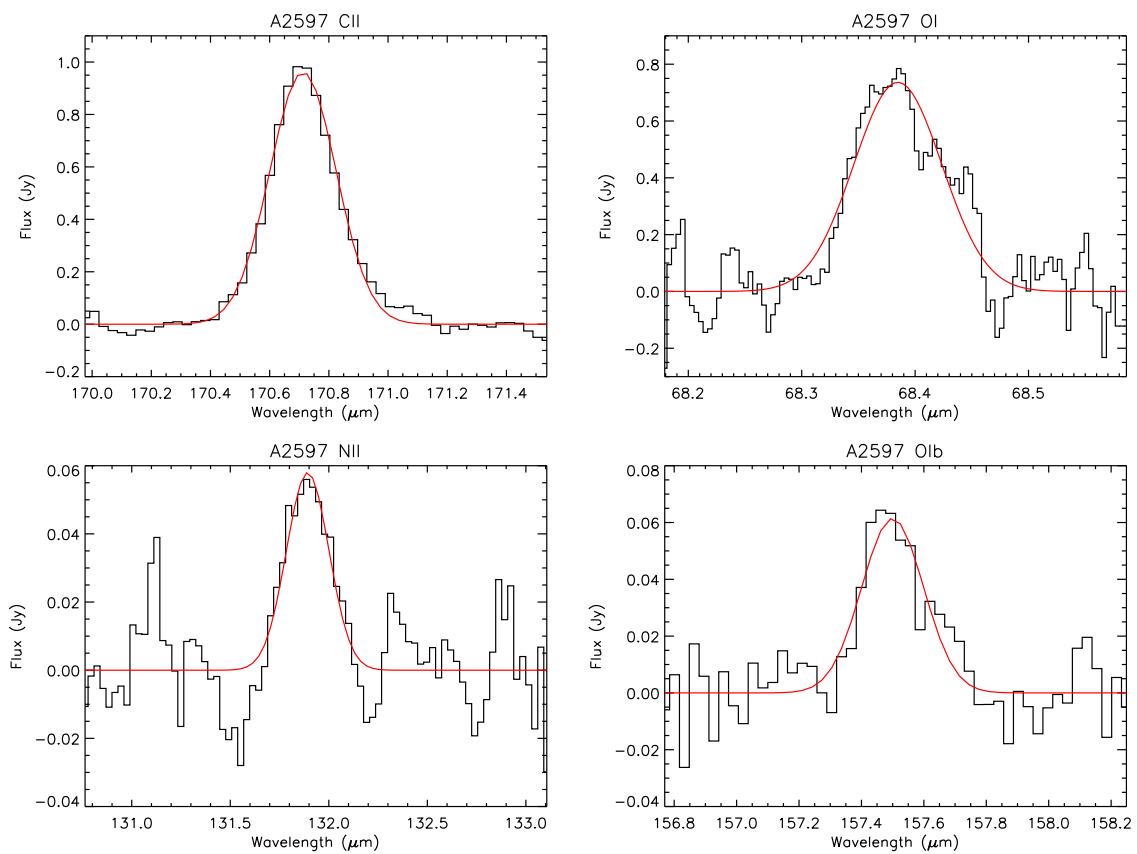


Figure 5.2 — *Herschel* PACS spectra of [CII], [OI] (63 μ m), [NII] and [OIb] (145 μ m) in A2597.

5.4 Discussion

The primary result from the SDP observations for this project is that the atomic cooling lines are present in both observed clusters. This first detection of these lines in cluster cores reinforces the importance of the cold gas in these environments. However, there are a number of questions that these detections raise.

How do the properties of the FIR lines compare to local LIRGs/ULIRGs? There have been several studies of local galaxies with ISO and high redshift galaxies using ground-based instrument that cover [CII] and [OI] (Malhotra et al. 1997, Maiolino et al. 2005, Hailey-Dunsheath et al. 2010). These studies show that the ratio of [CII] to FIR luminosity is a function of luminosity with relatively less [CII] emission for the most FIR luminous sources. Using the FIR data from Edge et al. (2010), we calculate the [CII] to FIR luminosity ratios are $10^{-2.4}$ and $10^{-1.9}$ for A1068 and A2597, respectively. The [CII]/FIR ratios of these two galaxies are comparable to those measured for galaxies of similar L_{FIR} (see Fig. 2 of Maiolino et al. (2005)). In particular, the [CII] to FIR luminosity ratio is lower for the more FIR luminous of the two galaxies. The ratio of [CII] to [OI] shows less variation (1.62 and 1.07) and is again consistent with other comparable galaxies (Luhman et al. 2003). Also our CO(1-0) to FIR luminosity ratios of $10^{-5.7}$ and $10^{-5.6}$ for A1068 and A2597 are consistent with star-forming local galaxies (Malhotra et al. 1997). So, despite potential differences in excitation, pressure and metallicity, the relative intensity of the atomic and molecular lines to the FIR luminosity do not distinguish the BCGs studied here from other FIR bright galaxies.

How do the dynamics of atomic and molecular lines compare? The relative velocity width of the atomic lines compared to the CO and MIR H₂ lines can provide important diagnostics for the dynamics and energetics of the various gas tracers. From the line width alone the resolution corrected line FWHM widths for the [CII] and [OI] lines are $\approx 330 \text{ km s}^{-1}$ and $\approx 400 \text{ km s}^{-1}$ for A1068 and A2597 respectively. This compares to $243 \pm 13 \text{ km s}^{-1}$ (Edge 2001) and $292 \pm 45 \text{ km s}^{-1}$ (Salomé, priv. comm.) for CO(2-1) for A1068 and A2597. In each case the FIR lines are a factor of ~ 1.35 broader. This is not due to any instrumental broadening in the PACS instrument as the two lines sampled have similar intrinsic line width despite being observed at very different resolution. Instead, this difference is more likely to be related to the lines being emitted from different regions within the BCG or in shocks. However, this clearly needs to be tested in more systems and through direct comparison of the [CII] and [OI] extent with that of CO.

How do the FIR line ratios constrain the gas properties? The relative strength of the FIR lines can constrain several key properties of the gas phase that dominates the emission. The main constraint we can determine directly from our current data is from the [CII] $158\mu\text{m}$ and [OI] 63 and $145\mu\text{m}$ lines for A2597. Kaufman et al. (1999) present photodissociation region (PDR) model predictions for the [OI] $145\mu\text{m}/63\mu\text{m}$ and [CII] $158\mu\text{m}$ to [OI] $63\mu\text{m}$ line ratios. Combining these two constraints for our observed [OI] $145\mu\text{m}/63\mu\text{m}$ ratio of 0.06 ± 0.02 and [OI] $63\mu\text{m}$ to [CII] $158\mu\text{m}$ ratio of 0.94 ± 0.05 , we estimate a density of $10^{3.3 \pm 0.5} \text{ cm}^{-3}$ and an incident FUV flux of G_0 of 150–1000 Habing units. These values of G_0 imply intrinsic FUV luminosities of $\approx 2 - 5 \times 10^{43} \text{ erg s}^{-1}$ if the clouds subtend 3–5 kpc. This is comparable to the observed FUV luminosities of these galaxies once dust absorption is taken into account (O’Dea et al. 2004).

5.5 Conclusions

These initial results from *Herschel* indicate that atomic cooling lines are present in the brightest cluster galaxies in cooling flow clusters. The intensity and velocity width of these lines is consistent with all the other observed tracers of cold gas in these systems implying they originate from the same population of clouds. The only apparent exception to this in our current observations is that the FIR lines appear to be systematically broader than the CO lines implying that the *relative* intensity of these lines varies with position within the BCG. The results that will come from our Open Time Key Project for 11 BCGs will expand greatly on those presented here with more lines and a greater range of BCG properties. Beyond this, the potential for *Herschel* to illuminate the properties of the cold gas that may fuel cold nuclear accretion in more distant clusters and local groups is vast.

5.6 Acknowledgements

We would like to thank the *Herschel* Observatory and instrument teams for the extraordinary dedication they have shown to deliver such a powerful telescope. We would like to thank the HSC and NHSC consortium for help with data reduction pipelines. J.B.R.O. thanks HSC, the *Herschel* Helpdesk and the PACS group at MPE for useful discussions. R. M. thanks the NHSC for the HIPE tutorials.

Bibliography

- Crawford, C. S., Allen, S. W., Ebeling, H., et al. 1999, MNRAS, 306, 857
Donahue, M., Jordán, A., Baum, S. A., et al. 2007, ApJ, 670, 231
Edge, A. C., 2001, MNRAS, 328, 762
Edge, A. C., & Frayer, D. T. 2003, ApJ, 599, L69
Edge, A. C., Oonk, J. B. R., Mittal, R., et al. 2010, A&A, submitted
Egami, E., Rieke, G. H., Fadda, D., et al. 2006, ApJ, 652, L21
Ferland, G. J., Fabian, A. C., Hatch, N. A., et al. 2009, MNRAS, 392, 1475
Hailey-Dunsheath, S., Nikola, T., Stacey, G. J., et al. 2010, ApJL, 714, L162
Jaffe, W., & Bremer, M. N., 1997, MNRAS, 284, 1
Kaufman, M. J., Wolfire, M. G., Hollenback, D. G., et al. 1999, ApJ, 527, 795
Luhman, M. L., Satyapal, S., Fischer, J., et al. 2003, ApJ, 594, 758
Maiolino, R., Cox, P., Caselli, P., et al. 2005, A&A, 440, L51
Malhotra, S., Helou, G., Stacey, G. J., et al. 1997, ApJ, 491, L27
McNamara, B. R., Wise, M. W., & Murray, S. S. 2004, ApJ, 601, 173
McNamara, B. R. & Nulsen, P. E. J. 2007, ARA&A, 45, 117
O’Dea, C. P., Baum, S. A., Mack, J., et al. 2004, ApJ, 612, 131
O’Dea, C. P., Baum, S. A., Privon, G., et al. 2008, ApJ, 681, 1035
Ott, S. 2010 in ASP Conference Series, Astronomical Data Analysis Software and Systems XIX, Y. Mizumoto, K. I. Morita, and M. Ohishi, eds., in press
Peterson, J. R., & Fabian, A. C. 2006, PhR, 417, 1
Pilbratt, G., et al. 2010, A&A, submitted

Poglitsch, A., et al. 2010, A&A, submitted

Salomé, P., & Combes, F. 2003, A&A, 412, 657

Salomé, P., & Combes, F. 2004, A&A, 415, L1

Sarazin, C. L., Burns, J. O., Roettiger, K., et al. 1995, ApJ, 447, 559

Chapter 6

Optical Line Emission in Brightest Cluster Galaxies

We present new observations in combination with photo-ionisation modelling of the optical line emitting gas for the Brightest Cluster Galaxies in the cool-core clusters Abell 2597, Abell 2204 and Sersic 159-03. The spectra show that these Brightest Cluster Galaxies are extreme examples of low ionisation nuclear emission line regions. Optical line emission is traced out to about 20 kpc from the nuclei. On large scales, the degree of ionisation and the density of the optical gas are found to decrease with distance from the nucleus.

The measured Balmer decrements are constant across tens of kpc in A2597 and A2204. These decrements are consistent with dust obscuration following a Milky-Way-type extinction law with $A_V \sim 1$. The Balmer decrements measured in S159 imply little to no dust obscuration. All three systems show strong line emission from [OI] and [NI]. These lines indicate the presence of an extended, warm, weakly ionised gas phase. The constancy of these lines relative to the Balmer lines within a single object as well as for a large sample of cool-core BCGs is striking.

Photo-ionisation by stars, AGN and bremsstrahlung are investigated using the MAPPING3 code for A2597. We find that stars cannot reproduce the observations. Both an AGN and bremsstrahlung can reproduce most of the optical line ratios within a factor of two. A pure AGN model or a model combining stars and bremsstrahlung provides the best fit to the data. The cooling rates per H-nucleus for the ionised, neutral and molecular gas at $T < 10^4$ are found to be comparable. Together with the constancy of the line ratios this strongly suggests that there is a single heating mechanism for these gas phases.

Our models show that this gas can be heated via secondary electrons created by primary photons with energies of about 40-100 eV. We consider a remnant cooling flow model in which an ultra-soft 300 eV component provides the required photons. This model does not violate the observational limits on a residual cooling flow in A2597.

(To be submitted)

J. B. R. Oonk¹, N. Bremer¹, W. Jaffe¹, B. Groves¹, M. N. Bremer²

¹Leiden Observatory, Leiden University, P.B. 9513, Leiden, 2300 RA, The Netherlands

²Department of Physics, H.H. Wills Physics Laboratory, Bristol University, Tyndall Avenue, Bristol BS8 1TL, United Kingdom

6.1 Introduction

Cool-cores are central $\sim 10^2$ kpc regions of rich galaxy clusters where the hot thermal X-ray emitting gas ($T \sim 10^8$ K) is dense enough to cool radiatively within a Hubble time (see Peterson & Fabian 2006; Fabian et al. 1994, for reviews). Cooling rates of the order of $10^{2-3} M_{\odot} \text{ yr}^{-1}$ have been estimated for this hot X-ray gas, but detailed X-ray spectroscopy shows that at most 10% of the X-ray emitting gas cools below one third of the virial temperature (e.g., Peterson & Fabian 2006). The solution most often invoked in the literature is that some form of reheating balances the radiative cooling of the X-ray gas, but the detailed nature of this process is unknown.

A similar problem concerns the cooler (10^{1-4} K) gas components within 50 kpc of the centers of these galaxy clusters. These emission-line nebulae are centered on the Brightest Cluster Galaxy (BCG) and emit far more energy than can be explained by the simple gas cooling (Heckman et al. 1989; Jaffe, Bremer & Baker 2005). The optical line emission would imply gas cooling rates up to $10^4 M_{\odot} \text{ yr}^{-1}$ (Heckman et al. 1989; Voit & Donahue 1997; Crawford et al. 1999). Such strong cooling rates do not agree with observations of cold gas in these systems (Edge 2001; Salome & Combes 2003).

The observations thus imply that these cooler gas phases also need to be reheated. The detailed reheating mechanism for this gas and whether it is linked to the reheating of the hot X-ray gas is currently not clear. Observations do show a strong correlation between the existence of these cooler gas nebulae and the existence of a cool-core as inferred from X-ray observations, suggestive of a strong link between the two (e.g. Crawford et al. 1999).

6.1.1 This Project

We present new, deep long-slit spectra of three Low Ionisation Nuclear Emission line Region (LINER) BCGs in cool-core clusters. The optical spectra contain a wealth of diagnostics. Previous investigations (Donahue & Voit 1991; Crawford & Fabian 1992; Voit et al. 1994; Ferland et al. 2009) have used the CLOUDY code (Ferland 1993; Ferland et al. 1998) to analyse the optical line emission in cool-core BCGs. Here we will investigate this gas using as an analysis tool the plasma code MAPPINGS III (Sutherland & Dopita 1993). The goals of this initial paper are to use simple photoionisation models to explore the physical conditions at various radii in the clusters, to verify that different codes yield similar results, and to investigate possible sources of energy input into the gas.

Our targets are LINER BCGs that we have previously observed in the infrared (Jaffe et al. 2005; Oonk et al. 2010). These objects were selected based on their high cooling rates, strong $H\alpha$, H_2 emission and low ionisation emission lines. The latter selection criterion was chosen in order to minimise the role that their AGN have on the global radiation field. Abell 2597 (hereafter A2597), Abell 2204 (hereafter A2204) and Sersic 159-03 (hereafter S159) have been the subject of numerous investigations and have been observed at many wavelengths from radio to X-rays (e.g. Johnstone, Fabian & Nulsen 1987; Heckman et al. 1989; Crawford & Fabian 1992; Allen 1995; Voit & Donahue 1997; Edge 2001; Wilman et al. 2002; O’Dea et al. 2004; Jaffe et al. 2005; Wilman et al. 2006, 2009; Oonk et al. 2010, 2011).

The direct goals of this paper are to (i) study the variation in the emission line ratios with distance to the nucleus and (ii) to study the impact of known sources of energy input on the

optical line emitting gas. In Section 2 we describe the reduction of the observations. In Section 3 we present the results of the observations. In Section 4 we show the results in terms of diagnostic line ratio diagrams. In Section 5 we perform an initial analysis of the properties for the optical line emitting gas. In Section 6 we investigate a grid of simple stellar, AGN and bremsstrahlung photoionization models. In Section 7 we present and explore our best-fit photoionisation model. In Section 8 we discuss our results and in Section 9 we present our conclusions.

Throughout this paper we will assume the following cosmology; $H_0=72 \text{ km s}^{-1} \text{ Mpc}^{-1}$, $\Omega_m=0.3$ and $\Omega_\Lambda=0.7$.

6.1.2 Targets

For A2597 the BCG is PGC 071390 at $z=0.0821$ (Voit & Donahue 1997) which corresponds to a luminosity distance 363 Mpc and an angular size scale $1.5 \text{ kpc arcsec}^{-1}$. For A2204 the BCG is ABELL2204_13 at $z=0.1517$ (Pimblet et al. 2006) which corresponds to a luminosity distance 702 Mpc and an angular size scale $2.6 \text{ kpc arcsec}^{-1}$. For S159 the BCG is ESO 291-G009 at $z=0.0564$ (Maia et al. 1987) which corresponds to a luminosity distance of 245 Mpc and an angular size scale of $1.1 \text{ kpc arcsec}^{-1}$.

6.2 Observations and Reduction

We have observed the central BCG in the three cool-core clusters with the Focal Reducer/low dispersion Spectrograph (FORS) in long-slit mode on the Very Large Telescope (VLT). The observations are summarised in Table 6.1. Similar, but less deep, optical spectroscopy for A2597, A2204, S159 has previously been presented by Johnstone, Fabian & Nulsen (1987); Crawford & Fabian (1992, 1993); Allen (1995); Heckman et al. (1989); Voit & Donahue (1997); Crawford et al. (1999); Wilman et al. (2006).

The spectra were taken with FORS in long-slit mode using two wavelength setups, a blue (short wavelength) and a red (long wavelength) setting. The slit positions are shown in Fig. 6.1. For A2597 two slit positions were observed, we will refer to these as A2597-NUC and A2597-OFF. For A2204 one slit position was observed, which we will refer to as A2204-NUC. For the A2597 and A2204 observations the central wavelengths were chosen so that the blue setting covers the wavelength range from [OII] 3727 Å to [OIII] 5007 Å and the red setting covers the wavelength range from $H\beta$ to [NII] 6584.

An additional red spectrum for the A2597-OFF position was taken with the central wavelength shifted further to the red so that the spectrum covers the range from [NI] 5200 Å to [SII] 6731 Å. This additional spectrum is only used to obtain information on the [SII] lines at 6717 Å and 6731 Å and is not discussed further in this work.

For S159 two slit positions were observed, these we will refer to as S159-NUC and S159-OFF. For the S159 observations the central wavelengths were chosen so that the blue setting covers the wavelength range from [OII] 3727 to [OIII] 5007 and the red setting covers the wavelength range from λ 5300 Å to [SII] 6731 Å.

The observations were taken in photometric conditions with a seeing better than 1 arcsec. The reduction is performed using dedicated IDL routines. The frames are dark and flat cor-

rected. Hot pixels, cosmics and artifacts are identified and interpolated over. The wavelength solution is obtained from arc frames and the spatial distortion of the slit is corrected.

The flux scale is set using spectroscopic standard stars. Continuum emission is subtracted from each BCG by using spectra from elliptical companion galaxies in the cluster. The observations for these companions were done on the same night, in the same weather conditions and with the same setup as the observations done for the BCGs.

6.3 Observational Results

The reduced spectra are shown in a two-dimensional form (wavelength vs. position) in Figs 6.2 - 6.4. Five slit positions were observed in three systems, c.f. Fig. 6.1. Line emission is detected in all five slits and found to be extended on scales of tens of kpc.

Optical line emission is detected out to 18 kpc north and 7 kpc south of the BCG nucleus in the A2597-NUC slit. The A2597-OFF slit also shows prominent line emission in several connected clumps over 20 kpc. A disconnected, weak clump is present in $H\alpha$, [NII] 6584 Å and [OII] 3727 Å emission, about 12 kpc northwards from the tip of the main emission structure along the slit. This clump is even more pronounced in the A2597-OFF observation for which the central wavelength was shifted towards the red. The location of this clump corresponds to the north-eastern filament observed in FUV, $Ly\alpha$ and $H\alpha$ (O’Dea et al. 2004; Jaffe et al. 2005; Oonk et al. 2011).

For A2204 only one slit position, centered slightly eastward of the BCG nucleus, was observed. In this BCG line emission is detected out to 18 kpc north and 18 kpc south of the peak in the optical continuum. In S159 two slit positions were observed. The S159-NUC slit is centered on the BCG nucleus along an axis with a position angle (PA) of about 40 degrees (relative to north and measured through east). In this slit most of the line emission is detected north-east of the nucleus, out to 9 kpc. This emission is smoothly connected to the nucleus. There is also line emission towards the south-west. This emission is concentrated in a clump about 3 kpc eastwards of the nucleus. The $H\alpha$ and [NII] 6584 Å emission indicate the presence of second clump about 8 kpc south-west of the nucleus.

The S159-OFF slit does not intersect the nucleus, but traces the line emission along an axis with a PA of about -25 degrees and is centered slightly eastward of the nucleus. It shows very extended line emission towards the north of the BCG, out to 31 kpc. There is also a small amount of line emission south-east of the BCG along this axis, out to about 4 kpc.

For the A2597-NUC, A2204-NUC and S159-NUC slit positions the observed peak intensity in the line emission agrees with the peak intensity of the optical continuum. For A2597-NUC and S159-NUC this position is consistent with the optical nucleus of the BCG. For A2204-NUC this position is slightly eastward of the nucleus. In all three cases we find that the line emission decreases rather smoothly with distance to the optical continuum.

The peak intensity of the line emission and of the optical continuum do not agree for the A2597-OFF and S159-OFF slit positions. In both cases we find that the decrease in line emission is not smooth with distance to the optical continuum. Several bright line emitting clumps are observed at various distances along the slit. With the exception of the northern-most clump in A2597-OFF, the clumps are observed to be embedded within a more diffuse component of low surface brightness line emission. From higher resolution imaging of these systems is it

known that the line emission is enhanced in narrow filaments (e.g. Donahue et al. 2000). It is therefore likely that the clumps observed here represent regions where our slits intersect these filaments.

Our low-spectral-resolution observations show that the optical line emission in all three BCGs has a complicated velocity structure. We will not present an analysis of this velocity structure here. Wilman et al. (2006) present the velocity structure of the optical gas in A2204 using integral-field spectroscopy. In Oonk et al. (2010) we present the velocity structure of the ionised and molecular gas in A2597 and S159 using near-infrared integral-field spectroscopy.

6.3.1 Spatially integrated spectra

The integrated spectra are shown in Figs 6.5-6.7 and the area over which they are integrated is specified in the caption of the corresponding figures. Integrated line fluxes are obtained from these integrated spectra using Gaussian fitting. We note that the line profiles at our spectral resolution are always well described by a Gaussian profile. Line fluxes are always given relative to $H\beta$ flux and the results are summarised in Tables 6.3 and 6.4. The only exception to this are the red S159 slits for which $H\beta$ was not measured and the line fluxes are given relative to $H\alpha$, see Table 6.5.

Due to the low spectral resolution of our spectra we have spectral features that are blended lines of the same atoms. These are the [OII] 3726 Å and [OII] 3729 Å lines, the [SII] 4069 Å and [SII] 4076 Å lines and [NI] 5198 Å and [NI] 5200 Å lines. We will refer to the sum of these lines as [OII] 3727 Å, [SII] 4069 and [NI] 5200 Å respectively.

There are also spectral features that are blended lines of different atoms. The HI 3888 Å ($H\zeta$) line is blended with the HeI 3889 Å line and we will refer to the sum of these lines as (HI+HeI) 3888 Å. Disentangling this blend is difficult. For a standard $T=10^4$ K and $n_e=100$ cm⁻³ gas and assuming case B recombination we find that $HI\ 3888/H\beta = 0.14$ and $HeI\ 3889/H\beta = 1.156$ (Osterbrock & Ferland 2006)). The observed line blend in our objects is consistent with almost pure HI 3888, but we cannot rule that a significant fraction is due to HeI 3889.

A second blend of lines detected in our objects is due to [NeIII] 3967 Å, [CaII] 3968 Å and HI 3970 Å ($H\epsilon$) line and we will refer to this blend as (NeIII+CaII+HI) 3966 Å. Assuming the same gas properties as above we find that $HI\ 3970/H\beta = 0.16$. This implies that most, but not all, of the flux in this blend is due to HI. The remainder is more likely contributed by [NeIII] 3967 than by [CaII] 3968, because [NeIII] is also detected at 3869 Å.

The remaining spectral lines can be separated in our spectra. In the innermost nuclear regions the strong increase in velocity dispersion broadens the lines considerably. In particular in A2204 where the slit also intercepted multiple velocity components. Separating the lines is more difficult here, but good multi-component Gaussian line fits were achieved everywhere. In the case of fitting the [NII] 6548 Å- $H\alpha$ -[NII] 6584 Å line complex we required that the line widths for all three lines are equal. This constraint is also applied when fitting the [OIII] 4959 and 5007 Å line pair, the [OI] 6300 and 6363 Å line pair, and the [SII] 6717 and 6731 Å line pair.

6.3.2 Variations along the Slit

We have plotted the spatial variation of the line emission, relative to $H\beta$, along each of the slits in Figs 6.8 - 6.10 for A2597, A2204 and S159. This investigation is limited by the signal-to-noise of the $H\beta$ line. Emission from the stronger lines is present in regions beyond where $H\beta$ was detected. The red spectra for S159 do not contain the $H\beta$ line and hence here we plot line flux relative to $H\alpha$.

Within each of the slits for A2597 the line ratios relative to $H\beta$ are observed to not vary greatly as function of distance. However, comparing the A2597-NUC slit with the A2597-OFF slit we find a significant decrease in the ionisation state of the gas. Relative to $H\beta$ the highest ionisation lines, i.e. [OII] 3727, [NeIII] 3869, [SII] 4069 and [OIII] 5007, decrease by at least a factor two from the nuclear region to the off-nuclear region.

Interestingly the lower ionisation lines, i.e. [OI] 6300 Å and [NI] 5200 Å, do not show this behavior. They remain constant relative to $H\beta$ not only within both slits but also upon comparing the two slits. These two neutral gas lines indicate the existence of a warm, extended, weakly ionised gas phase in these systems. We will discuss this phase in more detail in Section 6.7.

Similarly the Balmer line ratios also remain constant over the entire area probed by the two slits. The Balmer decrements in A2597 are consistent with a Milky-Way-type extinction law for $A_V \sim 1$ Miller & Mathews (e.g. 1972); Cardelli et al. (e.g. 1989). For the nuclear emission this agrees with a previous investigation by Voit & Donahue (1997). Our off-nuclear spectra now show that a similar amount of dust obscuration is present at large distances from the nucleus. Values for the Balmer decrements for all the clusters, and their conversion to extinction values are given in Table 6.2.

The A2204-NUC spectrum is very similar to that of A2597-NUC. The line ratios, relative to $H\beta$, showing the strongest changes are the highest ionisation lines. In particular [OIII] 5007 Å and [SII] 4069 Å both decrease by more than a factor two from the nucleus to the outer regions. The lower ionisation lines, [OI] 6300 Å and [NI] 5200 Å, also show a small decrease relative to $H\beta$, but less than a factor of two. The Balmer decrements in this system do not vary much as a function of position in this object and are consistent with Milky-Way-type extinction law for $A_V \sim 1$.

The S159 spectra are also similar to the A2597 spectra. The S159-NUC slit intersects the BCG nucleus and shows a clear decrease in the ratio of the high ionisation lines relative to $H\beta$ with distance from the nucleus. The ratio of the high ionisation lines to $H\beta$ is lower in the S159-OFF slit as compared to S159-NUC slit. There is some evidence for an increase in the ionisation state of the gas in the S159-OFF slit at 10 kpc from the peak in the optical continuum. This location also shows an increase in line intensity and in gas density. Again we observe that in this object the lower ionisation lines do not change as strongly. The [OI] 6300 Å line emission is constant, relative to $H\alpha$, within both slits and also upon comparing the two slits.

The Balmer decrements in the blue S159 slits are consistent with zero dust obscuration. This is very different from the high dust obscuration inferred for the other two systems. It is possible that the somewhat poorer stellar continuum subtraction for this object affects the Balmer lines. However, the spectra do not allow for strong deviations from the measured values. The red S159 spectra do not contain the $H\beta$ line and as such we are not able to investigate the $H\alpha/H\beta$ ratio for this object.

We thus find that all three BCGs decrease in the ionisation level of the gas with increasing distance from the nucleus. The only exception to this is the A2597-NUC slit. The gas here shows a constant ionisation within in the central 10 kpc from the nucleus. This implies that some process maintains the ionisation level of the gas in these regions. Interestingly these regions coincide with extended FUV and the radio emission (e.g. Oonk et al. 2011). The constancy of the low ionisation lines in A2597 and S159 is in good agreement with our previous near-infrared spectroscopic investigations (Jaffe et al. 2005; Oonk et al. 2010).

6.4 Diagnostic diagrams

A rough method to spectroscopically classify objects as star-forming or AGN dominated is to investigate their location in the so-called BPT diagrams (Baldwin et al. 1981). Here we focus on two such diagrams: (i) the $[\text{OIII}]5007/\text{H}\beta$ versus $[\text{NII}] 6584/\text{H}\alpha$ diagram and (ii) the $[\text{OIII}] 5007/\text{H}\beta$ versus $[\text{OI}] 6300/\text{H}\alpha$ diagram (see Fig. 6.12). The line ratios are chosen such that they are sensitive to the shape of the radiation field, whilst being insensitive to reddening by dust.

The y-axis in both diagrams is the $[\text{OIII}] 5007/\text{H}\beta$ ratio. This ratio is a proxy for the ionization parameter U . A large value implies that the photon density is high relative to the gas density. Values above unity for this ratio are typically seen in objects dominated by either vigorous star-formation or by a powerful AGN. We note that the $[\text{OIII}] 5007/\text{H}\beta$ ratio also depends on metallicity. An increase in the metallicity produces a decrease in this ratio because the cooling moves from the $[\text{OIII}] 5007$ line to the infrared fine structure lines (Stasinska 1980). Here we will assume that the gas metallicity is constant within each of our BCGs.

In order to further separate star-forming and AGN dominated objects we require a second line ratio on the x-axis. This could for example be $[\text{NII}] 6584/\text{H}\alpha$ or $[\text{OI}] 6300/\text{H}\alpha$. Both ratios are a proxy for the hardness of the incident radiation and larger values imply a harder spectrum i.e. there are relatively many photons with energies higher than 1 Rydberg that pass unabsorbed through the primary HII region and heat the neutral gas beyond.

Fig. 6.12 shows that our objects have a very low $[\text{OIII}] 5007/\text{H}\beta$ ratio, whilst having very high $[\text{NII}] 6584/\text{H}\alpha$ and $[\text{OI}] 6300/\text{H}\alpha$ ratios. This means that we classify these objects as neither star formation dominated (grey plusses in the figure) nor as AGN dominated (grey diamonds). In fact our BCGs are located in the so-called low-ionisation nuclear emission-line region (LINER) part of the standard BPT diagram (e.g. Heckman 1980; Filippenko 1996). In the original classification scheme an object is classified as a LINER if (i) $[\text{OII}] 3727/[\text{OIII}] 5007 > 1$ and $[\text{OI}] 6300/[\text{OIII}] 5007 > 0.3$ (Heckman 1980). In terms of the line ratios used in Fig. 6.12 this translates approximately to $[\text{OIII}] 5007/\text{H}\beta < 5$, $[\text{NII}] 6584/\text{H}\alpha > 0.6$ and $[\text{OI}] 6300/\text{H}\alpha > 0.1$.

Many normal galaxies show LINER type properties. Heckman (1980) finds that about one third of all spiral galaxies are LINERs. However, these galaxies only show LINER properties on rather small central scales, typically within a region less than 2 kpc from the nucleus. Cool-core BCGs show LINER properties over very extended regions with typical size of a few tens of kpc (e.g. Heckman et al. 1989; Crawford et al. 1999).

Evidently from our discussion of the changes in ionization state, the line ratios at different positions within our objects do not occupy a single position of the BPT diagrams. The nuclear

regions of our objects have higher values of $[\text{OIII}] 5007/\text{H}\beta$ as compared to the off-nuclear regions. This decrease is a factor 2-3 over a distance of about 10 kpc. Similarly there is a small decrease in the $[\text{NII}] 6584/\text{H}\alpha$ and $[\text{OI}] 6300/\text{H}\alpha$ ratio when comparing the off-nuclear regions to the nuclear region. The evolution of these ratios as a function of distance to nucleus is indicated by the arrows in Fig. 6.12. We thus find that our objects, especially their outer regions, show extreme LINER conditions.

The constancy of the $[\text{OI}]/\text{H}\alpha$ ratio within each of our targets is striking. Within a single system this ratio changes by less than a factor 1.5 over regions with sizes of about 20 kpc and probed with a spatial resolution of about 2 kpc. It is important to note here that $[\text{OI}] 6300$ line emission is observed only when a significant amount of warm, weakly ionised gas is present. We will discuss the physical conditions necessary to produce such a gas in more detail in Section 6.6. Here we note that classical HII regions do not produce a significant amount of $[\text{OI}] 6300$ emission. This directly implies that a significant non-stellar, high energy energy component must be present.

In Fig. 6.12 we plot as green circles the BCGs observed by Crawford et al. (1999). The measurements for most of the BCGs in the Crawford et al. (1999) sample are dominated by emission from the nuclear region. Combining the Crawford et al. (1999) sample with our BCGs we have a total of 56 BCGs for which the $[\text{NII}] 6584/\text{H}\alpha$ and $[\text{OIII}] 5007/\text{H}\beta$ ratios are reliably measured. For these objects we find a mean $[\text{OIII}] 5007/\text{H}\beta$ ratio of 0.69 ± 0.66 and a mean $[\text{NII}] 6584/\text{H}\alpha$ ratio of 1.11 ± 0.50 . Similarly, we have a total of 53 BCG measurements for which the $[\text{OIII}] 5007/\text{H}\beta$ and $[\text{OI}] 6300/\text{H}\alpha$ ratios are reliably measured. We find a mean $[\text{OIII}] 5007/\text{H}\beta$ ratio of 0.66 ± 0.66 and a mean $[\text{OI}] 6300/\text{H}\alpha$ ratio of 0.24 ± 0.06 for these objects. We thus observe that the spread in the $[\text{OI}] 6300/\text{H}\alpha$ ratio is significantly lower than in the $[\text{NII}] 6584/\text{H}\alpha$ ratio. The very low dispersion in $[\text{OI}] 6300/\text{H}\alpha$ over a large range in $[\text{OIII}] 5007/\text{H}\beta$ is intriguing and could be an important clue to the mechanism that heats the gas in cool-core BCGs.

To date it is still not well understood what powers the LINER emission in different objects. Strong AGN or vigorous star formation is ruled out by their low $[\text{OIII}] 5007/\text{H}\beta$ ratio. A variety of possibilities ranging from weak AGN (i.e. AGN with a low ionisation parameter), Wolf-Rayet stars, very hot O-stars, bremsstrahlung and shocks are discussed by Heckman et al. (e.g. 1989); Filippenko (e.g. 1996). In Section 6.6 we will use the MAPPINGS III photoionisation code to model the LINER emission in cool-core BCGs.

6.5 Gas properties

Some rough estimates for the properties of the gas in our targets can be directly derived from the observed line ratios (see Table 6.6). These estimates will be used as guidelines for our photoionisation models in Section 6.6. Prior to computing these estimates we correct our spectra for reddening by dust.

6.5.1 Dust

Assuming case B recombination, the reddening by dust can be estimated from the observed Balmer decrements. In A2597 and A2204 the measurements indicate significant reddening

(see Table 6.2). We find that the Balmer decrements in these BCGs are well described by a two-component dust model, consisting of (i) Galactic foreground and (ii) dust intrinsic to the BCG. Both dust components are consistent with an average Milky Way extinction law in the wavelength range covered by our optical spectra. This is consistent with previous investigations by Voit & Donahue (1997) and Oonk et al. (2011).

In this work we use the Milky Way extinction law by Miller & Mathews 1972 to de-redden our optical spectra. In Tables 6.3, 6.4 and 6.5 listing our measured line ratios we give values both corrected for extinction (in parenthesis) and uncorrected. In the case of S159 the $H\alpha/H\beta$ ratio is not measured in the same slit and therefore we do not provide a value for this ratio. The remaining Balmer decrements in the blue slits for S159 are consistent with zero reddening.

6.5.2 Temperature

There are several temperature sensitive line ratios in the optical wavelength range covered in this work (e.g. Osterbrock & Ferland 2006). Here we report gas temperatures derived from the $[NII] (6548+6584)/[NII] 5755$ ratio. Other temperature sensitive ratios are not used in this work, because only upper limits can be derived from them. For the spatially integrated spectra from the A2597-NUC and A2204-NUC slits we find a temperature of about 10000-12000 K in both objects. For the other slit measurements we can only report upper limits (see Table 6.6).

The relatively high gas temperatures found here are consistent with previous results by Voit & Donahue (1997) for A2597. Our measurements of the high $[OII] 3727/H\beta$ ratio in these systems supports this as well. This ratio depends strongly on the temperature and ionisation parameter gas. It also depends weakly on the metallicity of the gas. Our spectra indicate a low ionisation parameter ($\log(U) < -3$) for the the optical gas and in this case the $[OII] 3727/H\beta$ ratio is a good tracer of gas temperature.

6.5.3 Density

Commonly used line ratios to trace gas densities in the optical regime are $[OII] 3729/[OII] 3726$ and $[SII] 6717/[SII] 6731$. A higher value for either ratio implies a lower gas density at a given temperature (e.g. Osterbrock & Ferland 2006). We do not resolve the $[OII]$ line pair and as such we cannot use it. The $[SII]$ lines are resolved, but observed only in the S159 and the A2597-OFF spectra. In the latter case this was done using the wavelength shifted spectrum taken at the same position.

The A2597-NUC and A2204-NUC spectra do not include the $[SII]$ lines. Therefore we complement our data with the $[SII]$ measurements published by Voit & Donahue (1997) and Crawford et al. (1999), see Table 6.6. Strictly speaking the measurements by Voit & Donahue (1997) and Crawford et al. (1999) do not sample the exact same regions as our slits, but we believe both to be dominated by nuclear line emission and as such to be representative.

For spatially integrated spectra from the S159-NUC, S159-OFF and A2597-OFF slits we find the $[SII] 6717/[SII] 6731$ ratio to be in the range 1.4 to 1.6 (see Table 6.6). This implies low gas densities in the off-nuclear regions for both objects. A tight constraint on the density cannot be provided as the measured $[SII]$ ratios are so high that the measured values are in the saturated part of the line ratio versus density curve (e.g. Osterbrock & Ferland 2006). In our models below we will use a gas density of 50 cm^{-3} for these outer regions.

We have plotted the [SII] line ratio with distance along the slits in Fig. 6.11. The errors on [SII] line ratio are large and its use as a diagnostic at low densities is limited, however an interesting trend is apparent. The S159-NUC slit shows that the gas density decreases with distance from the nuclear region. A similar decrease is found for A2597 upon comparing our A2597-OFF [SII] measurements with the nuclear A2597 [SII] measurement by Voit & Donahue (1997). Decreasing gas density with distance from the nucleus has previously been found by Johnstone & Fabian (1988) for NGC 1275, the BCG in the Perseus cluster.

Both the S159-OFF and the A2597-OFF spectrum show variations in the [SII] line ratio that are consistent with local density increases away from the peak optical continuum. For S159-OFF there is an increase in the gas density about 10 kpc north of the continuum. For A2597-OFF there is a weak indication for an increase in the gas density at 5 kpc south of the continuum. Both cases coincide with regions having locally increased line emission intensity.

Our [SII] measurements are consistent with the range in values observed for a larger sample of BCGs by Crawford et al. (1999). For the 24 BCGs in their sample, where the [SII] lines were measured with a signal to noise greater than three, we find that the average [SII] ratio is 1.45 ± 0.47 . Crawford et al. (1999) also find variations in the [SII] ratio within BCGs. The variations in [SII] observed within individual objects are consistent with the clumpy, filamentary nature of the optical gas in these objects.

Future integral field observations will be able to establish the relationship between the gas density and its morphology in more detail. In order to investigate the low density gas in these objects in more detail a diagnostic different from the [SII] line ratio is required. We furthermore note here that the [SII] line ratio also depends weakly on the temperature of the gas. We have no reliable gas temperature measurements away from the central nucleus in our objects and thus we can not investigate whether a change in gas temperature could also contribute to the observed trends.

6.5.4 Metallicity

Gas metallicities can be reliably determined for HII regions and star-forming galaxies (e.g. Kewley & Dopita 2002; Nagao, Maiolino & Marconi 2006). We have applied the relation between the [OII] 3727 and [NII] 6584 lines by Kewley & Dopita (2002) to derive metallicity estimates for the gas in our BCGs. We find that the gas in these systems has a metallicity equal to or slightly larger than solar metallicity (see Table 6.6). There is an inherent uncertainty in this derivation, as it is not known if the metallicity relations derived for HII regions apply to BCGs.

Using stellar population models by Bruzual & Charlot (2003) we find that the stellar populations in these systems have a solar to slightly super-solar metallicity. This is consistent with our estimate of the gas metallicity, but we note that the gas metallicity does not need to be the same as the stellar metallicity.

6.5.5 Ionisation Parameter

We use the [OIII] 5007/[OII] 3727 ratio with the relation by Kewley & Dopita (2002) to derive the ionisation parameter U . We find a narrow range of values for the ionisation parameter in our BCGs, i.e. from $\log(U)=-3.6$ to $\log(U)=-3.3$ (see Table 6.6). The nuclear spectra have a

higher ionisation parameter than the off-nuclear regions. This trend was also observed using the [OIII] 5007/H β ratio in Section 6.4.

6.6 MAPPINGS III line modelling

The optical spectra show that the BCGs in A2597, A2204 and S159 are (extreme) LINERs (see Section 6.4). Currently it is not clear what process powers this emission, especially of such extended regions with sizes up to a few tens of kpc.

In the previous section we derived estimates for the global physical conditions in the optically emitting gas in these systems. This analysis is too general to lead directly to a specification of excitation mechanisms. Towards this end we reverse the procedure here; we will model the distribution of emitting atoms resulting from excitation by various photoionisation sources. From the resulting spectra we will find the characteristics of the sources that produce the best fits to our observations. We will find, as did other authors ((e.g. Johnstone & Fabian 1988; Donahue & Voit 1991; Crawford & Fabian 1992; Voit & Donahue 1997)) that stellar sources cannot explain the data, and we will consider several alternative scenarios.

Here we present an initial investigation into the heating and excitation of the optical line emitting gas under the assumption of a local photoionising source using the MAPPINGS III code. MAPPINGS III is an updated version of the MAPPINGS II code (Sutherland & Dopita 1993). With this code we explore three energy sources; (i) stars, (ii) AGN and (iii) bremsstrahlung. We will only consider primary energy inputs in the form of photons.

We compute grids of models for these energy sources. Results are presented for plane-parallel, isochoric models with a geometric dilution factor of 0.5. We run the models for two constant density regimes $n(\text{H})=50 \text{ cm}^{-3}$ and $n(\text{H})=300 \text{ cm}^{-3}$. We assume that the gas is in a dust-free environment with a metallicity equal to one solar metallicity. The detailed abundances used here are based on modelling of the Sun by Asplund, Grevesse & Sauval (2005) and these were previously used by Groves et al. (2008) to model starburst galaxies. Models including dust and with different geometries will be presented in a future paper. The models are temperature bounded and stopped when the temperature becomes less than a 1000 K.

From these grids we extract best-fitting models for the observed A2597-NUC and A2597-OFF spectra. The A2204 and S159 spectra are very similar to A2597 and therefore we believe that by limiting the discussion to A2597 we do not restrict ourselves to a particular case.

A number of spectral features, outside of the optical regime, will also be investigated. These are the near-infrared K-band ionised gas line ratios (Oonk et al. 2010) and the mid-infrared [NeIII] 15.5 μm to [NeII] 12.8 μm ratio (Jaffe & Bremer in prep.). In particular the latter ratio is of interest, because we find that this Neon ratio is about 0.4 for each of the three systems considered here.

Several studies find similar values for this Neon ratio in other cool-core BCGs (Ogle et al. 2010; Donahue et al. 2011). In particular this value for the Neon ratio is not only observed in the nuclear area but also in gaseous filaments far from the nucleus (Johnstone et al. 2007). The constancy of this ratio indicates that it could be an important constraint in distinguishing between different gas heating models. We note that our measurement of this Neon ratio in A2597 disagrees with a recent measurement by Donahue et al. (2011). These authors find the Neon ratio to be about 1 in A2597. In this work we will use our measurement.

Due to the difference in spatial resolution and spatial coverage for the infrared and optical spectra we will not use the infrared ratios as a hard constraint for our models. Here we will focus on fitting the optical lines and check whether the best-fitting optical models can also reproduce the infrared line ratios.

Our method in this section is to model three types of photoionisation spectra: stellar, AGN and bremsstrahlung. Within each type we explore a grid of models varying the intensity of the spectrum and its hardness in order to find: (i) the best-fitting models with respect to the $[\text{OII}] 3727/[\text{OIII}] 5007$ and the $[\text{NeIII}] 15.5/[\text{NeII}] 12.8$ ratio for the A2597-NUC spectrum, and (ii) to find the best-fitting models with respect to the $[\text{OII}] 3727/[\text{OIII}] 5007$ and the $[\text{OI}] 6300/\text{H}\alpha$ ratio for the A2597-OFF spectrum. The first investigation deals with the ionisation state of the gas and the second investigation deals with the heating problem of the gas. For these models we compare the model predictions for all stronger emission lines with the observed values. We will find that none of the models satisfactorily represents all the major line ratios. We will then consider combinations of the simple spectra and provide a more detailed fit to the full optical spectrum in Section 6.7.

6.6.1 Stars

It has already been shown in previous studies that stars alone cannot account for the observed optical spectrum in cool-core BCGs (e.g. Johnstone & Fabian 1988; Donahue & Voit 1991; Crawford & Fabian 1992; Voit & Donahue 1997). However, recent infrared and ultraviolet studies suggest that stars could be forming with rates up to $10^{1-2} M_{\odot} \text{ yr}^{-1}$ in these systems (e.g. O’Dea et al. 2008, 2010; Donahue et al. 2010; Oonk et al. 2011). Young stars may therefore contribute significantly to the radiation field heating the gas and so we deem it important to take this source as the starting point of our analysis.

We model stars as black body spectra in the energy range from 0 to 136 eV. Using MAP-PINGS III we investigate a two dimensional grid of stellar temperature T_{BB} and ionisation parameter U . The temperature is varied from 40000 to 80000 K in steps of 5000 K. The ionisation parameter is initially varied from $\log(U)=-5$ to $\log(U)=-1$ in steps of 0.5 dex. This grid is performed for two density regimes, $n(\text{H})=50 \text{ cm}^{-3}$ and $n(\text{H})=300 \text{ cm}^{-3}$. In each case the metallicity of the gas was set equal to solar metallicity. The results are summarised in Figs 6.13 and 6.14. These figures are somewhat complicated because they attempt to display information on four line ratios in a two dimensional plot.

The results of the model calculations for the primary BTP line ratios are shown as a grid of straight lines in the diagrams, as a function of the model parameters. On top of this grid we show as squares and triangles the loci of models having $[\text{NeIII}]/[\text{NeII}]$ and $[\text{OIII}]/[\text{OII}]$ ratios that lie within 10% of the observed values. The large green circle shows our data for A2597 and the smaller grey circles show BCGs from the sample by Crawford et al. (1999). In a successful model, then, the green observed data point would lie on the grid at a point where the triangle and square loci cross. We will use the grids to identify models with line ratios close to the A2597 measurements. We then explore the permitted parameter range around these particular models further by refining the step size in U .

In the case of A2597-NUC (Fig. 6.13) the stellar models can reproduce the measured $[\text{OIII}] 5007/[\text{OII}] 3727$ and $\text{NeIII} 15.5/\text{NeII} 12.8$ ratios at the point where the triangles and squares cross: $T_{BB}=55000 \text{ K}$ and $\log(U)=-3.625$. However, this is not the position of the green

dot in the figure. This model for A2597-NUC severely underpredicts the emission in the metal lines relative to the Balmer emission.

In the case of A2597-OFF (Fig. 6.14) we find that none of the stellar models are able to produce an [OI] 6300/H α ratio greater than 0.2. For comparison purposes we therefore define the best-fitting stellar model for A2597 as the model that reproduces the observed [OIII] 5007/[OII] 3727 ratio and is the closest to the measured [OI] 6300/H α ratio. This model has $T_{BB}=70000$ K and $\log(U)=-3.75$.

For both of the best-fitting stellar models the model line ratios for all stronger lines are compared to the observations in Tables 6.7 and 6.8. The high model value for the [NII](6548+6584)/NII(5755) ratio shows that the stellar models do not provide enough heat. This is confirmed by the low model value for the [OII] 3727/H β and [OI] 6300/H β ratios. For low ionisation parameters ($\log(U)<-3$) the [OII]/H β ratio is a tracer of gas temperature for a fully ionised gas. The stellar models investigated here cannot produce a [OII] 3727/H β above 4. Similarly the [OI]/H β ratio is a tracer of a warm, weakly ionised gas.

We can attempt to increase the gas temperature by lowering its metallicity, which reduces the cooling efficiency. However, in our models lowering the metallicity would lower the emission of metal lines relative to the Hydrogen even further. Investigating the same grid of stellar models with a 0.4 solar metallicity gas shows that this produces even worse fits to A2597 observations.

Another way to increase the temperature is to supply higher energy photons. The energy of the photons in excess of that necessary to ionise the gas is available for heating. At energies beyond ~ 30 eV the ejected electrons can create secondary electrons that then heat the gas further via collisions. If the flux of high energy photons is low enough then this process can provide a lot of heat whilst keeping the ionisation low. Two sources that can provide high-energy photons are AGN and bremsstrahlung and we will investigate these now.

6.6.2 AGN

Johnstone & Fabian (1988) and Heckman et al. (1989) show that an AGN in the form of a point-like radiation source cannot simultaneously explain the observed change of the optical line ratios and the distribution of line emission in cool-core BCGs. This implies that an AGN cannot be responsible for the heating of the gas at large distances from nucleus. However, radio observations show that cool-core BCGs have an AGN at their centres. Our optical spectra display that there is an increase in the ionisation state in the centre of these systems. This could indicate that the AGNs do contribute to radiation field here and hence we deem it important to also include this source in our investigation.

We model an AGN as a power law spectrum in the energy range 5-300 eV. The shape of the AGN spectrum is given by $I_\nu \sim \nu^\alpha$, with ν the frequency and α the spectral index. Using MAPPINGS III We investigate a two dimensional grid in spectral index and ionisation parameter. The spectral index is varied from -2.4 to -0.6 in steps of 0.2. The ionisation parameter is initially varied from $\log(U)=-5$ to $\log(U)=-1$ in steps of 0.5. This grid is performed for the same metallicity and densities as in Section 6.6.1. The results are summarised in Figs 6.13 and 6.14. After identifying good models for A2597 within this grid, we explore the parameter space further by refining the step size in U.

In the case of A2597-NUC ($n(H)=300 \text{ cm}^{-3}$) we find that the AGN models cannot simultaneously reproduce the measured [OIII]5007/[OII] 3727 and NeIII 15.5/NeII 12.8 ratios. Inde-

pendent of the spectral index, the measured [OIII] 5007/[OII] 3727 ratio only allows for a very narrow range in the ionisation parameter around $\log(U)=-3.75$. At the same time the measured NeIII 15.5/NeII 12.8 ratio requires $\log(U)<-4.5$. The best-fitting AGN model for A2597-NUC is defined as the model that reproduces the observed [OIII] 5007/[OII] 3727 ratio and is closest to the observed [NII] 6584/H α and [OI] 6300/H α in Fig. 6.13. This model has $\alpha=-1$ and $\log(U)=-3.75$. It produces too much emission in the Helium and metal lines relative to the Balmer emission, but it is able to reproduce most optical line ratios to within a factor of 2. The most problematic ratio is NeIII 3869/H β , which is a factor of three higher than measured.

In the case of A2597-OFF ($n(\text{H})=50 \text{ cm}^{-3}$), the AGN models can reproduce both the [OIII] 5007/[OII] 3727 and [OI] 6300/H α ratios for a single combination of $\alpha=-1.2$ and $\log(U)=-4$. This best-fitting A2597-OFF model reproduces most optical line ratios to within a factor of two. It has the same problem as the best-fitting model for A2597-NUC. In addition this model also produces too much emission in the SII 6717 and 6731 lines. The AGN models for A2597-OFF also allow for only a very narrow range in ionisation parameter around the best-fitting value. The line ratios for the best-fitting AGN models are summarised in Tables 6.7 and 6.8.

6.6.3 Bremsstrahlung

Several authors have previously considered bremsstrahlung as a mechanism to provide the high energy photons necessary to heat the gas (e.g. Johnstone & Fabian 1988; Heckman et al. 1989; Donahue & Voit 1991; Crawford & Fabian 1992). It is not clear whether or not there is enough bremsstrahlung present in order to account for all of the required energy. We will discuss this issue in more detail in Section 6.7

We model bremsstrahlung as an exponential law in the energy range 5-300 eV. The shape of the spectrum is given by $I_\nu \sim \exp(-h\nu/k_b T_{\text{eff}})$, with ν the frequency and T_X the effective temperature of the X-ray emitting plasma. Using MAPPINGS III we investigate a two dimensional grid in effective temperature and ionisation parameter. The effective temperature is initially varied from $\log(T_X)=6$ to $\log(T_X)=8$ in steps of 1. The ionisation parameter is initially varied from $\log(U)=-5$ to $\log(U)=-1$ in steps of 0.5. The results are summarised in see Figs 6.13 and 6.14.

After identifying good models for A2597 within this grid, we explore the parameter space further by refining the step size for both T_X and U . The results for A2597-NUC ($n(\text{H})=300 \text{ cm}^{-3}$) and A2597-OFF ($n(\text{H})=50 \text{ cm}^{-3}$) are similar to the best-fitting AGN models. This is expected as the shape of a bremsstrahlung spectrum resembles that of an AGN for $\alpha \approx 0$.

In the case of A2597-NUC ($n(\text{H})=300 \text{ cm}^{-3}$) we find that the bremsstrahlung models cannot simultaneously reproduce the [OIII] 5007/[OII] 3727 ratio and the NeIII 15.5/NeII 12.8 ratio. In fact, none of the bremsstrahlung models produce a [NeIII]/[NeII] ratio as low as the observed value. The best-fitting bremsstrahlung model for A2597-NUC is defined as the model that reproduces the observed [OIII] 5007/[OII] 3727 ratio and is closest to the observed [NII] 6584/H α and [OI] 6300/H α in Fig. 6.13. This model has $T_X=10^6 \text{ K}$ and $\log(U)=-3.75$.

In the case of A2597-OFF ($n(\text{H})=50 \text{ cm}^{-3}$) the bremsstrahlung models can reproduce both the [OIII] 5007/[OII] 3727 and the [OI] 6300/H α ratio for a single combination of $T_X=7 \times 10^5 \text{ K}$ and $\log(U)=-4$. This best-fitting model reproduces most optical line ratios within a factor of two.

The line ratios for the best-fitting bremsstrahlung models are summarised in Tables 6.7 and

6.8. The best-fitting bremsstrahlung models have the same problems as the best fitting AGN models. The bremsstrahlung models also allow for only a very narrow range in ionisation parameter around the best-fitting value.

6.7 Combining Stars and Bremsstrahlung

A number of interesting issues emerge from the modelling performed in the previous section. Unsurprisingly, we find that all three sources can reproduce the observed [OIII] 5007/[OII] 3727 ratio. A pure stellar model is able to simultaneously reproduce the observed [OIII] 5007/[OII] 3727 ratio and NeIII 15.5/NeII 12.8 ratio, but not simultaneously with the observed [OI] 6300/H α ratio. This indicates that higher energy photons such as those produced by an AGN or bremsstrahlung are necessary and this has been known from previous studies of infrared and optical emission line spectra (e.g. Johnstone & Fabian 1988; Heckman et al. 1989; Donahue & Voit 1991; Crawford & Fabian 1992; Voit & Donahue 1997; Johnstone et al. 2007; Hatch et al. 2005; Jaffe et al. 2005; Oonk et al. 2010).

We have shown that pure AGN or pure bremsstrahlung models can provide the high energy photons necessary reproduce the measured [OI] 6300/H α and [OIII] 5007/[OII] 3727 ratios, but not simultaneously with the NeIII 15.5/NeII 12.8 ratio. The best-fitting AGN and bremsstrahlung models give very similar results. Both are able to reproduce most optical line ratios within a factor of two, but both also systematically produce too much emission in the Helium and metal lines. In particular the NeIII 3869 line is much too bright relative to H β .

Although pure AGN and bremsstrahlung models provide a reasonable fit to the optical spectra we believe that there is still room for improvement in reproducing the A2597 observations. One possible solution to the above mentioned problems for the pure AGN and bremsstrahlung models could be to combine a low ionisation source, such as stars, with a higher ionisation source, such as AGN or bremsstrahlung. This leads us to consider a hybrid model combining stars and bremsstrahlung.

We do not investigate a combination of stars and AGN because previous studies by Johnstone & Fabian (1988) have shown that a distributed source of heating is required. This distributed source needs to provide the high energy photons that produce the strong OII and OI emission. Stars can not do this and thus a hybrid model combining stars and AGN seems unlikely. Alternatively, a hybrid model combining AGN and bremsstrahlung will produce an ionising spectrum similar to the combination of stars and bremsstrahlung. An AGN and bremsstrahlung hybrid model will be investigated in a future paper.

6.7.1 The combined model grid

The combined models start from a pure stellar model to which a fraction of a $T_X=10^7$ K bremsstrahlung model is added in incremental steps. This bremsstrahlung temperature is consistent with X-ray observations of the central 10 kpc for A2597 (e.g. McNamara et al. 2001, but see also the discussion in Section 6.7.3). The exact temperature of the bremsstrahlung component should not affect the modelling if it is high enough ($> 10^6$ K) because the bremsstrahlung spectral shape will not change much with increasing temperature except for the addition of very hard photons whose absorption cross sections are very low.

We investigate a three dimensional grid in stellar temperature T_{BB} , bremsstrahlung fraction, and ionisation parameter U . In this case U corresponds to the ionisation parameter for the combined ionising spectrum of stars and bremsstrahlung. The stellar temperature is varied from 40000 to 80000 K in steps of 5000 K. The ionisation parameter is initially varied from $\log(U)=-5$ to $\log(U)=-1$ in steps of 0.5 and the bremsstrahlung fraction is increased from 0% to 80% in steps of 20%. The metallicity of the gas is kept constant at 1.0 solar metallicity. Two density regimes, $n_H=300 \text{ cm}^{-3}$ and $n_H=50 \text{ cm}^{-3}$, are investigated.

For this combined investigation we use a set of six (strong) line ratios to constrain the models. These line ratios are given in Table 6.10. A model is accepted if it produces a line ratio within 10% of the measured value, with the exception of the [OIII] 5007/[OII] 3727 ratio for which we accept the model if it is within 30% of the measured value. The best-fitting model is defined as the model that has the most line ratios within the acceptable margins.

For both A2597-NUC and A2597-OFF, the best-fitting combined models provide equally good or slightly better fits to the observed spectrum than the best-fitting pure AGN model. Similar to the pure AGN and bremsstrahlung models we find that the combined models also allow for only a very small range in ionisation parameter. For A2597-NUC we find that any acceptable combined model must have a $\log(U)$ between -3.8 and -3.6. Similarly for A2597-OFF we find that $\log(U)$ must be between -3.9 and -3.7.

In the case of A2597-NUC ($n_H=300 \text{ cm}^{-3}$) the best-fitting combined model, that satisfies all six line ratios, consists of stars with $T_{BB}=68000 \text{ K}$ and a bremsstrahlung fraction of 80% for $\log(U)=-3.7$ (see Fig. 6.15). In terms of total flux the stars contribute 39% and bremsstrahlung contributes 61%. In terms of ionising flux the stars contribute 33% and bremsstrahlung contributes 67%. This combined model produces a marginally better fit to the spectrum than the best-fit AGN model. In particular it manages to produce slightly better values for the [OI], [NI] and [SII] lines relative to the Balmer lines. However, [NeIII], [MgI], [CaII] and the Helium lines remain a problem (see Table 6.7).

In the case of A2597-OFF ($n_H=50 \text{ cm}^{-3}$) the best-fit combined model, that satisfies all six line ratios, consists of stars with $T_{BB}=60000 \text{ K}$ and a bremsstrahlung fraction of 40% for a $\log(U)=-3.8$ (see Fig. 6.15). In terms of total flux the stars contribute 44% and bremsstrahlung contributes 56%. In terms of ionising flux the stars contribute 36% and bremsstrahlung contributes 64%. This model produces an equally good fit to the spectrum as best-fit pure AGN model. Emission from the Helium and metal lines, in particular [NeIII], remains a problem (see Table 6.8).

6.7.2 Exploring the best-fit combined models

In the previous sections we have shown that star+bremsstrahlung photoionization models produce acceptable fits to the strongest measured line ratios—principally the ratios of Oxygen lines to Hydrogen lines. This situation is unsatisfying for several reasons. First, some of the weaker lines are not well fit. More importantly, the model is *ad hoc*; we have no justification for including the bremsstrahlung radiation except that it improves the spectral fit.

In the following sections we try to improve this situation by investigating the nature of the successful MAPPINGS models in more detail. We cannot yet present a single self-consistent model for the gas phases that we observe, but (i) we will try to determine in detail which aspects of the incident spectra in the models are important to produce the correct output spectra, (ii)

we will explore possible explanations for the low observed Ne/O line ratios, and (iii) we will consider the overall energetics of the various gas phases in order to constrain the nature of *any* proposed heating mechanism.

An important limitation of these models is that they are *stratified* in ionisation structure and radiation spectrum. In other words there is a regular progression of ionisation states as we pass further into the gas, and photons absorbed in the initial regions are not available deeper into the gas. This type of model does not include the possibility that the *stellar* spectrum might follow this stratified scheme, but the *bremsstrahlung* spectrum arises from a diffuse source and enters the gas from a different direction.

Which photons are important?

In this section we use the MAPPINGS models to explore which photon energies contribute to the gas heating and the Ne/O line ratios in two areas of A2597. The results will determine the nature of any pure photoionization model of the warm gas emission. We will follow the spectral changes due to absorption and emission as we pass deeper into the cloud.

Fig. 6.15 shows the model spectra incident on the front of the model gas cloud for A2597-NUC and A2597-OFF. In the following we will refer to the unattenuated model spectrum incident on the cloud as the incident spectrum. The attenuated incident spectrum after passing through (part of) the model cloud will be referred to as the source spectrum. The best-fitting model fluxes incident on the model gas clouds for A2597-NUC and A2597-OFF, in units of $\text{erg s}^{-1} \text{cm}^{-2} \text{Hz}^{-1}$, differ by about a factor of 10. This is mostly due to the difference in gas densities used in the two models.

In Figs. 17 and 18 we show four spectra as a function of distance into the cloud for A2597-NUC and A2597-OFF. In consecutive columns these give the *source spectrum*, the *absorption spectrum* the [OII] differential emission and the [OI] differential emission. The absorption spectrum represents the photons removed passing through each distance step, i.e. the photons used to ionise and heat the gas at that distance. The differential emission spectra show the total emission in the two lines in each slab. Together these spectra allow us to determine in which regions this emission arises, and which photons are responsible for heating the gas there. In addition we plot in Fig. 19 the ionisation state of the important species.

Inspecting particularly the third and fourth columns of Fig. 17 we can for A2597-NUC identify that the [OII] emission, characteristic of classical HII regions, arises at distances less than $\sim 7 \times 10^{16} \text{ cm}$, equivalent to $N_H < 2 \times 10^{19} \text{ cm}^{-2}$, while the [OI] emission comes predominantly from $2 \times 10^{17} \text{ cm} < D < 3 \times 10^{17} \text{ cm}$, with a mixed transition region between. From the second column we can characterize the energy inputs as coming from photons absorbed by in several specific spectral regions: HI absorption above the Lyman continuum limit at 13.6 eV; HeI absorption above 24 eV; mixed metal absorptions in the range 20-50 eV; HeII Lyman continuum at 54 eV; and again mixed metals at $\sim 100 \text{ eV}$. The “mixed metals” are ionisations of [CII](24.4 eV), [NII](29.6 eV) and [OII](35.1 eV) and at the higher energies ionisations of higher ionization states, or of non-outer electrons. Lastly, the first row of column one shows us that the stellar model spectrum contributes most of the photons below $\sim 40 \text{ eV}$, while the bremsstrahlung spectrum contributes the more energetic photons.

From these plots we see that the classical HII region is heated primarily by photons absorbed by HI, HeI and HeII. The first two absorptions lie in the stellar emission region; we know that

this input spectrum cannot explain the [OII] line strength relative to the Balmer lines. Hence we conclude that, within the restrictions of the type of models we consider here, photons near and above the HeII Lyman limit are needed to explain the difference in line ratios relative to those of a standard HII region. In the transition region photons are mostly absorbed in the lower mixed metal region of 30-50 eV because the HeII photons have already been removed from the spectrum. The region where most of the [OI] emission arises is heated by the harder mixed metals absorption near 100 eV. At the end of the calculation, where the gas is too cool to emit the optical [OI] lines there is still a substantial amount of these harder photons. These would contribute to warming the molecular H₂ lines seen in the infrared spectra, which are not modelled in these calculations.

Inspecting in detail the columns in Fig. 18 we find that the same heating process proceeds in A2597-OFF as in A2597-NUC. This becomes clear when the models are viewed in Hydrogen column density instead of distance. The only real physical difference in the two heating models is therefore the gas density used in the two models.

From this discussion we can conclude that in order to explain the various Oxygen/Hydrogen line ratios in a *stratified* model, we must add photons between 30 and 100 eV. Over this entire range the energy fluxes νF_ν are only slightly below that of the stellar input near 13.6 eV. The absorption in these energy ranges has previously been observed by Crawford & Fabian (1992). In agreement with our results, Crawford & Fabian (1992) note that a model aiming to explain the optical line emission in A2597 does not require photons with energies above about 136 eV (10 Ry). We have tested this by repeating our best-fitting models with a high energy cut-off at 100 eV and find that indeed photons above this energy are not strictly necessary. This can also be deduced from Figs 17 and 18 where we observe that the flux of photons with energies above 100 eV is not significantly absorbed in the model.

The best-fitting models were optimised mainly to reproduce the Oxygen lines relative to the Balmer lines. In doing so, we find that these models cannot reproduce all of the observed line ratios. The most problematic ratios are those involving the [NeIII], HeII and [CaII] lines. It is particularly surprising that the [OIII] 5007/H β and [NeIII] 3869/H β ratios behave so differently in the model. The physical constants for these two transitions are very similar and their ionisation potentials differ by only about 6 eV.

To further investigate this issue, we show in Fig. 19 the ionisation state of Oxygen, Neon and Helium as function of distance into the cloud for the best-fitting combined models. From these figures it is clear that NeIII is the dominant ionisation state for Neon over most of the distance into the model cloud. On the other hand [OIII] never dominates the O ionisation state. The observed spectra show that the [OIII] 5007 line is brighter than the [NeIII] 3869 line. Only models with a high energy cut-off just below the energy necessary to ionise [NeII] to [NeIII] (i.e. 41 eV) can produce an [OIII] 5007/[NeIII] 3869 ratio that is greater than one. However, these models fail in producing the necessary level of [OI] emission because photons with energies above 54 eV are no longer present.

The low observed value of the [NeIII] 3869/H β ratio in the cooling cores could be caused by underabundant Neon in these systems (see also the discussion in Section 6.8), but this still would not explain the low observed infrared [NeIII]/[NeII] ratio. We have investigated possible problems in the way MAPPINGS III code treats Neon. We found that model grids derived for pure stars and AGN are in fact able to reproduce the [NeIII] 3869/H β and [OIII] 5007/H β ratios for a sample of AGN and starburst galaxies obtained from the Sloan Digital Sky Survey (M.

Shirazi & J. Brinchmann in prep.). The cooling core problem differs from the AGN/starburst problem in the extended outer low ionisation zone. When n_{HI}/n_e is not very small (i.e. $> 10^{-3}$) then charge exchange recombination of highly ionized atoms dominates over direct radiative recombination (Osterbrock & Ferland 2006, chapter 2.7). Thus an underestimate of the charge exchange coefficients for [NeIII] would appear as an overestimate of the [NeIII] emission in cooling cores, but not in classical HII regions.

The MAPPINGS III code considers charge exchange recombination reactions of [NeIII]-[NeV] with HI and HeI (Dopita & Sutherland 2003). Charge exchange is a difficult process to model and it is unclear how accurate the current treatment is. Further investigation of this subject falls outside the scope of this paper.

We can summarize the results of our study of stratified photoionisation models as: To match the observed [OII]/[OIII] and [OII]/H β line ratios, we require additional energy fluxes in the 30-60 eV spectral region of the same order of magnitude as the stellar source in the 13-24 eV region. Expressed as energy fluxes these are both of order $4 \times 10^{-2} \text{ erg cm}^{-2} \text{ s}^{-1}$ when $n_e \sim 300 \text{ cm}^{-3}$. To explain the [OI]/H α ratios we need a similar energy flux in the $\sim 100 \text{ eV}$ region. The models cannot explain the low observed [NeIII] strength.

Stratified versus non-stratified models

We have not computed in detail any models where the radiation is not stratified, i.e. where the higher energy photons come from a different direction than those that ionise most of the Hydrogen. This is because this situation required 2-D or 3-D modelling and the geometry is uncertain. It is likely in this case that the distinction between the intermediate energy photons that heat the [OII] region and the high energy photons that heat the [OI] regions disappears; the intermediate photons are not necessarily removed by passage through the [OII] region before reaching the [OI] region.

There are no well known single photon sources with spectra matching the stellar+bremstrahlung models. One possibility would be a blue-bump AGN (Elvis et al 1994), but such a source is ruled out by the requirement for an extended heat source (Johnstone & Fabian 1988; Heckman et al. 1989) (c.f. Section 6.8). Therefore it is tempting to assume that the excitation spectrum is in fact the superposition of two distinct sources, probably non-stratified. This assumption opens a new problem, namely the observed near-constancy of the [OI]/H α line ratio. If the higher energy photons come from, say, a diffuse XUV background (c.f. Section 6.7.3) we would expect to find warm neutral gas heating by this source in areas where there is no stellar ionisation. In these regions [OI]/H α would have a much higher value. In this model we might assume that neutral gas in the cooling-cores is found only in regions close to areas of star-formation. This eliminates the problem of regions emitting [OI] but no H α , but does not explain the constancy of the line ratio; variations in the distance from the stars to the end of the Hydrogen clouds would be reflected in a variation in the [OI]/H α ratio.

6.7.3 Gas heating in A2597

The previous section was limited to specific photoionisation models of the cooling core gas. Here we quantify the excess, non-stellar, heating (per Hydrogen nucleus) necessary to balance cooling in the different gas phases. The results should give us insights into the nature of the

energy sources which are more general than the specific model and may apply to other LINER-like BCGs. The gas phases we consider are:

1. The X-ray gas
2. The HII region where HII and [OII] emission arise
3. The low ionization [OI] emission region
4. The warm (~ 2000 K) molecular regions
5. The cooler (~ 500 K) molecular regions

The results of this discussion are summarized in Table 6.11.

Starting from the warmest gas phase, i.e. the X-ray emitting plasma, we find a cooling rate of about 2.4×10^{-24} erg s $^{-1}$ H $^{-1}$ in the region probed by the nuclear spectrum. Here we use the cooling curve from Raymond et al. (1976), a temperature of 2×10^7 K and a density of 0.08 cm $^{-3}$ for the plasma (Cavagnolo et al. 2009). Since most of this gas does not appear to cool to lower temperatures, a heating source of the same magnitude is needed to balance the X-ray emission. Over the central 20 kpc region in A2597 the density decreases by less than a factor 1.5 and the temperature increases by less than a factor of 2 (e.g. Pollack et al. 2005; Cavagnolo et al. 2009). The radiative cooling for a hot X-ray emitting plasma, via Bremsstrahlung, increases with the square of the density and decreases with the square root of the temperature. The X-ray emitting phase in the region probed by our off-nuclear spectrum thus requires a heating rate, at most a factor of 2 lower than in the nuclear region.

Next we investigate the HII/[OII] regions observed near the nucleus of A2597, i.e. A2597-NUC. From Fig. 17, we identify this as the region with $D < 7 \times 10^{16}$ cm, or equivalently $N_H < 2 \times 10^{19}$ cm since in our modelling we assumed $n_H = 300$ cm $^{-3}$. The first column of this figure shows that $\sim 4 \times 10^{-2}$ erg s $^{-1}$ cm $^{-2}$ has been removed from the incident spectrum. Most of this has been absorbed in the ionization of HI, HeI and HeII at energies just above 13.6, 24, and 54 eV, respectively. We estimate that roughly 1/2 of this flux has a stellar origin. The other half represents excess radiation from the non-stellar high-energy component, here modeled in the form of bremsstrahlung, that is necessary to create the peculiar cooling-core spectra, i.e. in particular the high [OII]/H β ratios. Dividing this result by the column density we find that the excess radiation removed by the gas amounts to $\sim 1 \times 10^{-21}$ erg s $^{-1}$ H $^{-1}$. We also estimate that only about 1/2 of this excess represents actual heating of the gas by the ejected electrons, the rest being radiated away as optically thin line emission when the ions recombine. We conclude that the cool-core spectra of the HII/[OII] regions require excess heating rates of $\sim 5 \times 10^{-22}$ erg s $^{-1}$ H $^{-1}$. The OFF model spectra are very similar in form to the NUC spectra. The column densities at the ends of the [OII] and [OI] zones are similar in both cases, but the incident fluxes in the OFF spectra are approximately a factor of 8 lower than the NUC spectra. The heating rates in Table 6.11 are proportional to this reduction.

The calculation of the heating in the [OI] zone is similar. Fig. 17 shows this to be the region from $D \simeq 8 \times 10^{16}$ cm to $D \simeq 3 \times 10^{17}$ cm, representing $N_H \simeq 6 \times 10^{19}$ cm $^{-2}$. The radiation absorbed in this zone amounts to $\simeq 5 \times 10^{-2}$ erg s $^{-1}$ cm $^{-2}$, mostly by metals in the energy range 60-150 eV. Thus the average absorbed energy is $\sim 8 \times 10^{-22}$ erg s $^{-1}$ H $^{-1}$. The physics of ionisation and recombination in this energy range is quite complicated, and it is difficult to

estimate the fraction of this energy which is available to general heating of the gas, especially Oxygen atoms, and how much is immediately reradiated as recombination line emission. For this work we will again assume that a fraction of $\sim 1/2$ or $4 \times 10^{-22} \text{ erg s}^{-1} \text{ H}^{-1}$ is available for heating.

Next we consider the warm H_2 gas emitting in the near-infrared. This gas was not included in the MAPPINGS III modelling. We estimate the cooling rates from the graphs presented by Maloney et al. (1996) based on temperature estimates derived from the observed line H_2 ratios (Jaffe et al. 2005; Oonk et al. 2010). These ratios indicate that the gas is in LTE with temperatures $\sim 2000 \text{ K}$ and densities $n_H \geq 10^6 \text{ cm}^{-3}$. Maloney et al. (1996) find an H_2 vibrational cooling rate $1 \times 10^{-22} \text{ erg s}^{-1} \text{ H}^{-1}$ for H_2 gas at 2000 K and a density $n_H = 10^5 \text{ cm}^{-3}$. In this temperature range the cooling rate is approximately proportional to the temperature. At the higher density implied by our measurements the H_2 vibrational cooling rate will increase to $\sim 5 \times 10^{-22} \text{ erg s}^{-1} \text{ H}^{-1}$. This is due to (i) a small increases in the cooling rate per molecule and (ii) an increase in the molecular fraction of the gas. Outside the central 10 kpc the warm H_2 phase is less well constrained. However, within uncertainties we find that its properties are consistent with those derived in the central region and we thus assign the same cooling rate to this gas (Jaffe et al. 2005; Oonk et al. 2010).

The final temperature phase that we will consider here is the cool H_2 phase measured with Spitzer in the mid-infrared (Jaffe & Bremer in prep.). Our spectra of A2597 show that this gas in the nuclear region is consistent with being in LTE at a temperature $T = 500 \text{ K}$ and a density $n_H \geq 10^6 \text{ cm}^{-3}$. There are no off-nuclear measurements of the cool H_2 phase for A2597. Maloney et al. (1996) find the total cooling rate for a gas at 500 K with a density $n_H = 10^5 \text{ cm}^{-3}$ to be about $5 \times 10^{-23} \text{ erg s}^{-1} \text{ H}^{-1}$, once again approximately proportional to the assumed temperature. The rate is dominated by [OI] line cooling at $63 \mu\text{m}$, and not by H_2 rotational cooling. This neutral ion transition has a relatively high critical density, $n_c \sim 5 \times 10^5 \text{ cm}^{-3}$, (Boreiko & Betz 1996), so we take the cooling rate to increase a factor of ~ 3 when increasing the density to $\sim 10^6 \text{ cm}^{-3}$. Thus we find the specific cooling/heating rate of this phase to be $\approx 2 \times 10^{-22} \text{ erg s}^{-1} \text{ H}^{-1}$.

Table 6.11 indicates the specific cooling rates for the near-nuclear ionised, neutral and molecular gas in the temperature regime $T = 500\text{--}10000 \text{ K}$ are all very similar, and considerably higher than for the X-ray gas. The off-nuclear warm gas exhibits cooling rates a factor of 8 or so lower, with the exception of the somewhat higher, and uncertain, value for the warm molecular gas. These values suggest that there is a single heating process balancing the cooling in the non-X-ray phases, that this process is per H-nucleus independently of the temperature or density, and that the heating rate decreases roughly an order of magnitude from the nuclear region $r \leq 5 \text{ kpc}$ to the halo region $10 < r < 20 \text{ kpc}$.

Photon heating of the warm gas

Above we showed that the excess heating rates for the different gas phases at temperatures below 10^4 K are very similar. This similarity, and the actual specific heating rates are probably valid outside the context of the specific models we used above. The independence of the heating rate on density, ionisation state and temperature suggests a mechanism involving ionisation of lower lying electrons of metal atoms or ions by energetic photons or particles. These ejected electrons then heat the surrounding medium. This type of model has been considered by (e.g.

Johnstone & Fabian 1988; Heckman et al. 1989; Voit & Donahue 1997; Jaffe & Bremer 1997; Ferland et al. 2009). In this section we assume that the heating in the [OI] and H₂ regions is caused by extreme ultraviolet (XUV) photons without the limits of the specific spectral models used above. These photons with energies above say 60 eV can penetrate into any of the warm gas phases. We will calculate the necessary flux of such photons as a function of their energy, and explore the possible connection to the soft X-ray cooling core emission.

We find above that we need a specific heating rate of $\sim 4 \times 10^{-22}$ erg s⁻¹ H⁻¹ in the each of the gas phases. Including energy that is immediately reradiated the necessary XUV flux is about 1×10^{-21} erg s⁻¹ H⁻¹. For photons falling on gas of solar metallicity, Maloney et al. (1996) find absorption cross sections per H-atom of $\sim 3 \times 10^{-19}$ cm² at 60 eV, dropping as E^{-3} to $\sim 1.2 \times 10^{-20}$ cm² at 150 eV. Thus the required XUV flux varies from 4×10^{-3} erg s⁻¹ cm⁻² for 60 eV photons, to 2×10^{-2} at 100 eV and 6×10^{-2} for 150 eV photons. In the stratified models each gas phase absorbs about this much flux at somewhat different wavelengths, so the total absorbed flux is somewhat higher, say ~ 0.08 erg s⁻¹ cm⁻² at 100 eV or ~ 0.02 erg s⁻¹ cm⁻² at 60 eV.

These fluxes are consistent with the spectra determined by MAPPINGS III, but indicate how the required flux changes with the assumed principal photon energy. The ionized gas seen in our A2597-OFF spectra has a lower density and a lower cooling rate; the required fluxes are about a factor of 10 lower than in the nuclear region. The fluxes are similar but slightly lower than those found by Donahue & Voit (1991) from CLOUDY simulations. The difference may lie in small differences in the code or in the assumed spectra.

We can now ask whether an extrapolation of the observed soft X-ray flux from A2597 is consistent with the required XUV flux just found. The A2597 cluster has an X-ray luminosity of about 1.5×10^{44} erg s⁻¹, in the 0.1-2.4 keV range (Cavagnolo et al. 2009). The temperature of this gas in the central 10 kpc radius is about 2 keV (e.g. Cavagnolo et al. 2009; McNamara et al. 2001). From Chandra archival images we estimate that within this radius the BCG has an X-ray luminosity of about 10^{43} erg s⁻¹ at ~ 2 keV. This corresponds to a 0.5-2 keV X-ray flux of about 10^{-3} erg s⁻¹ cm⁻². At these temperatures, free-free bremsstrahlung accounts only for a small fraction of the emission, and to estimate the XUV fluxes we use the models calculated in Kaastra et al. (2008) for gas at temperatures of 0.2, 1, and 5 keV. For the 1 keV spectra the XUV emission is principally near 100 eV and the integrated flux near this energy is about 0.3 times that in the 0.5-2 keV range, i.e. 3×10^{-4} erg s⁻¹ cm⁻². For 2 keV X-ray gas, the extrapolated XUV flux will be somewhat lower. This value just quoted is about a factor of 20 lower than that required to heat the OFF nuclear gas, and a factor 200 below that required for the nuclear gas. This conclusion agrees with that found by Crawford & Fabian (1992). XUV heating of the gas can only be considered plausible if there is a much softer X-ray component.

Gonzalez-Martin et al. (2009), in their analysis of Chandra and XMM observations of LINERS, find evidence for a very soft emission component in the central 2 arcsec (3 kpc) radius of A2597. This component has a temperature of $kT=370$ eV and contributes 40% of the total 0.5-2.0 keV luminosity of the galaxy, 4×10^{42} erg s⁻¹. When we interpolate between the spectra plotted in Kaastra et al. (2008) we estimate that the bulk of the XUV emission from this gas will be at ~ 60 eV. The XUV flux in this soft component will be about three times the 0.5-2 keV flux. For a radius of 3 kpc, the estimated 60 eV flux then becomes 0.01 erg s⁻¹ cm⁻². This is about a factor of two lower than the level found necessary above. We can conclude that XUV heating of the gas is plausible but only if the ultrasoft X-ray component is confirmed, is not

associated with the AGN itself, and if the emitted luminosity is confined to a small fraction of the projected surface area of the galaxy.

Other studies of A2597 have also indicated the presence of gas with temperatures between the hot X-ray plasma at 10^7 K and the optical HII emission at 10^4 K. Most notably Morris & Fabian (2005) find tentative evidence for soft X-ray emission at about 0.3 keV, and Oegerle et al. (2001) detect [OVI] emission indicative of gas at temperatures of about 3×10^5 K.

If these conjectures are true, then the emission regions may represent the true *cooling flow*: the small fraction of the X-ray halo of the BCG which avoids reheating and actually cools to the temperature phases we observe here. The XUV and optical line emitting regions would be filamentary and physically closely associated with each other, but both would have a low average surface filling factor. The emitted luminosity from this XUV component corresponds to a mass cooling rate of $\sim 40 M_{\odot} \text{ yr}^{-1}$. An cooling rate at this level is supported by the formation rate of young stars in several cooling core clusters, including A2597, and is not inconsistent with the X-ray data (McNamara et al. 2004; Rafferty et al. 2006).

6.8 Discussion

In this section we will shortly discuss our results and compare them with previous investigations. In Section 6.8.1 we discuss the low ionisation state of the cool gas in BCGs and what works and what does not for our photoionisation models of this gas. In Section 6.8.2 we compare our results with previous investigations and alternative models.

6.8.1 Warm, low-ionisation gas in BCGs

Optical spectra show that the BCGs in the A2597, A2204 and S159 clusters exhibit extreme LINER-like characteristics over tens of kpc in the optical wavelength regime. The spectra for these three objects are very similar. Constraints on the properties of the gas are obtained from individual line ratios involving Nitrogen, Sulphur and Oxygen (c.f. Section 6.5). We find that the gas is very warm ($T \sim 11000$ K), and has a density and ionisation degree that decreases with distance. A warm, weakly ionised gas phase, as traced by [OI] emission, is identified in all regions sampled by our spectra. The ratio of this [OI] emission relative to $H\alpha$ as a function of distance is found to be very constant in our BCGs.

It is difficult to determine accurate values for the gas temperature and density from single line ratios in the off-nuclear regions. Methods different from the ones used in Section 6.5 are necessary. For gas with a low ionisation parameter ($\log(U) < -3$) it may be possible to use [OII] 3727/ $H\beta$, in combination with [OIII] 5007/[OII 3727], as a temperature tracer instead of the [NII] lines. It is also important to obtain a tracer better than the [SII] lines for low density ($n < 100 \text{ cm}^{-3}$) gas.

Using the MAPPINGS III plasma code we have investigated heating by photoionisation for three sources that are available in BCGs; (i) stars, (ii) AGN and (iii) bremsstrahlung. The models were computed for a dust-free gas with a constant density and solar metallicity in a plane-parallel geometry. The models are tuned to A2597, but its similarity to other LINER-like BCGs allow the results to have a more general character. A stellar model can not reproduce the

observations as it lacks the high energy photons needed to heat the gas to high temperatures and create the warm, weakly ionised gas phase.

AGN and bremsstrahlung models can reproduce most of the observed line ratios within a factor of two. The AGN models provide a better fit to the spectrum than bremsstrahlung. A systematic issue for both is that they produce too much emission in the Helium lines and some of the metal lines, i.e. [MgI], [CaII] and [NeIII], relative to Hydrogen. The overproduction of [MgI] and [CaII] in our models is likely related to the lower abundance of these elements in the gas phase when this gas is dusty (e.g. Groves et al. 2008). Our models assume dust-free conditions. However, the Balmer decrements in A2597 and A2204 show evidence for a large amount of dust in these systems. The data for S159 does not require a significant amount of dust, but here the constraints are not very strong. We will discuss gas abundances in more detail in Section 6.8.2.

The optical [NeIII]/H β and infrared [NeIII]/[NeII] ratios are too high in our models involving AGN and/or bremsstrahlung. Neon is a noble gas which under normal conditions is not depleted onto dust grains. Also a lower abundance of Neon can not explain why [NeIII]/[NeII] is measured to be much lower than computed in our models. One possibility to explain the observations is that the charge transfer recombination coefficients for [NeIII] are underestimated in the MAPPINGS III code (c.f. Section 6.7.2).

The reason for the overproduction of the optical HeII and HeI lines in our models is not clear. An overestimate of the charge transfer recombination coefficient for HeIII to HeII can possibly increase the HeII emission in the models. Similarly, an overestimate of the charge transfer recombination coefficient for HeII to HeI may increase the HeI emission in the models. The latter reaction is not likely to contribute significantly to the HeI emission, because this reaction has a small cross-section (Osterbrock & Ferland 2006). The mismatch of the observed and modelled HeI emission could also be due to the relatively simple treatment of the HeI emission spectrum in MAPPINGS III, but we caution that any comparison is weak due to the difficulty in actually measuring these diagnostic lines.

We prefer bremsstrahlung over an AGN model, because the variation in the degree of ionisation for the gas is not consistent with ionisation by a central source (Johnstone & Fabian 1988; Heckman et al. 1989). In an attempt to improve the bremsstrahlung fit to the data we increased the level of lower energy (≤ 40 eV) ionising photons in our bremsstrahlung models by combining it with a stellar model. We find that this combination can reproduce the observations with an accuracy similar to the AGN spectra. The combined models are not very tightly constrained in terms of stellar temperature and bremsstrahlung fraction. A higher fraction of bremsstrahlung requires a warmer stellar temperature in order to fit the observations. The best-fitting models require very high stellar temperatures, but combinations with a stellar temperature as low as 45000 K and a bremsstrahlung fraction of 20% can still produce acceptable results.

The advantage of combining stars and bremsstrahlung is that both sources are distributed and their combined spectrum naturally explains the high far-ultraviolet to U-band fluxes in cool-core BCGs (e.g. Crawford & Fabian 1993; Oonk et al. 2011). The disadvantage of any combined model is that the optical spectra require a rather constant ionisation over large spatial scales. In particular the tight correlation between [OI] and H α is a problem for our model. Bremsstrahlung will contribute to both [OI] and H α emission, but stars contribute only to H α emission. The strong link between [OI] and H α would therefore require these sources to be distributed in the same way in cool-core BCGs. The existence of such a correlation we deem to

be unlikely.

The combination of stars and bremsstrahlung may not be very plausible. However, the shape of the combined ionising spectrum is still of interest, as it is able to reproduce the characteristic line spectra for cool-core BCGs. The heating required to balance cooling of the optical line emitting gas in A2597 can be derived from our best-fitting combined model. The heating required in the nuclear region of A2597 is about a factor of ten more than in the off-nuclear region.

The observed X-ray spectrum at 0.5-2 keV shows that in order to explain the 60 eV photons, required by our model, we need an ultra-soft X-ray component. This component could be related to a residual cooling flow in A2597. The photon flux required by our model does not violate the observational limits (Gonzalez-Martin et al. 2009; Morris & Fabian 2005), if we assume a small filling factor for the ultra-soft X-ray component.

An alternative way of supplying additional ionising photons in the nuclear region of A2597 could be the AGN. A combination of bremsstrahlung and AGN has not been investigated here, but is expected to provide a good fit to the data. Such a model, where the bremsstrahlung takes care of the large-scale heating and the AGN boosts the heating in the central few kpc may also aid in explaining the observed spread in the [OIII] 5007/H β ratio observed for cool-core BCGs.

The best-fitting combined models require a Hydrogen column density of about $2 \times 10^{20} \text{ cm}^{-2}$ in both the nuclear and the off-nuclear region of A2597. This column density is in good agreement with HI absorption measurements (O’Dea et al. 1994) and shows that the only real difference in the required heating for the two regions is the assumed gas density. This strong dependence of the gas heating on the gas density means that we need better observational constraints on the actual gas density structure in cool-core BCGs. Our current models are very simplistic in this sense, because they assume a constant gas density.

We find that the heating required to balance cooling in the molecular gas at 2000 K and 500 K in A2597 is of a similar magnitude as the optical gas in units of erg s^{-1} per H-nucleus. This suggests that single source of heating can balance gas cooling in all of the warm ($T < 10^4 \text{ K}$) gas phases. The heating of the hot X-ray plasma at $T \sim 10^{7-8} \text{ K}$ is of course not explained by any of our models. We use the bremsstrahlung emission from this plasma to heat the optical gas, but this plasma itself also needs to be heated. Currently the favored picture for this feedback process is kinetic energy from AGN outflows (e.g. see McNamara & Nulsen 2007, for a recent review).

6.8.2 Comparison with previous studies

A large number of studies aimed at explaining the optical emission line gas in cool-core BCGs have been carried out in the past (e.g. Johnstone & Fabian 1988; Heckman et al. 1989; Donahue & Voit 1991; Crawford & Fabian 1992; Voit et al. 1994; Voit & Donahue 1997; Crawford et al. 1999; Ferland et al. 2009). These studies first showed the low ionisation character of the optical line emission in BCGs. They also pointed out that this line emission is too large to simply be gas cooling through this phase and thus showed that a heating source is necessary. Many different heating models were proposed and here we will shortly summarise some of the main results of these investigations.

Photoionisation by hot stars was first investigated by Johnstone, Fabian & Nulsen (1987) and Johnstone & Fabian (1988). In agreement with our results they found that stars can not

reproduce the observed line ratios. Large-scale photoionisation by a central point source was ruled out by Johnstone & Fabian (1988) and Heckman et al. (1989). They showed that the radial variation of the ionisation parameter U is much smaller than expected for a central ionising source.

Having ruled out photoionisation by Stars and AGN, many authors proceeded to investigate bremsstrahlung (e.g. Heckman et al. 1989). These investigations focused mainly on self-irradiated cooling flows with gas condensing through a temperature phase of $T=10^{5-7}$ K. In this context Johnstone & Fabian (1988); Donahue & Voit (1991); Crawford & Fabian (1992); Voit et al. (1994) find that they can reproduce the observed line ratios in BCGs. Crawford & Fabian (1992), using methods similar to those presented here, found that such a model required X-ray fluxes inconsistent with the observations. The differences between the models and X-ray data in their work and what is presented here requires further investigation.

Crawford & Fabian (1992) also pointed out that the reason that ionisation by bremsstrahlung can explain the optical spectra is that in terms of $\nu \times F_\nu$ it provides a flat ionising spectrum in the 10-100 eV regime. They find that photons above this energy are not strictly necessary and this is in agreement with our results. Any source with a bremsstrahlung-like photoionisation spectrum will be able to reproduce the optical spectra for cool-core BCGs and this also explains why our AGN models are able to fit the observations.

Photoionisation is not the only way in which energy can be put into the gas. Alternative models include shocks and particle heating. Shocks are investigated by Donahue & Voit (1991) and Voit & Donahue (1997). They find that shocks in principle can produce optical spectra similar to the observations, but due to the very large mass flows involved and the absence of typical shock lines (i.e. [OIII] 4363 Å), they conclude that this is an unlikely scenario. It is also unlikely that shocks would produce the similar heating rates that we find in the different density and temperature phases for the warm $T < 10^4$ K gas.

Recently Ferland et al. (2009) have presented a detailed high-energy particle (i.e. cosmic rays) heating model for the ionised and molecular gas in the Horseshoe filament of NGC 1275. This is the first model that is able to fit both the ionised and the molecular gas emitting in the optical to mid-infrared regime. The model successfully reproduces most emission line intensities and ratios for this filament to within a factor of two. Our models reach a similar accuracy for A2597 but only for the ionised gas in the optical regime. A self-consistent model heating both the ionised gas and the molecular gas in BCGs with bremsstrahlung can currently not be done with the MAPPINGS III code.

The optical spectrum of NGC 1275 (Johnstone & Fabian 1988; Hatch et al. 2006) is very similar to the optical spectra of our objects. This suggests that the Ferland et al. (2009) model and our model are both viable solutions to heat the warm optical gas in cool-core BCGs. Comparing the two models we notice that the particle model matches the Helium and metal line emission in the optical spectra better than our models. This difference is surprising, because the heating mechanism is essentially the same in the models, i.e. collisional heating via secondary electrons (only the primaries differ).

We find that part of this difference is likely due to the different abundances used in the two models. We use the 1.0 solar abundances from the MAPPINGS III distribution, see Table 6.12. These abundances are based on modelling of the Sun by Asplund, Grevesse & Sauval (2005) and were previously used by Groves et al. (2008) to model starburst galaxies. We have experimented with lowering the overall metallicity in our models by using 0.4 solar abundances

from the MAPPINGS III distribution (Table 6.12). This does not resolve the problems and in fact provides a fit which is much worse than for the 1.0 solar abundances. In particular the Nitrogen and Oxygen abundances are too low in a 0.4 solar abundance gas to explain their observed line ratios relative to Hydrogen.

Comparing our 1.0 solar abundances with the Orion abundances used by Ferland et al. (2009) shows that Orion has significantly lower abundances of Neon, Magnesium and Calcium, see Table 6.12. We have experimented with these Orion abundances in our models and find that indeed we obtain more satisfactory results for these lines relative to Hydrogen. As discussed in Section 6.8.1 lower abundances for Magnesium and Calcium can arise from depletion of these elements onto dust grains, but this does not work for Neon (e.g. Groves et al. 2008).

A lower abundance for Neon does not change the infrared [NeIII]/Ne[II] ratio in our models. However, it is possible that charge exchange reactions play an important role for this ratio, see the discussion in Section 6.7.2)). The abundance of Helium is very similar for our models and Orion. It is therefore unlikely that the mismatch between the observed Helium lines and the models is caused by an abundance issue. Finally we note that Orion is somewhat overabundant in Nitrogen, relative to the 1.0 solar abundances (Table 6.12). If the same is true in cool-core BCGs, then this will make it easier to reproduce the high [NII] 6584/H α ratios.

Currently it is not clear what the actual abundances of the optical line emitting gas in cool-core BCGs are. Detailed observations are necessary to investigate this. In particular we need to determine the Neon abundance in these objects. Also a detailed investigation is necessary to determine why the Neon and Helium lines have much higher intensities relative to Hydrogen in our models as compared to Ferland et al. (2009).

6.9 Conclusions

In this work we present new, deep, optical, long-slit observations for the BCGs in the cool-core clusters A2597, A2204 and S159. We combine these measurements with a pilot investigation of the gas heating in these systems using the MAPPINGS III photoionisation code. This is to our knowledge the first time that this code has been used to model the optical line emission in cool-core BCGs.

- Optical line emission is traced out to about 20 kpc from the nuclei in the BCGs of A2597, A2204 and S159. This line emission is centred on the nucleus, from which it extends outwards in clumpy filaments.
- The optical spectra show that these BCGs are extreme examples of low ionisation nuclear emission line regions over the entire area where optical line emission is detected. This is probably a consequence of their selection on the basis of a high ratio molecular to ionized gas emission lines.
- The Balmer decrements in A2597 and A2204 are consistent with a Milky-Way-type extinction law for $A_V \sim 1$. These decrements are observed to be constant across the entire line emitting area, indicating that a significant amount of dust is present in these systems. The Balmer decrements in S159 are consistent with no dust, though it should be noted that, unlike A2597 and A2204, H α /H β could not be measured in this system.

- The degree of ionisation for the gas decreases with distance from the nucleus in all three systems. This decrease is slower than expected for photoionisation by a central point source such as an AGN. The gas along the A2597-NUC slit shows a constant degree of ionisation out to 5 kpc from the nucleus. The region sampled by this slit lies within the FUV and radio bright area of A2597 (e.g. Oonk et al. 2010; O’Dea et al. 2004)
- The strength and constancy of the [OI] 6300 Å and [NI] 5200 Å emission relative to the Balmer lines indicates the presence of a warm, weakly ionised gas phase extending out to about 20 kpc from the nucleus in all three BCGs.
- The tight correlation between [OI] and H α within individual cool-core BCGs, as well as for cool-core BCGs as a sample, is suggestive of a single heating source common to all cool-core BCGs.
- Measurements of the [SII] line ratio indicate that on large scales the density of the gas decreases with distance from the nucleus in A2597 and S159. The outer regions in both systems show bright clumps that coincide with local increases in the gas density.
- We have used the MAPPINGS III code to model photoionisation of the optical line emitting gas in cool-core BCGs. The results are consistent with previous investigations (Johnstone & Fabian 1988; Donahue & Voit 1991; Crawford & Fabian 1992; Voit et al. 1994; Ferland et al. 2009) using the CLOUDY code (Ferland et al. 1998) and can be summarised as follows;
 1. Pure stellar models cannot explain the observations, because stars do not produce the high-energy photons necessary to heat the gas to the observed temperatures.
 2. Pure AGN and bremsstrahlung models can supply the necessary high-energy photons and both are able to reproduce most optical line ratios within a factor of two.
 3. A pure AGN model provides a better fit to the observations than the pure bremsstrahlung models.
- Pure AGN and bremsstrahlung models systematically produce too much emission in the Helium lines and in some of the metal lines. In particular the Neon and Helium lines are problematic. Charge exchange reactions in a partially ionised gas may be important for these lines and needs more investigation.
- Discarding the best-fitting AGN models on arguments by Johnstone & Fabian (1988) and Heckman et al. (1989) we find that a combination of stars and bremsstrahlung can produce an equally good fit to observations. However, we argue that these combined models are not very plausible, because they require very hot stars and an uncomfortable link between these stars and the diffuse X-ray emission on 1-20 kpc scales.

- The best-fitting combined model may not be physically plausible, however it still provides insights into how the optical line emitting gas in BCGs can be heated using photons. In particular the model shows that photons in the energy range 40-100 eV are required to explain the observed [OI] emission. This agrees with a previous investigation by Crawford & Fabian (1992).
- Based on the Oxygen ionisation fraction in the best-fitting combined model we have split the optical line emitting gas into two components, a fully ionised phase (traced by [OII]) and a weakly ionised phase (traced by [OI]). Comparing these two gas phases with the cooler molecular gas ($T=10^{2-3}$ K) we find that the cooling rates, in units of $\text{erg s}^{-1} \text{H}^{-1}$, for all these phases are within an order of magnitude of each other.
- The best-fitting combined model implies that a high-energy (i.e. ~ 60 eV) photon flux of about $10^{-19} \text{ erg s}^{-1} \text{ Hz}^{-1}$ is necessary to heat the optical gas in the nuclear region of A2597. The off-nuclear region in A2597 requires a high-energy photon flux lower by about a factor of ten. A remnant cooling flow model with an ultra-soft 300 eV component can provide the required photons. Such a model does not violate the observational limits on the residual cooling flow in A2597.

We have obtained optical integral field spectroscopy in order to further investigate spatial variations in the gas properties of these systems. We will also use this data, in combination with deep X-ray maps, to present a detailed two-dimensional analysis of the thermal balance for the optical line emitting gas in a future paper.

Acknowledgements

JBRO wishes to thank J. Brinchmann and M. Shirazi for useful discussions. The FORS observations were taken at the Very Large Telescope (VLT) facility of the European Southern Observatory (ESO) as part of projects 63.N-0485 and 69.A-0444.

Bibliography

- Allen S. W., MNRAS, 1995, 276, 947
Asplund M., Grevesse N., Sauval A. J., 2005, ASP Conf. Ser. 336, eds T.G. Barnett & F. N. Bash
Baldwin J. A., Phillips M. M., Terlevich R., 1981, PASP, 93, 5
Begelman M. C., Fabian A. C., 1990, MNRAS, 244, 26
Boreiko R. T., Betz A. L., 1996, ApJ, 464, L83
Bruzual A.G., Charlot S., 2003, MNRAS, 344, 1000
Cardelli J. A., Clayton G. C., Mathis J. S., 1989, ApJ, 345, 245
Cavagnolo K.W., Donahue M., Voit G. M., Sun M., 2009, ApJS, 182, 12
Conselice C. J., Gallagher J. S., Wyse R. F. G., 2001, AJ, 122, 228
Crawford C. S., Fabian A. C., 1992, MNRAS, 259, 265
Crawford C. S., Fabian A. C., 1993, MNRAS, 265, 431

- Crawford C. S., Allen S. W., Ebeling H., Edge A. C., Fabian A. C., 1999, *MNRAS*, 306, 857
- Crawford C. S., Hatch N. A., Fabian A. C., Sanders J. S., 2005, *MNRAS*, 363, 216
- Donahue M., Voit G. M., 1991, *ApJ*, 381, 361
- Donahue M., Mack J., Voit G. M., Sparks W., Elston R., Maloney P. R., 2000, *ApJ*, 545, 670
- Donahue M., Jordan A., Baum S. A., Cote P., Ferrarese L., Goudfrooij P., Macchetto D., Malhotra S., O’Dea C. P., Pringle J. E., Rhoads J. E., Sparks W. B., Voit, G. M.
- Donahue M., Bruch S., Wang E., Voit G. M., Hicks A. K., Haarsma D. B., Croston J. H., Pratt G. W., Pierini D., O’Connell R. W., Böhringer H., *ApJ*, 715, 881
- Donahue M., de Messieres G. E., O’Connell R. W., Voit G. M., Hoffer A., McNamara B. R., Nulsen, P. E. J., arXiv, 1103.1410
- Dopita M. A., Sutherland R. S., *Astrophysics of the diffuse universe*, 2003, Springer Verlag
- Edge A. C., 2001, *MNRAS*, 328, 762
- Edge A. C., Wilman R. J., Johnstone R. M., Crawford C. S., Fabian A. C., Allen S. W., 2002, et al., *MNRAS*, 337, 49
- Elvis M., Wilkes B. J., McDowell J. C., Green R. F., Bechtold J., Willner S. P., Oey M. S., Polomski E., Cutri R., 1994, *ApJS*, 95, 1
- Fabian A. C., Nulsen P. E. J., Stewart G. C., Ku W. H. M., Malin D. F., Mushotzky R. F., 1981, *MNRAS*, 196, 35
- Fabian A. C., Crawford C. S., Edge A. C., Mushotzky R. F., 1994, *MNRAS*, 267, 779
- Fabian A. C., Celotti A., Blundell K. M., Kassim N. E., Perley R. A., *MNRAS*, 331, 369
- Fabian A. C., Sanders J. S., Taylor G. B., Allen S. W., Crawford C. S., Johnstone R. M., Iwasawa K., 2006, *MNRAS*, 366, 417
- Fabian A. C., Johnstone R. M., Sanders J. S., Conselice C. J., Crawford C. S., Gallagher J. S., Zweibel E., 2008, *Nat.*, 454, 968
- Fabian A. C., Sanders J. S., Williams R. J. R., Lazarian A., Ferland G. J., Johnstone R. M., 2011, arXiv 1105.1735
- Falcke H., Rieke M. J., Rieke G. H., Simpson C., Wilson A. S., 1998, *ApJ*, 494, 155
- Ferland G. J., University of Kentucky Department of Physics and Astronomy Internal Rep.
- Ferland G. J., Korista K. T., Verner D. A., Ferguson J. W., Kingdon J. B., Verner E. M., 1998, *PASP*, 110, 761
- Ferland G. J., Fabian A. C., Hatch N. A., Johnstone R. M., Porter R. L., van Hoof P. A. M., Williams R. J. R., 2009, *MNRAS*, 392, 1475
- Filippenko A. V., 1996, *ASPC*, 103, 17
- Gonzalez-Martin, O., Masegosa, J., Marquez, I., Guainazzi, M., Jimenez-Bailon, E., 2009, *A&A* 506, 1107
- Groves B., Dopita M. A., Sutherland R. S., Kewley L. J., Fischera J., Leitherer C., Brandl B., van Breugel W., 2008, *ApJS*, 176, 438
- Hatch N. A., Crawford C. S., Fabian A. C., Johnstone R. M., 2005, *MNRAS*, 358, 765
- Hatch N. A., Crawford C. S., Johnstone R. M., Fabian A. C., 2006, *MNRAS*, 367, 433
- Hatch N. A., Crawford C. S., Fabian A. C., 2007, *MNRAS*, 380, 33
- Heckman T. M., 1980, *A&A*, 87, 152
- Heckman T. M., Baum S. A., van Breugel W. J., McCarthy, P., 1989, *ApJ*, 338, 48
- Irwin J. A., Stil J. M., Bridges T. J., 2001, *MNRAS*, 328, 359
- Jaffe W., Bremer M.N., 1997, *MNRAS*, 284, 1
- Jaffe W., Bremer M.N., van der Werf P.P., 2001, *MNRAS*, 324, 443

- Jaffe W., Bremer M.N., Baker K., 2005, MNRAS, 360, 748
- Johnstone R. M., Fabian A. C., Nulsen P. E. J., 1987, MNRAS, 224, 75
- Johnstone R. M., Fabian A. C., 1988, MNRAS, 233, 581
- Johnstone R. M., Hatch N. A., Ferland G. J., Fabian A. C., Crawford C. S., Wilman R. J., 2007, MNRAS, 382, 1246
- Kaastra J. S., den Boggende A. J., Brinkman A. C., Ferrigno C., den Herder J. W., Mewe R., Tamura T., de Vries C., Cottam J., Kahn S. M., Paerels F. B. S., Peterson J. M., Rasmussen A. P., Branduardi-Raymont G., Sakelliou I., Audard M., Güdel M., Erd C., 2001, ASPC, 234, 351
- Kaastra J. S., Paerels F. B. S., Durret F., Schindler S., Richter P., arXiv, 0801.1011
- Kewley L. J., Dopita M. A., 2002, ApJS, 142, 35
- Maia M. A. G., da Costa L. N., Willmer C., Pellegrini P. S., Rite C., 1987, AJ, 93, 546
- Maloney P. R., Hollenbach D. J., Tielens A. G. G. M., 1996, ApJ, 466, 561
- Markwardt C. B., 2009, ASPC, 411, 251
- McNamara B. R., O'Connell R. W., 1992, ApJ, 393, 579
- McNamara B. R., O'Connell R. W., 1993, AJ, 105, 417
- McNamara B. R., Wise M. W., Nulsen P. E. J., David L. P., Carilli C. L., Sarazin C. L., O'Dea C. P., Houck J., Donahue M., Baum S., Voit M., O'Connell R. W., Koekemoer A., 2001, ApJ, 562, 149
- McNamara B. R., Nulsen P. E. J., 2007, ARA&A, 45, 117
- McNamara B.R., Wise M. W., Murray S.S., 2004, ApJ, 601, 173
- Miller J. S., Mathews W. G., 1972, ApJ, 172, 593
- Morris R. G., Fabian A. C., 2005, MNRAS, 358, 585
- Nagao T., Maiolino R., Marconi A., 2006, A&A, 459, 85
- O'Dea C. P., Baum S. A., Gallimore, J. F., 1994, ApJ, 436, 669
- O'Dea C. P., Baum S. A., Mack J., Koekemoer A. M., Laor A., 2004, ApJ, 612, 131
- O'Dea C. P., Baum S. A., Privon G., Noel-Storr J., Quillen A. C., Zufelt N., Park, J., Edge A., Russell H., Fabian A. C., Donahue M., Sarazin C. L., McNamara B., Bregman J. N., Egami E., 2008, ApJ, 681, 1035
- O'Dea K. P., Quillen A. C., O'Dea C. P., Tremblay G. R., Snios B. T., Baum S. A., Christiansen K., Noel-Storr J., Edge A. C., Donahue M., Voit G. M., 2010, ApJ, 719, 1619
- Oegerle W. R., Cowie L., Davidsen A., Hu E., Hutchings J., Murphy E., Sembach K., Woodgate B., ApJ, 560, 187
- Ogle P., Boulanger F., Guillard P., Evans D. A., Antonucci R., Appleton P. N., Nesvadba, N., Leipski C., 2010, ApJ, 724, 1193
- Onk J. B. R., Jaffe W., Bremer M. N., van Weeren R. J., 2010, MNRAS, 405, 898
- Onk J. B. R., Hatch, N. A., Jaffe W., Bremer M. N., van Weeren R. J., 2011, MNRAS, 414, 2309
- Osterbrock D. E., Ferland G. J., 2006, Astrophysics of Gaseous Nebulae and Active Galactic Nuclei, University Science Books.
- Peterson J. R., Fabian A. C., 2006, PhR, 427, 1
- Pimblet K. A., Smail I, Edge A. C., O'Hely E., Couch W. J., Zabludoff A. I., 2006, MNRAS 366, 645
- Pollack L.K., Taylor G. B., Allen S.W., 2005, MNRAS, 359, 1229
- Rafferty D. A., McNamara B. R., Nulsen P. E. J., Wise M. W., 2006, ApJ, 652, 216

-
- Raymond J. C., Cox D. P., Smith B. W., 1976, *ApJ*, 204, 290
Salome P., Combes F., 2003, *A&A*, 412, 657
Salome P., Combes F., Revaz Y., Downes D., Edge A. C., Fabian A. C., 2011, *A&A*, 531, 85
Stasinska G., 1980, *A&A*, 85, 359
Sutherland R. S., Dopita M. A., 1993, *ApJS*, 88, 253
Voit G. M., Donahue M., Slavin J. D., 1994, *ApJS*, 95, 87
Voit G. M., Donahue M., 1997, *ApJ*, 486, 242
Voit G. M., Cavagnolo K. W., Donahue M., Rafferty D. A., McNamara B. R., Nulsen P. E. J., 2008, *ApJ*, 681, 5
Wilman R. J., Edge A. C., Johnstone R. M., Fabian A. C., Allen S. W., Crawford C. S., 2002, *MNRAS*, 337, 63
Wilman R. J., Edge A. C., Swinbank A. M., 2006, *MNRAS*, 359, 93
Wilman R. J., Edge A. C., Swinbank A. M., 2009, *MNRAS*, 395, 1355

Date	Source	Grism	Slit Width	Exptime
1999-07-14	A2597-NUC	600R/600B	2.0/2.0	1000/1000
1999-07-14	A2597-OFF	600R/600B	2.5/2.5	3600/3600
1999-07-15	S159-NUC	600R/600B	2.5/2.5	1000/1000
1999-07-15	S159-OFF	600R/600B	2.5/2.5	2700/3600
2002-05-04	A2204-NUC	600R	2.5	540
2002-05-05	A2204-NUC	600R/600B	2.5/2.5	1200/1200

Table 6.1 — VLT FORS long-slit spectroscopy. Observations summary.

Name	$A_{V,MW}$	$A_{V,BCG}$	$H\delta/H\beta$	$H\gamma/H\beta$	$H\alpha/H\beta$
A2597-NUC	0.10	1.10	0.19 (0.25)	0.40 (0.49)	4.52 (2.95)
A2597-OFF	0.10	1.10	0.19 (0.25)	0.42 (0.51)	4.44 (2.90)
A2204-NUC	0.31	1.40	0.15 (0.22)	0.38 (0.50)	5.29 (2.92)
S159-NUC	0.04	0.00	0.34	0.63	-
S159-OFF	0.04	0.00	0.26	0.51	-

Table 6.2 — Dust in A2597, A2204 and S159. The Milky Way foreground dust is taken from Schlegel et al. (1998). The Dust intrinsic to the BCG is calculated using the MM72 extinction law in combination and assuming the dust-free case B stellar Balmer decrements i.e. $H\delta/H\beta=0.26$, $H\gamma/H\beta=0.47$, $H\alpha/H\beta=2.87$ (Osterbrock & Ferland 2006). The observed Balmer decrements are given in columns 4-6. In parentheses the de-reddened values are given for comparison. Note that for S159 the $H\alpha/H\beta$ was measured in the same slit and therefore we do not give a value for this ratio. The remaining Balmer decrements in S159 are consistent with zero dust.

Line	Wavelength	A2597-NUC	A2597-OFF	A2204-NUC
OII	3727	5.06 ± 0.05 (7.36)	3.11 ± 0.15 (4.51)	3.52 ± 0.05 (6.04)
NeIII	3869	0.22 ± 0.01 (0.31)	<0.11 (0.16)	0.19 ± 0.01 (0.30)
Hζ+HeI	3888	0.09 ± 0.01 (0.12)	<0.11 (0.15)	0.12 ± 0.01 (0.19)
NeIII+CaII+Heε	3966	0.17 ± 0.01 (0.23)	0.20 ± 0.05 (0.27)	0.17 ± 0.01 (0.26)
SII	4069	0.21 ± 0.01 (0.27)	<0.13 (0.17)	0.17 ± 0.01 (0.25)
Hδ	4104	0.19 ± 0.01 (0.25)	0.19 ± 0.04 (0.25)	0.15 ± 0.01 (0.22)
Hγ	4340	0.40 ± 0.01 (0.49)	0.42 ± 0.04 (0.51)	0.38 ± 0.01 (0.50)
HeII	4686	0.02 ± 0.01 (0.03)	-	0.02 ± 0.01 (0.02)
Hβ	4861	1.00 (1.00)	1.00 (1.00)	1.00 (1.00)
OIII	4959	0.21 ± 0.01 (0.20)	0.09 ± 0.04 (0.09)	0.17 ± 0.01 (0.16)
OIII	5007	0.65 ± 0.01 (0.61)	0.19 ± 0.05 (0.18)	0.57 ± 0.02 (0.53)
NI	5200	0.34 ± 0.01 (0.31) ^a	0.24 ± 0.05 (0.22) ^a	0.49 ± 0.02 (0.42) ^a
NII	5755	0.06 ± 0.01 (0.05)	<0.09 (0.07)	0.08 ± 0.01 (0.06)
HeI	5874	0.08 ± 0.01 (0.06) ^a	0.16 ± 0.03 (0.12) ^a	0.12 ± 0.01 (0.08) ^a
OI	6300	1.41 ± 0.02 (0.97)	1.09 ± 0.08 (0.75)	1.41 ± 0.03 (0.83)
OI	6363	0.41 ± 0.01 (0.28) ^b	0.25 ± 0.05 (0.17) ^b	0.57 ± 0.03 (0.33)
NII	6548	1.44 ± 0.03 (0.94)	1.04 ± 0.09 (0.68)	2.12 ± 0.06 (1.17)
Hα	6563	4.52 ± 0.05 (2.95)	4.44 ± 0.21 (2.90)	5.29 ± 0.10 (2.92)
NII	6584	3.75 ± 0.04 (2.44)	2.84 ± 0.14 (1.85)	6.66 ± 0.12 (3.65)
SII	6717	-	1.43 ± 0.09 (0.91)	-
SII	6731	-	0.93 ± 0.07 (0.59)	-

Table 6.3 — A2597 and A2204: Measured line ratios relative to Hβ for the spatially integrated slits. The corresponding observed Hβ intensities are 8×10^{-15} erg s⁻¹ cm⁻² for A2597-NUC, 1×10^{-15} erg s⁻¹ cm⁻² for A2597-OFF and 7×10^{-15} erg s⁻¹ cm⁻² for A2204 (all uncorrected for extinction). In parentheses we give the extinction corrected line ratios. Upper limits for undetected lines are calculated as 3*RMS*FWHM.

^a line is affected by stellar absorption.

^b line is affected by telluric emission.

Line	Wavelength	S159-NUC	S159-OFF
OII	3727	4.43 ± 0.37	3.17 ± 0.16
NeIII	3869	<0.23	<0.12
Hζ+HeI	3888	<0.23	<0.12
NeIII+CaII+Heε	3966	0.48 ± 0.10	0.27 ± 0.05
SII	4069	0.18 ± 0.08	0.08 ± 0.04
Hδ	4104	0.34 ± 0.09	0.26 ± 0.05
Hγ	4340	0.63 ± 0.11	0.51 ± 0.06
HeII	4686	-	-
Hβ	4861	1.00	1.00
OIII	4959	0.25 ± 0.09	0.09 ± 0.05
OIII	5007	0.43 ± 0.10	0.18 ± 0.05
NI	5200	<0.24 ^a	0.27 ± 0.06 ^a

Table 6.4 — S159: Measured line ratios relative to Hβ for the spatially integrated blue slits. The corresponding integrated Hβ intensity is 2×10^{-15} erg s⁻¹ cm⁻² for S159-NUC and 2×10^{-15} erg s⁻¹ cm⁻² for S159-OFF (all uncorrected for extinction). The measured Balmer decrements are consistent with zero dust and hence we do not provide extinction corrected line ratios. Upper limits for undetected lines are calculated as 3*RMS*FWHM.

^a line is affected by stellar absorption.

Line	Wavelength	S159-NUC	S159-OFF
NII	5755	<0.04	<0.03
HeI	5874	- ^a	- ^a
OI	6300	0.24 ± 0.02	0.20 ± 0.01
OI	6363	0.09 ± 0.02	0.08 ± 0.01
NII	6548	0.33 ± 0.02	0.28 ± 0.01
H α	6563	1.00	1.00
NII	6584	1.18 ± 0.03	0.92 ± 0.02
SII	6717	0.55 ± 0.02	0.32 ± 0.01
SII	6731	0.38 ± 0.02	0.22 ± 0.01

Table 6.5 — S159: Measured line ratios relative to H α for the spatially integrated red slits. The corresponding integrated H α intensity is 7×10^{-15} erg s $^{-1}$ cm $^{-2}$ for S159-NUC and 8×10^{-15} erg s $^{-1}$ cm $^{-2}$ for S159-OFF (all uncorrected for extinction). We note we measure relative to H α because these slits did not cover H β . The blue slits showed that the S159 measurements are consistent with zero dust and hence we do not provide extinction corrected line ratios. Upper limits for undetected lines are calculated as $3 \times \text{RMS} \times \text{FWHM}$.

^a line is affected by stellar absorption.

Slit	Temperature	Density	Metallicity	Ionisation parameter
A2597-NUC	11100 ± 1100	300 ^a	0.92	-3.39
A2597-OFF	<16900	<50	1.07	-3.59
A2204-NUC	10900 ± 1000	1000 ^b	1.27	-3.35
S159-NUC	<16300	<50	1.39	-3.34
S159-OFF	<15800	<50	1.44	-3.50

Table 6.6 — Gas properties. Estimates from single line ratios. The temperature in units of Kelvin is estimated from the NII(6548+6584)/NII(5755) ratio, using the relation given in Osterbrock & Ferland (2006). For the temperature derived in A2597-NUC and A2204-NUC a density of 300 cm $^{-3}$ was assumed. For the remaining cases a density of 50 cm $^{-3}$ was assumed. The density is estimated in units of cm $^{-3}$ from the SII(6717)/SII(6731) ratio, using the relation given in Osterbrock & Ferland (2006). For the derived densities a gas temperature of 11000 K was assumed. The metallicity in units of solar metallicity Z_{\odot} is estimated from the NII(6584)/OII(3727) ratio, using the relation given in Kewley & Dopita (2002). For the S159 observations we assumed that H α /H β =2.87 (case B recombination with no dust) to link the NII and OII lines. The ionisation parameter in the form of log(U) is estimated from the OIII(5007)/OII(3727) ratio using the relation given in Kewley & Dopita (2002).

^a For A2597-NUC the measurement of the SII lines by Voit & Donahue (1997) is used.

^b For A2204-NUC the measurement of the SII lines by Crawford et al. (1999) is used.

Line	Wavelength	Observed	Stars	AGN	bremstrahlung	Combined
OII	3727	7.36	2.24	6.17	8.04	6.45
NeIII	3869	0.31	0.05	0.90	1.19	0.87
H ζ +HeI	3888	0.12	0.21	0.24	0.24	0.24
CaII	3934	<0.02	0.12	0.56	0.77	0.58
NeIII+CaII+H ϵ	3966	0.23	0.23	0.72	0.92	0.72
SII	4069	0.27	0.04	0.16	0.19	0.14
H δ	4104	0.25	0.26	0.26	0.26	0.26
H γ	4340	0.49	0.46	0.47	0.47	0.47
MgI	4567	<0.02	0.54	0.28	0.17	0.23
HeII	4686	0.02	<0.01	0.19	0.30	0.15
H β	4861	1.00	1.00	1.00	1.00	1.00
OIII	4959	0.20	0.05	0.19	0.27	0.22
OIII	5007	0.61	0.15	0.55	0.78	0.63
NI	5200	0.31 ^a	0.02	0.49	0.43	0.44
NII	5755	0.05	0.01	0.03	0.04	0.03
HeI	5874	0.06 ^a	0.14	0.19	0.18	0.18
OI	6300	0.97	0.07	1.23	1.25	1.07
OI	6363	0.28 ^b	0.02	0.40	0.40	0.35
NII	6548	0.94	0.40	0.83	1.03	0.83
H α	6563	2.95	2.94	2.94	2.94	2.93
NII	6584	2.44	1.18	2.44	3.03	2.43
SII	6717	1.51 ^c	0.63	2.14	2.20	1.70
SII	6731	1.20 ^c	0.55	1.67	1.74	1.34

Table 6.7 — The best-fitting MAPPINGS III models for A2597-NUC with gas properties $Z=Z_{\odot}$ and $n(\text{H})=300 \text{ cm}^{-3}$. The observed line ratios are corrected for extinction by dust. The stars model has $T_{BB}=55000 \text{ K}$, $\log(U)=-3.625$. The AGN model has $\alpha=-1.0$ and $\log(U)=-3.75$. The bremsstrahlung model has $T_X=10^6 \text{ K}$ and $\log(U)=-3.75$. The combined model consists of a stellar model with $T_{BB}=68000 \text{ K}$ and 80% of a bremsstrahlung model with $T_X=10^7 \text{ K}$. This combined model has $\log(U)=-3.6875$. For the models we report all lines with a flux at least one tenth of $\text{H}\beta$ within the wavelength range probed by our observations.

^a line is affected by stellar absorption.

^b line is affected by telluric emission.

^c These [SII] line values are taken from Voit & Donahue (1997) and extinction corrected.

Line	Wavelength	Observed	Stars	AGN	bremsstrahlung	Combined
OII	3727	4.51	2.84	4.53	5.44	4.55
NeIII	3869	<0.16	0.13	0.54	0.68	0.54
H ζ +HeI	3888	<0.15	0.22	0.24	0.25	0.24
CaII	3934	<0.15	0.16	0.38	0.53	0.40
NeIII+CaII+HeI	3966	0.27	0.28	0.52	0.64	0.53
SII	4069	<0.17	0.05	0.12	0.16	0.11
H δ	4104	0.25	0.26	0.26	0.26	0.26
H γ	4340	0.51	0.46	0.46	0.46	0.46
MgI	4567	<0.16	0.50	0.22	0.18	0.23
HeII	4686	<0.16	0.02	0.15	0.21	0.11
H β	4861	1.00	1.00	1.00	1.00	1.00
OIII	4959	0.09	0.07	0.09	0.08	0.09
OIII	5007	0.18	0.21	0.26	0.23	0.25
NI	5200	0.22 ^a	0.03	0.29	0.29	0.35
NII	5755	<0.07	0.01	0.02	0.03	0.02
HeI	5874	0.12 ^a	0.16	0.18	0.19	0.19
OI	6300	0.75	0.13	0.75	0.88	0.82
OI	6363	0.17 ^b	0.04	0.25	0.29	0.27
NII	6548	0.68	0.47	0.68	0.82	0.65
H α	6563	2.90	2.94	2.93	2.93	2.94
NII	6584	1.85	1.38	2.00	2.42	1.92
SII	6717	0.91	0.93	2.04	2.57	1.79
SII	6731	0.59	0.67	1.44	1.81	1.26

Table 6.8 — The best-fit MAPPINGS III models for A2597-OFF with gas properties $Z=Z_{\odot}$ and $n(\text{H})=50 \text{ cm}^{-3}$. The observed line ratios are corrected for extinction by dust. The stars model has $T_{BB}=70000 \text{ K}$ and $\log(U)=-3.75$. The AGN model has $\alpha=-1.2$ and $\log(U)=-3.875$. The bremsstrahlung model has $T_X=7\times 10^5 \text{ K}$ and $\log(U)=-4$. The combined model consists of a stellar model $T_{BB}=60000 \text{ K}$ and 40% of a bremsstrahlung model with $T_X=10^7 \text{ K}$. This combined model has $\log(U)=-3.8125$. For the models we report all lines with a flux at least one tenth of $H\beta$ within the wavelength range probed by our observations.

^a line is affected by stellar absorption.

^b line is affected by telluric emission.

Line	Wavelength [μm]	Observed	Stars	AGN	bremsstrahlung	Combined
NeIII/NeII	15.5/12.8	0.39 ^a	0.41	2.61	4.39	3.18
Br γ /Pa α	2.16/1.88	0.08	0.08	0.08	0.08	0.08
Br δ /Pa α	1.95/1.88	0.05	0.05	0.05	0.05	0.05
FeII/Pa α	1.81/1.88	0.19	0.32	1.76	1.57	1.46

Table 6.9 — The best-fitting MAPPINGS III models for A2597-NUC. The parameters for the best-fitting models are specified in the caption of Table 6.7.

^a The [NeII] 12.8 μm and [NeIII] 15.5 μm line data is from Jaffe & Bremer (in prep.). The near-infrared line data is from Oonk et al. (2010).

Line Ratio	A2597-NUC	A2597-OFF
OIII 5007/OII 3727	0.08 ± 0.02	0.04 ± 0.02
OII 3727/H β	7.36 ± 0.74	4.51 ± 0.45
OIII 5007/H β	0.61 ± 0.06	0.18 ± 0.02
NI 5200/H β	0.31 ± 0.03	0.24 ± 0.02
OI 6300/H α	0.33 ± 0.03	0.26 ± 0.03
NII 6584/H α	0.83 ± 0.08	0.64 ± 0.06

Table 6.10 — Line ratio constraints for combined stars and bremsstrahlung models. Column 2 specifies the line ratio constraints for the A2597-NUC spectrum. Similarly, Column 3 specifies this for the A2597-OFF spectrum. The tolerance on the line ratios for an acceptable fit have been set to 10%. This also takes into the systematic uncertainties. The only exception to this is the [OIII] 5007/[OII] 3727 ratio where we accept the model value if it is within 30% of the measured value.

Gas phase	T(NUC) K	n(NUC) cm ⁻³	n \times Λ (NUC) erg s ⁻¹ H ⁻¹	T(OFF) K	n(OFF) cm ⁻³	n \times Λ (OFF) erg s ⁻¹ H ⁻¹
X-ray	2×10^7	8×10^{-2}	2×10^{-24}	3×10^7	6×10^{-2}	2×10^{-24}
[OII]	12000	$3 \times 10^{+2}$	5×10^{-22}	12000	$5 \times 10^{+1}$	6×10^{-23}
[OI]	4000	$3 \times 10^{+2}$	4×10^{-22}	4000	$5 \times 10^{+1}$	5×10^{-23}
H ₂ (2000 K)	2000	$1 \times 10^{+6}$	5×10^{-22}	2000	$1 \times 10^{+6}$	3×10^{-22}
H ₂ (500 K)	500	$1 \times 10^{+6}$	2×10^{-22}	-	-	-

Table 6.11 — Radiative cooling rates for A2597. Columns 2-4 give the temperature, density and specific cooling rates for gas in the nuclear region. Columns 5-7 give the same quantities for the off-nuclear region.

Element	MAPPINGS III (1.0 z_{\odot})	MAPPINGS III (0.4 z_{\odot})	FERLAND-2009 (Orion)
He	-1.01	-1.079	-1.022
Li	-11.3	-11.69	-10.268
Be	-10.9	-11.29	-20.000
B	-9.0	-9.39	-10.051
C	-3.59	-4.25	-3.523
N	-4.22	-4.91	-4.155
O	-3.34	-3.74	-3.398
F	-6.10	-6.49	-20.000
Ne	-3.91	-4.30	-4.222
Na	-5.75	-6.15	-6.523
Mg	-4.47	-4.82	-5.523
Al	-5.61	-6.00	-6.699
Si	-4.49	-4.85	-5.398
P	-6.48	-6.88	-6.796
S	-4.79	-5.19	-5.000
Cl	6.40	-6.79	-7.000
Ar	-5.20	-5.59	-5.523
K	-7.05	-7.45	-7.959
Ca	-5.64	-6.04	-7.699
Fe	-4.55	-4.76	-5.523
Ni	-5.68	-6.08	-7.000

Table 6.12 — Gas abundances in \log_{10} relative to H. Column 2 shows the abundances for 1.0 solar metallicity gas cloud in MAPPINGS III. Column 3 shows the same, but now for a 0.4 solar metallicity gas cloud. Column 4 shows the abundances used and by Ferland et al. (2009). There are significant differences between these abundances and they have a strong impact on model results. Of particular importance here is the difference in ratio of the Oxygen to Neon abundances in our abundances and those used by Ferland et al. (2009).

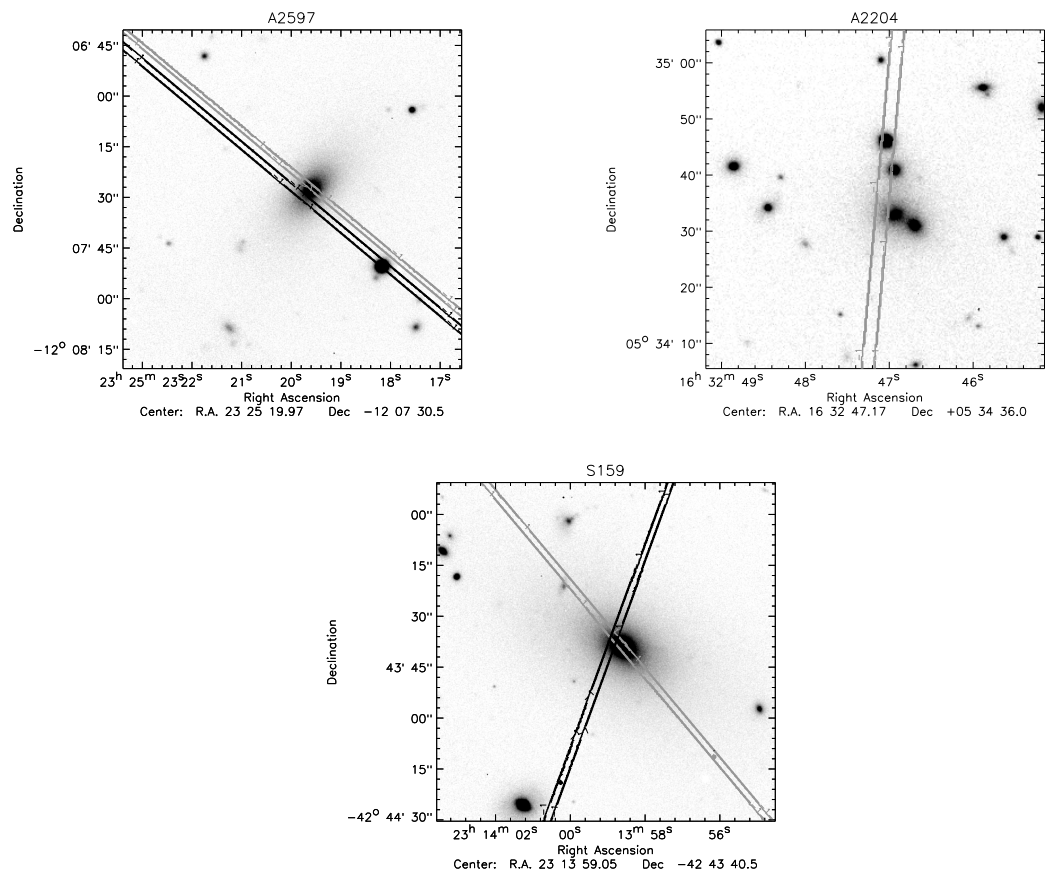


Figure 6.1 — FORS long-slit positions shown overlaid on optical images of A2597, A2204 and S159. (Top left) A2597, the A2597-NUC slit is in grey and A2597-OFF is in black. (Top right) A2204, the A2204-NUC slit is in grey. (Bottom) S159, the S159-NUC slit is in grey and S159-OFF is in black.

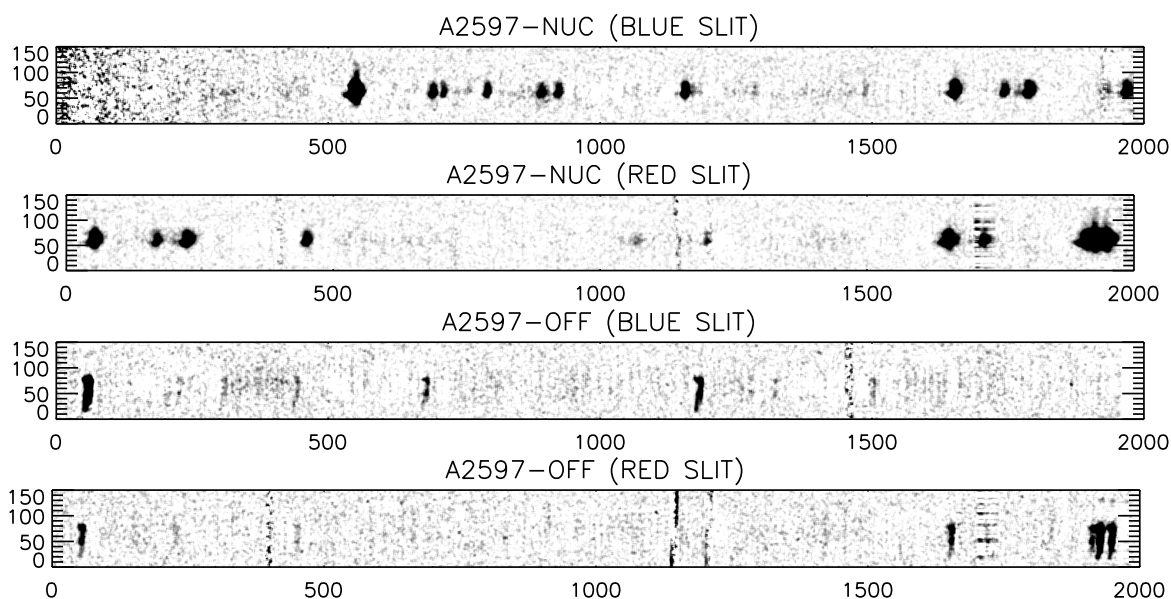


Figure 6.2 — A2597: Continuum subtracted FORS 2D Spectra. The peak optical continuum position corresponds to pixel 60 on the y-axis for A2597-NUC and to pixel 70 on the y-axis for A2597-OFF. Increasing values on the y-axis are northwards along the slits. The spectra have been smoothed lightly and are scaled to enhance the low surface brightness flux. The x-axis corresponds to the spectral axis along the slit and it is given in units of pixels, with one pixel being approximately 1 Angstrom. The y-axis corresponds to the spatial axis along the slit in units of pixels, with one pixel being 0.2 arcsec.

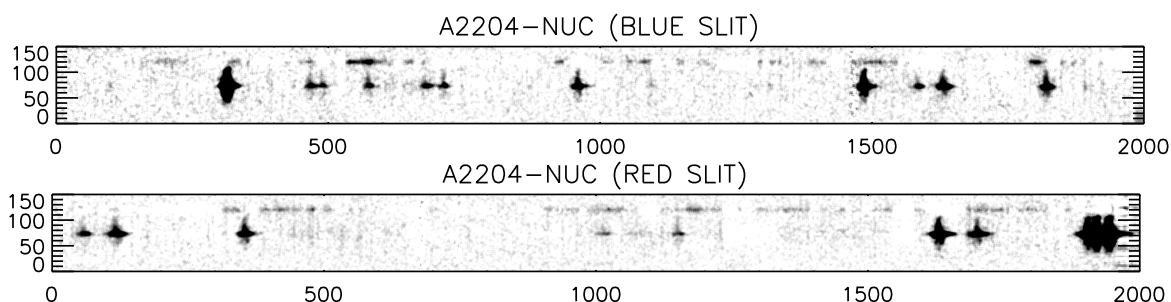


Figure 6.3 — A2204: Continuum subtracted FORS 2D Spectra. The peak optical continuum position corresponds to pixel 75 on the y-axis for A2204-NUC. Increasing values on the y-axis are northwards along the slits. The same smoothing and pixel-scale as in Fig. 6.2 has been applied.

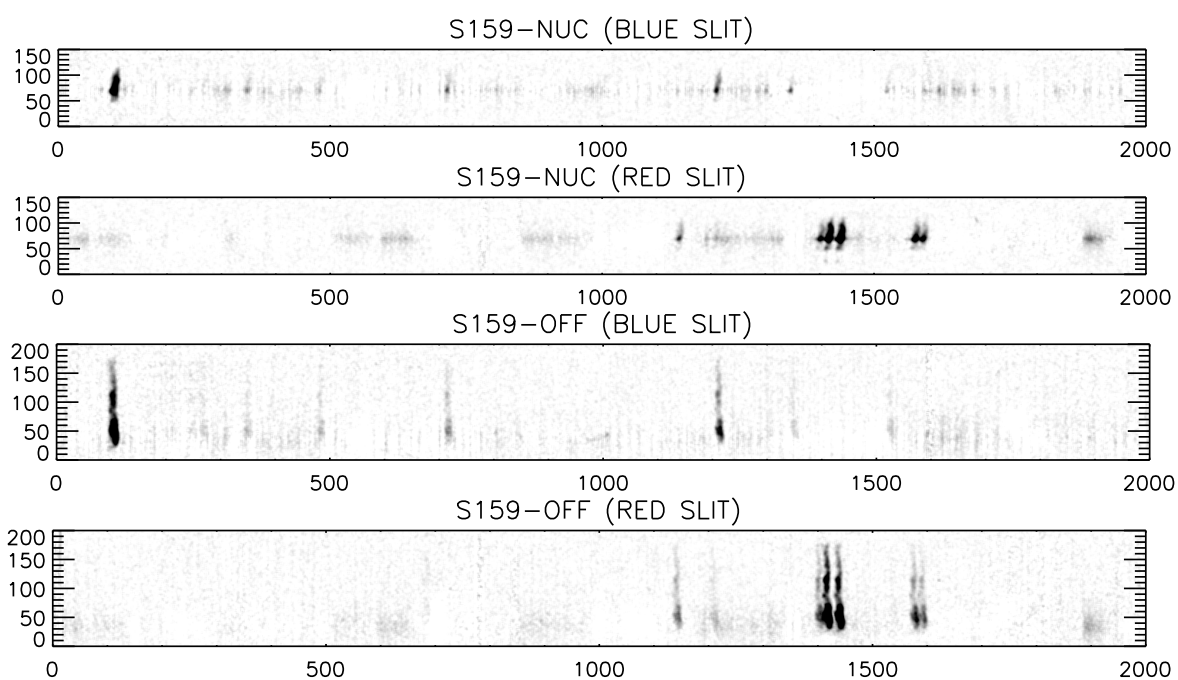


Figure 6.4 — S159: Continuum subtracted FORS 2D Spectra. The peak optical continuum position corresponds to pixel 70 on the y-axis for S159-NUC and to pixel 35 on the y-axis for S159-OFF. Increasing values on the y-axis are northwards along the slits. The same smoothing and pixel-scale as in Fig. 6.2 has been applied.

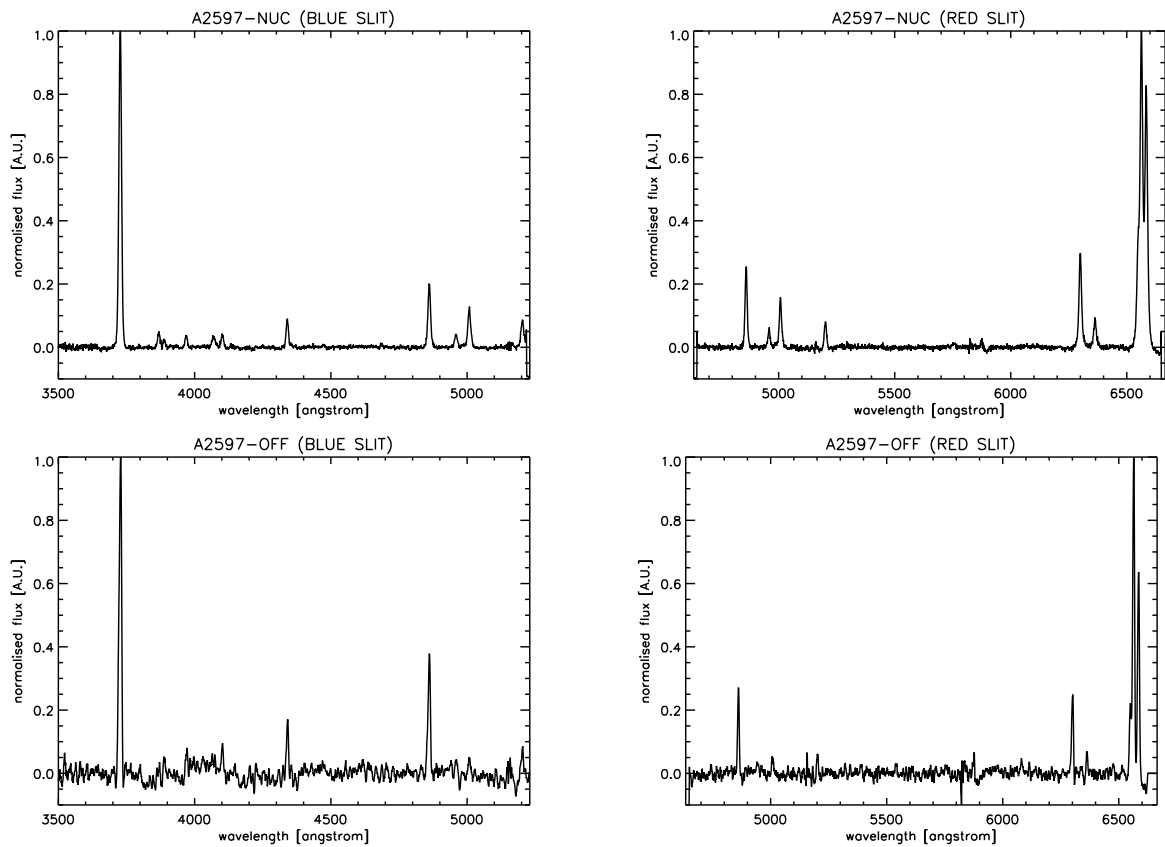


Figure 6.5 — A2597: FORS spatially integrated spectra. (Top) A2597-NUC. The spectra were integrated from pixel 40 to pixel 90 on the y-axis in Fig. 6.2 (Bottom) A2597-OFF. The spectra were integrated from pixel 20 to pixel 90 on the y-axis in Fig. 6.2.

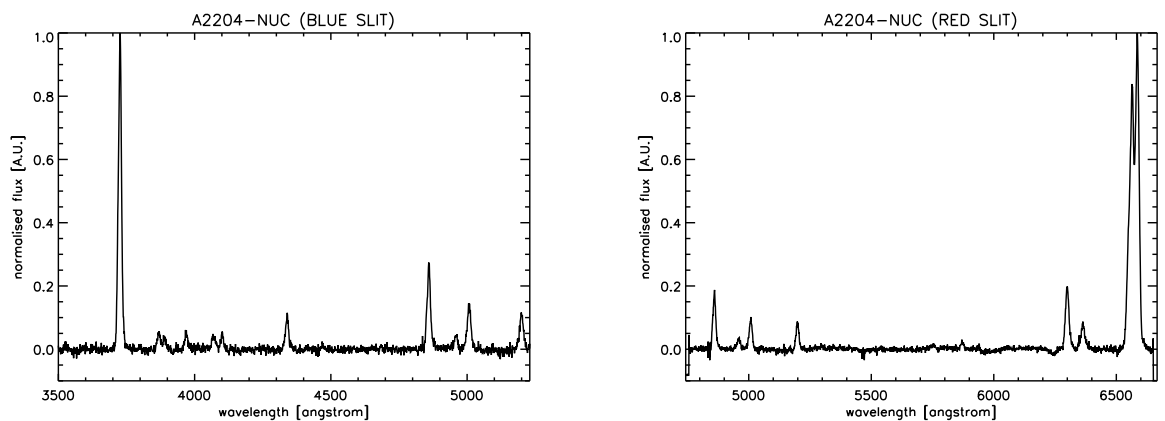


Figure 6.6 — A2204: FORS spatially integrated spectra for A2204-NUC. The spectra were integrated from pixel 40 to pixel 110 on the y-axis in Fig. 6.3.

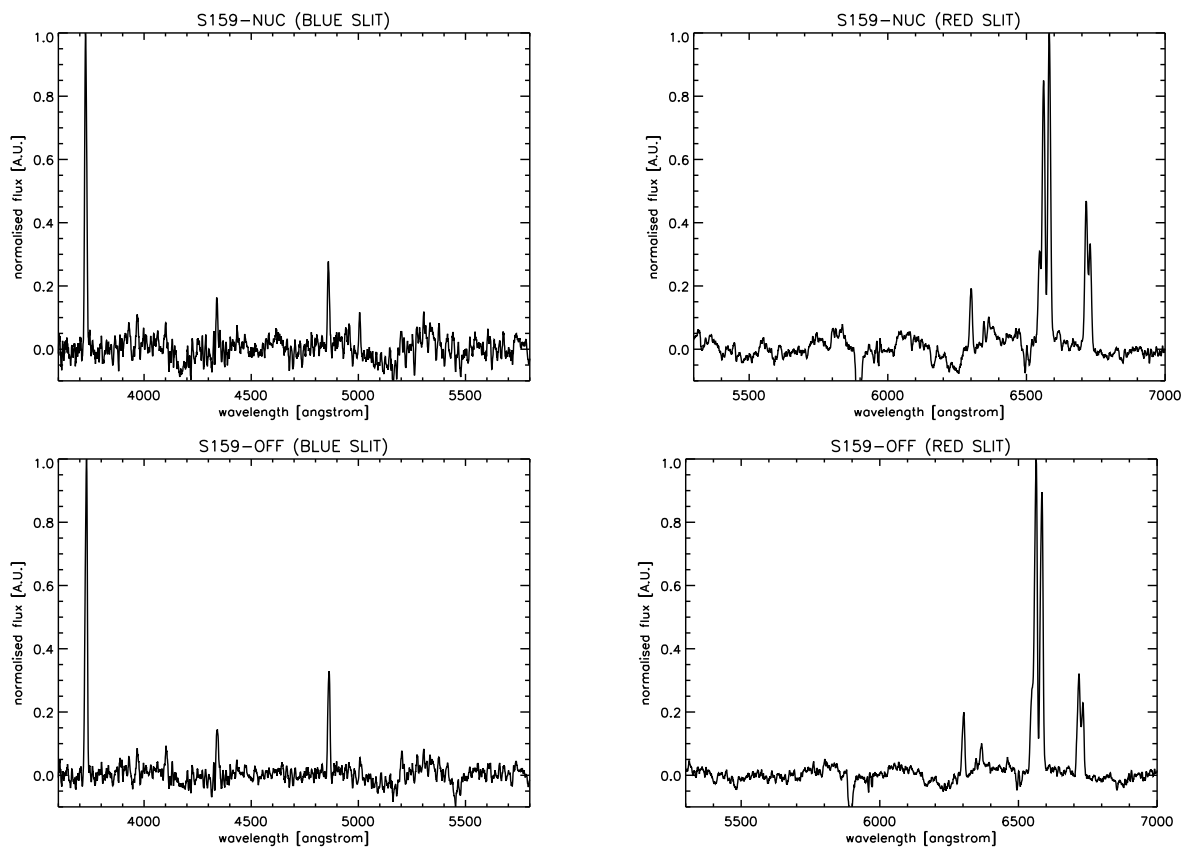


Figure 6.7 — S159: FORS spatially integrated spectra. A light smoothing of 4 pixels FWHM along the spectral axis has been applied to the data. (Top) S159-NUC. The spectra were integrated from pixel 50 to pixel 100 on the y-axis in Fig. 6.4. (Bottom) S159-OFF. The spectra were integrated from pixel 30 to pixel 160 on the y-axis in Fig. 6.4.

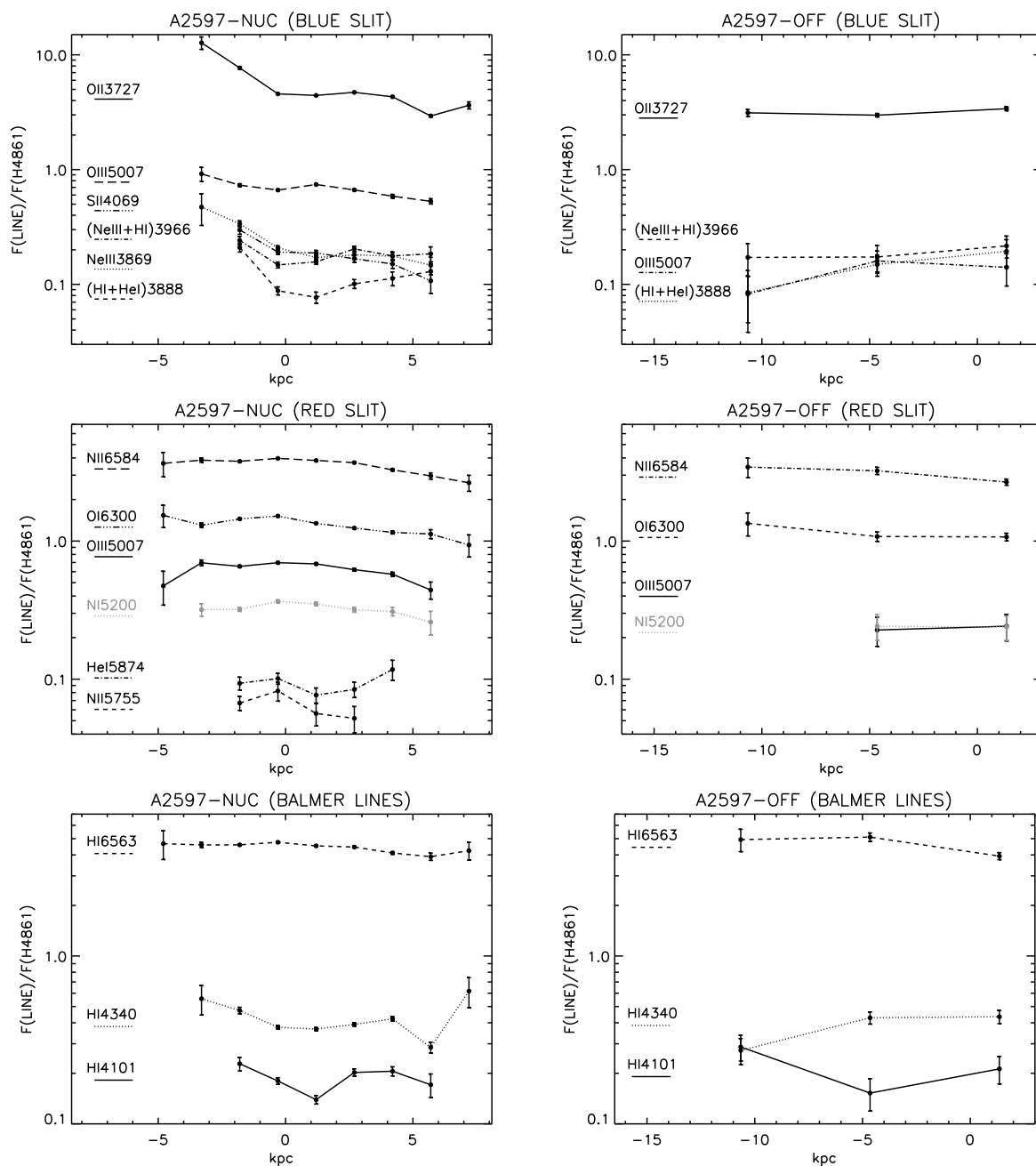


Figure 6.8 — A2597: Measured line ratios relative to $H\beta$ as a function of distance along the slits. The centre of the distance axis is defined as the position along the slit that corresponds to the peak in the optical continuum emission. Note that for the off-nuclear slits this peak does not correspond to the position BCG nucleus. (Top-Left) Blue slit for A2597-NUC. (Top-Right) Blue slit for A2597-OFF. (Middle-Left) Red slit for A2597-NUC. (Middle-Right) Red slit A2597-OFF. (Bottom-Left) The hydrogen Balmer lines for A2597-NUC. (Bottom-Right) The hydrogen Balmer lines for A2597-OFF. The centers of the emission in A2597-NUC and A2597-OFF are given with respect to the peak in optical continuum emission in each of the slits.

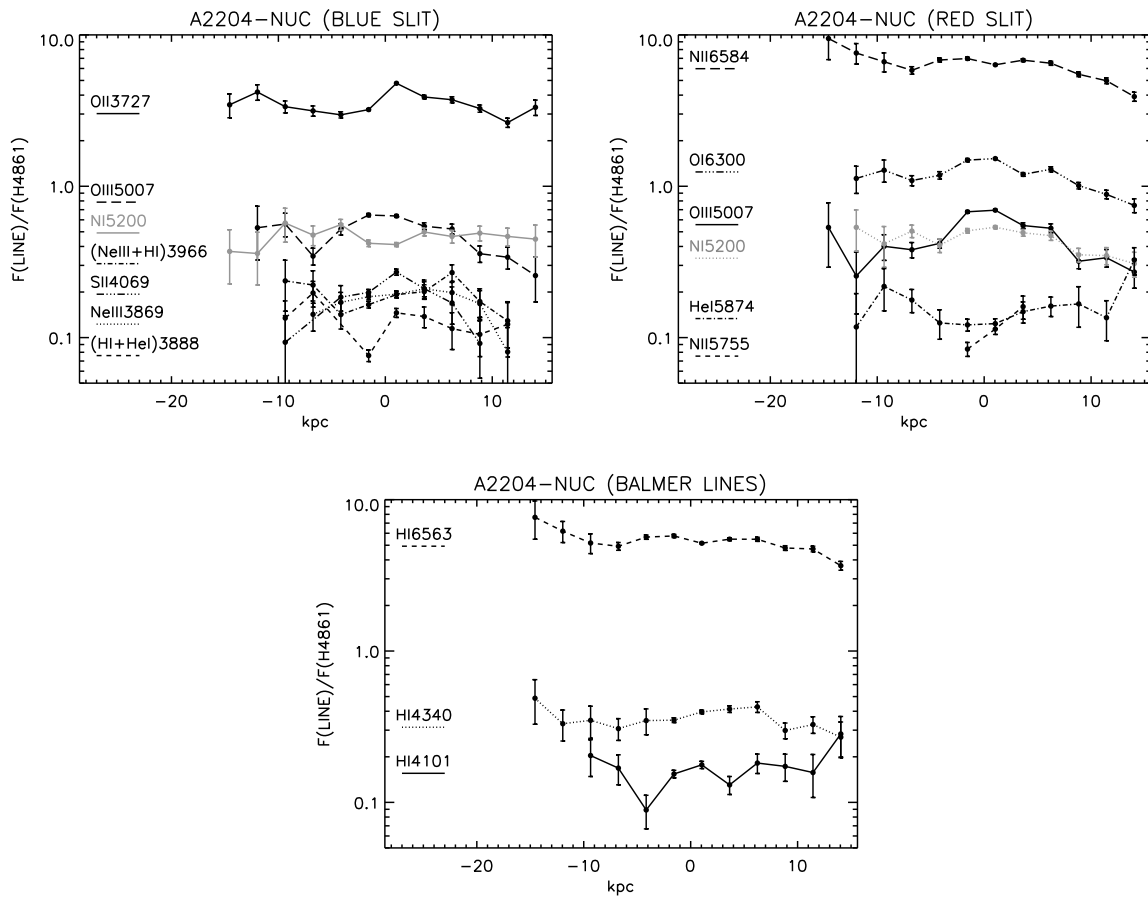


Figure 6.9 — A2204: Measured line ratios relative to H β as a function of distance along the slits. (Top-Left) Blue slit for A2204-NUC. (Top-Right) Red slit for A2204-NUC. (Bottom-Middle) The hydrogen Balmer lines for A2204-NUC. The center of the emission in A2204-NUC is given with respect to the peak in the optical continuum emission

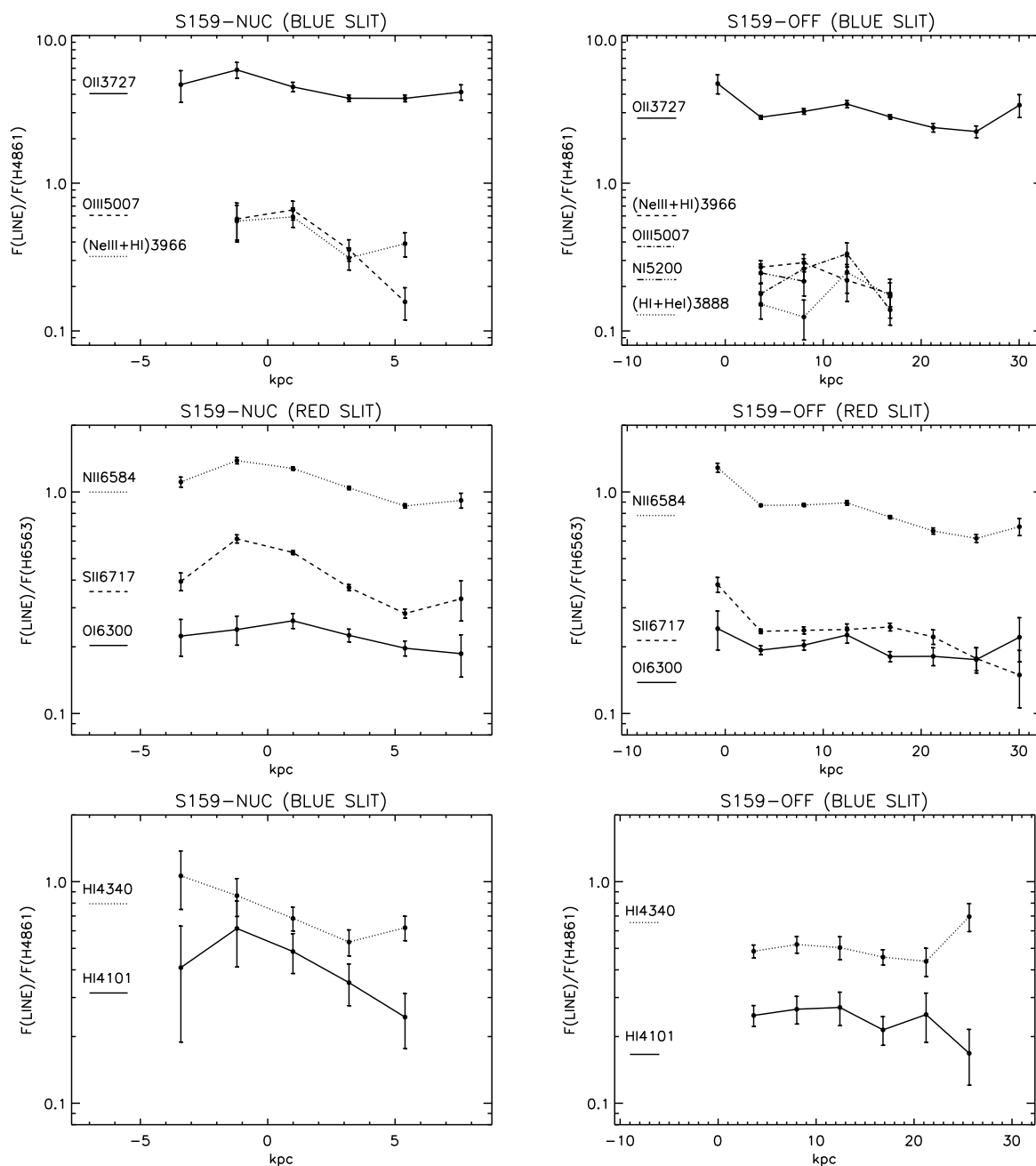


Figure 6.10 — S159: Measured line ratios relative to $H\beta$ as a function of distance along the blue slits and relative to $H\alpha$ as a function of distance along the red slits. (Top-left) Blue slit for S159-NUC. (Top-Right) Blue slit for S159-OFF. (Middle-Left) Red slit for S159-NUC. (Middle-Right) Red slit for S159-OFF. (Bottom-Left) The hydrogen Balmer lines for S159-NUC. (Bottom-Right) The hydrogen Balmer lines for S159-OFFM1-NUC. The centers of the emission in S159-NUC and S159-OFF are given with respect to the peak in optical continuum emission in each of the slits.

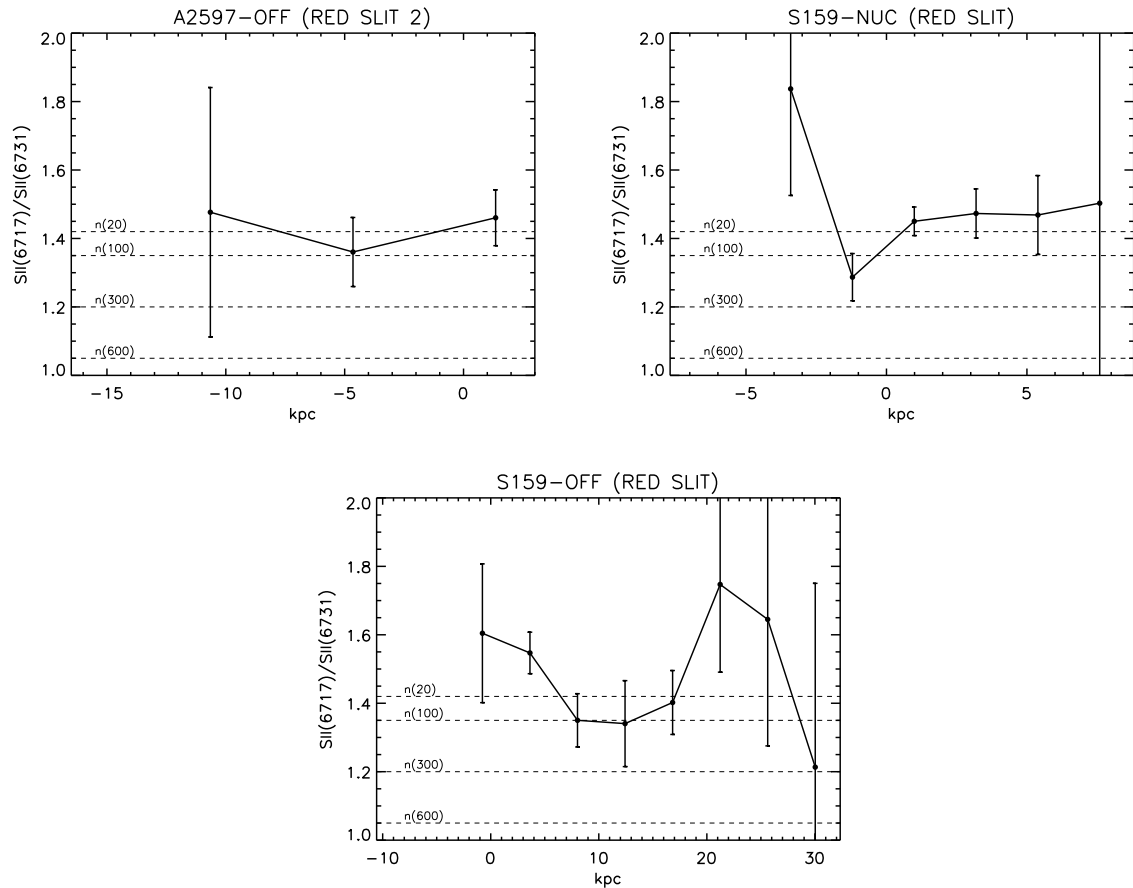


Figure 6.11 — [SII] 6717/[SII] 6731 line ratio as a function of distance along the slit. (Top-Left) A2597-OFF. The SII lines here are obtained from an exposure for which the position is the same, but the central wavelength was shifted with respect to the A2597-OFF spectrum discussed in the text. Note that there is a weak decrease of the line ratio at -5 kpc, this location is consistent with the bright blob south of the optical continuum. (Top-Right) S159-NUC. The line ratio increases with distance to the nucleus. (Bottom-Middle) S159-OFF. The line ratio shows a prominent decrease at 10 kpc. This location coincides with a bright blob to the north of the optical continuum. From top to bottom the dashed horizontal lines in each figure show the SII line ratio value corresponding to gas densities of 20, 100, 300 and 600 cm^3 . Gas temperatures of 11000 K were assumed.

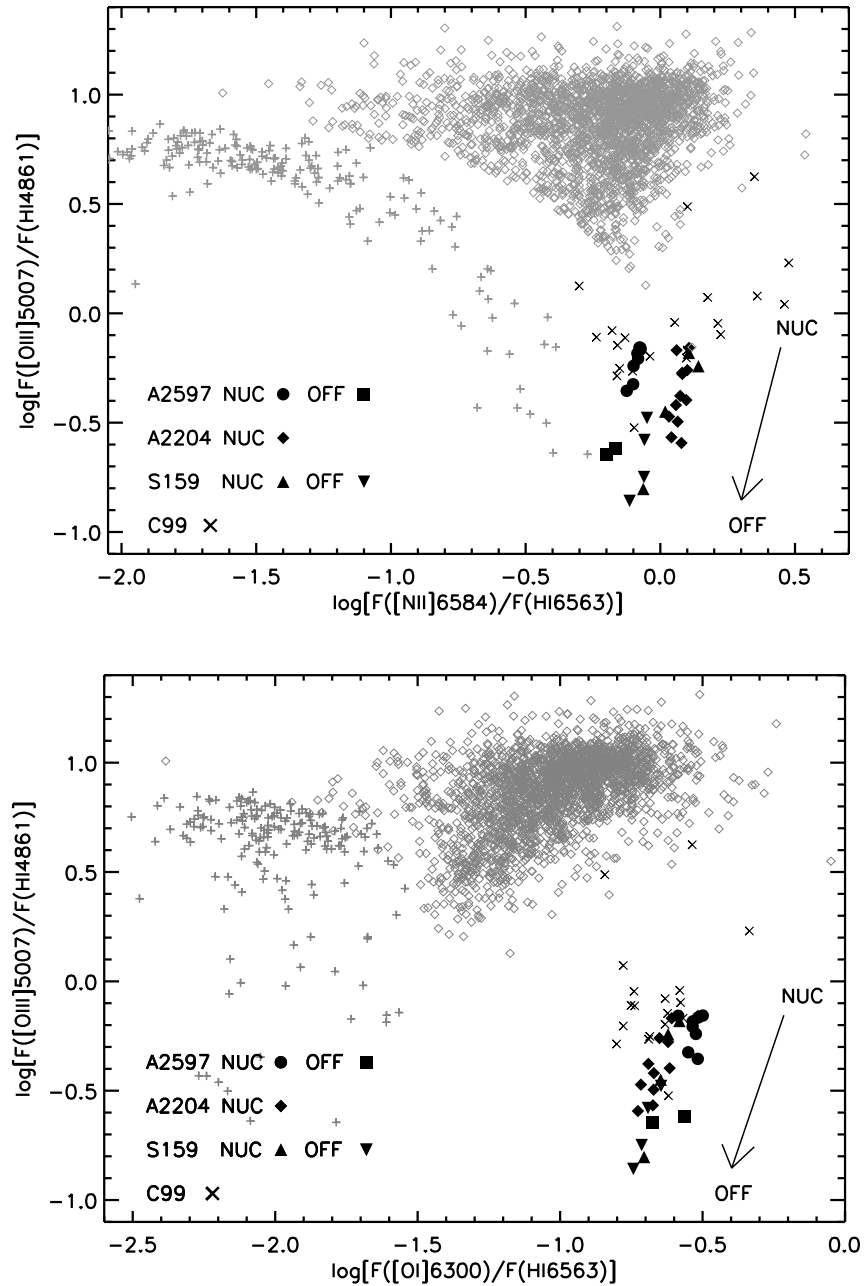


Figure 6.12 — Observed BPT diagrams. (Top) $\text{Log } [OIII]5007/H\beta$ vs. $\text{Log } [NII]6548/H\alpha$. (Bottom) $\text{Log } [OIII]5007/H\beta$ vs. $\text{Log } [OI]6300/H\alpha$. The $[OIII]5007/H\beta$ ratio drops by a factor of about 3 for each of the BCGs from the nuclear to the off-nuclear regions. In contrast the $[OI]6300/H\alpha$ ratio drops by only about 25 per cent over the same area. The filled black points are measurements for A2597, A2204 and S159 along their respective slits. The arrow indicates how the line ratios evolve with distance from the nucleus. The black X-symbols are BCGs from Crawford et al. (1999). Only those BCGs for which the lines have been measured with a signal-to-noise of at least 3 are plotted here. The grey crosses are starburst galaxies and the grey diamonds are AGN. Both samples are taken from the Sloan Digital Sky Survey (M. Shirazi & J. Brinchmann in prep.). Note that for clarity reasons we have omitted to plot LINER galaxies from the Sloan Digital Sky Survey.

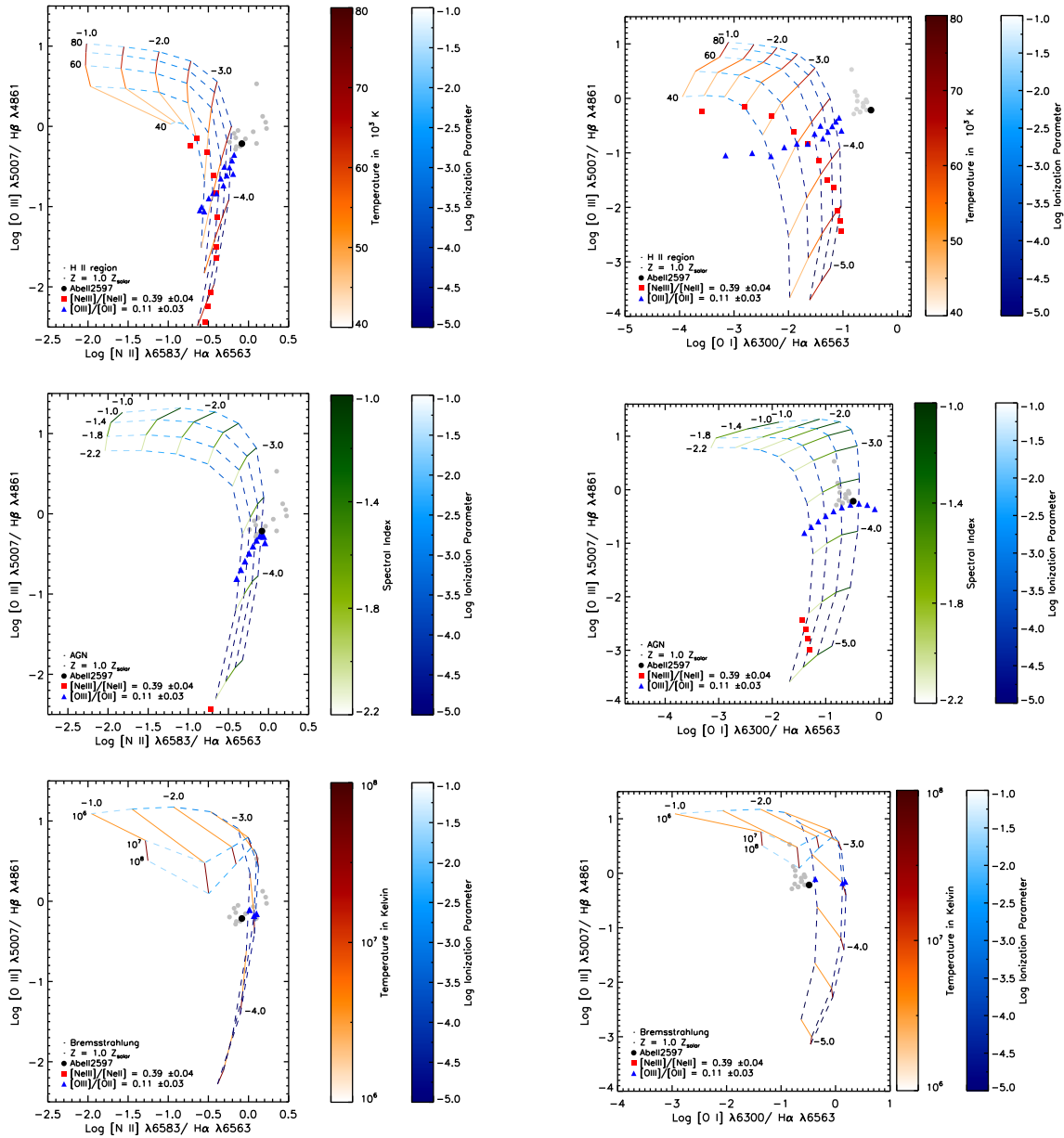


Figure 6.13 — Model BPT diagrams for A2597-NUC (density $n_H=300 \text{ cm}^{-3}$) and metallicity $Z=1.0 Z_\odot$). The left column shows $[\text{OIII}] 5007/\text{H}\beta$ vs. $[\text{NII}] 6584/\text{H}\alpha$. The right column shows $[\text{O III}] 5007/\text{H}\beta$ vs. $[\text{O I}] 6584/\text{H}\alpha$. The top row shows the stellar models, the middle row shows the AGN models and the bottom row shows the bremsstrahlung models. The models are coded according to the two parameter investigation. For the stellar models the lines show how the models evolve for different values of the ionization parameter $\log(U)$ (*dashed*) and temperature T_{BB} (*solid*). For the AGN models the lines show how the models evolve for different values of the ionization parameter $\log(U)$ (*dashed*) and spectral index α (*solid*). For the bremsstrahlung models the lines show how the models evolve for different values of the ionization parameter $\log(U)$ (*dashed*) and temperature T_X (*solid*). The black circle shows the measured position of A2597-NUC. The triangles and squares show the locus in the parameter space of the models producing the measured values for the $[\text{OIII}] 5007/[\text{OII}] 3727$ (triangles) and $[\text{NeIII}] 15.5/[\text{NeII}] 12.8$ (squares) ratios. The grey circles are BCGs from Crawford et al. (1999). We note that for the bremsstrahlung models the $[\text{Ne III}]/[\text{Ne II}]$ ratio is always larger than 0.4 and hence no squares are plotted.

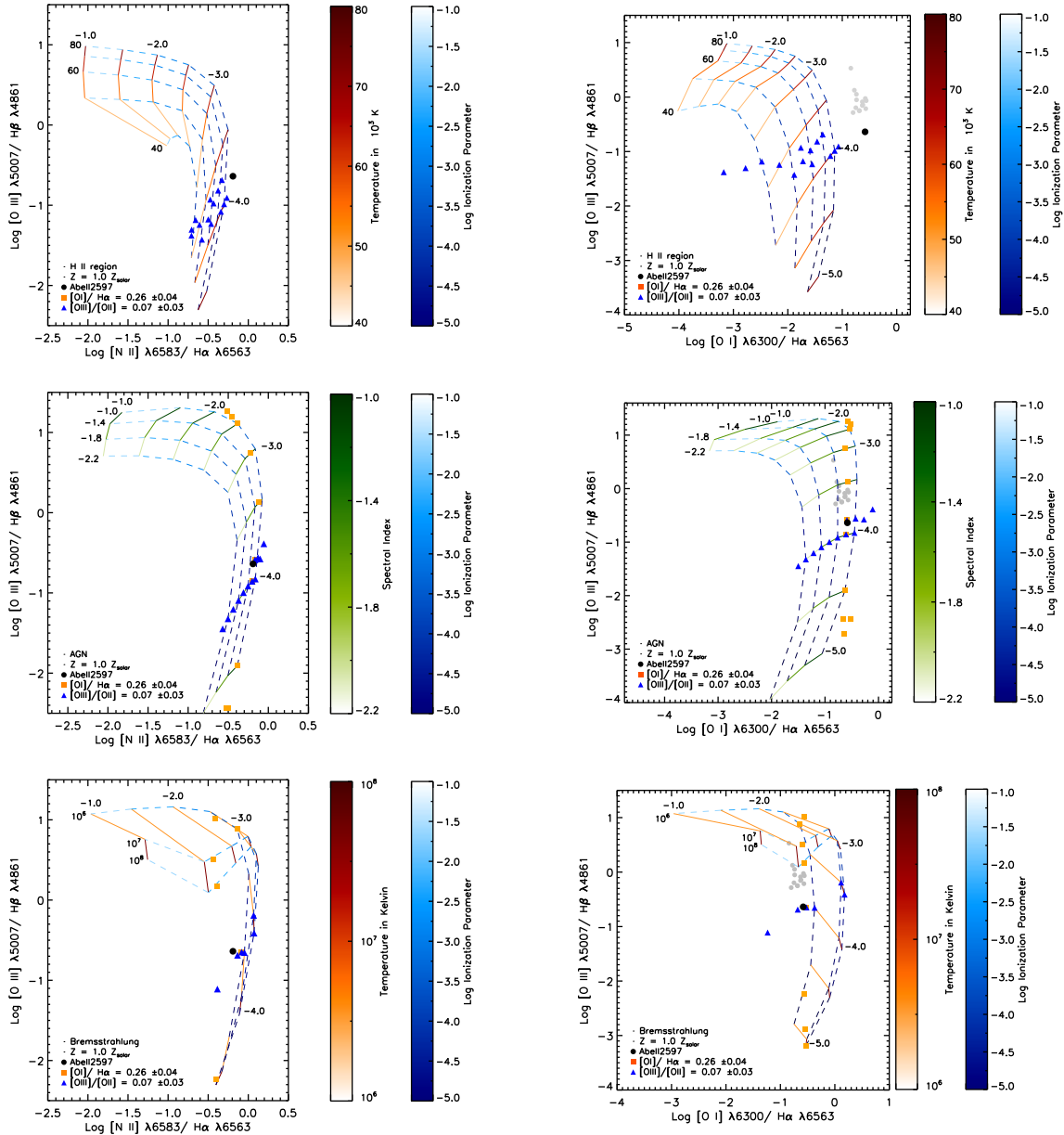


Figure 6.14 — Model BPT diagrams for A2597-OFF (density $n_H=50 \text{ cm}^{-3}$ and metallicity $Z=1.0 z_\odot$). The left column shows $[\text{OIII}] 5007/\text{H}\beta$ vs. $[\text{NII}] 6584/\text{H}\alpha$. The right column shows $[\text{O III}] 5007/\text{H}\beta$ vs. $[\text{O I}] 6300/\text{H}\alpha$. The top row shows the stellar models, the middle row shows the AGN models and the bottom row shows the bremsstrahlung models. The models are represented in the same way as in Fig. 6.13. The black circle shows the measured position of A2597-OFF. The coloured triangles and squares show where in the parameter space of the models obtain the measured values for the $[\text{OIII}] 5007/[\text{OII}] 3727$ (triangles) and $[\text{O I}] 6300/\text{H}\alpha$ (squares) ratio. The grey circles are BCGs from Crawford et al. (1999). We note that for the stellar models the $[\text{O I}] 6300/\text{H}\alpha$ ratio is always less than 0.2 and hence no squares are plotted.

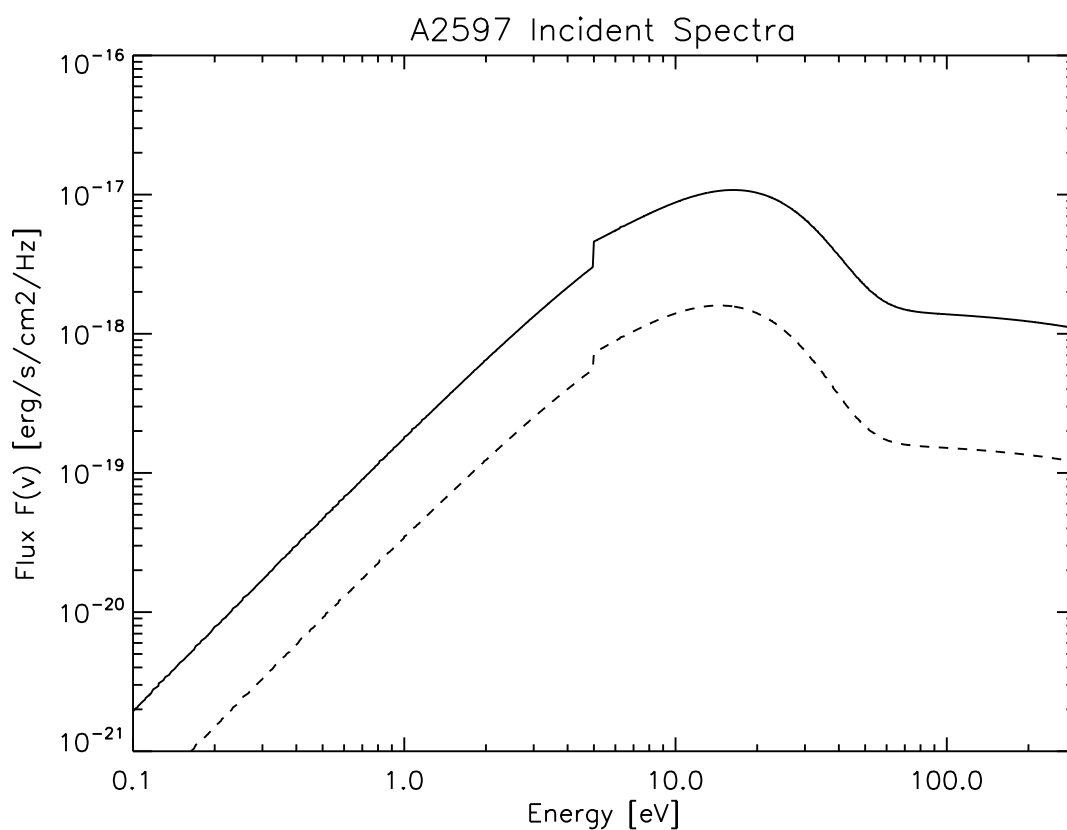


Figure 6.15 — A2597: Best-fitting combined stars and bremsstrahlung model spectra incident on front side of the model gas cloud for A2597-NUC (*solid line*) and A2597-OFF (*dashed line*). The stellar bump near 10 eV and the flat bremsstrahlung curve at higher energies are evident.

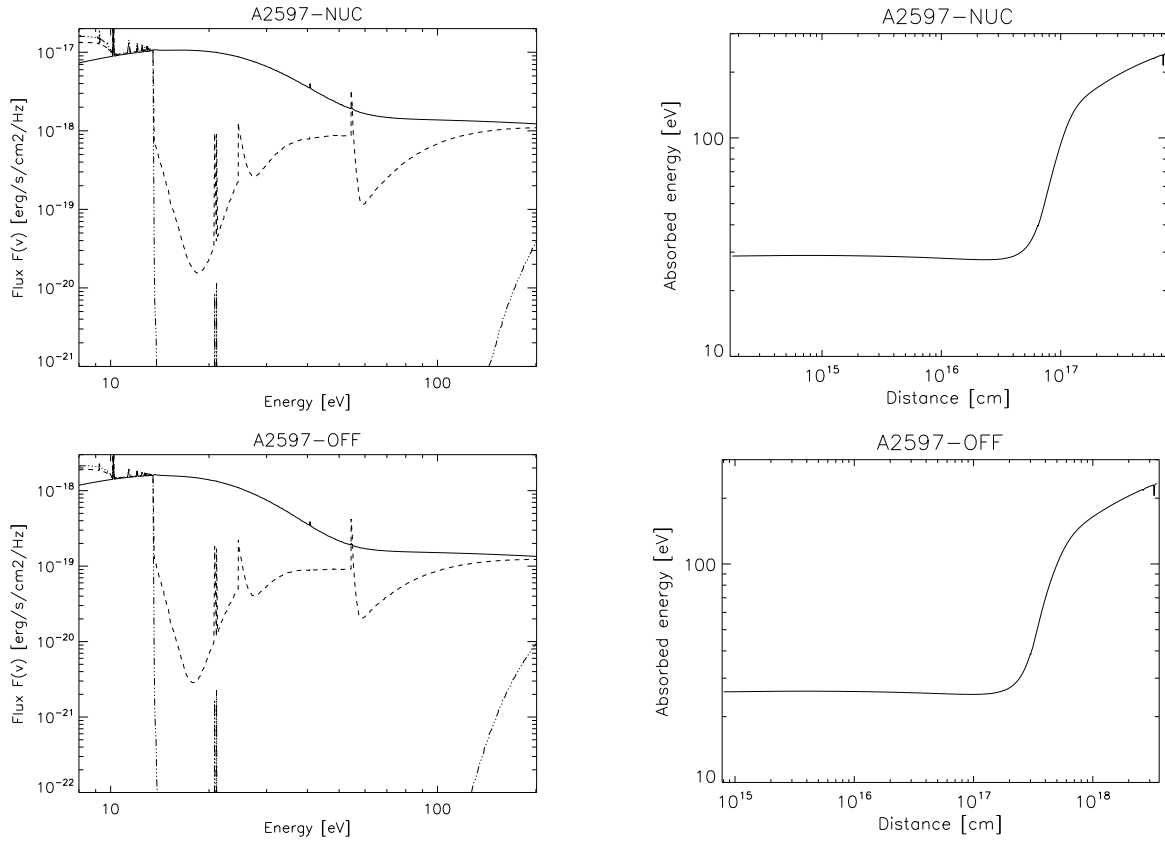


Figure 6.16 — A2597: (*Left column*) Zoom-in on the source spectrum at three distances for the best-fitting combined stars and bremsstrahlung model for A2597-NUC (*Top-left*) and A2597-OFF (*Bottom-left*). The solid line corresponds to the photon spectrum after passage through the first step of the model cloud, i.e. after a distance of 2×10^{14} cm for A2597-NUC and 8×10^{14} cm for A2597-OFF. The dashed line corresponds to the spectrum at the transition region from the OII to the OI zone, i.e. after a distance of about 7×10^{16} cm for A2597-NUC and 3×10^{17} cm for A2597-OFF. The dot-dash line corresponds to the spectrum at the backside of the cloud, i.e. after a distance of 8×10^{17} cm for A2597-NUC and 3×10^{18} cm for A2597-OFF. Note that the total Hydrogen column densities traversed by the photon spectra for A2597-NUC and A2597-OFF are very similar, i.e. $N_H \sim 2 \times 10^{20} \text{ cm}^{-2}$. (*Right column*) Flux weighted, average, absorbed photon energy as a function of distance for the best-fitting combined stars and bremsstrahlung model for A2597-NUC (*Top-right*) and A2597-OFF (*Bottom-right*). A more detailed picture showing what photon energies are absorbed at a given distance is presented in Appendix C.1.1.

C.1 Best-fitting models.

In this appendix we show the photon spectra and ionisation fractions as a function of distance into the model cloud for our best-fitting combined Stars and bremsstrahlung model for A2597.

In Section C.1.1 we show the model photon spectra for A2597-NUC and A2597-OFF at a number of selected distances into the model cloud. Each row has 4 panels and corresponds to one specific distance into the model cloud. This distance D is written on top of the first panel. The first panel shows the attenuated incident spectrum after passing through (part of) the model cloud. This spectrum is referred to as the *source spectrum*. The second panel shows the photons removed passing through each distance step, i.e. the photons used to ionise and heat the gas at the distance D . The width W of this distance step is written on top of the second panel. This spectrum is referred to as the *absorption spectrum*. Panels three and four show respectively the emission in the OII and OI lines for the distance step with width W at a distance D into the model cloud, as specified in the previous panels one and two.

Note that the total Hydrogen column density traversed by both the A2597-NUC and A2597-OFF is similar, i.e. $N_H \sim 2 \times 10^{20} \text{ cm}^{-2}$. Also note that the transitions and thus widths of the OII and OI zones happens at similar Hydrogen column densities. The only important physical difference in the two models is therefore the assumed gas density. The photon spectra presented here are discussed in more detail in Section 6.7.2

In Section C.1.2 we show the ionisation fractions of important elements as a function distance into the model cloud for A2597-NUC and A2597-OFF. These ionisation fractions are discussed in more detail in Section 6.7.2

C.1.1 Photon spectra A2597

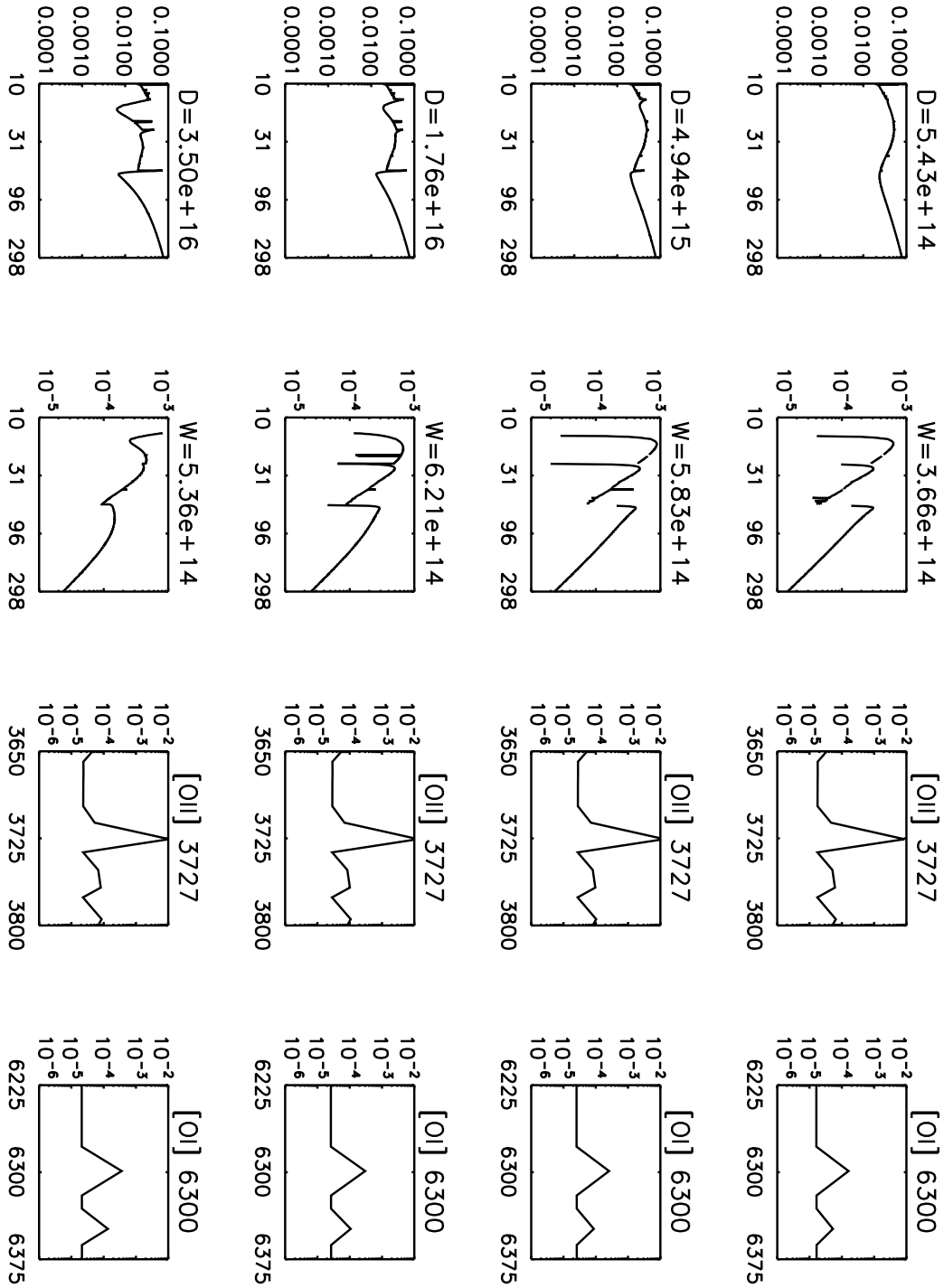


Figure 17 — A2597-NUC: Photon spectra for the best-fitting combined Stars and bremsstrahlung model for selected model slabs at distances from 5.4×10^{14} to 3.5×10^{16} cm into the cloud. Each row corresponds to a single slab with width W at a distance D into the model cloud. These rows consist of four panels showing in sequence the source spectrum, the absorption spectrum, the [OII] 3727 line spectrum and the [OI] 6300 line spectrum. The relevant values for D and W are written on top of panels 1 and 2 in each row. The x and y axes in each panel are photon energy in units of eV and photon energy flux $\nu \times F_\nu$ in units of $\text{erg s}^{-1} \text{cm}^2$.

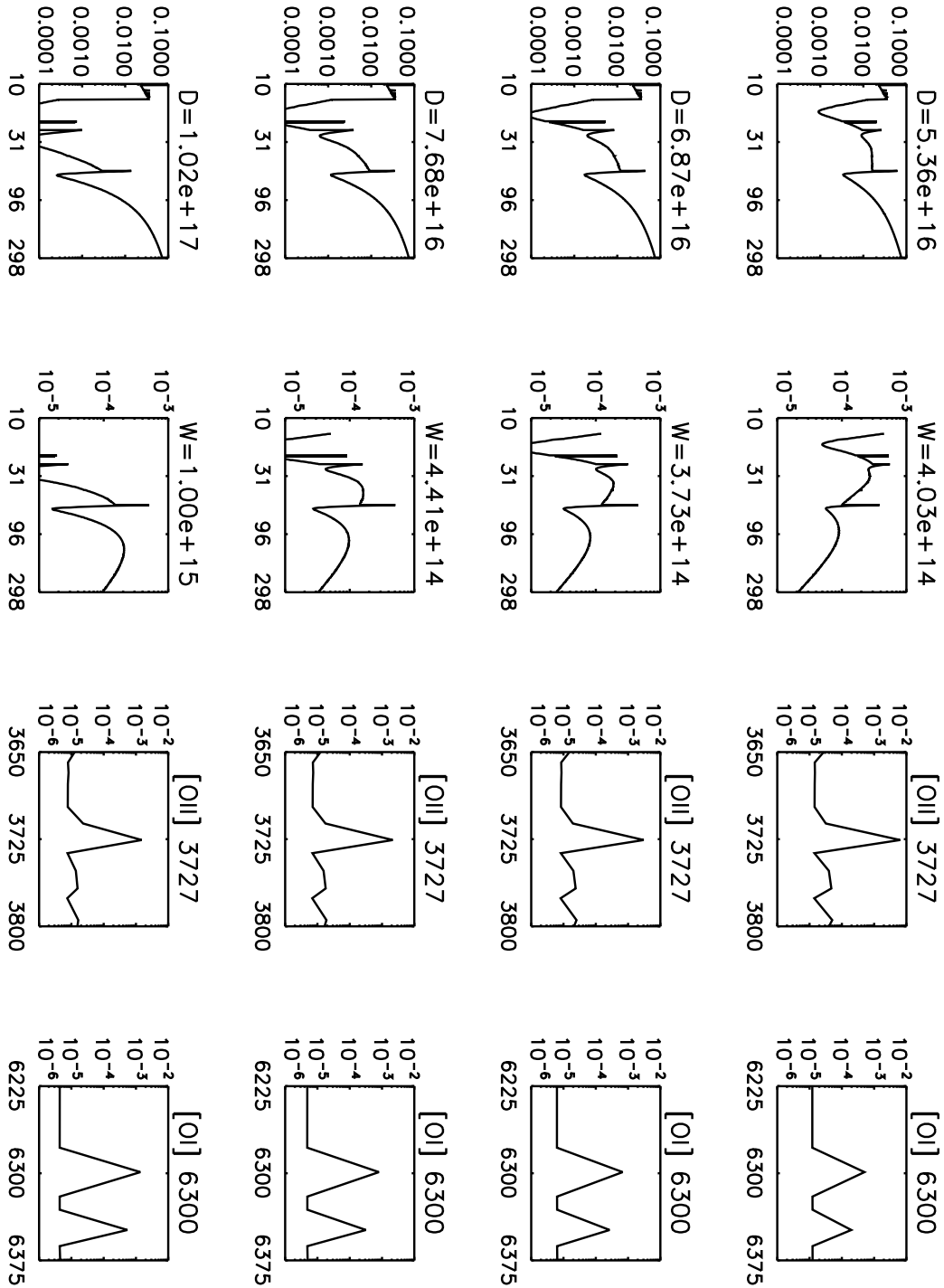


Figure 17 — (Continued) Photon spectra for the best-fitting combined Stars and bremsstrahlung model for selected model slabs at distances from 5.4×10^{16} to 1.0×10^{17} cm into the cloud.

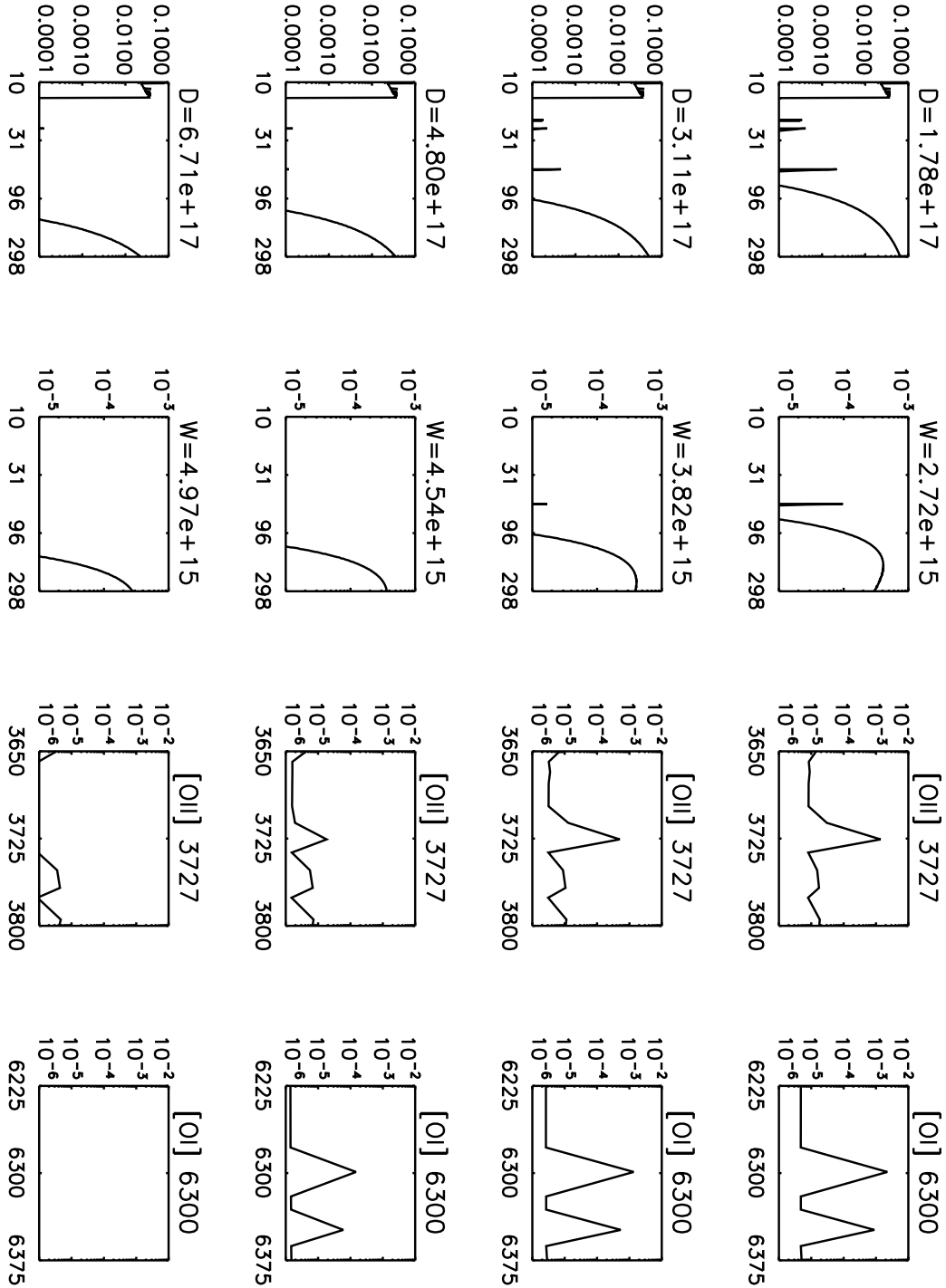


Figure 17 — (Continued) Photon spectra for the best-fitting combined Stars and bremsstrahlung model for selected model slabs at distances from 1.8×10^{17} to 6.7×10^{17} cm into the cloud.

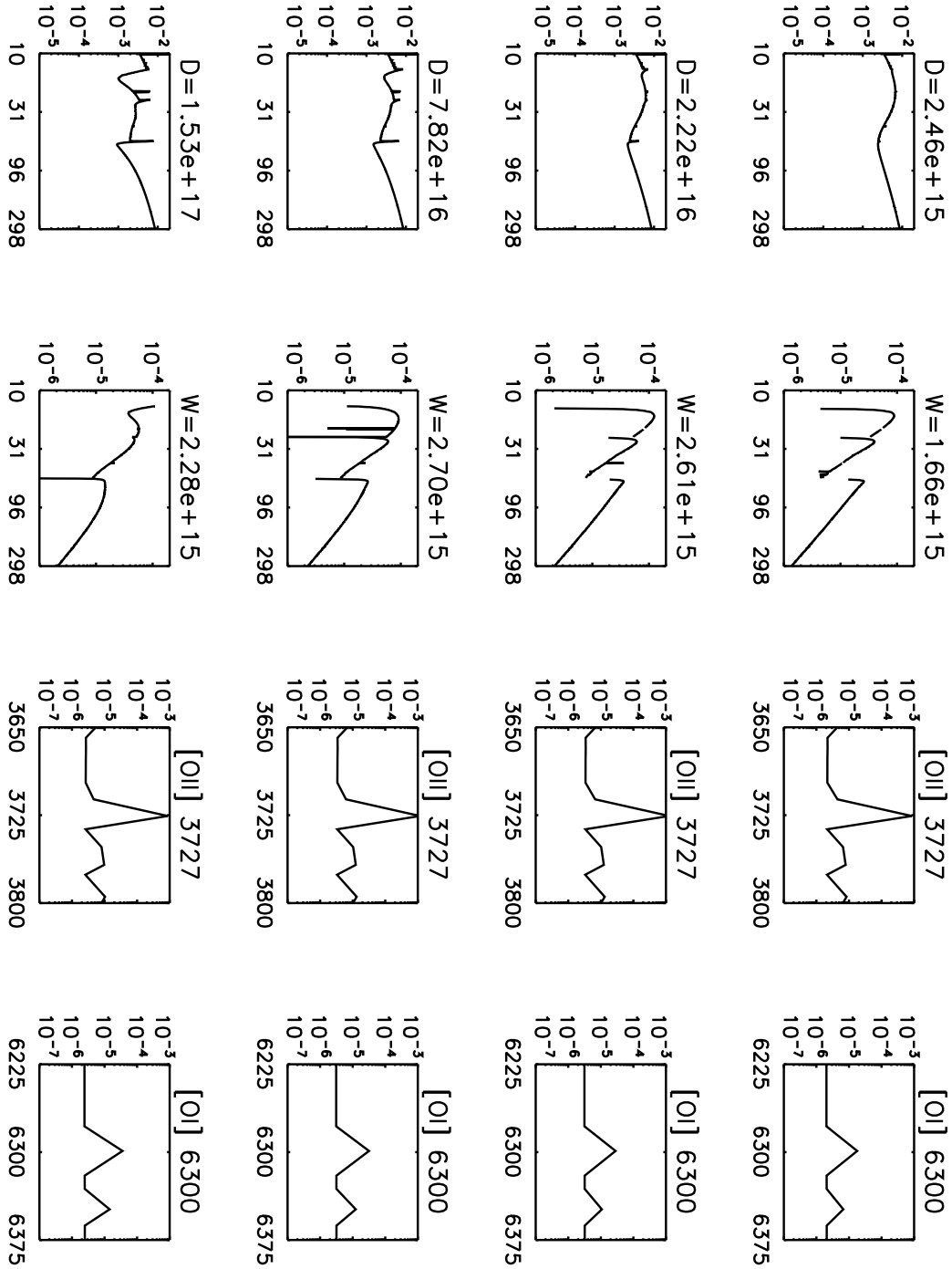


Figure 18 — A2597-OFF: Photon spectra for the best-fitting combined Stars and bremsstrahlung model for selected model slabs at distances from 2.5×10^{15} to 1.5×10^{17} cm into the cloud. Each row corresponds to a single slab with width W at a distance D into the model cloud. These rows consist of four panels showing in sequence the source spectrum, the absorption spectrum, the [OII] 3727 line spectrum and the [OI] 6300 line spectrum. The relevant values for D and W are written on top of panels 1 and 2 in each row. The x and y axes are the same as in Fig. 17.

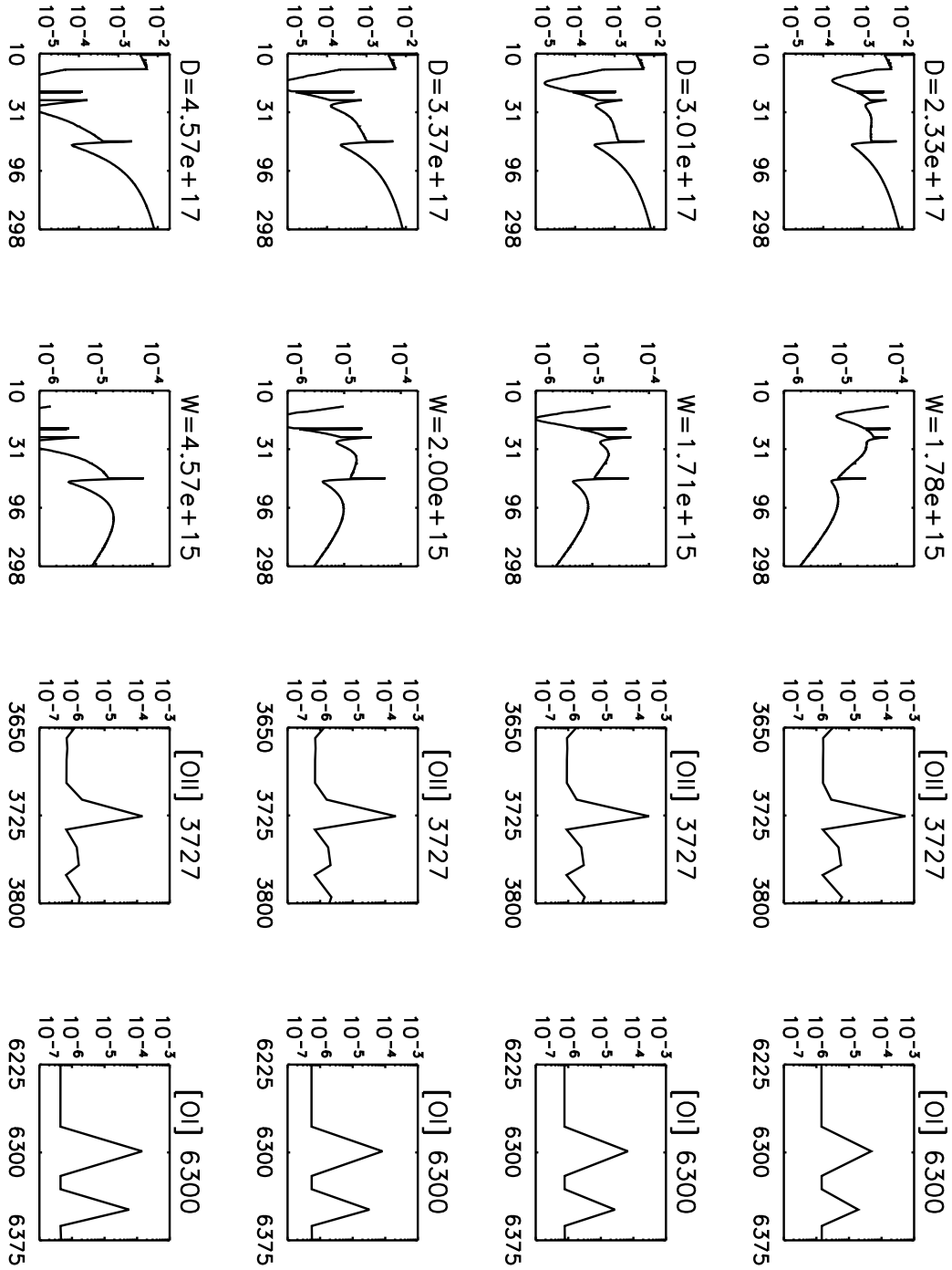


Figure 18 — (Continued) Photon spectra for the best-fitting combined Stars and bremsstrahlung model for selected model slabs at distances from 2.3×10^{17} to 4.6×10^{17} cm into the cloud.

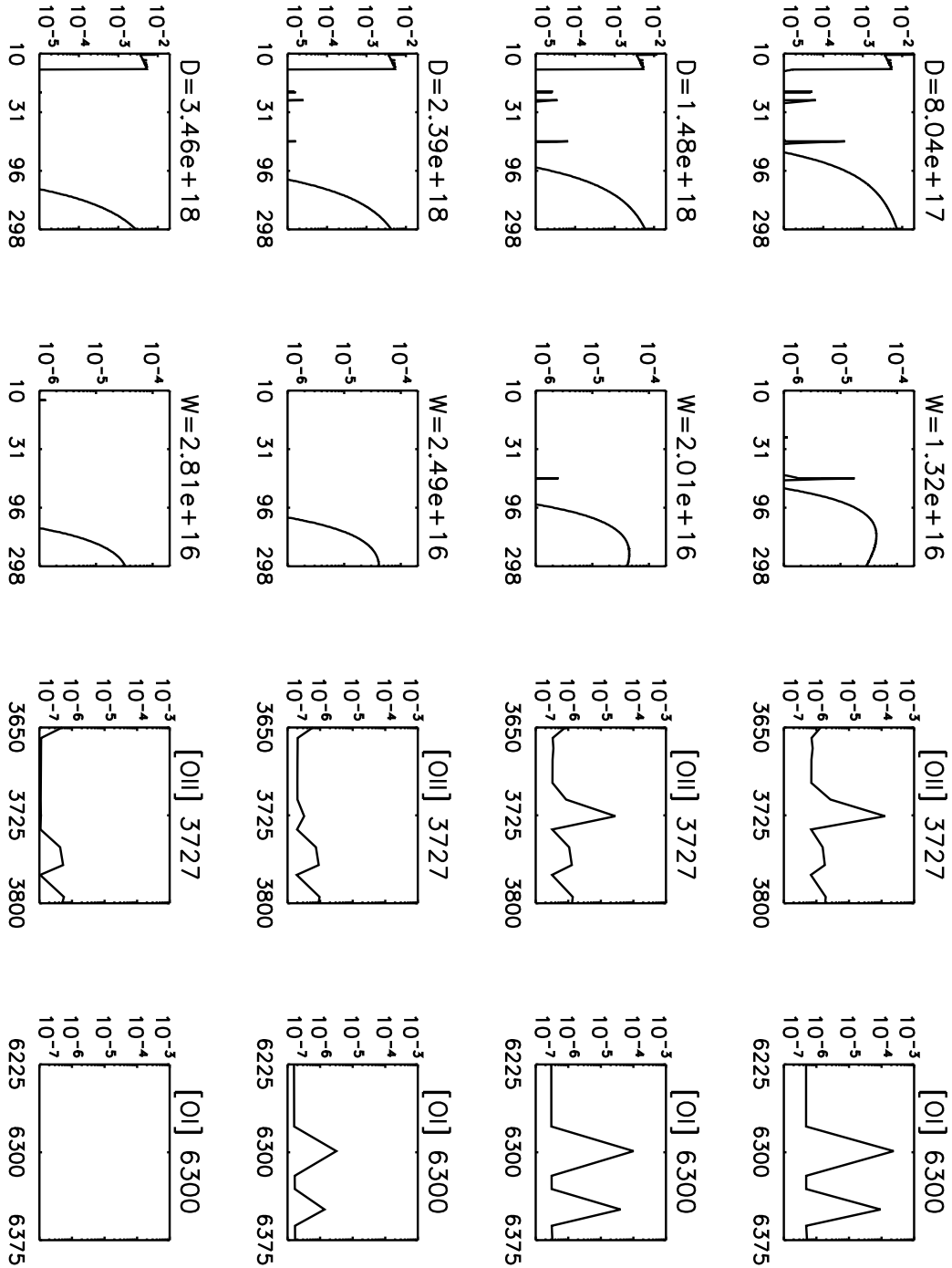


Figure 18 — (Continued) Photon spectra for the best-fitting combined Stars and bremsstrahlung model for selected model slabs at distances from 8.0×10^{17} to 3.5×10^{18} cm into the cloud.

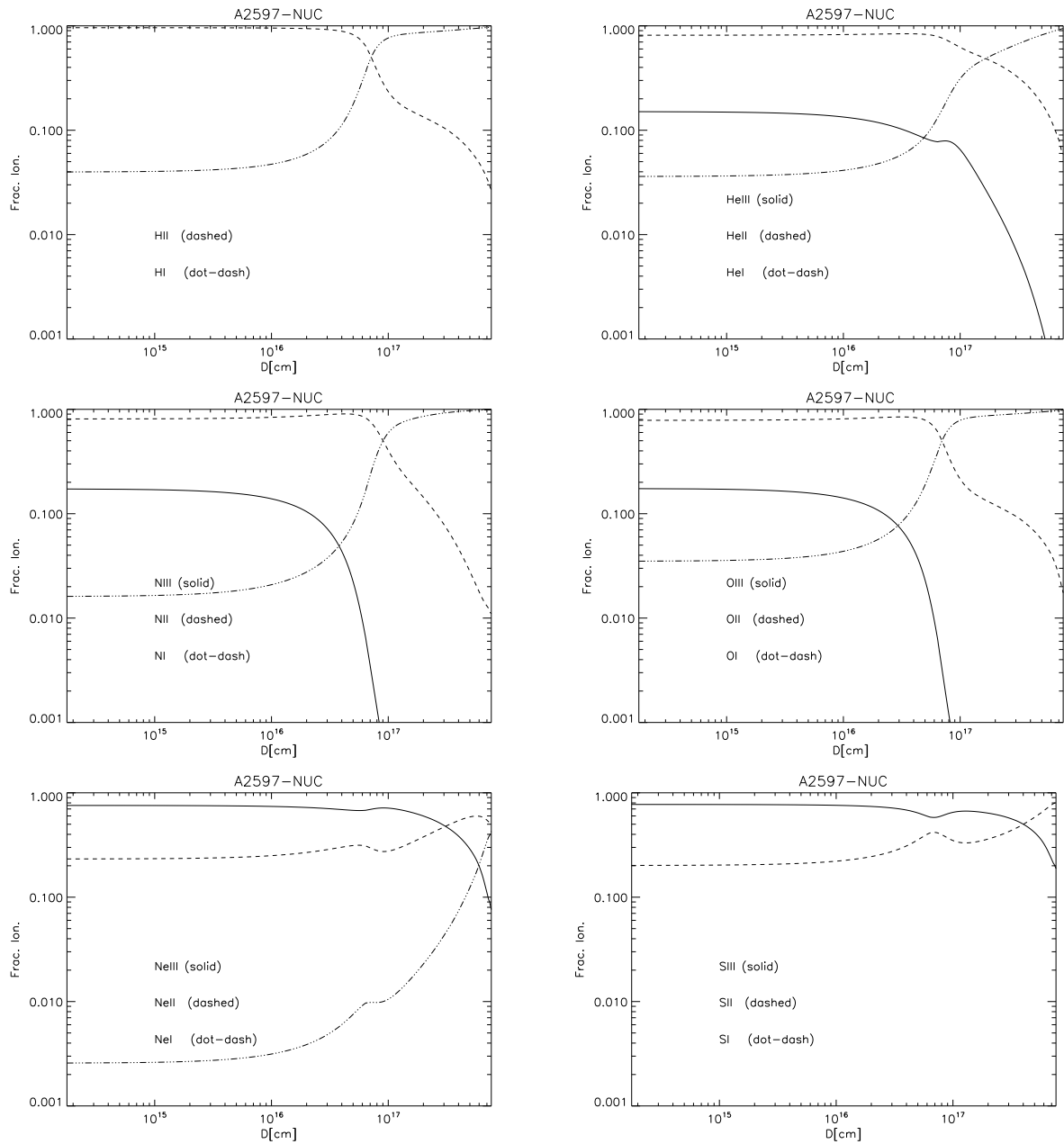


Figure 19 — A2597-NUC. Fractional Ionisation of Hydrogen, Helium, Nitrogen, Oxygen, Neon and Sulphur as a function of distance into the best-fitting combined Stars and bremsstrahlung model cloud.

C.1.2 Ionisation fractions A2597

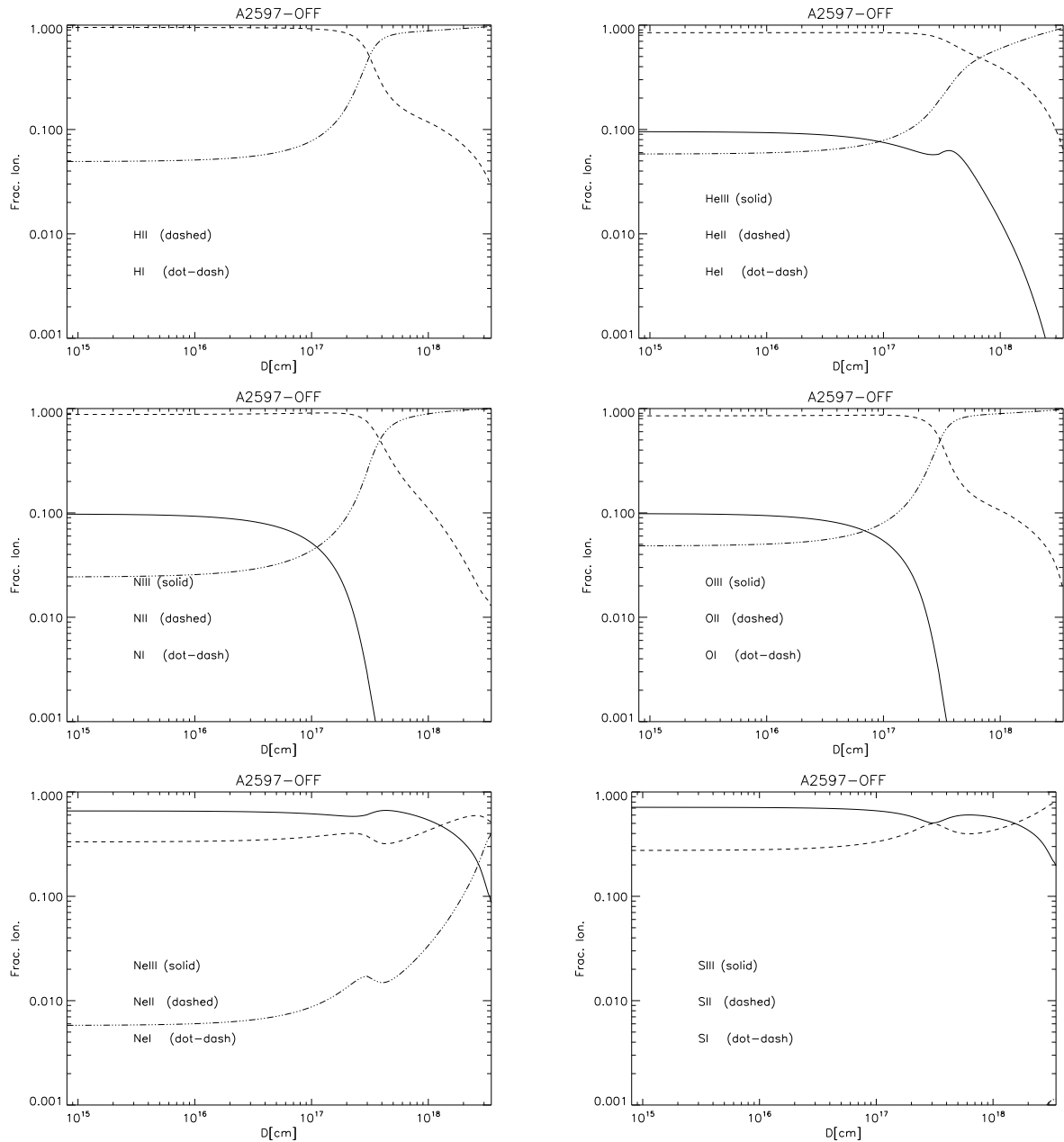


Figure 20 — A2597-OFF. Fractional Ionisation of Hydrogen, Helium, Nitrogen, Oxygen, Neon and Sulphur as a function of distance into the best-fitting combined Stars and bremsstrahlung model cloud.

Nederlandse samenvatting

Clusters van Sterrenstelsels

Clusters van sterrenstelsels zijn oorspronkelijk ontdekt door Charles Messier en William Herschel. Hun extragalactische aard werd voor het eerst bevestigd door Vesto Slipher en Edwin Hubble. Deze clusters zijn, voor zover bekend, de meest massieve ($M \sim 10^{13-15} M_{\odot}$, waarbij $1 M_{\odot}$ gelijk is aan de massa van onze zon), gravitationeel gebonden structuren in het heelal. Zij zijn ook de eerste objecten waarvoor werd ontdekt dat er donkere materie nodig is. Fritz Zwicky wees ons hierop in 1937. Recente onderzoeken laten zien dat de baryonische (ofwel zichtbare) materie maar 16% van de totale massa in clusters vertegenwoordigt. De resterende 84% bevindt zich in een onbekende vorm die donkere materie genoemd wordt. Ongeveer 80% van de baryonen bevindt zich in het intracluster medium (ICM), dit is het gas tussen de sterrenstelsels in de clusters. De resterende 20% bevindt zich in de sterren die tezamen de sterrenstelsels in de clusters opmaken (zie bijv. Peterson & Fabian 2006, voor een recente samenvatting).

Een van de hoofddoelen in de moderne Sterrenkunde is het begrijpen van de vorming van de grote-schaal structuren in het heelal en de evolutie van sterrenstelsels. Clusters van sterrenstelsels bieden ons de mogelijkheden om juist dit te doen. Modellen van hiërarchische formatie van structuren voorspellen dat de meest massieve objecten, d.w.z. clusters, het laatst en dus nu vormen. Onderzoeken naar de samenklontering van sterrenstelsels maakt het ons mogelijk om kosmologische modellen te verfijnen. De dichte en drukke omgeving heeft een grote invloed op de evolutie van sterrenstelsels in clusters en maakt het ons mogelijk om belangrijke processen zoals het strippen van gas (frictie) en kinematische segregatie (dynamische frictie). De lens-effecten van clusters maakt het tevens mogelijk om cluster massa's, de eigenschappen van donkere materie en de details van sterrenstelsels op hoge roodverschuiving te bestuderen.

Het is in de laatste jaren duidelijk geworden dat clusters van sterrenstelsels vooral geschikt zijn om de terugkoppeling (feedback) processen te bestuderen waarvan verondersteld wordt dat die de koeling van gas verhinderen (zie bijv. Peterson & Fabian 2006; McNamara & Nulsen 2007). Het koelen van heet gas om sterren te vormen is essentieel voor de groei van sterrenstelsels. Tegelijkertijd laten kosmologische simulaties zien dat in deze sterrenstelsels een efficiënte vorm van terugkoppeling nodig is om stervorming vroegtijdig te stoppen. Dit is noodzakelijk om ervoor te zorgen dat de sterrenstelsels niet te massief worden en dat hun helderheden niet te blauw worden. De centrale sterrenstelsels in clusters zijn, voor zover bekend, de meest massieve sterrenstelsels. De nabijheid van deze objecten maakt hun tot ideale laboratoria waar gas koeling, de groei van sterrenstelsels, en terugkoppelingsprocessen in zeer veel detail bestudeerd kunnen worden. Deze terugkoppelingsprocessen zijn het onderwerp van mijn proefschrift en ze spelen een belangrijke rol in formatie van structuren voor all lengte- en tijdschalen.

Cool-core Clusters

Clusters van sterrenstelsels groeien, op dezelfde manier als sterrenstelsels, door massa van hun omgeving op te nemen of dor middel van fusies met andere clusters. Naar schatting hebben 20% van alle clusters nu of zeer recent een fusie ondergaan. De rest is in een (bijna) ontspannen (quasi-relaxed) toestand. Ongeveer de helft van deze ontspannen clusters hebben centrale gebieden waar heet Röntgen gas met een temperatuur van honderd miljoen Kelvin ($T \sim 10^8$ K) een dichtheid heeft die hoog genoeg is zodat deze, via haar eigen straling, kan koelen op een tijdschaal die kleiner is dan de leeftijd van het heelal. Wij noemen deze objecten *cool-core clusters*, ofwel clusters met koele kernen. In de literatuur worden deze objecten ook wel *cooling flow clusters* genoemd. In het centrum van de koele kern bevindt zich het centrale dominante (cD) sterrenstelsel. Deze cD sterrenstelsels zijn, voor zover bekend, de grootste sterrenstelsels. Ze domineren in helderheid over de andere sterrenstelsels in de cluster en daarom worden ze ook wel *Brightest Cluster Galaxies* (BCG) genoemd.

Heet gas met een temperatuur $T > 10^7$ K

Röntgen afbeeldingen van cool-core clusters laten zien dat deze objecten koele kernen hebben (zie bijv. Peterson & Fabian 2006). Modellen voor gas koeling voorspellen dat in de koele kernen koelstromen met massa's tot $1000 M_{\odot}$ /jaar kunnen plaats vinden. De tijdschaal waarop het hete X-ray (honderd miljoen graden kelvin) koelt is typisch een miljard jaar binnen een gebied ter grootte van een paar honderd kiloparsec (1 kiloparsec is 3260 lichtjaren wat overeenkomt met ongeveer 3×10^{16} meter). In het afgelopen decennium, Röntgen spectroscopie met *XMM Newton* en *Chandra* heeft ons laten zien dat vrijwel niets van dit hete gas afkoelt naar een temperatuur minder dan tien miljoen graden Kelvin (zie bijv. Peterson & Fabian 2006). De mechanismen die verdere koeling verhinderen worden momenteel hevig bediscussieerd, maar in het algemeen bevatten zij allemaal een vorm van verhitting van het gas.

Het momenteel meest populaire machanisme verhit het gas door middel van het werk verricht door de jets welke ontstaan bij het actieve zwarte gat (AGN) in the centrum van de BCG. In dit model werkt de AGN als een thermostaat voor het ICM, via jets, waarbij de kleinste schaal structuren nauw verbonden zijn met de grootste schaal structuren. De AGN jets manifesteren zich zelf als radio jets en bubbels. De interactie tussen de jets en het hete gas is afgeleid uit het feit dat de jets zich daar bevinden waar er lokaal minder Röntgen gas is. Deze gebieden noemt men ook wel *X-ray cavities*, ofwel Röntgen gaten. Vanuit een kinematisch oogpunt bevatten de jets genoeg energie om het hete gas te verhitten en koeling te voorkomen, er is echter weinig bekend over hoe dit in detail zou moeten gebeuren.

In een typische cool-core cluster moet een energiestroom van $L_X \sim 10^{44}$ erg/s (koeling door middel van straling) gecompenseerd worden door verhitting.

Koel gas met een temperatuur $T < 10^4$ K

Ook al koelt vrijwel niets van het hete Röntgen gas in cool-core clusters onder een temperatuur van tien miljoen graden Kelvin, bevatten de koele kernen toch wel degelijk een

significante hoeveelheid koel gas met een temperatuur minder dan tienduizend graden Kelvin. Koud (30 graden Kelvin) gas met massa's tot $10^{10-11} M_{\odot}$, afgeleid uit metingen van koolstofmonoxide, is gevonden in de meest massieve objecten (zie bijv. Edge 2001; Salome & Combes 2003). Metingen met hoge ruimtelijke resolutie laten zien dat dit gas opgesloten zit in dunne, lange filamenten in een gebied ter grootte van 50 kiloparsec gecentreerd op de BCG (e.g. Donahue et al. 2000; Fabian et al. 2008; Salome et al. 2011).

Aanzienlijk kleinere hoeveelheden geïoniseerd en moleculair gas met temperature tussen de honderd en tienduizend graden Kelvin worden ook in deze systemen gevonden. Deze gas fasen hebben ook een probleem met koeling ten gevolge van straling. De emissie van dit gas is veel te helder om overeen te komen met gas dat door dit temperatuur regime koelt. Dit gas moet daarom ook verhit worden (zie bijv. Heckman et al. 1989; Voit & Donahue 1997; Jaffe et al. 2005). De gas fasen die het meest problematisch zijn, zijn het geïoniseerde gas met een temperatuur van tienduizend graden Kelvin en het warme moleculaire gas met een temperatuur van 2 duizend graden Kelvin. Het geïoniseerde gas heeft een typische helderheid $L_{HII} \sim 50 \times L_{H\alpha} \sim 10^{43-44} \text{ erg s}^{-1}$ (Heckman et al. 1989; Crawford et al. 1999; Jaffe et al. 2005). Het warme moleculaire gas heeft een typische helderheid $L_{H_2} \sim 10 \times L_{H_2 1-0 S(1)} \sim 10^{43} \text{ erg s}^{-1}$. Hier hebben we aangenomen dat het moleculaire gas zich in local thermisch evenwicht (LTE) bevindt (zie bijv. Jaffe et al. 2005; Onk et al. 2010).

Het koudere moleculaire gas draagt niet veel bij aan de totale helderheid van het koele gas en dus draagt het ook niet veel bij aan het koeling probleem. Indien we aannemen dat het moleculaire gas met een temperatuur van 400 graden Kelvin zich in LTE bevindt dan vinden we een typische helderheid $L_{H_2} \sim 3 \times L_{H_2 0-0 S(1)} \sim 10^{42} \text{ erg s}^{-1}$ voor dit gas. In het temperatuur regime tussen dit gas en het koude gas met een temperatuur van 30 K wordt de gas koeling overgenomen van de moleculaire lijn emissie door de ver-infrarode emissie lijnen van neutrale en geïoniseerde atomen, zoals [OI] op $63 \mu\text{m}$ en [CII] en $157 \mu\text{m}$ (Maloney et al. 1996). Onze metingen met de Herschel-ruimtetelescoop laten nu voor de eerste keer zien dat BCGs in cool-core clusters sterk stralen in deze lijnen. De totale emissie in de ver-infrarode lijnen is ongeveer $L_{FIR,line} \sim 10^{43} \text{ erg s}^{-1}$.

Het koeling probleem voor de koele gas fasen ziet er op het eerste gezicht misschien minder moeilijk uit dan het koeling probleem voor het hete Röntgen gas, omdat de totale koeling ten gevolge van straling nooit meer is dan dat van het hete gas. Er zijn echter belangrijke verschillen met betrekking tot de lengte- en tijdschalen waarop verhitting nodig is. Het hete Röntgen gas vereist verhitting voor een gebied met een diameter van ongeveer 200 kiloparsec. Het koele gas vereist een vergelijkbare hoeveelheid verhitting in een gebied met een diameter van maar ongeveer 50 kiloparsec. Dit betekent dat een veel grotere hoeveelheid energie per volume eenheid nodig is om het koele gas te verhitten.

De tijdschalen waarop deze verhitting nodig is verschillen ook zeer veel. De koele gas fasen met hun hoge dichtheden hebben een veel kortere koelingstijd dan het hete Röntgen gas met zijn lage dichtheid. Dit betekent dat daar waar het mogelijk is om het hete gas te verhitten met sporadische AGN uitbarstingen, dat dit niet zal werken voor het koele gas. Het koele gas vereist een continue vorm van verhitting.

Dit proefschrift

De laatste vier jaar heb ik gewerkt aan metingen en interpretatie van de massa, temperatuur, excitatie en dynamische structuur van de baryonische gas fasen in cool-core clusters. In het bijzonder heb ik mij gericht op het koele gas met een temperatuur $T \sim 10^{2-4}$ K. De metingen gepresenteerd in dit proefschrift hebben het mij mogelijk gemaakt om in detail de distributie and toestand van dit gas te vergelijken met Röntgen en radio structuren in de koele kernen van deze clusters. Het gas dat straalt in het Röntgen regime representeert de primaire bron van massa in het systeem. Het gas dat straalt in het radio regime representeert de primaire bron van energie-input.

Hoofdstuk 2

In hoofdstuk 2 bespreken wij nabij-infrarode metingen gemaakt met de integral-field spectrograaf *Spectrograph for INtegral Field Observation in the Near-Infrared* (SINFONI) gemonteerd op de *Very Large Telescope* (VLT). We hebben de BCGs in de cool-core clusters *Abell 2597* en *Sersic 159-03* geobserveerd. Met behulp van onze eigen reductie scripts hebben wij, voor het eerst, het geïoniseerde en warme moleculaire gas in deze systemen drie-dimensionaal in kaart gebracht. Het gas bevindt zich in filamentaire structuren tot op afstanden van 20 kiloparsec van de kern van de BCG. We vinden dat het geïoniseerde en moleculaire gas sterk met elkaar verbonden zijn in zowel distributie, intensiteit en dynamica. We detecteren indicaties voor een interactie van de AGN met het gas in de centrale 2-3 kiloparsec. Buiten dit gebied is het gas in een dynamisch koude toestand. Waarom dit dynamisch koude gas niet naar de centrum van de BCG valt zal nog verklaard moeten worden. In overeenstemming met eerdere twee-dimensionale onderzoeken laten wij zien dat er een serieus koeling probleem is voor het de koele gas fasen in cool-core clusters (zie bijv. Heckman et al. 1989; Jaffe et al. 2005). Het moleculaire gas blijkt in LTE met een temperatuur $T \sim 2000$ graden Kelvin te zijn. Dit impliceert dat het moleculaire gas een hoge dichtheid ($n \geq 10^6 \text{ cm}^{-3}$) heeft en niet in druk-evenwicht met het geïoniseerde gas is (Jaffe et al. 2005).

Hoofdstuk 3

In hoofdstuk 3 bespreken wij ver-ultraviolette (FUV) beelden gemaakt met de *Advanced Camera for Surveys* (ACS) gemonteerd op de *Hubble ruimtetelescoop* (HST) en optische beelden gemaakt met de *FOcal Reducer and low-dispersion Spectrograph* (FORS) gemonteerd op de VLT. We hebben de BCGs in de cool-core clusters *Abell 2597* en *Abell 2204* geobserveerd. De hoge ruimtelijke resolutie observaties gemaakt met de HST laten zien dat de FUV continuum emissie zich in uitgestrekte filamentaire structuren bevindt. Deze structuren zijn gecentreerd op de kern van de BCG. We hebben, voor het eerst, de twee-dimensionale distributie van het ratio van FUV tot optisch licht in de centrale 20 kiloparsec van de BCGs in kaart gebracht. Wij vinden dat dit ratio in de kern van de BCG en in de uitgestrekte filamenten hoog is. Als de emissie wordt geïnterpreteerd in termen van jonge sterren, dan is de aanwezigheid van een grote hoeveelheid zeer hete O-sterren vereist. Het vereiste aantal is hoog

maar niet in tegenspraak met de huidige schattingen voor de stervorming in deze systemen. Echter, indien we onze metingen corrigeren voor stof en de continuum emissie van het gas in de BCG dan vinden wij dat de temperaturen van de vereiste sterren onredelijk hoog worden en dat een puur stellaire interpretatie niet volstaat. Simpele, niet-stellaire modellen, falen eveneens om de metingen te verklaren. Een meer gedetailleerd onderzoek is nodig om de herkomst van het hoge ratio van het FUV tot optisch licht te bepalen.

Hoofdstuk 4

In hoofdstuk 4 bespreken wij ver-infrarode (FIR) beelden gemaakt met de *Photodetector Array Camera and Spectrometer* (PACS) en de *Spectral and Photometric Imaging Receiver* (SPIRE) gemonteerd op de *Herschel ruimtetelescoop* (Herschel). We hebben de BCGs in de cool-core clusters *Abell 1068*, *Abell 2597* en *Zw3146* (*Zw3146* is tevens bekend als *ZwCl 1021.0+0426*) geobserveerd. De FIR continuum emissie wordt ruimtelijk niet opgelost door de instrumenten aan boord van *Herschel*. We presenteren, voor het eerst, goed bepaalde spectrale energie verdelingen voor de FIR stof emissie in deze BCGs. We passen simpele, gemodificeerde zwarte-lichaam stralingsmodellen toe op de metingen van stof emissie in het 24-850 μm gebied. Dit laat zien dat ten minste twee temperatuur componenten nodig zijn om de data te kunnen verklaren. Deze twee componenten hebben vergelijkbare temperaturen in alle drie objecten. De eerste component heeft een temperatuur van ongeveer 20 graden Kelvin en de tweede component heeft een temperatuur van ongeveer 50 graden Kelvin. De koudste component domineert de totale stof massa in deze systemen. De FIR heldere BCGs in *Abell 1068* en *Zw3146* hebben een stof massa van ongeveer $10^{8-9} M_{\odot}$. De FIR zwakke BCG in *Abell 2597* heeft een stof massa die ongeveer een factor tien lager is. Het ratio van gas tot stof massa is ongeveer honderd in alle drie de BCGs.

Hoofdstuk 5

In hoofdstuk 5 bespreken wij FIR integral field spectrografische metingen gemaakt met PACS gemonteerd op de *Herschel ruimtetelescoop*. We hebben de BCGs in de cool-core clusters *Abell 1068* en *Abell 2597* geobserveerd. We detecteren, voor de eerste keer, de sterke atomaire koelingslijnen van [CII], [NII] en [OI] in deze BCGs. De lijn emissie wordt ruimtelijk niet opgelost door PACS en impliceert de aanwezigheid van moleculaire gas massa's groter dan $10^9 M_{\odot}$. De FIR lijn ratios in deze BCGs verschillen niet significant van lokale, FIR-heldere sterrenstelsels en de excitatie kan dan ook verklaard worden met een stellaire bron. Het huidige niveau van absolute flux calibratie voor deze metingen is van de orde van 50% en dus niet erg goed. In de toekomst zal deze absolute calibratie sterk verbeterd worden en zullen de lijn ratios opnieuw geanalyseerd moeten worden. Tevens zullen de lijn ratios in de context van niet-stellaire modellen, zoals verhitting door hoog energetische deeltjes (Ferland et al. 2009) of hoog energetische fotonen (Donahue & Voit 1991), getest moeten worden. De breedtes van de FIR lijnen zijn consistent met optische en nabij-infrarode metingen. Echter, deze zijn aanzienlijk breder (ongeveer 35%) dan de lagere rotationele lijnen van koolstofmonoxide (Edge 2001; Salome & Combes 2003). De FIR lijn profielen in beide BCGs tonen bewijs voor

het bestaan van meerdere snelheids componenten in het gas.

Hoofdstuk 6

In hoofdstuk 6 bespreken wij optische, spectroscopische metingen gemaakt met FORS gemonteerd op de VLT, in combinatie met *MAPPINGS III* (Groves 2004) photoionisatie modellen. We hebben de BCGs in de cool-core clusters *Abell 2597*, *Abell 2204* en *Sersic 159-03* geobserveerd. We vinden dat deze BCGs extreme voorbeelden zijn van stoffige, *Low Ionisation Nuclear Emission line Regions* (LINERS) over schalen van tientallen kiloparsec. Het optische [OI] to H α ratio is zeer hoog en constant in deze systemen in vergelijking met andere soorten van sterrenstelsels. Dit soort lijn ratios kunnen niet door sterren geproduceerd worden. Met behulp van *MAPPINGS III* hebben wij drie alternative bronnen van excitatie onderzocht voor *Abell 2597*; (i) AGN, (ii) Bremsstrahlung, (iii) een combinatie van sterren en Bremsstrahlung. In overeenstemming met eerdere onderzoeken vinden wij dat deze modellen de meeste lijn ratios tot op een factor 2 nauwkeurig kunnen verklaren. De meest problematische ratios komen van lijnen die afkomstig zijn van Helium en Neon. AGN modellen kunnen uitgesloten worden op basis van de afname in de graad van ionisatie met afstand tot de kern van de BCG (Johnstone & Fabian 1988; Heckman et al. 1989). Een, enkele, diffuse bron van ionisatie, zoals bijv. Bremsstrahlung, is waarschijnlijker. Energetisch gezien is dit mogelijk voor *Abell 2597*, maar alleen als we aannemen dat er een zeer zwakke Röntgen stralings component bestaat. Er zijn indicaties voor het bestaan van een dergelijke component in *Abell 2597*. Het is echter niet duidelijk of dit model op alle cool-core BCGs toegepast kan worden. Er is een alternatief model voorgesteld waarin hoog energetische deeltjes de bron van ionisatie zijn (Ferland et al. 2009). Dit model kan de data ook verklaren.

Vooruitzicht

De laatste tien jaar is er een enorme toename geweest in de hoeveelheid observationele metingen voor cool-core BCGs. Met name hoge resolutie Röntgen metingen en integral-field spectroscopie in het optisch, nabij-infrarood en submillimeter regime. In de komende jaren zullen nieuwe telescopen, zoals de *Atacama Large Millimeter Array* (ALMA), de *James Webb Space telescope* (JWST), de *Extended Very Large Array* (EVLA), de *Low Frequency Array* (LOFAR) en de *European Extremely Large Telescope* (E-ELT) op het podium verschijnen.

Observaties van cool-core BCGs met deze telescopen zullen dit onderzoeksveld verder revolutioneren. Samen met reeds bestaande metingen zal het mogelijk worden om gedetailleerde kaarten van gas verhitting versus gas koeling te maken met gemeenschappelijke ruimtelijke resolutie van 1 boogseconde of beter. Dit zal het ons mogelijk maken om als functie van positie in de cluster de gas koeling te volgen van een temperatuur rond de honderd miljoen graden Kelvin tot tien graden Kelvin, en om deze koeling te vergelijken met gedetailleerde Röntgen en radio kaarten.

Betere metingen van belangrijke gas eigenschappen, zoals dichtheid, temperatuur en metaal gehalte, zijn dringend nodig. Voor sommige gas fasen, zoals het warme H $_2$ gas, zal dit mogelijk zijn met de nieuwe telescopen die hierboven genoemd zijn. Voor andere gas fasen, zoals het

geïoniseerde gas in het optische regime, zullen nieuwe methodes ontwikkeld moeten worden om de eigenschappen van dit gas beter te bepalen.

Bibliografie

- Böhringer H., Voges W., Fabian A. C., Edge A. C., Neumann D. M., 1993, *MNRAS*, 264, 25
Birzan L., Rafferty D. A., McNamara B. R., Wise M. W., Nulsen P. E. J., 2004, *ApJ*, 607, 800
Crawford C. S., Allen S. W., Ebeling H., Edge A. C., Fabian A. C., 1999, *MNRAS*, 306, 857
Donahue M., Voit G. M., 1991, *ApJ*, 381, 361
Donahue M., Mack J., Voit G. M., Sparks W., Elston R., Maloney P. R., 2000, *ApJ*, 545, 670
Dunn R. J. H., Fabian A. C., *MNRAS*, 373, 959
Edge A. C., 2001, *MNRAS*, 328, 762
Fabian A. C., Johnstone R. M., Sanders J. S., Conselice C. J., Crawford C. S., Gallagher J. S., Zweibel E., 2008, *Nat.*, 454, 968
Ferland G. J., Fabian A. C., Hatch N. A., Johnstone R. M., Porter R. L., van Hoof P. A. M., Williams R. J. R., 2009, *MNRAS*, 392, 1475
Groves B. A., 2004, *Dust in Photoionized Nebulae*, Ph.D. Thesis, Australian National University, Australia
Heckman T. M., Baum S. A., van Breugel W. J., McCarthy, P., 1989, *ApJ*, 338, 48
Jaffe W., Bremer M.N., Baker K., 2005, *MNRAS*, 360, 748
Johnstone R. M., Fabian A. C., 1988, *MNRAS*, 233, 581
Maloney P. R., Hollenbach D. J., Tielens A. G. G. M., 1996, *ApJ*, 466, 561
McNamara B. R., Wise M., Nulsen P. E. J., David L. P., Sarazin C. L., Bautz M., Markevitch M., Vikhlinin A., Forman W. R., Jones C., Harris, D. E., *ApJ*, 534, 135
McNamara B. R., Nulsen, P. E. J., 2007, *ARA&A*, 45, 117
Oonk J. B. R., Jaffe W., Bremer M. N., van Weeren R. J., 2010, *MNRAS*, 405, 898
Oonk J. B. R., Hatch, N. A., Jaffe W., Bremer M. N., van Weeren R. J., 2011, *MNRAS*, 414, 2309
Peterson J. R., Fabian A. C., 2006, *PhR*, 427, 1
Salome P., Combes F., 2003, *A&A*, 412, 657
Salome P., Combes F., Revaz Y., Downes D., Edge A. C., Fabian A. C., 2011, *A&A*, 531, 85
Voit G. M., Donahue M., 1997, *ApJ*, 486, 242
Wrathmall S. A., Gusdorf A., Flower D. R., *MNRAS*, 2007, 382, 133

Curriculum vitae

Ik ben geboren op 2 Augustus 1981 te Hengelo in Overijssel (Nederland). Ik heb met veel plezier tot mij twaalfde levensjaar in Markvelde (nu gemeente Hof van Twente) gewoond. Het boerenleven daar gecombineerd met een goede school en kleine klassen heeft zeker positief bijgedragen and de persoon die ik vandaag de dag ben.

Mijn twaalfde de tot twintigste levensjaar heb ik in Denemarken doorgebracht. De ouderwetse stijl van lesgeven op de Realskole in Vinderup en het Gymnasium in Struer, was waardevol en hebben in grote mate bijgedragen aan mijn keuze om sterrenkunde in Leiden te gaan studeren.

Tijdens mijn studie heb ik als sterrenkunde student ook mogen profiteren van het natuurkundig onderzoek aan de Universiteit Leiden. Met veel plezier heb ik eerst als student en later als student-assistent in de groep van Giorgio Frossati meegewerkt aan het MiniGRAIL project om zwaartekrachtsgolven te meten.

De sterrenkundige studentonderzoeken hebben mij naar verschillende oorden op aarde gebracht. Van zowel mijn klein onderzoek aan het Max Planck Institut für extraterrestrische Physik (MPE) in Munchen met W. Collmar en mijn groot onderzoek aand het Radio Astronomy Lab (RAL) in Berkeley met A. Bolatto heb ik zeer genoten. In Leiden werden deze onderzoeken ondersteund door Huub Röttgering en Frank Israel.

Na mijn studie Sterrenkunde in Leiden gaf Walter Jaffe mij de mogelijkheid om op de Sterrewacht Leiden door te gaan met mijn promotieonderzoek naar clusters van sterrenstelsels. Mijn werk heb ik gepresenteerd op conferenties in Nederland, Italië, Brazilië en India. Ik ben tevens voor werkbezoeken naar Madrid en Parijs geweest. Aan de Sterrewacht Leiden ben ik drie jaar lang als werkcollegeassistent bij het college sterren betrokken geweest.

Tijdens mijn promotie heb ik mogen waarnemen met de Very Large Telescope (VLT) van het European Southern Observatory (ESO) in Chile. Deze telescoop staat in de Atacama woestijn. Dit is de droogste plek op aarde, maar tijdens mijn verblijf aldaar regende en het sneeuwde het zoveel zodat we geen enkel lichtdeeltje op hebben kunnen vangen. Ik heb tevens twee keer mogen waarnemen met de Giant Metre-wave Telescope (GMRT) in India.

Het observeren van clusters van sterrenstelsels met o.a. een radiotelescopen is zeker iets wat ik in de komende jaren zal voortzetten bij Stichting Astronomisch Onderzoek in Nederland (ASTRON).

Nawoord

In de 10 jaar tijd die ik in Leiden heb doorgebracht is de Sterrewacht een stabiele factor in mijn leven geweest. De onderzoeken die ik heb mogen uitvoeren onder de supervisie van Frank Israel en H. Röttgering waren gekenmerkt door een hoge mate van vrijheid. Deze vrijheid, mits goed beheerd, vindt ik van groot belang voor fundamenteel onderzoek.

Reinout, Ernst en Maarten bedankt voor de discussies tijdens de vele lunches en koffiekwartiertjes die we samen doorbrachten. Niruj, Nina, Marcel, Mehdi, Sarah, Cyril and Rowin thanks for being great office mates over the years. I greatly enjoyed being part of such a dynamic and creative office atmosphere. David, Tycho, Aart en Erik, zonder een goed systeembeheer kan er geen goed onderzoek gedaan worden.

I wil hier tevens graag iedereen verbonden aan de Sterrewacht Leiden bedanken voor jullie hulp gedurende de laatste tien jaar. Ik ben het Leids Kerkhoven Bosscha Fonds dankbaar voor hun financiële steun.

Mam en pap bedankt voor jullie steun tijdens dit hele traject. Zonder jullie was dit alles niet mogelijk geweest. Ondanks de vele, lange reizen vanuit het westen van het land is het altijd fijn om weer thuis in het oosten te zijn. Zusjes, Yvonne en Pauliene, bedankt voor jullie hulp. Zonder jullie was mijn leven waarschijnlijk een stuk saaier geweest.

Stephanie you came into my life as an officemate during a grey and cold winter day. You immediately captured my heart and mind. I would like to thank you for your love and support. A life without you is unimaginable, I love you and I always will. I would also like to take this opportunity to thank my family in law for warmly welcoming me into their lives.

